Understanding Polar Atmosphere-Ocean-Sea Ice Momentum Transfer Using Remote Sensing and Modeling Techniques

Dissertation submitted by

Alexander Mchedlishvili

to fulfill the requirements
for the degree of

Doctor of Natural Sciences (Dr. rer. nat.)

to

Faculty 1
Physics and Electrical Engineering
University of Bremen

Date of Submission: 26.03.2024

Reviewers:

Reviewer 1: **Dr. Gunnar Spreen**
Institute for Environmental Physics
University of Bremen

Reviewer 2: **Prof. Dr. Christian Haas**
Alfred Wegener Institute
Helmholtz Centre for Polar and Marine Research

Date of Colloquium: 18.06.2024

Abstract

Over the last half a century, the Arctic sea ice extent and volume have been decreasing as a result of the amplified warming taking place in the Arctic. Similarly, the Antarctic summertime sea ice extent maximum has been the lowest in the satellite record for the last three years. As sea ice at both poles is changing in a warming climate, it is necessary to better understand the fundamental processes that determine sea ice properties such as extent, thickness, volume and drift. These processes, namely dynamic and thermodynamic ones, are triggered by the surrounding atmosphere and ocean. The overarching goal of this dissertation is to study dynamic processes while also considering thermodynamic aspects. Chapter 3 delves into the above-mentioned dynamic and thermodynamic processes at mesoscale in the study of polynya events and thin sea ice anomalies above Maud Rise in the Antarctic. Chapter 4 looks at parameters that quantify dynamics, specifically at drag coefficients (C_d) that determine the momentum transfer between the atmosphere and sea ice, on a pan-Arctic scale. Finally, Chapter 5 implements the derived estimates of drag from observations into a coupled regional atmosphere-ocean-sea ice model in order to investigate the impact of variable drag on sea ice properties Arctic-wide.

The Weddell Sea Polynya (occurring in 1974-1976 and 2016-2017) is an excellent case study in the impact of mesoscale as well as synoptic scale processes on sea ice. My analysis of the events corroborates past studies that identify the Weddell Sea polynya as one that is driven by dynamic as well as thermodynamic processes. In addition, using satellite-borne microwave imaging radiometers, large thin sea ice anomalies have been identified in polynya-free years (2010-2020). Given the reported links between the polynya and different dynamic and thermodynamic ocean and atmosphere processes, our results suggest that when an insufficient amount of these processes are active, a thin sea ice anomaly may emerge instead.

The neutral sea ice-atmosphere C_d data-set is the first-ever assessment of drag on both pan-Arctic spatial and sub-yearly temporal scales. Leveraging the high resolution of Ice, Cloud and land Elevation Satellite 2 (IS2), as well as near-coincident Operation IceBridge (OIB) airborne surveys of sea ice topography, it was possible to observe the spatiotemporal evolution of drag from November 2018 to May 2022. My results showed the ice area directly north of the Canadian Archipelago and Greenland to have a C_d consistently above 2.0×10^{-3}, while for most of the multiyear ice portion of the Arctic it is typically around $\sim 1.5 \times 10^{-3}$. The first-year and young ice portion of the Arctic has a comparatively lower C_d ($\sim 9 \times 10^{-4}$) with an increase along the marginal ice zone that exceeds 1.5×10^{-3}. This dataset was then used to derive a parameterization linking C_d to coincident IS2 sea ice thickness measurements, which was implemented into the regional atmosphere-ocean-sea ice model HIRHAM-NAOSIM. By running the model with and without the implementation, my results showed reasonable albeit small differences between the sea ice properties modelled by the two runs. Using sensitivity studies that varied the coefficients and integration of the C_d parameterization, I was then able to explain the differences observed. The main findings from the model study are that atmospheric and oceanic drag have the opposite effect on both sea ice drift and thickness on a pan-Arctic scale, and that over a period of three years, regardless of the range in drag variability, the impact of drag on sea ice in a coupled model is typically small in magnitude (<5% differences in both sea ice drift and thickness).

Contents

1 Introduction

This dissertation will detail the results reached over the span of my doctoral project. The main subject of my study throughout this time period was sea ice. Thus, in this introduction I aim to cover all aspects of sea ice, to then describe what I have contributed in our understanding of it in later chapters. Before delving in however, I believe it is important to first look back to truly appreciate how far we have come in the study and observation of remote polar regions. For it is precisely this advancement that has allowed me to do the science which I will be presenting on in this dissertation. As such, though the technological limitations and the associated uncertainties are very much a part of my findings, I find it remarkable that the data sets presented here were able to be produced at all: a sentiment, I hope the reader will share with me upon reading this dissertation.

For more than a millenium, the only recorded account of sea ice came from Pytheas of Massalia who had journeyed to northwestern Europe ca. 325 BCE. Though his findings became widely known during the Age of Antiquity, his records of it did not survive. Nevertheless, his journey and findings are mentioned by his successors, and though Pytheas was often discredited, his descriptions were to become the only written account sea ice for centuries to come. One such mention by Strabo goes over Pytheas' description of the waters sorrounding Thule, the land that was thought to be furthest north which is likely either modern-day Iceland or Norway. Pytheas' description of the seas surrounding Thule detail an area "where land properly speaking no longer exists, nor sea nor air, but a mixture of these things, like a "marine lung", in which it was said that earth and water and all things are in suspension as if this something was a link between all these elements, on which one can neither walk nor sail." (Strabo 1917).

With such an esoteric description, it is not surprising that the exploration of such other-worldly places was limited for a sizeable portion of human history. It would be the vikings, a people likely unfamiliar with Pytheas' account, who would next advance our understanding of the ice-covered seas. In fact, just some years after Naddodd, a Norwegian viking that was blown off-course on his voyage to the Faroe Islands, had found Iceland in ca. 860 CE, We begin to have a 1200 year record of sea ice near the shores of Iceland after its settlement in ca. 870 CE (Polyak et al. 2010).

Here it is important to acknowledge that pre-inuit cultures that predate the vikings, and even Pytheas, were very much present in areas with sea ice. It is safe to say that they were much better informed on the properties of sea ice than the rest of the world as they co-existed with it for nearly 4 millenia. It is therefore unfortunate that no written record of theirs exists and the rest of the world was left in the dark with regard to polar ice caps until the above-mentioned findings.

It would be much later, in the period since 1870, when a systematic record of the sea-ice margin around the Arctic Ocean would be compiled (Polyak et al. 2010). This record varies in quality and content over time and is only properly supported by direct observations of sea ice around the Arctic Ocean since 1953. Despite the many scientific discoveries from the daring voyages into the

Arctic and Antarctic polar ice caps, there was still little that could be done to monitor the thickness, roughness and and concentration of sea ice on large spatial scales.

Importantly, our knowledge on the Arctic polar ice pack had evolved throughout the 1900s thanks to the studies conducted by the scientific stations on sea ice that were maintained both by the Americans and the Soviets. Daring under-ice voyages, first by the USS Nautilus (1958) and then by USS Queenfish (1970) (McLaren 1989), finally helped us understand the thickness distribution of the Arctic ice pack, but repeated pan-Arctic measurement only became possible with satellites. While the TIROS weather satellites managed to look at the Arctic from orbit as early as the 1960s, without being able to see through clouds and being unable to see either pole in its respective winter, the observation of remote polar regions still had a long way to go. It would be in 1972, when the newly launched Nimbus-5 Electrically Scanning Microwave Radiometer (ESMR) instrument would revolutionize sea ice remote sensing. This instrument would be the first to grant daily and monthly averaged sea ice concentration (SIC) for both the Arctic and the Antarctic (Parkinson et al. 2004). Since then, satellite coverage of polar regions has only improved. Fast-forward to today and it can easily be said that we are now in the golden age of sea ice observation with multiple satellites measuring sea ice properties in parallel, and in-situ and airborne campaigns helping to validate the collected data.

To summarize, we have gone from viewing sea ice as a suspension of earth and water that could be neither walked nor sailed on, to walking, sailing, swimming under and flying over it. Finally, in order to fully understand sea ice properties we need to be able to observe it regularly, and that is precisely what passive microwave instrumentation onboard satellites has achieved. This advancement cannot be likened to simply mapping a continent or a similar one-time discovery as the repetition of measurement is essential to monitor the dynamic environment that is the sea ice pack. Without regularity, we cannot hope to study how the system evolves in time. Without sufficient spatial coverage, we can only study a part of the whole system. As discussed later in this study, the current methods are by no means perfect and compromises with regard to both spatial and temporal coverage are often made as a result of technological and physical limitations. However, I count myself very fortunate to be investigating sea ice in this day and age. Despite dealing with satellite remote sensing data products on a regular basis I still find it astounding that we can report on the sea ice extent and volume, of both polar ice packs, every day of every year since the respective satellites measuring these quantities have been in orbit.

Now that we have covered the history of sea ice observations, it is time to focus on what the scientists have been observing. Namely, what are the properties of sea ice, what is their spatial and temporal distribution, and how is sea ice changing in a warming climate.

1.1 What is sea ice?

Sea ice is frozen saltwater. At first read, this makes it out to be rather simple. However, through this basic definition we can already infer how unique this material is. Let us start with dissecting frozen water, or ice. Thanks to its hexagonal lattice crystalline structure, it is one of the few solids that is less dense and therefore lighter than its liquid state. This is the reason ice floats and why ice formation typically begins at the top of a body of water. The temperature of maximum density of freshwater, for example, is 4 °C. Thus if the atmosphere above a freshwater lake cools below 4 °C, water directly at the surface that is cooled to 4 °C will be pushed down as it has become as dense as it can be. This will continue until the whole water body is at 4 °C, and the top-most layer freezes rapidly as it can no longer sink. After the formation of this initial layer, the thickening of it follows slowly as the cold temperatures penetrate through the ice layer. Add some salt into the mix, as is the case with ocean water, and the whole situation changes! Namely, the temperature of maximum density of saltwater is lower than its freezing point (Petrich et al. 2017). Importantly, the sea ice itself is still less dense than saltwater, but in its liquid state, the cooler the saltwater becomes, the more it sinks. Except when it is stratified, i.e., separated into different layers with salinity and temperature differences. In this case, the saltwater in the top-most layer, the surface mixed layer, will completely cool until ice formation sets in. Like so, once the top layer freezes, it can become thicker relatively quickly as it surrounded by saltwater that has been cooled to freezing temperatures.

Ice being less dense than water is a consequence of its microstructure, wherein the mean distance between the water molecules is larger when they are arranged in a solid crystalline structure as opposed to when they float close to one another due to their polarity. Here again, the introduction of salt complicates things! Only a very few sea salt ions can exist within the ice microstructure due to their size and electric charge. The majority, including both Na^+ and Cl^-, are not incorporated (Petrich et al. 2017). This means they are ejected and are often relegated to small liquid inclusions or slowly pushed out from below the ice. These concentrated liquid inclusions, also called brine inclusions, are yet another reason sea ice is so different from freshwater ice. Light that hits the sea ice is scattered due to a contrast in refractive indices of the constituent materials, namely the ice crystals and the brine inclusions. This is the reason why sea ice is less transparent than freshwater ice, and it is also the reason why it has a higher albedo.

Albedo is the fraction of the incident short-wave radiation reflected from a surface. The more reflective the surface, the higher this fraction becomes. Freshwater ice lets more than three-quarters of incident short-wave radiative flux pass through whereas sea ice reflects more than half of it. This means sea ice has a higher albedo than freshwater ice, and incidentally it is also higher than the albedo of open water by a factor of 10 (Petrich et al. 2017). If we look at our planet as a whole, this means far more energy is being absorbed where there is open water as compared to where there is ice.

Decreasing sea ice area results in more overall absorption, which has very important consequences that will be discussed in further detail in Section 1.4.

Now that we have transitioned from the microstructure of sea ice to its macroscale properties, we can cover how the ice layer interacts with the surrounding ocean, atmosphere and in some cases, land (see Section 1.2). Between the liquid ocean and the atmosphere above, sea ice forms a highly dynamic barrier. Ocean currents and winds directly influence the distribution of sea ice and are the drivers of dynamic thickening and thinning, i.e., thinning due to break up caused by divergence and thickening via convergence-driven pressure ridge formation (Haas 2017). This motion is facilitated through friction, specifically drag, which is the force acting opposite to the relative motion of an object (sea ice floes) with respect to a surrounding fluid (ocean and atmosphere). The sea ice layer can be considered as barrier because of its many properties that damp the thermodynamic and dynamic exchange between the atmosphere and ocean. First and foremost, it acts as an insulator that reduces the heat exchange between the relatively warmer ocean and the seasonally much colder atmosphere. This is also the reason why sea ice can only reach a certain thickness ($\sim$1-3 m for a large majority of the Arctic ice pack in winter months), because at a certain point, the oceanic heat flux will exceed the conductive heat flux through thick ice which inhibits further ice growth (Haas 2017). In addition, it dampens the momentum transfer between the atmosphere and ocean, e.g., wind-driven waves can be strongly attenuated by the sea ice cover. Last but not least, as mentioned previously, sea ice has a high albedo and thereby reflects a lot of the incoming short-wave radiation that would otherwise be absorbed by the ocean, which would then warm. Thus, sea ice can be likened to the attire of nomadic Bedouin tribesmen, which shelters the body from the desert heat during the day, the cold during the night, the winds when they are present and the short-wave radiation of the desert sun.

1.2 Antarctic sea ice cover

Unlike the story of Pytheas mentioned earlier, wherein he crossed the Arctic circle and found Arctic sea ice in 325 BCE, the exploration of the Antarctic sea ice would only follow ca. 2 millennia later, in January of 1773 CE, when James Cook crossed the Antarctic circle (Meredith et al. 2017). Perhaps the most obvious reason for this time lag is the primary difference between the Arctic and the Antarctic: the former is an ocean surrounded by land and the latter is a landmass surrounded by ocean. Incidentally, the land surrounding the Arctic, i.e., North America and Eurasia, has very much been a home to many humans since prehistoric times. The Antarctic continent on the other hand, has had neither human activity prior to its discovery nor a means by which humans could reach it before the Age of Discovery.

As the Antarctic continent is surrounded by the Southern Ocean which is home to the largest current system in the world, the Antarctic Circumpolar Current (ACC), the sea ice that surrounds it is very much influenced by oceanic activity. The ACC transports approximately $130 \times 10^6\,\mathrm{m^3\,s^{-1}}$

of water eastward around the Antarctic, thereby influencing the ice pack during the austral winter when the outer edge of the Antarctic sea ice pack hitches a ride on the eastward moving waters. Closer to the continent lie a few cyclonic sub-polar gyres that make the motion of sea a little more interesting. Cyclonic gyres in the southern hemisphere rotate clockwise, most notably in the two sheltered seas of the Antarctic continent: the Weddell Sea and Ross Sea. As the Antarctic ice pack is not constrained by a land barrier, it is therefore not surprising that the difference between its maximum extent of 19×10^6 km^2 and minimum of 3×10^6 km^2, is 1.5 larger than the seasonal change in the Arctic (Meredith et al. 2017).

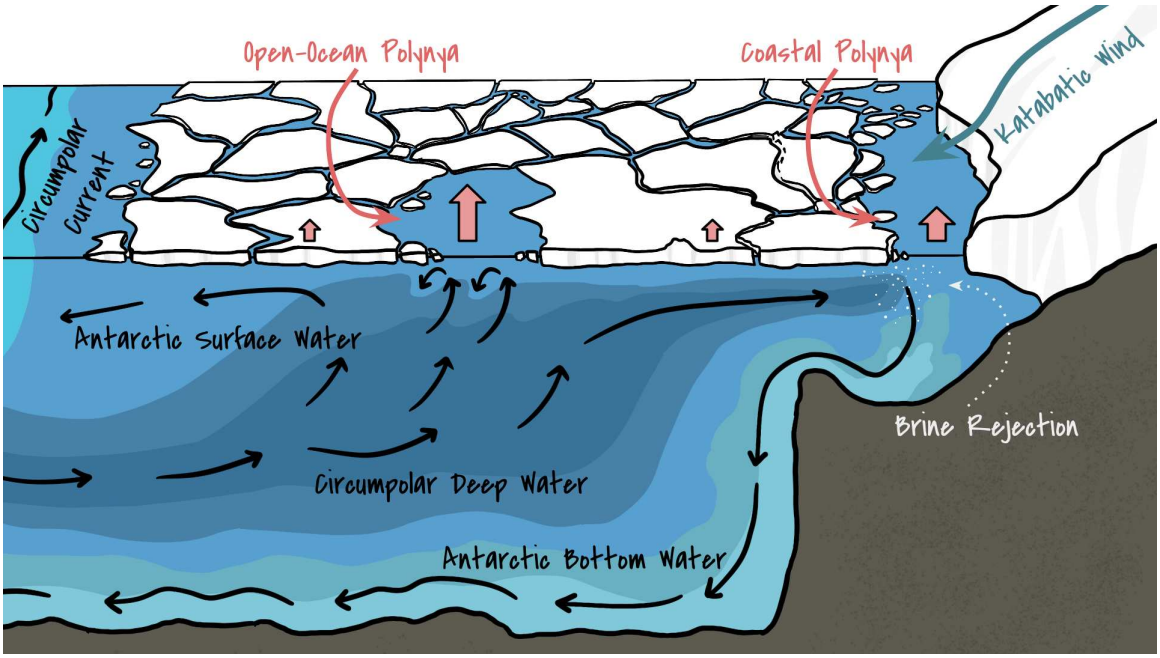

Figure 1.1: A schematic describing the meridional circulation pattern of the Southern Ocean near the Antarctic continental shelf. The cross-section includes an example of an open-ocean polynya and coastal polynya with arrows that describe physical processes that cause their formation (based on a schematic by Gordon et al. (1988)).

The formation of sea ice in the Antarctic is primarily occurring in polynyas. The term polynya refers to large openings in sea ice that maintain their ice-free conditions for extended periods of time. They are further subdivided into two categories: latent-heat or coastal polynyas and sensible-heat or open-ocean polynyas. The former are mechanically driven, primarily by katabatic winds that cascade down the Antarctic continent. The heavy gravity-driven cold air falls off the continent and advects the sea ice away from the Antarctic coast. Under these conditions, land has the most pronounced effect on sea ice as it essentially facilitates its production. With the ice advected away from the coast, the cold winds then help freeze the exposed waters to form new sea ice. Upon freeze-up, the formation of sea ice keeps the surrounding waters at a freezing temperature through

the latent heat of fusion (energy required to melt ice into water). Thus, through a combination of different phenomena, the coastal polynyas are excellent sea ice producers that are far more efficient than the nearby ice-covered areas. They also play a key role in modifying shelf water properties, e.g., through brine rejection during ice formation, which then has a direct impact on the formation of Antarctic Bottom Water (Meredith et al. 2017).

The other type of polynyas are are typically found away from the coast, hence open-ocean, and are generally thought to be thermally driven via the oceanic sensible heat flux melting the ice from below. In the case of the Antarctic, the heat flux originates from the relatively warm Circumpolar Deep Water that is brought to the surface (as shown in Fig. 1.1). Reoccurring open ocean polynyas are often linked to warm water anomalies that are responsible for their formation. A famous example of such an anomaly in the Antarctic is above the Maud Rise seamount in the Weddell Sea. There the seamount facilitates the upwelling of warm water by interacting with nearby ocean currents. As such, this polynya is one of the few recurring sensible-heat polynyas since its cause is partly linked to a fixed thermal anomaly. However, as will be made clearer in Chapter 3, the thermal anomaly is not the principal cause. And in fact, it has since been found that dynamic atmospheric influences are just as necessary to cause the formation of the polynya as thermal processes, making it more of a hybrid polynya rather than a purely sensible-heat one (Heuzé et al. 2021; Mchedlishvili et al. 2022).

Before moving on to the Arctic (Section 1.3), it is also important to mention another element that plays an important role for both polar sea ice packs: snow. However, the reason we focus on it in this Section is because, on average, the Antarctic ice pack gets far more snow than its northern counterpart (Haas 2017). Another consequence of the Antarctic being surrounded by oceans is that it has a continuous supply of moisture. In addition, Antarctic sea ice collects the snow blown off continental ice shelves. Snow plays an important role as an additional and more potent source of insulation. With enough snow, the sea ice–atmosphere heat flux can be diminished to the point that the ocean begins to more readily melt the ice from below. Additionally, dry snow further enhances sea ice albedo.

1.3 Arctic sea ice cover

The Arctic is essentially a landlocked sea, the one major connection the Arctic Ocean has with the rest of the world's oceans is through Fram Strait where the circumpolar shallow continental shelf is broken. Incidentally, these shelf areas account for ca. 50% of the Arctic sea floor, especially in the Russian Arctic and the Bering Strait. As this system is so isolated, the two currents that are present are both wind-driven. Namely, the Transpolar Drift that crosses the Arctic from Siberian Coast and the anti-cyclonic Beaufort Gyre over the Canada Basin (Cottier et al. 2017).

The seasonal cycle of the Arctic sea ice pack is such that it reaches its maximum extent of about $15 \times 10^6\,\mathrm{km}^2$ in March and a minimum of about $5 \times 10^6\,\mathrm{km}^2$ in September (Cottier et al. 2017).

With 5 million km^2 of sea ice typically left over every year, the Arctic has more Multiyear Ice (MYI) than the Antarctic. MYI is ice that has survived multiple summers (melt seasons) but first began as First-Year Ice (FYI). The transition occurs once the next freezing season is reached, thereby the FYI has successfully survived the full year and become MYI. These two ice types have notably different properties. MYI generally has a higher albedo and is thicker than FYI. Similarly, a longer lifetime results in more collisions and therefore more pressure ridging, resulting in a rougher surface. FYI, on the other hand, is comparatively smoother, thinner and with a lower albedo. Young ice, a subset of FYI with a thickness below 30 cm, is the most fragile and smooth ice type when formed in calm water conditions (common in the Arctic).

As mentioned, more MYI also implies an overall increase in thickness of the ice pack; therefore, the Arctic ice pack is thicker than the Antarctic one. Reasons for this however, are a bit more extensive than just ice age. For one, the Arctic ocean receives approximately 10% of the world's river run-off, freshening the surface mixed layer. This results in it being very stable and able to inhibit ocean heat flux. The Antarctic on the other hand has a much saltier and not well stratified mixed layer, resulting in an ocean heat flux bigger than that of the Arctic by a factor of 10 (Haas 2017). Other reasons are the generally divergent behaviour of Antarctic pack ice due to lack of surrounding landmasses, the fact that it is typically extends to lower latitudes (as for north as 55°S), and the snow-induced melting from below mentioned in Section 1.2 (Haas 2017).

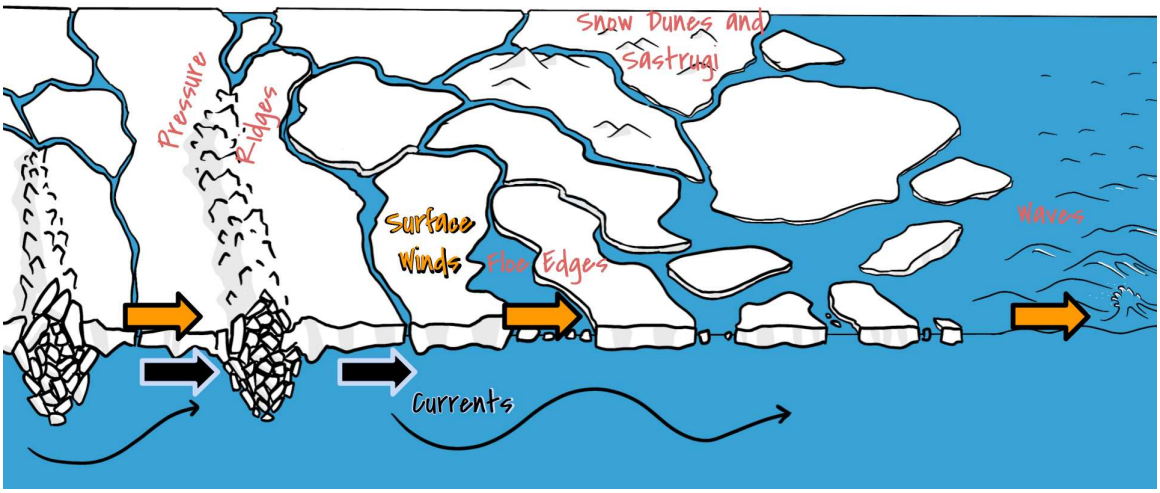

Figure 1.2: A schematic showing large distinct obstacles (marked in red) able to generate form drag when interacting with surface winds (marked in orange). In the case of pressure ridges and floe edges, surface currents (marked in black) can also impart form drag.

Topical to a large portion of this dissertation is the increased pressure ridge formation in the MYI portion of the Arctic. More pressure ridges increase the drag that the sea ice floes experience. Namely, form drag which is the drag associated to large distinct obstacles that is prevalent for

sea ice areas with lots of ridges or exposed floe edges (Arya 1975). Skin drag, which accounts for centimeter-scale roughness, is prevalent across all surfaces including sea ice but does not show nearly as much variation. Though pressure ridges are not unique to MYI and can occur anywhere thicker ice floes collide, sea ice that has existed multiple years is more likely to have undergone this process at some point in its lifetime. In addition to pressure ridges, floe edges also generate form drag, as do rubble fields, hummocks, snow dunes and sastrugi in areas with heavy precipitation. Open water, which is also present throughout the Arctic Ocean in leads, polynyas and the Marginal Ice Zone (MIZ), has its own associated skin drag as well as form drag caused by ocean waves that form further away from the sea ice floes. In the case of the Arctic, it is the thick MYI portion north of Greenland and the Canadian Archipelago, as well as MIZ, that is able to impart the largest form drag both above and below the sea ice. Below the sea ice layer, certain features like pressure ridges and floe edges, protrude even more so below than above the water surface, thereby generating more drag at the sea ice–ocean interface.

1.4 The effects of climate change on sea ice

Arctic sea ice is perhaps one of the best indicators of anthropogenic climate change. Since being able to monitor the Arctic sea ice pack, we have seen it decrease in area, thickness, and therefore also volume (Meier 2017). Through passive microwave imagery since 1972 (see Section 1), sea ice extent has been monitored for over half a century now. In this time, we have observed a considerable decline of -13.3% per decade (relative to the 1982-2010 average) in summer and -2.3% per decade in winter (Meier 2017). On regional scales, there is a decline in all sectors (save for the Bering Sea during winter and spring), and it is most prevalent near the ice edge.

This decline is partly caused by a phenomenon known as Arctic Amplification (AA), wherein the Arctic warms faster than the rest of the world as global temperatures rise (as can be seen in Fig. 1.3). The ratio at which the Arctic warms as compared to the rest of the world has been initially reported to be two-fold (Cohen et al. 2020), and more recently found to be as high as four-fold (Rantanen et al. 2022). Indeed, over a similar time-span during which we have observed sea ice decline, we have found AA to be prominent in the annual surface air temperature trends (Serreze et al. 2011). Both sea ice decline and AA are related to one another through the sea ice–albedo feedback, wherein as the sea ice area decreases, newly exposed dark open water areas absorb incoming solar radiation more readily than the bright sea ice. This creates a positive feedback loop that leads to an increase in sea ice melt and an increase in average temperatures across the Arctic. The way this process affects the annual cycle of sea ice is as follows: the summer melt period will lengthen as a result of increased temperatures, and the top layer of the ocean warming up due to incoming solar radiation will also contribute to this melt. In winter, all this added heat in the ocean surface mixed layer will inhibit sea ice growth and result in a thinner ice layer. Thinner ice will more readily melt the next

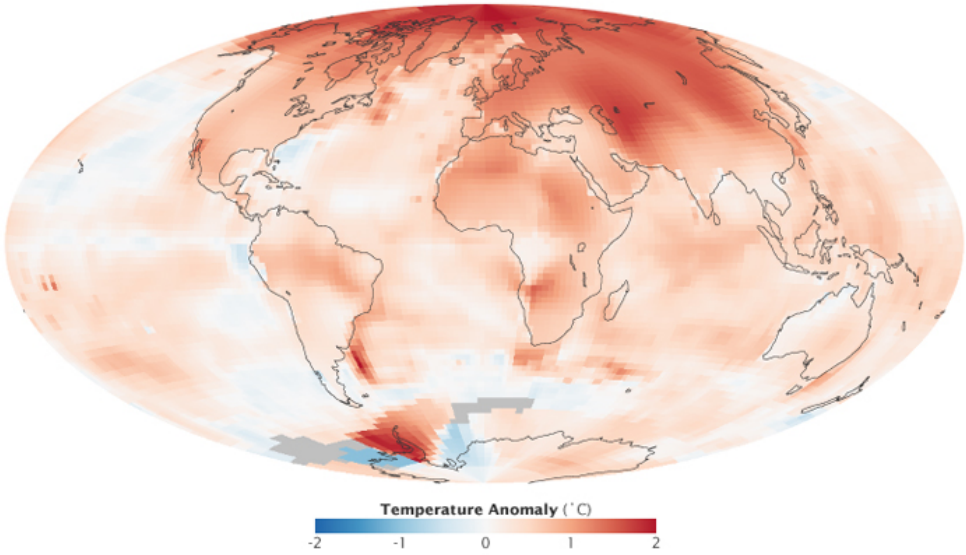

Figure 1.3: A figure showing global temperature anomalies for the 2000 to 2009 time period in degrees Celsius deviated from the 1951 to 1980 regional norms. Source: https://climate.nasa.gov/news/927/arctic-amplification

summer, and the cycle continues (Serreze et al. 2011). Importantly, AA has other driving feedback loops, e.g., lapse-rate and Planck feedbacks, that are not directly tied to sea ice.

Thus, AA is tied not only to sea ice area but also its thickness. Thickness is a quantity that is harder to measure from space than area since most satellites can only observe surface characteristics and are unable to see through the ice layer. Before the satellite era, monitoring sea ice thickness (SIT) was temporally and spatially sparse (primarily in the form of upward-looking sonars mounted on submarines mentioned in Section 1). Regular monitoring of pan-Arctic SIT began with the dawn of satellite and airborne altimetry (Meier 2017) (see Section 2.2 for technical details). In the early 1990s, with the launch of ESA European Remote-Sensing Satellites 1 and 2 which were radar altimeters, and thereafter in 2003, with the more capable NASA Ice, Cloud and land Elevation Satellite (ICESat) laser altimeter put into orbit, SIT could be monitored on pan-Arctic scales. This was supplemented with airborne Operation IceBridge (OIB) surveys because of instrument limitations and the eventual failure of ICESat in 2009. Shortly after, ESA's CryoSat-2 was launched in 2010, and in 2018, Ice, Cloud and land Elevation Satellite 2 (IS2) was put into orbit as well. Thus, thanks to the the radar altimeter on board CryoSat-2 and the laser altimeter on board IS2, we now have the most extensive coverage of Arctic sea ice with both satellites operating in tandem. In addition, advances in microwave remote sensing have also shown promise in measuring thin SIT during freeze-up with

satellites such as ESA's Soil Moisture Ocean Salinity (SMOS) and NASA's Soil Moisture Active Passive (SMAP) (Huntemann et al. 2014).

Putting all these SIT data together, we observe an overall thinning of Arctic sea ice (Meier 2017). In addition, through the use of passive microwave and active scatterometer data, it can also be seen that MYI is disappearing. Thus, the Arctic is transforming into a primarily FYI-dominated ocean with comparatively thinner sea ice cover. This thinning has big consequences for many aspects of the Arctic climate system, but perhaps most relevant to this dissertation is the reduction of rough MYI which generates more drag than the smoother FYI. With less MYI, the average drag force between sea ice and the surrounding atmosphere and ocean is likely going to decrease. What this means on longer time scales is however not clear as a thinner ice pack is less compact and thus more susceptible to wind stress. In general, Arctic sea ice drift speed has been observed to be increasing throughout the last decades (Spreen et al. 2011).

The story of the Antarctic is more complicated with regional variations in sea ice extent, an overall increase over long timescales and three recent consecutive all-time minima. As such, it is difficult to observe linkages between the behaviour of the Antarctic sea ice pack and global climate change. One reason for this is that the Antarctic sea ice pack is highly dynamic on account of it being exposed to the open Southern Ocean. As such, wind is the predominant factor driving sea ice motion since there are no surrounding landmasses to constrain the pack ice (Stammerjohn et al. 2017). Another reason is the sparsity of data: unlike in the Arctic, there have been less in-situ measurement campaigns in the Antarctic. Nevertheless, changes forced by global climate change are affecting the area, the surface air temperatures have increased all over Antarctica and precipitation, ocean warming and regional ocean freshening are also on the rise (Stammerjohn et al. 2017). Differentiating changes in Antarctic sea extent driven by variability and the effects of climate change will be ever more important as the global average surface temperature continues to rise.

1.5 Dissertation structure and main research questions

Notably, in this introduction Section, we have covered both Arctic and Antarctic sea ice. While the differences are important in understanding the fundamental nature of sea ice on Earth, the main reason for describing them was to prepare the reader for the studies discussed in this dissertation. Namely, studies about sea ice from both hemispheres, linked to one another by the overarching topic of sea ice dynamics and atmosphere-ocean-sea ice momentum transfer.

The first study is based on a paper built on the work done for my master thesis. The thesis as well as the paper that followed pertains to the Weddell Sea Polynya, a latent-heat open-ocean polynya off-coast Antarctica. While a lot of the work involved was completed during the duration of the master project, it was only after the start of the PhD that the paper materialized. As such, it finds itself in this dissertation since the study encompasses more, despite its smaller size, than the thesis it is based upon. This study includes a literature review of papers that look at the drivers

behind the Weddell Sea Polynya. In addition, the time period investigated is longer than the two years looked at in the thesis and reflects the full life-time of the satellites used. The two main hypotheses of the study that pertain to this dissertation, presented as research questions (**RQ**s) 1 and 2, are contained in the box below:

RQ1 Is sea ice–atmosphere momentum transfer as important as oceanic sensible heat flux transfer in forming the Weddell Sea Polynya?

RQ2 What happens when the different drivers behind the formation of the Weddell Sea Polynya do not occur simultaneously?

The title of the publication that serves as the basis of Chapter 3 is *Weddell Sea polynya analysis using SMOS–SMAP apparent sea ice thickness retrieval* and it is published in *The Cryosphere*.

Going from Chapter 3 to 4, we not only change hemisphere but also the scope; while the first study aims to look at dynamics on regional scales, namely in the near vicinity of 2016-2017 occurrence of the Weddell Sea Polynya, the second study looks at the whole Arctic sea ice pack. The parameter analysed is the sea ice–atmosphere momentum transfer, in the form of drag coefficients, on a pan-Arctic scale. In addition to the overarching topic of sea ice dynamics, the first and second chapters are related to one another through the use of satellite remote sensing. However, while for the detection of the Weddell Sea Polynya sea ice anomalies, passive radiometer data was used, for the study of pan-Arctic drag, an active satellite altimeter was employed. In this way, small topography variations were related to drag coefficients using a parameterization (Garbrecht et al. 2002) previously evaluated on airborne data. **RQ**s 3 and 4, based on this study, are as follows:

RQ3 Can sea ice–atmosphere momentum transfer be better resolved in both space and time through the use of high-resolution altimeter data?

RQ4 Does the satellite-based analysis of drag coefficients reveal the annual evolution of drag and if so, how does it behave?

The title of the publication that serves as the basis of Chapter 4 is *New estimates of pan-Arctic sea ice–atmosphere neutral drag coefficients from ICESat-2 elevation data* and it is published in *The Cryosphere*.

The last focus and task of this PhD project was to evaluate the retrieved drag coefficient data in a coupled regional atmosphere-ocean-sea ice model. This task was accomplished through the use of the coupled model HIRHAM-NAOSIM. Thus Chapters 4 and 5 represent the full story of the drag coefficient study from its retrieval to its implementation. The latter, is the implementation and first

look at obtained results which is meant to be a preliminary study towards a better representation of drag coefficients in coupled models. The final study is meant to address the last two **RQ**s of this dissertation:

RQ5 Is sea ice thickness a reliable proxy for form drag coefficients and can this relation represent the influence of form drag in a coupled atmosphere-ocean-sea ice model?

RQ6 Is the impact of form drag significant within a model simulation spanning a period of 3 years? And if not, is more time needed to observe notable changes?

Last but not least, I would like to direct the reader to Appendix D, where my science communication projects, as well as the inspirations behind them, are discussed. Science communication is a much-needed transfer of knowledge from scientists to non-experts in a given field. Through this transfer, the public at large can better understand the world around them and use scientific information to make informed decisions. Especially in the case of environmental sciences, these informed decisions can, in turn, help mitigate future climate catastrophes.

2 Theory and methods

In this chapter, I explain the common theme linking the studies in this dissertation: sea ice dynamics. Though covered to a lesser extent in Chapter 1, as well as in the introduction sections of the included studies, here we will look at the bigger picture to set the stage for later discussions. The following summary of sea ice dynamics is applicable to sea ice at both poles, with subtle differences that can be reflected in the parameters used in the governing equations.

While instrument-specific details are contained within Chapters 3 and 4, their fundamental principles are very briefly elaborated on. Therefore in Section 2.2, I will also briefly summarize the general information on remote sensing methods used for the studies presented in this project.

Lastly, we will look at coupled regional atmosphere-ocean-sea ice modelling of the Arctic climate system, the basic components of such models as well as how they function in tandem. While Chapter 5, contains the specifics that pertain to the study at hand and the model used (HIRHAM-NAOSIM), in this Chapter, the component models as well as the coupling used in all such models will be discussed.

2.1 Sea ice motion

We start from Newton's second law, $m\frac{d\vec{u}}{dt} = \vec{F}$, and modify the terms such that they are specific to the motion of sea ice. Thus $\vec{F}$ becomes the forcing that acts on sea ice and $\vec{u}$ is the motion or drift of sea ice. Next, as we are considering sea ice as a whole and not a single floe, continuum mechanics modifications are necessary. For one, depending on the dimensions of space considered, m becomes the mass per unit area or volume for ice continuum particles. Second, the force due to the internal ice stress field $\vec{\nabla} \cdot \vec{\Sigma}$ is included in $\vec{F}$, and third, the Eulerian frame is used to ascertain the advective acceleration terms. With these considerations taken into account, we may now rewrite Newton's second law as the Cauchy equation of motion of a continuum (Leppäranta 2005):

$$\rho \left(\frac{\partial \vec{u}}{\partial t} + \vec{u} \cdot \vec{\nabla} u \right) = \vec{\nabla} \cdot \vec{\Sigma} + \vec{F}_{ext}, \tag{1}$$

where ρ represents the density of sea ice. Notably the left hand side becomes the summation of internal ($\vec{\nabla} \cdot \vec{\Sigma}$) and external forces ($\vec{F}_{ext}$) acting on the sea ice. These forces represent the stress due to interactions between ice floes $\boldsymbol{\sigma}$, the pressure p applied by the surrounding atmosphere and ocean, as well as the external body forcing caused by Earth's gravity. Adding the Coriolis acceleration to the inertial term and writing the force due to gravity as the gradient of the geopotential height of the sea surface $\vec{\nabla}\Phi$, we may write the momentum equation for sea ice as:

$$\rho \left(\frac{\partial \vec{u}}{\partial t} + \vec{u} \cdot \vec{\nabla} u + 2\vec{\Omega} \times \vec{u} \right) = \vec{\nabla} \cdot (\boldsymbol{\sigma} - p\boldsymbol{I}) - \rho \vec{\nabla} \Phi, \tag{2}$$

where p represents pressure, $\boldsymbol{I}$ is the unit tensor, and $\boldsymbol{\sigma}$ is the stress tensor (where **bold** characters are second-order tensors). This is the equation of motion valid for all three dimensions of space, from here, vertical integration through the thickness h of ice would be necessary to derive the general form of the equation of motion of sea ice on the surface plane. But as this rigorous mathematical proof is not needed to understand the underlying physics of the research presented in this dissertation, we will instead use the following, already integrated and simplified form:

$$\rho h \left(\frac{\partial \vec{u}}{\partial t} \right) = \vec{\nabla} \cdot \boldsymbol{\sigma} + \vec{\tau}_a + \vec{\tau}_w - \rho h \left(\vec{g} \Delta H - f_c \hat{k} \times \vec{u} \right), \tag{3}$$

where each term has units of force per unit area of ice cover. The divergence of the two-dimensional stress $\vec{\nabla} \cdot \boldsymbol{\sigma}$ represents the internal ice forces, and the atmosphere-ocean stresses $\vec{\tau_a} + \vec{\tau_w}$ are derived from external pressure p through the boundary condition that the ice shear stress must match the shear stresses of air and water (Leppäranta 2005). The horizontal pressure gradient $\vec{\nabla} p$ integrates to zero in the ocean and is small enough in the atmosphere to be neglected (Leppäranta 2005). The vertical component of the Coriolis acceleration arising from the eastward velocity component as well as vertical motion are neglected, and therefore $2\vec{\Omega} \times \vec{u}$ is reduced to $f_c \hat{k} \times \vec{u}$ where $f_c = 2\Omega \sin \phi$ is the Coriolis parameter and $\hat{k}$ is the unit vector normal to the ice surface directed into the atmosphere. The gradient of the geopotential height of the sea surface $\vec{\nabla}\Phi$, upon integration and simplification, results in the sea surface term $\vec{g}\Delta H$, where H is the sea surface dynamic height and $\vec{g}$ is the acceleration due to gravity. Lastly, in our simplified equation, the advective acceleration term $\vec{u} \cdot \vec{\nabla} u$ is neglected, as it is small compared to the terms that remain.

Incidentally, the resulting momentum balance equation is what was derived through the Arctic Ice Dynamics Joint Experiment (AIDJEX) in the 1970s. This venture, funded by the United States and Canada, was conducted by measuring atmospheric, oceanic and sea ice motion and stresses to understand sea ice dynamics. Assessing the terms in the equation, and comparing them to measurements, it becomes evident that wind is most often the primary driving force (Leppäranta 2005). Wind stress is balanced by the ice-ocean drag and internal friction. Together, these three dominating forces are the primary determinants of sea ice motion (Feltham 2008). This means that on large time scales, the Coriolis acceleration and sea surface tilt are both significantly smaller than the other three and therefore we can rewrite the equation yet again in sufficiently simple terms as:

$$m\vec{a} = \vec{F_i} + \vec{\tau_a} + \vec{\tau_w}, \tag{4}$$

where m is the mass per unit area in $\mathrm{kg\,m^{-2}}$ and $\vec{a} = \frac{d\vec{u}}{dt}$ is the change in drift speed in $\mathrm{m/sec^2}$. F_i is the force due to internal stresses, which for this study we do not need to further dissect. With this simplified derivation we can appreciate what sea ice dynamics is based on, what it accounts for and how many minor forces at play are neglected on account of their magnitude. We now dive deeper into the driving force of sea ice, the atmospheric stress term $\vec{\tau_a}$, and explain how it connects the studies contained within this dissertation.

The atmospheric turbulent surface flux of momentum is highly relevant for Chapter 3, the basis for Chapter 4, and again important in interpreting the results of Chapter 5. The generalized turbulent surface flux equation is

$$\vec{\tau} = \rho C_d(z) U(z) \left(\vec{U}(z) \cos\theta \ + \sin\theta \, \hat{k} \times \vec{U}(z) \right), \tag{5}$$

which is also featured in Chapter 4 as equation 9. In the case of the atmospheric turbulent surface flux of momentum $\vec{\tau}_a$, the parameters included are as follows: ρ is the air density, $\vec{U}(z)$ is the difference in air and ice velocities at a given height z and $U(z)$ is its magnitude, $\hat{k}$ is the vertical unit vector, $C_d(z)$ is the drag coefficient and θ is the turning angle (for further details on equation 9 see Section 4.1). Since winds are much faster than the drift of sea ice, $\vec{U}(z)$ is typically equated to the air velocity $\vec{U}_a$. The analysis of wind speed and direction is one of the primary goals in Chapter 3 where we attempt to attribute sea ice thickness anomalies of 2016 and 2017 polynya occurrences to dynamic as well as thermodynamic drivers. As mentioned in section 1.2, there is sufficient evidence (e.g., Campbell et al. 2019; Francis et al. 2019; Wilson et al. 2019) supporting the notion that the polynya at Maud Rise is not purely a latent heat polynya and linkages between dynamic forcing via local as well as large scale atmospheric events has been shown. Wind-induced dynamics have a significant impact on the sea ice layer, which, under the right conditions, can aid in the formation of polynyas. It is the katabatic winds that fall off the continent that form the coastal polynyas that are primary sea ice producers in the area, and as we further corroborated in Chapter 3, they also play a major role in other Antarctic sea ice events further away from the Antarctic coast.

The focus of the study in Chapter 4 is the drag coefficient $C_d(z)$ which represents the coefficient that helps quantify sea ice-atmosphere drag, the resistance force of the atmosphere. The amount of momentum transfer between sea ice and atmosphere depends on the drag coefficient, which itself is related to the sea ice roughness. As shown, $\vec{\tau_a}$ is a part of the momentum balance of sea ice and what is perhaps the main determinant in the drift of sea ice on average. Therefore, quantifying the drag coefficient Arctic-wide is necessary to better explain and model Arctic sea ice drift patterns. Moreover, since the drag coefficient depends on sea ice roughness which is not uniform across the sea ice pack, assuming a constant drag coefficient will misrepresent the Arctic climate system – hence the need for its spatiotemporal analysis.

Finally, the effects of a spatiotemporally varying drag coefficient, which is related to the turbulent surface flux of momentum according to equation 9, is investigated within an Arctic coupled model framework. Specifically, its effects on sea ice drift velocity $\vec{u}$ (and therefore its temporal derivative $\frac{d\vec{u}}{dt}$) as well as sea ice thickness which is directly related to mass per unit area m. In summary, the effect of drag coefficients on pan-Arctic sea ice dynamics is the principal topic of Chapter 5, making it fit nicely within the overarching topic of this dissertation.

2.2 Remote sensing methods

Satellite remote sensing is another connecting factor in the studies presented in this dissertation. As such the general methods behind passive microwave radiometry and altimetry will be discussed here, while the specifics of the Advanced Microwave Scanning Radiometer 2 (AMSR2), Soil Moisture Ocean Salinity (SMOS), Soil Moisture Active Passive (SMAP) and Ice, Cloud and land Elevation Satellite 2 (IS2) are covered in the relevant studies presented in the following chapters. Both passive microwave radiometry and altimetry have been successfully used to study sea ice parameters. Passive microwave radiometry is traditionally used for sea ice concentration retrievals (e.g., Spreen et al. 2008) but has also shown capabilities in retrieving thin sea ice thickness (e.g., Kaleschke et al. 2013; Huntemann et al. 2014; Paţilea et al. 2019) as well as ice age (e.g., Shokr et al. 2008; Ye et al. 2016a; Ye et al. 2016b; Melsheimer et al. 2023). Satellite altimetry meanwhile has been primarily used for freeboard (thickness of sea ice above the water surface) and sea ice thickness determination but has since also found uses in sea ice roughness assessment (e.g., Mchedlishvili et al. 2023; Ricker et al. 2023) and ridge detection (e.g., Duncan et al. 2022).

2.2.1 Passive microwave radiometry

As briefly mentioned in Chapter 1, passive microwave radiometry is ideal for observing sea ice since it can do so all year round and without the impediment of clouds. Here we will discuss the process by which passive radiometetry detects sea ice and distinguishes it from the surrounding water. Water has high dielectric values and therefore low emissivity, as a result, it is radiometrically colder than sea ice which has a higher emissivity (Shokr et al. 2015). In addition, unlike for sea ice, the difference in the microwave emission of water between the horizontal and vertical polarization is large. Both the qualities can be leveraged in sea ice concentration retrieval, but most algorithms hinge on the second feature as it is pronounced at all frequencies (Shokr et al. 2015). At higher frequencies (>10 GHz), weather filters are necessary as the cloud water content, integrated water vapor and surface wind over the ocean can all disrupt the retrieval. The influence of these weather phenomena needs to be removed before applying sea ice concentration retrieval algorithms.

Depending on the methods and frequencies used, different results can be attained. Typical methods specific to sea ice concentration retrieval include solving linear algebraic equations representing decomposition of the radiometric observation into water and ice types (Cavalieri et al. 1984), solving a simplified version of a radiative transfer equation (in the case of atmospheric influences at higher frequencies) (Kaleschke et al. 2001; Spreen et al. 2008), and minimizing a cost function that represents the difference between actual and modeled observations (presented as a function of ice concentration) (Kongoli et al. 2011). Like water and ice, First-Year Ice (FYI) and Multiyear Ice (MYI) also have different radiometric temperatures. This difference allows for the determination of ice type using passive microwaves, though this procedure is further complicated by thaw-freeze cycles in the snow or increased surface roughness which causes ambiguity between the two ice types.

Utilizing data from scatterometers, active satellite-borne instruments that provide radar backscatter, in addition to passive microwave instruments, can further aid to differentiate between ice types. Lastly, sea ice thickness can also be assessed given the ice is thin and ideally snow-free. As sea ice first begins to form the salt is ejected quite rapidly, therefore the salinity in the upper ice layer varies with ice thickness. This variation has an impact on the dielectric value of sea ice, and therefore also its emissivity (Shokr et al. 2015). By analyzing the ratio between the horizontal and vertical polarization components of the emitted radiation, thickness can be inferred. This retrieval can then be further improved by using low (L-band) frequencies with deeper penetrative properties, which allows for the measurement of ice thickness (up to 50 cm) (Kaleschke et al. 2010; Huntemann et al. 2014).

2.2.2 Satellite altimetry

Altimetry is used in polar ocean regions mainly to determine sea ice thickness, and recently also sea ice roughness (e.g., Duncan et al. 2022; Mchedlishvili et al. 2023). For thickness the measured parameter that is leveraged is freeboard, the height difference between the sea ice and open waters surfaces. By measuring the freeboard, and considering the density of ice, water and snow, the thickness of the ice layer can be estimated. The two types of altimeters used for sea ice are lidar and radar operating in the visible and microwave frequencies, respectively. This difference is quite important as radar is able to penetrate the snow layer, thereby bypassing it and directly measuring the ice surface height. In either case, the correct measurement of sea ice freeboard is essential as any uncertainty is magnified in the computed sea ice thickness (Shokr et al. 2015). Information on the snow density needs to be known for both methods as it impacts the thickness calculated from freeboard.

The primary advantage of using altimeters instead of passive microwave and e.g., thermal infrared, is the ability to measure all possible sea ice thicknesses. Everything from centimeter-thick FYI to a few meters thick MYI can be estimated with the basic relation between freeboard and total thickness. The few examples of satellite altimeters used for sea ice measurements, e.g., the pioneering Ice, Cloud and land Elevation Satellite (ICESat) lidar, CryoSat-2 radar and the more recent IS2 lidar, have all been quite successful at retrieving sea ice thickness. However, it is using IS2 with its unprecedented along-track resolution ($\sim$0.7 m), that the analysis of sea ice roughness and the ability to resolve individual ridges has first been made possible. The methods by which surface feature properties are retrieved by Advanced Topographic Laser Altimeter System (ATLAS) on board IS2 is further elaborated on in Section 4.2.1 of Chapter 4.

As IS2 plays an important role in a large part of this dissertation, here we will discuss the working principles of the altimeter system on board the satellite. While Section 4.2.1 includes information on quantities (e.g., footprint, segment length, vertical uncertainties, etc.) that are important for interpreting IS2 ATLAS data in the Chapter 4 study, here we focus on the technical design and data processing aspects of ATLAS. As mentioned, ATLAS uses lidar by sending out and detecting laser

pulses with a wavelength of 532 nm (Kwok et al. 2021a; Kwok et al. 2021b). Using the Hamamatsu photomultiplier tubes within the apparatus, ATLAS detects more than 15% of the photons reflected back to the receiver such that each photon is time-tagged and geolocated (Yang et al. 2019). Accurate geolocation happens as a result of the low timing error (<285 ps) of the instrument which ensures precise time-tagging of detected photons. The short dead time of 3 ns (Yang et al. 2019), i.e. the lag between the detection of photons, allows for rapid photon counting. Once the photons have been time-tagged and geolocated, prior to surface finding, ATLAS processing separates background and surface photons based on their distance from the primary height distribution (Kwok et al. 2021b). Here background photons can come from a variety of sources, e.g., stray light and dark counts within the lidar instrument or scattered sunlight at the laser wavelength.

ATLAS sends out low pulse-energy lasers using its six-beam configuration that allows for cross-track sampling with reduced power demands. Based on the photon-counting microlaser altimeter theory first established in Degnan (2002), each of these six beams profile the surface with a 10 kHz pulse rate, such that a sufficient amount of photons from each pulse return to ATLAS and are detected by the photomultipliers. For more on the positioning of these beams at the surface and the resulting laser footprint please refer to Section 4.2.1. Importantly, the IS2 observatory is in a 92° inclination orbit. This allows ATLAS to map up to 88° latitude in both the Northern and Southern Hemispheres (Kwok et al. 2019b). The data density is highest directly south of 88° North and north of 88° South (see Fig. B1), making IS2 an excellent candidate for polar surface measurements.

With IS2 technical capabilities as well as coverage in mind, let us now touch on the processing, specifically how the received surface photon distributions are converted to surface height estimates. For the purpose of surface finding there exists an expected surface return or a photon height distribution $s_e(h)$, given by

$$s_e(h; h_0, w) = s_t(h) * G(h; h_0, w), \tag{6}$$

such that $s_e(h)$ is modeled as a convolution of the ATLAS system impulse response $s_t(h)$ with a Gaussian surface height distribution $G(h)$ of width w and height h_0 (Kwok et al. 2019b). The $*$ symbol in the above equation is the convolution operator. In order to determine the surface height from a received photon height distribution $s_r(h)$, the best match between $s_r(h)$ and the expected return $s_e(h)$ is found. This matching is done based on a similarity computed as the square difference between $s_r(h)$ and $s_e(h)$ as

$$e^2(h_0, w) = 1/N \sum_N \left(s_r(h_i) - s_e(h_i; h_0, w)\right)^2, \tag{7}$$

where $\sum_N s_r(h_i) = 1$, $\sum_N s_e(h_i; h_0, w) = 1$ and the argument $e^2(h_0, w)$ quantifies the similarity such that the lower this argument gets, the higher the similarity. After this template matching procedure, an estimate of the height $\hat{h}_0$ and the apparent width $\hat{w}$ of the surface height distribution is derived as follows

$$\{\hat{h}_0, \hat{w}\} = \text{argmin}\left(e^2(h_0, w)\right). \tag{8}$$

The location on the surface $\{\hat{h}_0, \hat{w}\}$ with the highest similarity, and therefore the best match, is where $e^2(h_0, w)$ attains its minimum value over a domain defined by $h_0 \in [h_1, h_2]$ and $w \in [w_1, w_2]$. Importantly the two height distributions $s_r(h)$ and $s_e(h)$ need to be normalized for this computation as a priori knowledge of the expected strength of the surface returns is not available (Kwok et al. 2019b). The quality of the surface finding process is then determined by the number of signal photons used and the bin size of the constructed distribution histogram for $s_r(h)$. These distribution histograms are not constructed from individual pulses but rather when a sufficient amount of photons (150) are aggregated over a variable number of pulses. Therefore, there are always set amounts of photons and fixed bin size for the processing of ATLAS returns, thereby improving their quality and reducing uncertainty (down to $\sim$2 cm). Collecting a sufficient amount of photons in the shortest amount of time, and therefore over the shortest possible distance, depends on the strength (or reflectivity) of the surface return. As a result, the spatial resolution of the height profiles and length of the height segments are directly proportional to signal strength. In other words, both the resolution (on average $\sim$30 m) and segment length (on average $\sim$20 m) are variable with each measurement along the altimeter track. Once the along-track surface heights are computed from the processed global geolocated data (ATL03/L2), they are thereafter classified as ATL07/L3A over sea ice and open-water leads. This is the data used in Chapter 4 for the estimation of form drag coefficients, and the use of as well as associated uncertainties of ATL07/L3A are discussed in Sections 4.2.1, 4.2.3 and 4.3.5.

2.2.3 Airborne altimetry

Lidar can also be mounted on an aircraft in an airborne survey, and by virtue of being closer to the surface, can achieve a higher resolution than space-borne lidar instruments. The principles are the same as for satellite altimetry mentioned in Section 2.2.2, however, given the aircraft does not continuously orbit the planet and therefore has a much smaller spatial coverage, they need to maximize this coverage during flights. As a result, with the advance of technology, modern airborne lidar surveys typically measure two-dimensional surface profiles oriented along the flight direction. Two examples of such airborne lidar instruments used in the study of sea ice are the Altimeter Laser Scanner (ALS) used during the IceBird campaigns (Jutila et al. 2022) as well as the Multidisciplinary drifting Observatory for the Study of Arctic Climate (MOSAiC) (Hutter et al. 2023), and the Airborne Topographic Mapper (ATM) used during Operation IceBridge (OIB) (Studinger 2013) which plays a central role in Chapter 4 and is therefore covered in detail in section 4.2.2. OIB collected data using ATM between ICESat (2003-2009) and IS2 (2018-present) missions in an effort to fill the gap in the satellite data record of sea ice surface measurements (Yi et al. 2022). In addition, there are the Arctic flights since the launch of IS2, such as those conducted in April 2019 that were near-coincident with IS2 satellite tracks. These underpasses helped validate IS2 measurements (Kwok et al. 2019a) and were essential in deriving a scaling factor for the IS2-retrieved

form drag coefficients (Mchedlishvili et al. 2023). The use of this dataset as well as its application in the IS2 sea ice–atmosphere form drag retrieval can be found in Section 4.3.1 of Chapter 4.

2.3 Coupled regional atmosphere-ocean-sea ice modelling

The final chapter deals with the coupled regional atmosphere-ocean-sea ice model HIRHAM–NAOSIM, as such, here the basics of such a model setup will be reviewed.

In general, such a model, as the name implies, should be able to resolve processes in the atmosphere, ocean and sea ice as well as be able to exchange information between these domains. This is accomplished through a combination of atmospheric, oceanic and sea ice models with some coupling framework that is driven by a designated coupling software (assuming the full model domain contains no land). Each component accounts for the processes present in the respective domain. These models include both dynamic and thermodynamic components. As a general overview, the atmospheric model must contain a dynamical core responsible for solving the equations of motion for air movement and some type of radiation parameterization. Similarly, the ocean model must also solve ocean circulation equations to describe the underlying currents, as well as the thermodynamics and the associated heat exchange. Sea ice is an added complexity in coupled models in the polar regions with its own associated dynamics and thermodynamics. All these domains have their own additional processes such as cloud microphysics for the atmosphere, the influence of salinity and vertical mixing for the ocean, and the influence of snow cover and albedo for sea ice. Models often have the challenge of including as many physical processes as possible to better align model results with observations, while at the same time keeping the computational costs low.

For a coupled model, there needs to be data exchange between the model components, thereby simulating the interactions between atmosphere, ocean and sea ice. The time-stepping of the individual model components must be in some way synchronized to allow for a regular data exchange. Lastly, the exchange of data must follow the mass, energy and momentum balance for the whole model. In the case of HIRHAM-NAOSIM, the atmospheric model HIRHAM5 and ocean-sea ice model NAOSIM are coupled via Yet Another Coupler (YAC) 1.2.0 (Dorn et al. 2019). This coupling software allows for parallelized interpolation and communication between the components. Intermediate procedures like remapping and nearest neighbor interpolation ensures that though the grids of the atmosphere and ocean-sea ice models differ, the information exchange can happen at all grid cells in both models. The time step of coupling is 1 hour such that every hour the two model components share information with one another. The coupling domain is defined as the overlap area of the two model components, wherein the grid cells that represent land are excluded and masked as uncoupled cells, which are not considered.

While global models are better suited for representing the full climate system of the whole Earth, regional models can afford to better represent mesoscale processes thanks to their higher resolution. This advantage gives them the potential to better resolve climate feedbacks associated with mesoscale

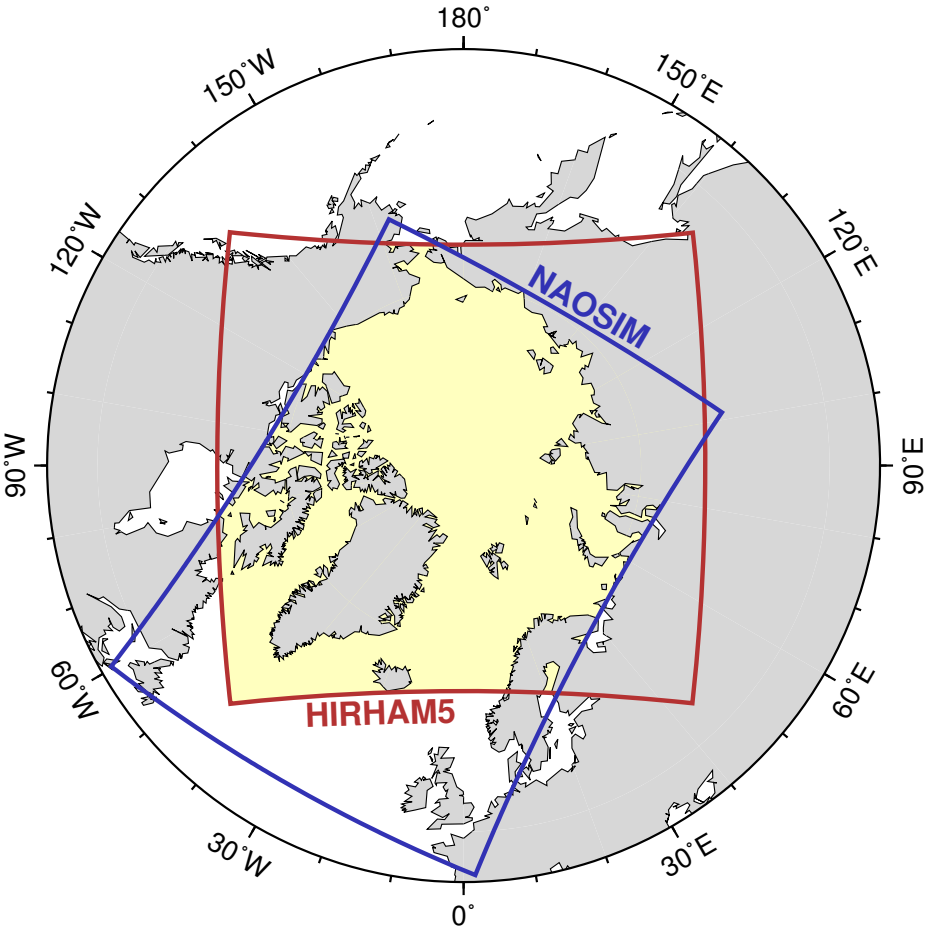

Figure 2.1: The geographical domain coverage of the atmospheric component HIRHAM5 and ocean–ice component NAOSIM. The area highlighted in yellow indicates the coupling domain and comprises 20,583 (out of 43,600) HIRHAM5 grid cells and 200,951 (out of 366,850) NAOSIM grid cells. The figure is taken from Dorn et al. (2019) which is licensed under an open access Creative Commons CC BY 4.0 license. Permission to reproduce this figure has been granted by authors of the article, who retain all copyrights according MDPI policy.

features (Cassano et al. 2017). Regional models can serve as a test bed for the future generation of global ones that will be run at a comparable resolution. Another advantage is the possibility of including tailored physical parameterizations able to improve model performance locally. Such parameterizations run the risk of deteriorating model performance in other geographical regions in a global model. Thus, regional models tend to offer a wider range of possible parameterizations that can be tested in them as compared to global models (Cassano et al. 2017).

A prominent disadvantage with using regional models lies with the need for lateral boundary conditions (LBCs). LBCs are the edges of the model's spatial domain and they affect the mass and

energy fluxes in and out of the model. The data used as lateral boundary forcing for LBCs are from global climate models or reanalysis data, which themselves might have biases, thereby propagating biases to the regional model. Additionally, two-way feedbacks between the simulated region climate and the outside (in this case represented by the LBCs) cannot be properly simulated. On the other hand, the required LBCs can be varied to assess how they impact the sensitivity of the regional climate (Cassano et al. 2017). Moreover, LBCs are a consequence of any given regional model, as even to have a closed boundary is a condition in and of itself. In the case of the current version of HIRHAM-NOASIM version 2.2 (HN2.2), HIRHAM5 and NAOSIM have their own respective LBCs, both of which are in some part driven by ECMWF Reanalysis 5th Generation (ERA5). Specifically, ERA5 reanalysis data are used for the lateral boundaries of HIRHAM5, as well as parts of both models that lie outside the coupling domain (HIRHAM5's lower and NAOSIM's upper boundaries) (Aue et al. 2023). Ocean Reanalysis System 5 (ORAS5) data (Zuo et al. 2019) are used for NAOSIM's lateral boundaries. The data used for the forcing for both model components depends on what is required for them to incorporate from outside the coupling domain, for example, in the case of NAOSIM, temperature, salinity, ice thickness, and ice concentration fields from ORAS5 are used.

2.3.1 Reproducing observed climate patterns

The goal of any climate model is to reproduce observed climate patterns to then better predict future developments in climate conditions. Thus, here we discuss the capability as well as constraints of a coupled regional atmosphere-ocean-sea ice model in reproducing the observed climate state. Here again we will predominantly focus on HIRHAM-NAOSIM as it is the model used for the study in Chapter 5 and therefore highly relevant.

An important initial step in testing how well a given model reproduces the observed climate conditions is model spin-up. The spin-up is the process by which the model is initialized from a state of rest to a state that accurately represents the physical system being investigated. For HIRHAM-NAOSIM, in testing the performance of version 2.0 (Dorn et al. 2019), a coupled spin-up run for the period 1979-2000 was necessary prior to the ensemble of 10 hindcast simulations over the period 1979-2016. This spin-up run reached a quasi-stationary seasonal-cyclic state of equilibrium for the mid-1980s and all ensemble members were initialized with ocean and sea ice fields that were representative of the steady state of the specific model configuration (Dorn et al. 2019). Thus a model spin-up run is meant to reach a given equilibrium state in which transient processes gradually settle. The duration of the process can vary depending on the model complexity. In addition, proper initialization is crucical. In the case of a coupled model like HIRHAM-NAOSIM, the coupled spin-up run itself needed to be initialized with ocean and sea ice fields from a 20-year-long NAOSIM run which started from rest (Dorn et al. 2019).

Next it is important to dissect what an "ensemble of 10 hindcast simulations" means and what the terminology refers to. Ensemble simulations refer to a group of model runs that are run with slight variations in initial conditions. The variation is meant to explore the range of possible outcomes and

assess model output uncertainties. In addition, by looking at the results of multiple runs, as well as longer time periods like months as opposed to days (e.g., Dorn et al. 2007; Dorn et al. 2009; Dorn et al. 2012; Dorn et al. 2019), short-term fluctuations are averaged out, thereby providing a clearer picture of the underlying climate signal. "Hindcast" refers to the type of study that was conducted, namely one that tries to recreate past climate conditions rather "forecasting", i.e., predicting future ones. Importantly, this ensemble was driven by ERA-Interim as ERA5 was only implemented later in HN2.2 (Aue et al. 2023).

The Dorn et al. (2019) study, which presents the improvements of HIRHAM-NAOSIM version 2.0 over 1.2, reports that with a higher horizontal and vertical resolution, the enhancement of model components as well the integration of the YAC coupler, the model output agreed better with observation-based data sets. The sea ice cover and volume of the upgraded model was in better agreement with the Pan-Arctic Ice Ocean Modeling and Assimilation System (PIOMAS), and in general reduced a lot of the biases present version 1.2 (Dorn et al. 2019). Even so, some biases remained, especially summertime biases which were of similar magnitude to that of version 1.2. Specifically, as compared to PIOMAS sea ice volume (derived from observed sea ice extent), there is still a negative bias of more than $2 \times 10^3\,\mathrm{km}^3$ in most months (Dorn et al. 2019). Dorn et al. (2012) report that the model's ability to reproduce observed summer sea-ice retreat depends partly on the sea ice volume at the beginning of the melting period. Thus, all biases within a given parameter impact other dependant parameters, further separating the model from reality. That is why improvements, such as the ones from HIRHAM-NAOSIM version 1.2 to 2.0, and now to 2.2, is so important as we close the gap between model and observations. In order to close this gap, better parameterizations and implementation of physical phenomena based on observations is necessary to recreate the Arctic climate system within a model. Once the gap is adequately closed, and a model accurately reproduces historical observational data, we can use it to study the future evolution of the climate system.

3 Weddell Sea polynya analysis using SMOS–SMAP apparent sea ice thickness retrieval

The following chapter is based on the published paper *Weddell Sea polynya analysis using SMOS–SMAP apparent sea ice thickness retrieval*. The paper is featured in *The Cryosphere* journal, which is published by Copernicus Publications on behalf of the European Geosciences Union. I am the main author of this publication, with co-authors Gunnar Spreen, Christian Melsheimer and Marcus Huntemann. I carried out the analysis of the satellite remote sensing data and wrote the initial draft of the paper. Subsequently, the co-authors contributed by suggesting edits based on their expertise, helping me to prepare the paper for submission. Lastly, two anonymous reviewers provided further edits, which improved the paper to the state featured in the journal, as well as in this chapter. The chapter includes minor adjustments to the published paper to better integrate the work into the dissertation.

This chapter features a study on the open ocean polynyas of the Weddell Sea and is meant to address **RQ**s 1 and 2 detailed in Chapter 1. The study focuses in on an area on top of the Maud Rise seamount within the Weddell Sea region, that has repeatedly featured open-ocean polynyas. Within this area, after 40 years of intermittent, smaller openings, a larger, more persistent polynya appeared in early September 2017, and remained open for approximately 80 days until spring ice melt. Findings of this study suggest that polynya-favourable activity in the Maud Rise area is taking place more frequently and on a larger scale than previously assumed. As with the chapter that follows, this study makes use of satellite remote sensing data. Namely, by investigating thin (<50 cm) apparent sea ice thickness (ASIT) retrieved from the satellite microwave sensors Soil Moisture Ocean Salinity (SMOS) and Soil Moisture Active Passive (SMAP), a large ($\sim 300 \times 10^3$ km^2) thin sea ice anomaly over Maud Rise was identified in September 2018. In addition, this study includes a similar analysis of all years from 2010 until 2020 in the SMOS sea ice thickness record. Throughout this analysis it is demonstrated that L-band microwave radiometry from the SMOS and SMAP satellites can provide additional useful information, which helps to better understand dynamic sea ice processes like polynya events when compared to the use of satellite sea ice concentration products alone.

In terms of the overarching topics of sea ice dynamics and atmosphere-ocean-sea ice momentum transfer, this study uses ECMWF Reanalysis 5th Generation (ERA5) surface wind data to corroborate previous findings (e.g., Campbell et al. 2019; Francis et al. 2019; Wilson et al. 2019) the strong impact that storm activity can have on sea ice above Maud Rise. Finding a clear link between the surface wind data and the occurrence of the polynya further supports the theory that the evolution of the Weddell Sea polynya is controlled by local atmospheric as well as oceanographic variability.

3.1 Introduction

From 1974 to 1976, for three consecutive winters, the satellite microwave radiometer record shows a roughly $250 \times 10^3\,\mathrm{km}^2$ opening in the sea ice cover near the Maud Rise seamount that is now known as the Weddell Polynya (Carsey 1980). After these repeated polynya openings, for the next 40 years the few polynya events were comparatively smaller (Campbell et al. 2019) and often in the form of a low sea ice concentration (SIC) halo around Maud Rise (Lindsay et al. 2004). 2016 and more so 2017 were the largest and longest-lived polynyas since 1976 (e.g., Swart et al. 2018; Cheon et al. 2019; Campbell et al. 2019; Jena et al. 2019). For the purposes of this paper, we refer to both the 1970s Weddell Polynya (e.g., Carsey 1980; Martinson et al. 1981; Motoi et al. 1987) and 2010s Maud Rise Polynya (e.g., Cheon et al. 2019; Jena et al. 2019) occurrences as Weddell Sea polynya to signify any sizeable sea ice opening near Maud Rise.

The Weddell Sea polynya is an anomalous opening in sea ice that is generally classified as an open-ocean polynya (Maqueda et al. 2004). An open-ocean or 'sensible heat' polynya is distinguished from the coastal 'latent heat' polynya by being maintained and opened by upwelling and/or mixing as opposed to wind-driven ice advection. The main mechanism that preconditions the Weddell Sea polynya is described by Martinson et al. (1981) as the winter surface layer becoming dense through heat loss and brine rejection from ice formation, resulting in density overturning (Martinson et al. 1981; Martinson et al. 1998) which deepens the mixed layer and initiates deep convection. Deep convection and heat ventilation into the mixed layer are thought to be primary causes for the Weddell polynya (Martinson et al. 1981; Steur et al. 2007; Wilson et al. 2019; Cheon et al. 2019).

One of the primary mean-state factors that precondition polynya at Maud Rise is the lack of strong stratification (Gordon et al. 1990; McPhee et al. 1996). Weak stratification leaves the ocean susceptible to density overturning and is facilitated by winter surface mixed layer salt content as well as the topography present at Maud Rise. Another polynya-favourable factor that is reported on is the anomalously warm waters found over the flanks of the rise, with a colder cap of water lying over the top of the rise (e.g., Gordon et al. 1990; Bersch et al. 1992; Martinson et al. 1998; Lindsay et al. 2004; Muench et al. 2001; Wilson et al. 2019). Muench et al. (2001) went further to describe how interactions between the mean flow (eastern limb of the Weddell Gyre) and topography (Maud Rise) preconditions the area above Maud Rise for anomalously high vertical heat fluxes, which favors thinner sea ice. Due to the presence of Maud Rise and the surrounding elevated Warm Deep Water, the 23–year mean sea ice concentration (SIC) for the months of July through November (1979–2001) shows a distinct halo of low ice concentration with a diameter of about 300 km (Lindsay et al. 2004). A factor that contributes to the existence of said halo and, by extension, the Weddell Sea polynya that occur locally is the cyclonic eddies that adhere to the flanks of the rise (Steur et al. 2007; Holland 2001). Northeast of Maud Rise specifically, is where Holland (2001) suggested water columns leaving the seamount are stretched and acquire cyclonic vorticity thereby applying divergent strain to the sea ice layer from below.

Cheon et al. (2019) described the 2016 and 2017 Weddell Sea polynya formation process in detail by explaining the preconditioning as well as the large-scale climate events that lead to it. They discussed large-scale atmospheric influences, specifically the influence of positive Southern Annular Mode (SAM) which intensifies the negative wind stress curl over the Weddell Sea and thereby the Weddell Gyre which, in turn, weakens upper ocean stratification. In addition to large-scale climate processes, localized atmospheric forcing has been shown to impact the ice layer from above (e.g., McPhee et al. 1996; Goosse et al. 2000; Francis et al. 2019; Campbell et al. 2019; Wilson et al. 2019; Heuzé et al. 2021). As early as 1996, during the Antarctic Zone Flux Experiment (McPhee et al. 1996) it was shown that storms featuring gusts of up to $25\,\mathrm{m\,s^{-1}}$ can produce ocean heat fluxes that exceed $100\,\mathrm{W\,m^{-2}}$. Under weak stratification that encourages heat ventilation from below, the thermocline is exposed to more intense wind-driven turbulent mixing aiding the formation of the polynya (Wilson et al. 2019; Campbell et al. 2019). Francis et al. (2019) went further to state that anomalous atmospheric influence triggers polynya formation which they hypothesized was the case for the 2017 Weddell Sea polynya. Ice divergence due to strong winds enables rapid ice production and brine rejection that prevents stabilization from ice melt as wind-driven turbulent mixing entrains warm and saline water into the surface mixed layer (Campbell et al. 2019).

This study contributes to the recently-emerging understanding of direct atmospheric influence over the Maud Rise region and supports the notion that the Weddell Sea polynya is not purely an ocean-driven polynya (Heuzé et al. 2021). However, the primary investigation is done during polynya-free years. Through analysis of the thin ($<$50 cm) sea ice thickness (SIT) product (which for the purposes of this study we relabel as apparent SIT or ASIT for reasons elaborated on in Section 3.2.1) from the spaceborne passive microwave sensors Soil Moisture Ocean Salinity (SMOS) and Soil Moisture Active Passive (SMAP), we aim to challenge the notion that anomalous activity atop Maud Rise is purely a binary phenomenon. Rather, the Weddell Sea polynya is the result of independent as well as dependent preconditioning effects that occasionally but not exclusively interfere with one another constructively to form the polynya, like in 2016, 2017 and mid-1970s. Using the ASIT retrieval over years where the polynya did not occur, we aim to identify low sea ice thickness areas that demonstrate anomalous behaviour taking place in the absence of the Weddell Sea polynya suggesting that the existence of polynya-favorable conditions, although present, are insufficient to produce the polynya. Previous studies used satellite sea ice concentration to analyse the size and development of the polynya. Since 2010, the SMOS satellite has allowed us to analyse thin ice area anomalies, i.e., thinning of ice on the same scale as the polynya that is subject to similar underlying causes.

3.2 Data and methods

For this study a combined SMOS-SMAP SIT retrieval and SMOS SIT retrieval (for time periods preceding the installment of SMAP in 2015) are used to identify low sea ice thickness areas above

Maud Rise. In addition, the ARTIST sea ice (ASI) algorithm is used to access sea ice concentration and ERA5 meteorological reanalysis data is used to look at winds at the surface level.

3.2.1 SMOS-SMAP Apparent Sea Ice Thickness Retrieval

The space-borne passive microwave sensors Soil Moisture Ocean Salinity (SMOS) and Soil Moisture Active Passive (SMAP) are working at 1.4 GHz (L-band) which allows information on the thickness of thin sea ice to be obtained (Paţilea et al. 2019; Huntemann et al. 2014; Tian-Kunze et al. 2014). From modeling and observations it has been established that emission at L-band show sensitivity to ice thickness up to about 50 cm (Kaleschke et al. 2010). The atmosphere has negligible influence on surface emission at L-band (Zine et al. 2008; Kaleschke et al. 2013). The footprint size of both sensors is around 40 km (Paţilea et al. 2019).

The SMOS-SMAP SIT retrieval builds upon its predecessor SMOS SIT retrieval (Huntemann et al. 2014). The SMOS SIT retrieval uses the average of horizontally and vertically polarized brightness temperatures as well as the polarisation difference (i.e., the difference between horizontally polarized and vertically polarized brightness temperature) averaged over the incidence angle range between 40° and 50° from the synthetic aperture antenna observations. SMAP , on the other hand, uses a real aperture antenna and observes the earth surface at a fixed incidence angle of 40° resulting in a narrower swath than SMOS (Paţilea et al. 2019). The combined SMOS-SMAP thin ice sea ice thickness retrieval improves the SMOS retrieval by adapting it to SMAP with the modification that uses fixed 40° incidence angle observations instead of average in the range 40 to 50°. This is achieved by fitting a function to the brightness temperature to incidence angle relation for all overflights of a geographic location of one day. This results in an average resolution of approximately 43 km. In addition, a linear regression between the SMOS and SMAP brightness temperatures at a 40° incidence angle is performed to align the brightness temperatures of the two instruments with a root mean square difference at horizontal and vertical polarization of 2.7 and 2.8 K, respectively (Paţilea et al. 2019). The combined SIT retrieval offers more stable sea ice thicknesses, which are less influenced by radio-frequency interference. Because of the up to 12 h difference in the Equator crossing time between SMAP and SMOS, ice thicknesses retrieved from the daily mean brightness temperatures are more likely to include more of the brightness temperature variations within a day, which also helps the stability of the retrieval. Therefore, we prefer the use of the combined SMOS-SMAP SIT retrieval above the SMOS-only one for the study of SIT over Maud Rise in cases when it is available.

SIC data (Section 3.2.2) is used for comparison with the SIT data. The SMOS-SMAP retrieval algorithm assumes near-100% SIC when retrieving SIT and since we look at a region prone to polynya and low SIC (Lindsay et al. 2004), it is important to consider this factor. The SMOS-SMAP SIT retrieval has no SIC dataset correction implemented because uncertainty of SIC algorithms at high concentration and their covariation at thin thicknesses will cause high amounts of error (Paţilea et al. 2019). Using SIC maps and data in combination with SIT counterparts, we can better infer

the location and degree of error in our SIT retrieval. As a general rule, the SMOS-SMAP as well as SMOS SIT retrievals tend to underestimate the sea ice thickness at SIC below 100%; the degree to which this underestimation occurs is heavily influenced by the SIC value. However this interaction between SIC and SIT retrievals is two-sided as most sea ice concentration algorithms show less than 100% SIC for thicknesses below 30 cm (Heygster et al. 2014). Paţilea et al. (2019) estimated the uncertainty at 90% SIC from SIT values up to 50 cm. The higher the SIT that is being retrieved the higher the uncertainty, e.g., an area that is 90% SIC and 50 cm thick is expected to be retrieved as only 28 cm. This is simply the limitation imposed by the penetration depth into sea ice at the given frequency (Kaleschke et al. 2010) and is also why the retrieval is capped at 50 cm as any attempt to retrieve thicker SIT values would be accompanied by an even higher amount of error.

Both the SMOS-SMAP and SMOS are empirical retrievals that were initially developed for monitoring the sea ice thickness of growing sea ice in the Arctic during freeze-up through comparison with a Cumulative Freezing Degree Days (CFDD) model and thereafter calibration and validation using observations (Huntemann et al. 2014). As such, this compromises the validity of the sea ice thicknesses retrieved in areas that are prone to polynya. While the degree by which the ice thins is difficult to quantify in terms of uncertainty, our analysis has shown that the pattern of thin ice anomalies above Maud Rise is not random nor is it identical to the distribution of low SIC areas, and instead adheres to the general understanding of processes present in the region. As a result for the purposes of this study, we present the retrieved SIT values as ASIT that is meant to depict the distribution of sea ice that is subject to sea ice thinning rather than the exact thickness of each individual pixel. We take this approach in part due to the low sea ice concentrations that are to be expected near Maud Rise (Lindsay et al. 2004), as well as the melting conditions at the end of the winter season which neither of the SMOS retrievals were originally made for. While the SMOS-SMAP retrieval from a physical point of view works for both hemispheres there is a lack of validation data in the Antarctic. Uncertainty from flooded ice and slush caused by snow pushing down the sea ice such that water floods from the sides or from below through the cracks is expected to influence the SIT retrieval. These events are not typical for thin ice and can happen in both hemispheres, but might be more common in the Antarctic. The uncertainty caused by the flooding cannot be assessed without in-situ measurements. As such, no attempt at calculating ice volume was made in this study so as not to carry over errors that affect the retrieved ASIT values.

3.2.2 ASI ice concentration algorithm

The ARTIST Sea Ice (ASI) algorithm calculates SIC from the difference between brightness temperatures at 89 GHz at vertical and horizontal polarizations which are retrieved by the Advanced Microwave Scanning Radiometer 2 (AMSR2) onboard the Global Change Observation Mission-Water (GCOM-W1) satellite. This polarization difference is then converted into SIC using pre-determined fixed values for 0% and 100% SIC polarization differences known as tie points. It is known from surface measurements that the polarization difference of the emissivity near 90 GHz is similar for

all ice types and much smaller than for open water (Spreen et al. 2008). At 89 GHz the spatial resolution with 5 km is the highest of all AMSR2 channels but the atmospheric influence is high also. This effect is dealt with in a bulk correction for atmospheric opacity and by implemented weather filters over open water. Because the Bootstrap (BBA) (Comiso et al. 1997) algorithm uses the 19 and 37 GHz channels, which are less sensitive to atmospheric phenomena, it is also used to essentially filter the produced ASI SIC concentration by setting SIC to zero where the Bootstrap algorithm retrieves less than 5% SIC. The finalized and filtered ASI SIC data has 6.25 km^2 grid resolution.

3.2.3 ERA5 climate reanalysis

ERA5 atmospheric reanalysis data is used to study direct atmospheric forcing on the opening of the polynya as well as on anomalous regional sea ice thinning to investigate whether the Weddell Sea polynya is purely ocean-driven or maintained by a combination of both processes.

ERA5 provides a detailed record of the global atmosphere, land surface and ocean from 1950 onwards. It replaces the ERA-Interim reanalysis (spanning 1979 onwards) and is based on the Integrated Forecasting System (IFS) Cy41r2. ERA5 benefits from a decade of developments in model physics, core dynamics and data assimilation (Hersbach et al. 2020). In addition to a significantly enhanced horizontal resolution of 31 km, compared to 80 km for ERA-Interim, ERA5 has hourly output throughout.

Campbell et al. (2019) reported that there was sufficient agreement between mean sea level pressure (MSLP) data obtained from the SANAE-AWS weather station and the nearest ERA-Interim grid cell for ERA-I to be used in gathering signs of storm activity as it skillfully represented MSLP variability near Maud Rise. ERA5 is a reanalysis with a higher temporal and spatial resolution than ERA-I. It improves upon its predecessor in terms of information on variation in quality over space and time as well as an improved troposphere modelling (Hersbach et al. 2020). As a result, for the purposes of this study, it should offer a better, or at least identical, assessment of the wind speeds near Maud Rise that are going to be cross-referenced with the presented ASIT retrievals in this study.

3.3 Results

The left image in Fig. 3.1 shows a standard Southern Hemisphere SMOS-SMAP ASIT retrieval at grid resolution of 12.5 km (actual SIT product resolution is lower, section 3.2.1). The black frame (northwest corner: 61.78°S, 3.57°W, southeast corner: 67.88°S, 13.11°E), which is zoomed in on the right, shows austral winter sea ice above Maud Rise (66°S, 3°E) and it is the area this study focuses on. All time series as well as individual maps included are evaluated for and depicting the area within the black frame, respectively.

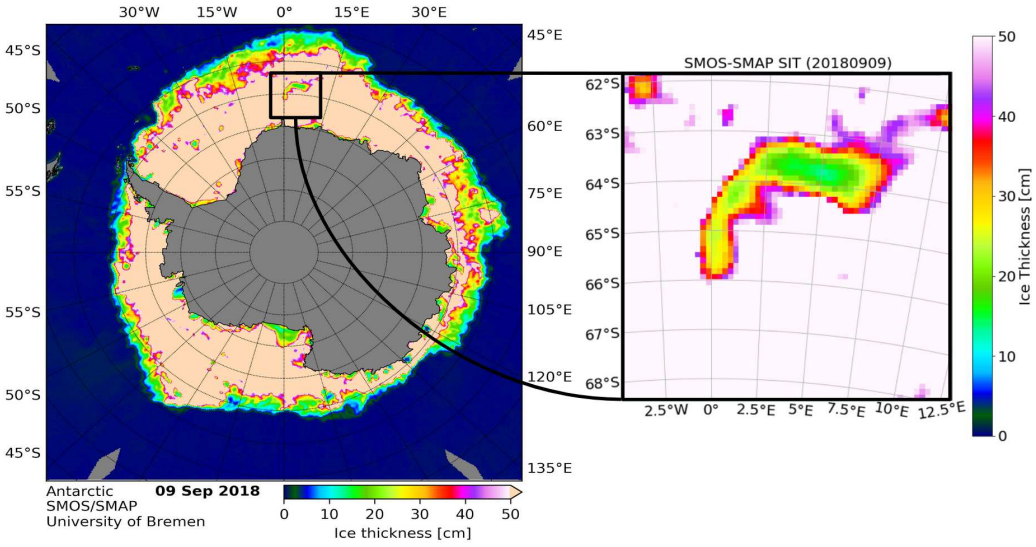

Figure 3.1: Left: SMOS-SMAP apparent sea ice thickness (ASIT) retrieval for the sea ice zone around Antarctica from 9 September 2018. The segment contained in the black square depicts sea ice above Maud Rise (66°S, 3°E). Right: the zoomed-in local SMOS-SMAP ASIT of the outlined region which serves as the boundaries of all time series generated in this study.

Figure 3.2 shows the full 11-year record of SMOS sea ice thickness from 2010 to 2020 above Maud Rise. For a detailed analysis of the anomalous sea ice behaviour atop Maud Rise, the years 2017 and 2018 are chosen. In 2017 the largest Weddell Sea polynya of this century occurred, and the following year 2018 also exhibits anomalous thin ice behaviour as will be shown later. The full 11-year time series will be discussed at the end of the Result Section. In 2017 the polynya showed the largest extent and is open the longest time period since the 1976; in 2018 there was no polynya but sea ice thinning is observed over multiple weeks. Here the advantage of the SMOS-SMAP ice thickness retrieval shows its strength by detecting anomalous sea ice behaviour where traditional sea ice concentration datasets cannot. This section presents findings that suggest a previously unrecognized similarity between the two September anomalies.

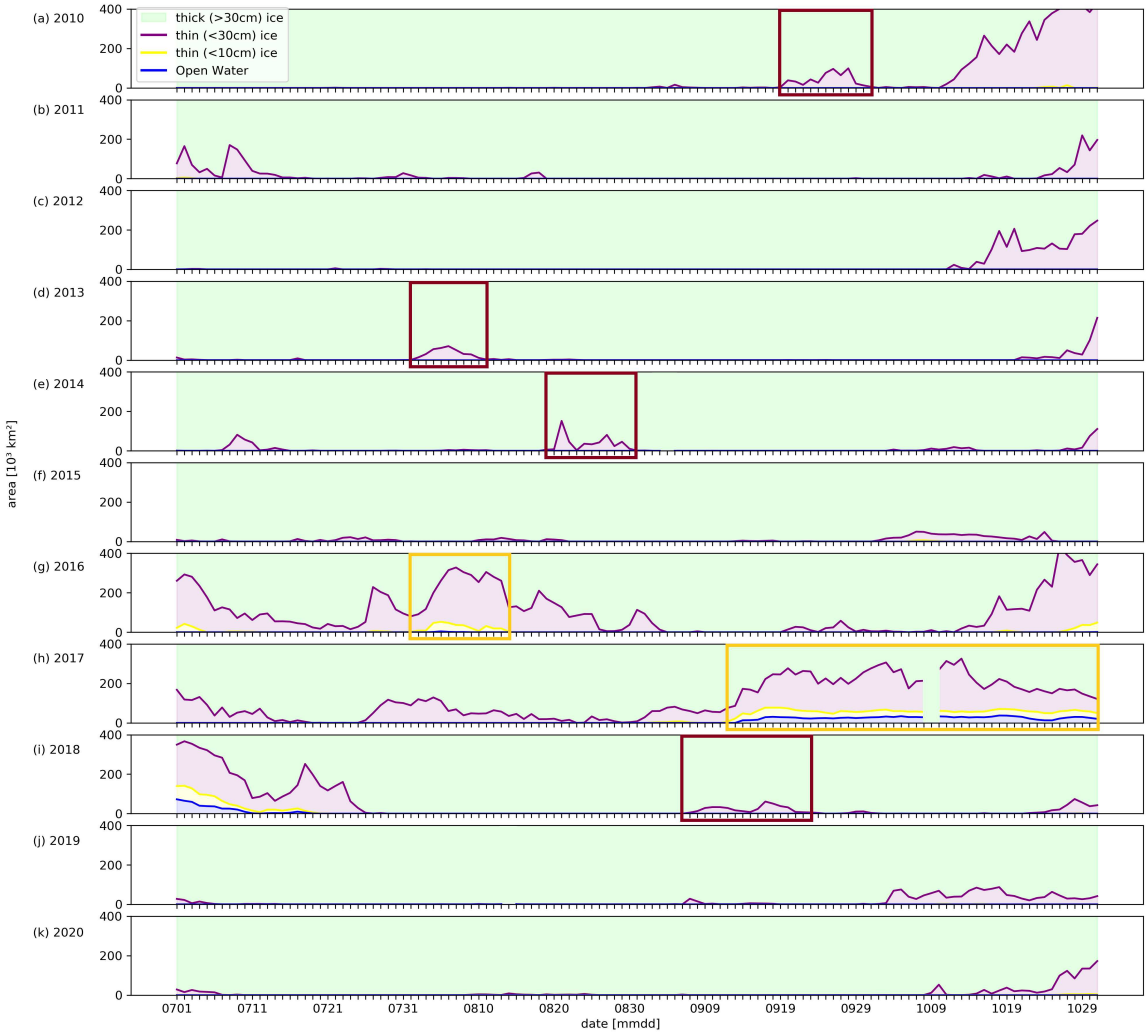

Figure 3.2: (a-k) the SMOS apparent sea ice thickness (ASIT) retrieval time series from 2010 to 2020 over the area of interest outlined in Fig. 3.1. Each line represents sea ice below a thickness threshold shown in the legend in the top left (blue: open water, yellow: <10 cm ice, red: <3 cm ice). Each filled-in area represents sea ice within the range set by the lines (blue: open water area, yellow: 0-10 cm ice, red: 10-30 cm ice, green: >30 cm ice). Polynya events are highlighted in yellow whereas ice thinning anomalies are highlighted in red (see also maps in Fig. 3.7). Years 2017 and 2018 are discussed in more detail in this manuscript.

Fig. 3.3 shows maps of the SMOS-SMAP ASIT development from 11 to 13 September in 2017 and Fig. 3.4 for the same three days in 2018. The SMOS-SMAP ASIT maps are accompanied by ASI SIC counterparts at a nominal resolution of 6.25 km covering the same region for comparison.

The 2017 Weddell Sea polynya is a well-documented event and its preconditioning as well as existence until melt of that year has been shown via in situ ocean data and also satellite imagery; most commonly via SIC retrieval (e.g., Campbell et al. 2019). Here the advantages of SMOS-SMAP ASIT retrieval are limited by the high open water fraction but nevertheless help to demonstrate the full extent of the anomaly that SIC maps of the region can only partially depict (see Fig. 3.3). Additionally, the ASIT maps in Fig. 3.3 show a broader gradient of ASIT encompassing a larger area on all sides of the polynya than the sharp SIC gradients surrounding the polynya in the ASImaps. While the coarser 12.5 km SMOS-SMAP ASIT data product is less resolved than the 6.25 km ASI SIC data counterpart, we do not expect any underestimation of area by ASIretrieval as it is estimating open water as a percentage on a sub-footprint scale. In Fig. 3.3 we can see a substantial difference between both the scale and gradient between the SMOS-SMAP ASIT and ASI SIC data maps.

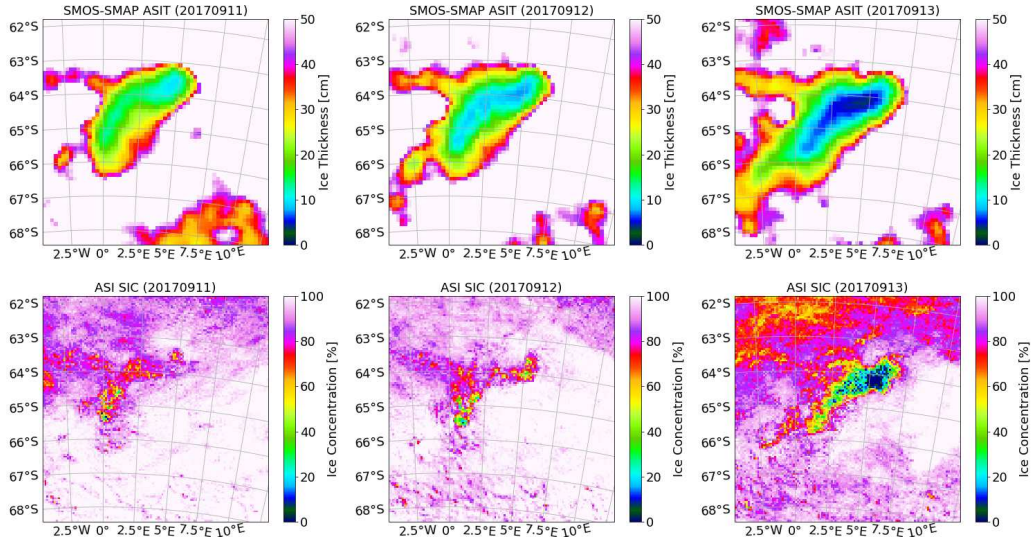

Figure 3.3: SMOS-SMAP ASIT (top row) and ASI SIC (bottom row) retrieval of the days leading up to the 2017 Weddell Sea Polynya: 11–13 September 2017.

Similarly for 2018, we show a side-by-side comparison of SMOS-SMAP ASIT and ASI SIC maps (Fig. 3.4). On 11 and 12 September 2018, the low SIC halo (Lindsay et al. 2004) can be seen in the ASI SIC maps as a thin ring surrounding Maud Rise. Interestingly the SMOS-SMAP ASIT map counterparts for that time period instead show a wide-scale thinning; what we will refer to as the SIT anomaly from now on. While the the bottom portion of the halo is not visible in the ASIT record, the northeastern crescent is enlarged, indicating a much wider area of anomalous activity than suggested by the SIC maps. 13 September 2018 tells a different story wherein the SIC map can no longer distinguish the halo feature whereas its SMOS-SMAP counterpart still contains the thinning from previous days. For a better resolved image from visual Moderate Resolution Imaging

Spectroradiometer (MODIS) data of both the Weddell Sea polynya of 2017 and the SIT anomaly of 2018 see Fig. A2. Such images are only available for cloud free conditions and thus cannot be used to monitor the polynya development in detail.

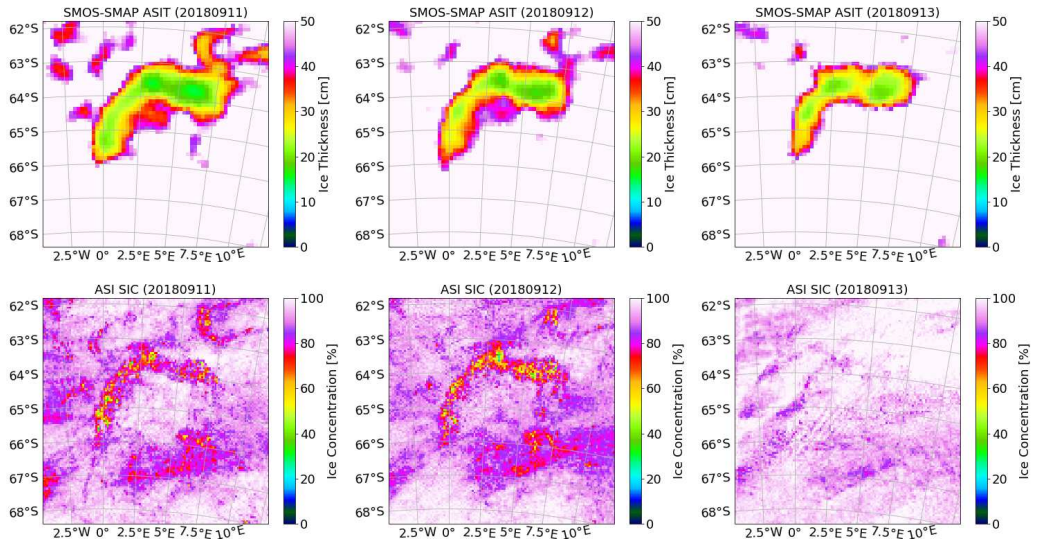

Figure 3.4: SMOS-SMAP ASIT (top row) and ASI SIC (bottom row) retrieval of the days during the 2018 sea ice anomaly: 11–13 September 2018.

Fig. 3.5 depicts the Weddell Sea polynya until the end of September 2017 as well as the weeks leading up to the event. Atmospheric data (Fig 3.5a) in the form of wind speed derived from 10-m u and v components of wind velocity vectors at 1000 hPa are presented as daily average (in blue) and maximum (in red) magnitude in the region of interest. Interpreting Fig. 3.5a as compared to the lower polynya area and thickness plots, we see that the highest maximum (in red) and mean (in blue) wind speed both coincide with the 13 September polynya opening date. This agrees with the general conclusions reached by both Campbell et al. (2019) and Francis et al. (2019). From the ASI SIC record (Fig. 3.5b), we can see both the similarities it shares with the ASIT record (Fig. 3.5c) as well as clear differences that will be further discussed below. Important to note is that the blue line in both SIC and ASIT records represents the area that is classified as open water, so 0% sea ice concentration and 0 cm thick ice (so no ice at all), respectively. These lines are also present in the 2018 Fig. 3.6b and 3.6c but are consistently at 0 km^2 and therefore hidden because of the overlap with low SIC and low ASIT lines.

3.3 Results

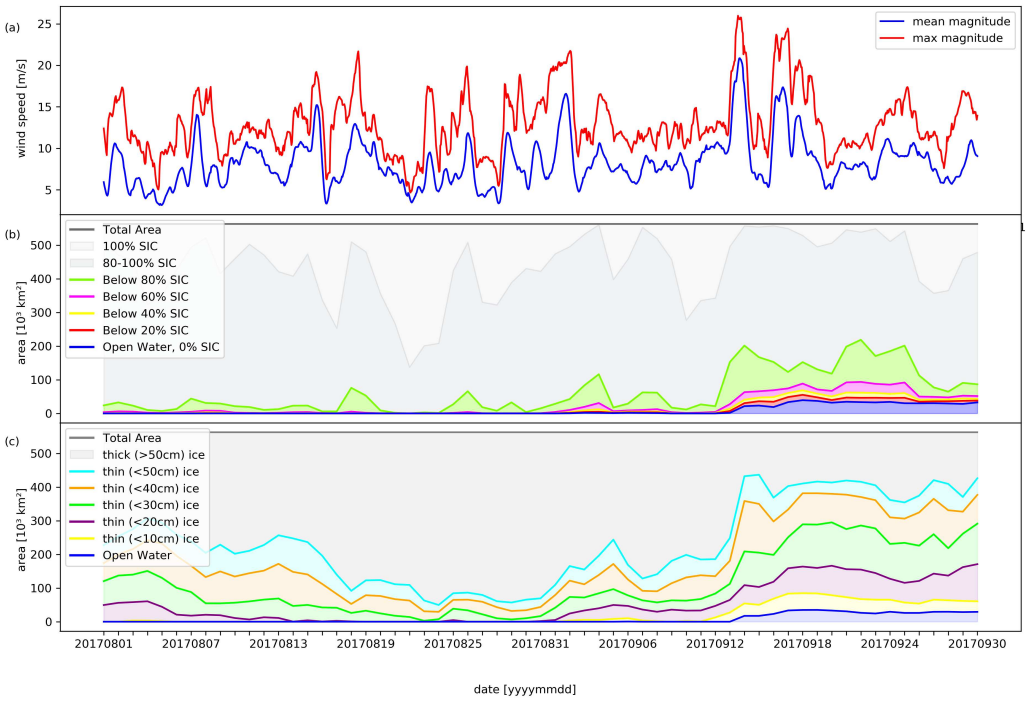

Figure 3.5: August–September 2017: (a) Daily ERA5 wind speed at 1000 hPa (red: daily maximum; blue: mean computed for the region outlined by the bounding box in Fig. 3.1). (b) ASI SIC where each line represents ice that falls below a SIC value shown in the legend. Each filled-in area represents sea ice within the range set by the lines such that all the colours match the colour of the lines that are directly above them (e.g. the green shading below the green line represents 60–80% SIC area). The uppermost grey line represents total area (562.5×10^3 km^2) and the variation in shading below it is as follows: light grey is for all area that is 100% SIC and the darker grey is reserved for all that fall between 80 and 100% SIC. (c) SMOS-SMAP ASIT where each line represent sea ice below a thickness shown in the legend. Each filled-in area represents sea ice within the range set by the lines such that all the colours match the colour of the lines that are directly above them (e.g. the cyan shading below the cyan line represents 40-50 cm ASIT area). The grey line represents total area (562.5×10^3 km^2) like in the SIC plot and the grey shading represents sea ice that is identified to be >50 cm. All plots cover the area of interest outlined in Fig. 3.1.

August and September 2018, shown in the time series plots of Fig. 3.6, is the time period of interest for this research, where the area that featured a polynya the year prior shows a low SIT anomaly. Looking at the ASIT record for the two months (Fig. 3.6c), we can see the area thinner than 50 cm (brown line) exceeds 250×10^3 km^2 (17–20 Sep) and ice thinner than 20 cm (green line) is detected on multiple days (8–12 Sep, 16–19 Sep) in an anomaly spanning almost the entirety of September. SIC time series (Fig. 3.6b) seems to vaguely reflect the SIT anomaly of late September

by sporadic episodes of below 80% SIC (purple line) but does not describe the anomaly like the ASIT record does. No area below 40% SIC is detected and thus no significant open water area prevailed that year. Notably we can see the highest mean (9–10 Sep) at the start of the SIT anomaly and the highest maximum at the same time as the peak of the anomaly (17–18 Sep).

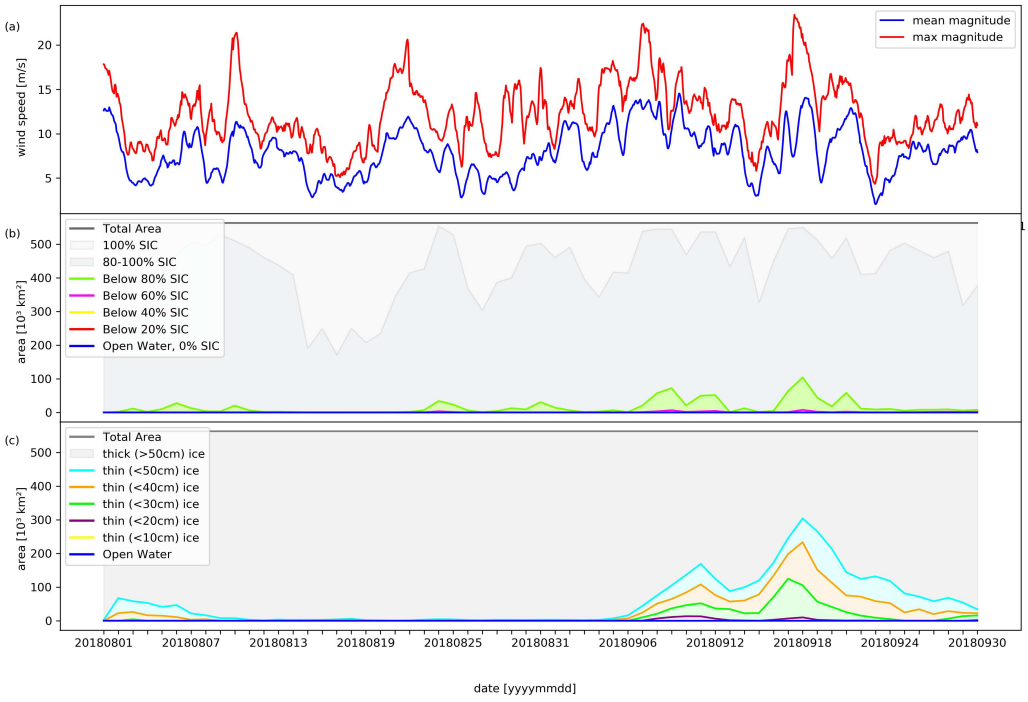

Figure 3.6: Same format as Fig. 3.5 for August–September 2018. See Fig. 3.5 caption for specifications.

In Fig. 3.2 we show the entire 11-year SMOS record in the form of a time series. For the time periods highlighted with colored frames, maps of the ice anomaly are shown in Fig. 3.7. Time frames highlighted in yellow are the 2016 and 2017 Weddell Sea polynya events whereas red frames surround the periods of ice thinning anomalies. Notably, ice thinning anomalies seem to have a higher frequency of occurrence.

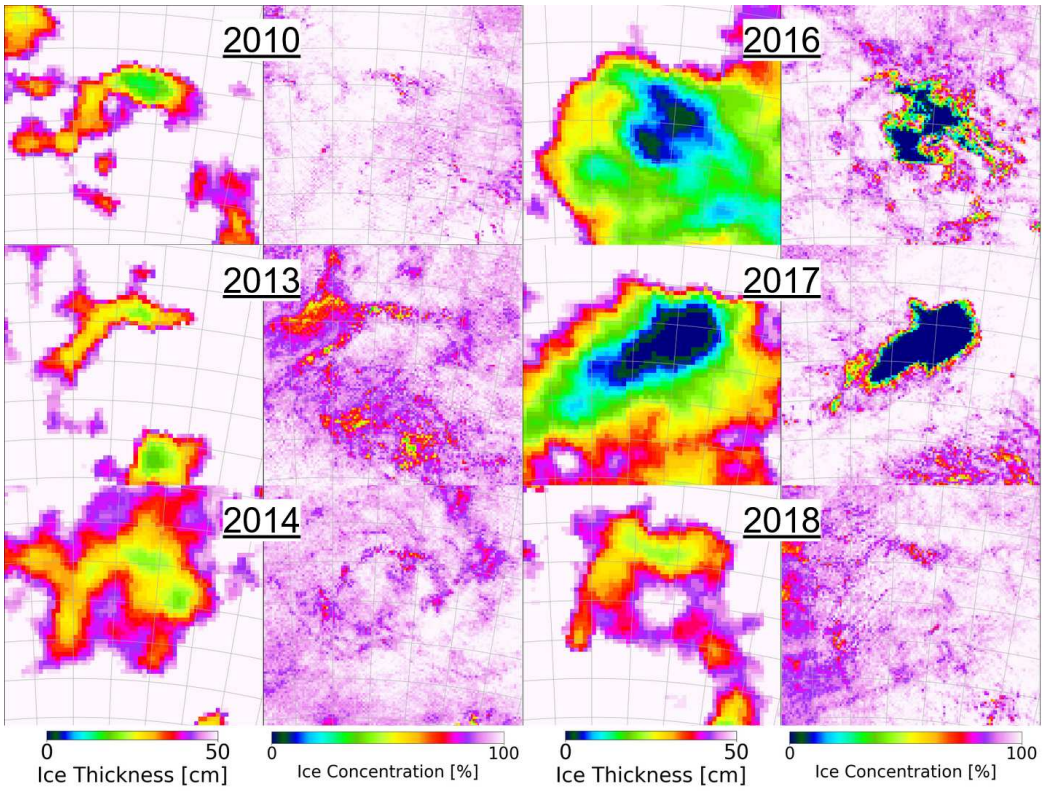

Figure 3.7: ASI SIC and SMOS ASIT retrieval maps covering all major thinning events that can be seen in the 11-year SMOS record (Fig. 3.2). All maps cover the area of interest outlined in Fig. 3.1 with and all the grid-lines remaining identical (removed here to maximize the size of each map).

3.4 Discussion

The individual maps Fig. 3.3 and Fig. 3.4 for 2017 and 2018, respectively, are useful for accessing fine details of low ASIT distributions as well as comparing the ASIT retrieval with ASI SIC. By capturing the low sea ice thickness anomaly in 2018 and at the beginning of the 2017 polynya event in the ASIT record we can infer that there were residual polynya-favourable effects that produced a forcing that was insufficient to open the polynya but sufficient to still impact the overlying sea ice. This is similar to the 1970s polynya cases, where the 1973 smaller polynya preceded the larger Weddell Sea polynya visible from 1974 to 1976 (e.g., Martinson et al. 1981; Motoi et al. 1987; Comiso et al. 1998; Cheon et al. 2019). Cheon et al. (2019) attribute the lack of any polynya in 2018 in part to the positive state of the Southern Annular Mode inducing fresh surface water conditions effectively capping warmer deep water convection and the weakening of the Weddell Gyre in the years that followed its peak activity in 2015 and 2016. This study aims to present a more complete

perspective where rather than an abrupt change from the largest Weddell Sea polynya in 2017 to lack thereof we observe a waning of this phenomenon with peak activity in 2017.

In order to analyse the time periods during which the polynya of 2017 (Fig. 3.5) and the sea ice anomaly of 2018 (Fig. 3.6) occurred, we view the respective time series. In Fig. 3.5c we see a progression of events in terms of ASIT of how the 2017 polynya formed and expanded. First and foremost we observe a major regional ice thinning in early August that peaks on the fourth of August. Looking at Fig. 3.5b we can see how much smaller the area affected by SIC variations is and how it is different in behaviour to the ASIT time series. At this point in time, low-SIC area is small and predominantly above 80%. This is especially true during the brief period (6–12 Sep) leading up to the polynya, which is promising because it suggests a lack of low SIC-induced ASIT values due to the SMOS-SMAP ASIT retrieval full ice cover assumption. In total, compared to the $50 \times 10^3\,\mathrm{km}^2$ of below 100% SIC area, sea ice thinner than 50 cm spans over $300 \times 10^3\,\mathrm{km}^2$ of the region of interest. Following the period mentioned (6–12 Sep), we see the sudden peak (12–13 Sep) in both lower sea ice concentrations and thin sea ice. Based on Fig. 3.3, we see that this smaller opening in sea ice (Campbell et al. 2019), paved way to the Weddell Sea polynya of the year 2017.

Campbell et al. (2019) report on the highly variable salt content in the vicinity of Maud Rise during this time period in 2017 indicative of cycles of melt and refreeze. Thus the negative feedback of melting sea ice wasn't able to fully re-stratify the ocean. This is reflected in the ASIT record (Fig. 3.5b) as large parts of the ice pack appear to be thin ice, especially when compared to (Fig. 3.6b) where there is no thinning prior to the 2018 anomaly. Weak stratification coupled with strong winds (Campbell et al. 2019) (Fig. 3.5a, 1–2 Sep) enhanced turbulent mixing and entrained heat into the surface mixed layer. Francis et al. (2019) report on the unusual amount of cyclones during 2017 austral winter while Martinson et al. (1998) detail how such events may serve to reduce the bulk stability of the water column. In Fig. 3.3 we can see the much larger scale effect this is having on ASIT rather than SIC in Fig. 3.5b and Fig. 3.5c, respectively. While the thinning can be attributed to the entrained heat, salt is also entrained from water below which reduces stability (Martinson et al. 1998). In addition to atmospheric effects, Campbell et al. (2019) attribute the 2016 and partly 2017 polynyas to salinity fluxes from deep water into the mixed layer. Thus, the sea ice melts from below due to added heat and the melt-water is unable to stabilize the water column due to the salinity flux, facilitating thinning of sea ice and its eventual melting that results in the Weddell Sea polynya of 2017.

Fig. 3.6 shows that 2018 is less anomalous than 2017 for the first one and half months until the sea ice anomaly begins to form on the 6 of September 2018. There is an initial thinning and occasional sporadic "below 80%" SIC events distributed throughout the period. Notably, the events on 24 August and 31 August, seen in Fig. 3.6b could be lead openings in thick pack ice as there is no thinning recorded in the ASIT retrieval for those days. The sea ice anomaly itself, as can be seen in Fig. 3.6c, is very well defined in the ASIT record and has a clear beginning and an end. Notably, of the two consecutive low ASIT area peaks (7–13 September and 15–21 September), the

first is characterized by ice thinner than 20 cm for a longer period that the second which instead has a much larger area thinner than 50 cm. This anomaly follows a period of relatively strong mean and maximum wind speed from 3 August to 13 Sep (Fig. 3.6) towards the East and Southeast directions (Fig. 3.9) that could imply wind-driven turbulent mixing influencing the sea ice anomaly in much the same way the added heat and salinity fluxes preconditioned the polynya the year before (Campbell et al. 2019). Due to the lack of in-situ ocean data analysis from the 2018 period and the absence of such analysis in this study, any proposed ocean-driven polynya preconditioning is purely speculative. Nevertheless, it can be assumed that the negative feedback of melting sea ice freshened the mixed layer thereby stabilizing the water column and suppressing further exchange with Warm Deep Water from below (Wilson et al. 2019).

Through the comparison of our ASIT and SIC data with ERA5 atmospheric data we can speculate what wind conditions are favourable for polynya formation. Fig. 3.8 show the wind conditions on 13 September 2017 where for several hours strong winds ($20\,\mathrm{m\,s^{-1}}$) prevailed above the region of interest suggesting heavy storm activity, corroborating the findings of Campbell et al. (2019) and Francis et al. (2019). In contrast, regional winds in September 2018 are consistently below $15\,\mathrm{m\,s^{-1}}$ (mean) and areas of strong wind seem to be localised around rather than on top of Maud Rise (not shown) like on September 7 Fig. 3.9. It is hard to say whether stronger storms during the sea ice anomaly of 2018 would have caused a polynya to open as it is not known quantitatively how much different factors contribute to the formation of the polynya. But it is clear that atmospheric forcing is a strong contributing factor especially towards the start of the polynya. Thereafter also turbulent mixing of warm salty water plays an increasing role (Campbell et al. 2019).

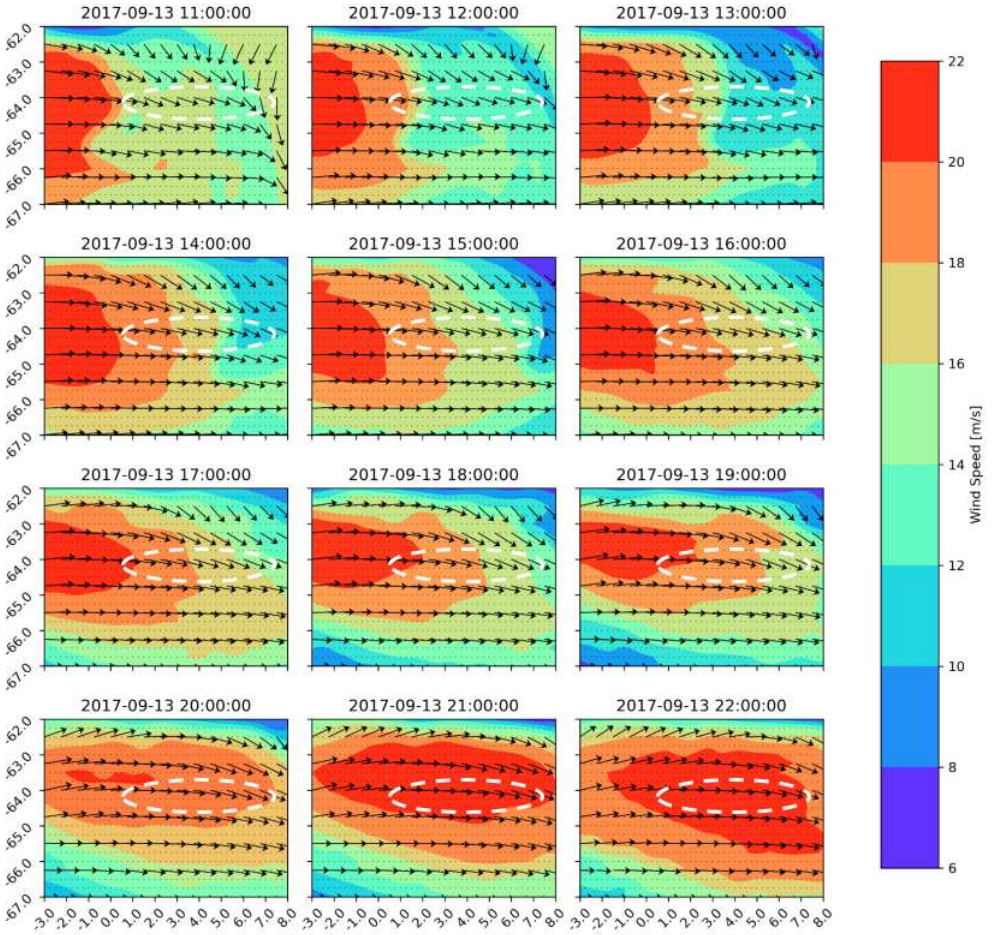

Figure 3.8: ERA5 quiver and contour plots of wind activity above Maud Rise for 9 hours on 13 September 2017, the day the 2017 Weddell Sea polynya rapidly expands. All times are reported as UTC. The polynya extent from 13 September 2017 is shown as a white dashed reference oval. All plots cover the area of interest outlined in Fig. 3.1.

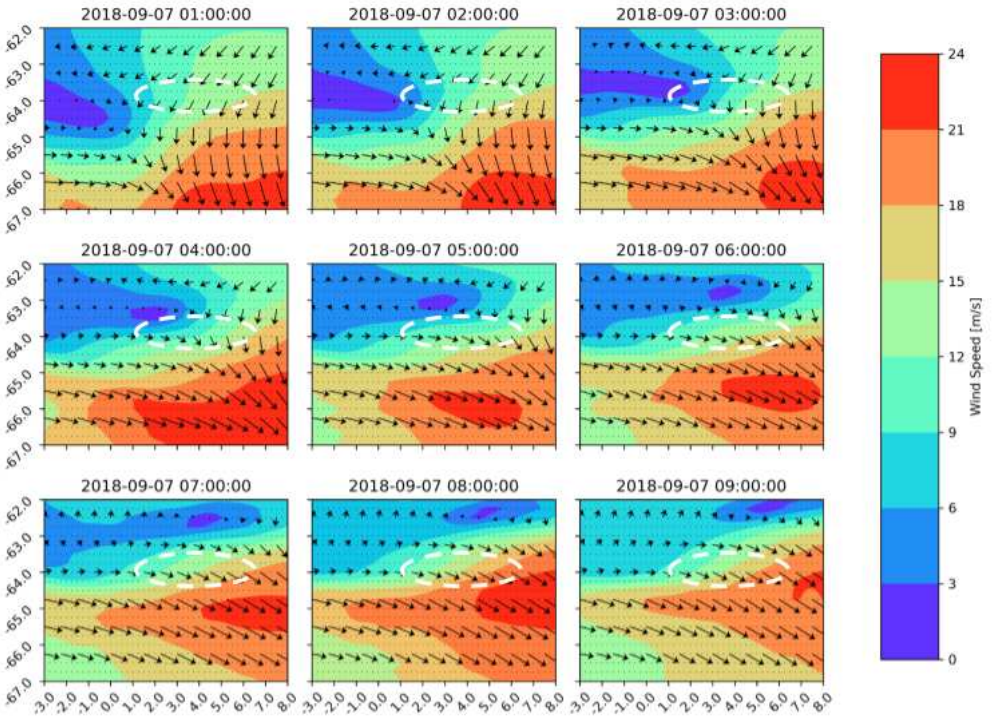

Figure 3.9: ERA5 quiver and contour plots of wind activity above Maud Rise for 9 hours on 7 September 2018, the day the 2018 sea ice anomaly starts to form. All times are reported as UTC. The sea ice anomaly extent (ASIT<30 cm) 7 September 2018 is shown as a white dashed reference oval. All plots cover the area of interest outlined in Fig. 3.1.

Lastly, we use the SMOS ASIT retrieval instead of the combined SMOS-SMAP to also include years before 2015 (the year when SMAP was put into orbit) to make a consistent 11 year SMOS ASIT time series over the months of July, August, September and October (Fig. 3.2) that fully includes the freezing periods of the relevant region over the years. Notably, the sea ice thinning of 2018 is by no means an isolated event and the Maud Rise region seems to be regularly subject to sea ice thinning events. While the SIC record offers two prominent anomalous events: the Weddell Sea polynya of 2016 and 2017, respectively (highlighted in yellow in Fig. 3.2), it is through the ASIT retrieval that we identify all other anomalies that have occurred over the years. Specifically, years in which the polynya did not occur but still showed signs of ice thinning are 2010, 2013, 2014 and 2018 (not counting thinning episodes that follow freeze-up or precede melt); they are highlighted in red in Fig. 3.2. In Fig. 3.7, we look specifically at the events highlighted in Fig. 3.2 to get a better picture

of ice thinning anomalies and polynya throughout the 11-year SMOS record. The similarities of these anomalous events further consolidate the idea of many polynya-favourable events taking place in the region with each having their own effect on the ice cover (e.g., Martinson et al. 1981; Holland 2001; Steur et al. 2007; Cheon et al. 2019; Francis et al. 2019; Campbell et al. 2019; Wilson et al. 2019; Heuzé et al. 2021).

3.5 Conclusions

From the SIC data product it is known that major Weddell Sea polynya events occurred in August 2016 (3-9 Aug) and September 2017 (13 Sep until melt of that year), respectively. From the SMOS-SMAP ASIT record we now know that the episodes of anomalous wintertime sea ice loss span a wider time span than previously assumed. With the sea ice anomaly of 2018 (5-30 Sep) as well as thinning events in 2010, 2013 and 2014 that can be identified in Fig. 3.2, we can assume that anomalous behaviour of sea ice above Maud Rise is more pronounced than previously suggested by SIC data and is indicative of a more regular pattern of thin sea ice in the region.

By analysing the three different data products (ASIT, SIC and ERA5 meteorological reanalysis) and comparing them with one another, we tested the two hypotheses proposed in this manuscript: whether atmospheric forcing influences the sea ice region above Maud Rise and more importantly, whether ASIT retrieval is a viable candidate for the study of the Weddell Sea polynya. As previously reported on (e.g., McPhee et al. 1996; Francis et al. 2019; Campbell et al. 2019; Wilson et al. 2019; Heuzé et al. 2021) we corroborate that direct atmospheric forcing is very much involved in wide-scale drops in ASIT and SIC above Maud Rise, in addition to oceanographic forcing.

The notion that strong winds are responsible for the Weddell Sea polynya is not a new one (Martinson et al. 1981; McPhee et al. 1996), but it is still generally classified as an open-ocean polynya (Maqueda et al. 2004). Explanations that tie together the atmospheric and oceanic processes that cause the Weddell Sea polynya generally do not include direct atmospheric forcing, rather indirect large-scale atmospheric involvement is mentioned in the form of the negative wind stress curl intensifying the Weddell Gyre (e.g., Cheon et al. 2014; Cheon et al. 2015; Cheon et al. 2018; Cheon et al. 2019; Campbell et al. 2019). In addition to the 2017 polynya (Fig. 3.5), we observe wind activity influencing the sea ice anomaly of 2018 (Fig. 3.6). Without in-situ oceanographic data, it is difficult to access what caused the anomaly of 2018, however the possibility of wind-driven preconditioning is not unlikely based on the analysed reanalysis data as well susceptibility of the Maud Rise region to wind-induced perturbations (McPhee et al. 1996). Wind-induced ice-ocean shear can deepen the mixed layer via turbulent mixing resulting in the entrainment of warm saline water from below, which as shown in Campbell et al. (2019) can lead to a polynya. However, it is also known that impact of strong winds is heavily determined by the regional stratification of the ocean (Wilson et al. 2019). Thus we can speculate that there was wind stress being applied to the

ice above Maud Rise in 2018, which lead to ice melting but was insufficient in deepening and thereby warming the mixed layer to the point where large areas of ice could have completely melted.

Important to note is that for this study also other parameters were calculated from the base ERA5 data products like atmospheric divergence and curl (not shown), which have also been used to identify direct atmospheric forcing (Heuzé et al. 2021). In the end, strength of the wind magnitude present above the region is most directly connected with drops in ASIT and SIC. We observe the wind magnitude to be more influential than wind direction, which although sporadic, is generally towards the East as the area is dominated by westerlies. This is likely due to the scale of the area analysed, as upon investigating the relation between wind and polynya formation on larger scales as done in Francis et al. (2019), diverging winds facilitated by cyclones have been shown to aid polynya formation. Also worth mentioning is the work done by Francis et al. (2020) that demonstrate the impact of moisture-carrying atmospheric rivers during polynya years which in addition to increasing snow fall, which effectively decouples the sea ice from the cold atmosphere once precipitated, brings clouds that trap the outgoing long-wave radiation locally resulting in further ice melting. As such, atmospheric rivers are yet another process that aid in the formation of the Weddell Sea polynya. With so many processes driving the formation of the polynya it is thus no surprise to see more regularity in sea ice anomalies in the region, as the 11-year ASIT time series has shown (Fig. 3.2). However, often melting of ice produces a strong negative feedback that suppresses further entrainment of deep ocean heat thereby halting convection and polynya formation, hence the rarity of this occurrence. Thus in most of the years the forcing was not strong enough to open the polynya and only the ASIT record shows the imprint of the sea ice anomaly. With strong storm activity, the previously mentioned negative feedback can be overridden by entraining enough Warm Deep Water such that the ice is fully melted (Francis et al. 2019; Campbell et al. 2019; Wilson et al. 2019). Moreover, it is the combination of these polynya-favourable forcings that cause the Weddell Sea polynya but each have their own effect on the sea ice cover. We cannot fully quantify these effects with the data presented in this manuscript. Given the full ASIT record (Fig. 3.2), we may speculate that other than the mean-state factors, other processes that lead to the polynya like deep convection (Martinson et al. 1981), wind-driven turbulent mixing (Wilson et al. 2019; Campbell et al. 2019) and sea ice divergence (Francis et al. 2019) as well as the influence of SAM(Cheon et al. 2019) tend not to occur simultaneously. Otherwise we would expect more fully open polynya events, instead we see in our 11-year record that the thin sea ice anomaly is a more frequent occurrence indicative of some but not all of these processes taking place separately.

As for the effectiveness of ASIT analysis, we have demonstrated that it offers information that is unique as compared to standard SIC-based analysis of the region. While influenced by SIC, the SMOS-SMAP ASIT retrieval has demonstrated itself as an additional source of information that provides reasonable data about the ice conditions above Maud Rise. Most impressive are periods of near-100% SIC and low ASIT, e.g., during periods leading up to polynya. For example when the polynya opens, the large heat loss from the ocean often causes thin sea ice to grow, which soon

shows up as 100% SIC but is correctly shown as large-scale thin ice area in the SMOS-SMAP dataset. Based on our limited sample size of two polynya (2016 & 2017) within the 11-year SMOS-SMAP ASIT record (Figs. 3.5 and A1), austral winters that featured the Weddell Sea polynya are easily distinguishable from those that did not. Looking at Fig. 3.2, while we identify sea ice anomalies in years other than in 2016 and 2017, the two polynya years seem to feature large areas of anomalously thin ice prior to the occurrence of both the Weddell Sea polynya of 2016 and 2017. 2017 in particular features prolonged wide-scaled thinning that is corroborated by the weak ocean stability indicative of cycles of melt and refreeze presented in Campbell et al. (2019). Here we identify the potential of using the retrieval to predict Weddell Sea polynya but acknowledge the fact that more research needs to be conducted in this direction to validate this hypothesis and cannot comment on the robustness of this method in relation to other early detection criteria (e.g., Heuzé et al. 2021). When the polynya is open, the ASIT signal from the retrieval is unlikely to provide accurate ice thickness data due to large areas of open water influencing the signal. As mentioned before, low SIC affects the ASIT record. Thus we would like stress once again that due to the potential uncertainties in this study the ASIT record serves mainly as an indicator of anomalous sea ice activity rather than a means by which to quantify the exact degree of thinning or calculate ice volume change in the region.

In 2018, a polynya-free year, ASIT retrieval has shown that the beginning and end of a sea ice anomaly that, at its peak (18 Sep: <50cm sea ice region with an area of $300 \times 10^3\,\mathrm{km}^2$), reached an estimated area larger than the United Kingdom. It is apparent that the SIT anomaly covered a much wider area than the area where low SIC (most likely minor lead openings) is recorded. This type of analysis, able to detect anomalous activity above Maud Rise, paves the way for a better understanding of the underlying processes that not only drive the polynya but are in fact affecting the sea ice more often than previously thought possible. The ASIT retrieval would benefit most if evaluated with direct atmospheric and oceanographic measurements, and while ERA5 atmospheric reanalysis data partly accommodates for the atmospheric component, comparisons with in-situ oceanographic measurements or model-generated best fits, like the Southern Ocean State Estimate (Mazloff et al. 2009), to better understand coincident ocean properties is highly encouraged and needed. An extension of the 11-year SMOS time series is needed to better quantify the regularity and how often such polynya-type ice anomaly events occur. As both SMOS and SMAP are science missions with no planned follow ups there is a chance that we will have a gap in the current L-band radiometry capability in space. However, with the future, operational Copernicus CIMR mission (planned launch 2028; `https://cimr.eu/`) some continuation of the ASIT time series will be possible.

In conclusion, through comparisons between ASIT and ERA5 data we corroborate the idea that the Weddell Sea polynya is not purely ocean-driven and instead also facilitated by direct atmospheric forcing. As for ASIT retrieval from L-band microwave radiometers like SMOS ad SMAP : it is an effective tool at monitoring sea ice conditions above Maud Rise and capable of collecting more substantial information than its SIC counterpart. Rather than substitute SIC retrieval though,

the two should be used in conjunction with one another to aid the scientific understanding of the processes taking place and it should be added as yet another tool at trying to understand the unique and complex processes present in the Maud Rise region.

4 New estimates of pan-Arctic sea ice–atmosphere neutral drag coefficients from ICESat-2 elevation data

The following chapter is based on the published paper *New estimates of pan-Arctic sea ice–atmosphere neutral drag coefficients from ICESat-2 elevation data*. The paper is featured in *The Cryosphere* journal, which is published by Copernicus Publications on behalf of the European Geosciences Union. I am the main author of this publication, with co-authors Christof Lüpkes, Alek Petty, Michel Tsamados and Gunnar Spreen. I carried out the development of the new retrieval method, conducted the analysis of the data and wrote the initial draft of the paper. Subsequently, the co-authors contributed by suggesting edits based on their expertise, helping me to prepare the paper for submission. Lastly, two anonymous reviewers provided further edits, which improved the paper to the state featured in the journal, as well as in this chapter. The chapter includes minor adjustments to the published paper to better integrate the work into the dissertation.

This chapter is on the development of the pan-Arctic sea ice–atmosphere neutral drag coefficient retrieval and addresses **RQ**s 3 and 4 detailed in Chapter 1. Unlike Chapter 3, Chapter 4 explores sea ice in the Northern Hemisphere and at a synoptic/pan-Arctic scale instead of mesoscale. Despite these differences, the two studies are related through the use of satellite remote sensing, as well as the analysis of sea ice–atmosphere interactions. While drag coefficients were not explicitly mentioned in Chapter 3, it was the drag force exerted by surface winds on the sea ice layer that led to the observed dynamically induced thinning of the sea ice field above the Maud Rise seamount. In this chapter we retrieve drag coefficient estimates for the entire Arctic ice pack, based on satellite altimeter data as well as passive microwave radiometer data.

The retrieval is based on estimating pan-Arctic momentum transfer via a parameterization which links sea ice–atmosphere form drag coefficients with surface feature height and spacing retrieved from the Ice, Cloud and land Elevation Satellite 2 (IS2). Though IS2 is unable to resolve these features as well as airborne surveys, it has a higher along-track spatial resolution than other contemporary altimeter satellites. As some narrow obstacles are effectively smoothed out by the IS2 ATL07 spatial resolution, near-coincident high-resolution Airborne Topographic Mapper (ATM) elevation data from NASA's Operation IceBridge (OIB) mission is used to scale up the regional IS2 drag estimates. By also incorporating drag due to open water, floe edges and sea ice skin drag, an assessment of the total drag coefficients is made possible. Accordingly, a spatiotemporal analysis of total drag across the Arctic was conducted for the period November 2018 to May 2022. The date boundaries mark the period when IS2 became operational, and when the work on the paper this chapter is based on was concluded, respectively.

4.1 Introduction

Arctic sea ice is heterogeneous with respect to several characteristics including its concentration, thickness, and roughness (e.g., Thorndike et al. 1975; Bourke et al. 1987). The understanding of how these parameters vary with space and time is important for several reasons, including its impact on human activities, e.g. navigation, and its impact on the physical system, e.g. the transfer of momentum and energy between the atmosphere and ocean.

Studies of Arctic sea ice have arguably focused more on constraining variability in concentration and thickness, towards estimating sea ice volume and its variability in time and space. However, the surface roughness of sea ice also exhibits strong spatial and temporal variability (e.g., Andreas et al. 2010; Lüpkes et al. 2012; Castellani et al. 2014; Petty et al. 2017) which needs to be better understood. Surface roughness can be related to the neutral drag coefficient by applying the Monin-Obukhov theory. Since the roughness length for momentum and the scalar roughness length for heat and moisture occur also in the non-neutral transfer coefficients, surface roughness directly impacts not only momentum transport but also the transfer of heat and moisture between the atmosphere and the underlying surface. Rougher surfaces can create more turbulence and enhance mixing, thereby influencing the stability of the atmospheric boundary layer (e.g., Garratt 1992; Schneider et al. 2022; Lüpkes et al. 2015). Due to its impact on momentum and heat transport over and below the sea ice layer, surface roughness is a fundamental parameter influencing the distribution of sea ice (e.g., Yu et al. 2020; Brenner et al. 2021). Both its relevance for heat and moisture transfer as well as momentum transfer are described by the Monin-Obukhov theory for the determination of turbulent fluxes, where surface roughness serves as an essential parameter (e.g., Lüpkes et al. 2012; Lüpkes et al. 2015). The process of becoming rough is driven in-part by pressure ridging, which redistributes ice vertically, as well as the presence of snow features such as dunes and sastrugis (e.g., Arya 1975; Hopkins 1998; Petty et al. 2016). Summer melt can facilitate the smoothing of obstacles like ridges but can also increase roughness through ice melt (e.g., Andreas et al. 2010; Landy et al. 2015; Castellani et al. 2014). Rougher sea ice is generally found in the thick, multiyear ice regions north of the Arctic Archipelago and Greenland. Landfast rough ice in these areas is an important factor for determining transportation routes for local residents and industry (Dammann et al. 2018). Newly formed first-year ice is typically much smoother, although this division is complicated by the accumulation of snow and its ability to smooth out ice surface variability (e.g., Garbrecht et al. 2002). Observational (e.g., Castellani et al. 2014) and model studies (e.g., Tsamados et al. 2014) suggest that sea ice roughness varies more with space, e.g. between first-year ice and multiyear ice regions, than it does with time, e.g. between freeze-up and melt seasons. With the decline of rough multiyear ice due to recent sea ice minima (e.g., Stroeve et al. 2012), the Central Arctic as well as areas north of Eurasia and Alaska are predominantly composed of first-year ice during winter months and are therefore smoother in comparison (e.g., Castellani et al. 2014; Petty et al. 2017).

4 NEW ESTIMATES OF PAN-ARCTIC SEA ICE–ATMOSPHERE NEUTRAL DRAG COEFFICIENTS FROM ICESAT-2 ELEVATION DATA

4.1 Introduction

The roughness of sea ice is heavily linked with its motion as a result of momentum and energy transfer between ocean, sea ice and atmosphere. Disregarding the proportionally little Arctic sea ice that is fastened to the surrounding landmasses, the remaining majority is subject to motion from the balance of drag forces from ocean currents and winds as well as internal forces (e.g., Thorndike et al. 1982; Steele et al. 1997). Ice motion redistributes ice and snow around the Arctic and controls the rate of discharge from the Arctic basin. The balance of forces governing this motion is described in the momentum balance equation for sea ice, in which the interactions between ice, atmosphere and ocean are quantified via drag coefficients. The turbulent surface flux of momentum $\vec{\tau}$ that describes this interaction is as follows

$$\vec{\tau} = \rho C_d(z) U(z) \left(\vec{U}(z) \cos\theta \ + \sin\theta \, \hat{k} \times \vec{U}(z) \right) \tag{9}$$

where ρ is the air density, $\vec{U}(z)$ is the difference in air and ice velocities at a given height z and $U(z)$ is its magnitude, $\hat{k}$ is the vertical unit vector and θ is the turning angle. The drag coefficient C_d is usually written as a product of the neutral drag coefficient C_d^n and a surface roughness dependent stability function f_m (e.g., Garratt 1992; Birnbaum et al. 2002; Lüpkes et al. 2015; Gryanik et al. 2018). The height above sea level z is most commonly set to a reference height of 10 m to match the layer for which the Monin-Obukhov theory for the determination of turbulent fluxes is valid. It is furthermore nearest to the lowest height level of high-resolution climate and weather prediction models. The neutral drag coefficient C_d^n assumes a neutrally stratified atmospheric surface layer, and is the key parameter that is investigated in this study. The total drag coefficient over a given sea ice surface is commonly subdivided into a contribution from skin drag $C_{d,s}$, caused by microscale roughness, and a contribution by form drag $C_{d,f}$, caused by large distinct obstacles (Arya 1973; Arya 1975). This division is the basis for the drag parameterization developed by Garbrecht et al. (2002). The derived parameterization is developed for estimating the form drag component of the total neutral 10 meter drag coefficient $C_{d10,f}^n$ from the distribution of distinct obstacles and their heights relative to the surface.

The difference in air and ice velocities $\vec{U}(z)$ varies in space and time and thus also the associated momentum transfer and drag forces show a corresponding variability. Given the changing Arctic climate, and the above-mentioned shift from multiyear ice to first-year ice, we can expect that, with a changing distribution of spatial roughness, the associated drag forces will change also. It is therefore in our best interest to help constrain drag coefficients to better model sea ice–atmosphere momentum transfer and in turn, the Arctic climate system. In this study, we will be focusing on the interaction between the atmosphere and sea ice and the related atmospheric (wind) drag force, but will avoid extrapolating our findings to the equally important interaction between ocean and sea ice since our observations are limited to satellite and airborne measurements.

The Garbrecht et al. (2002) parameterization, discussed further in subsequent sections, has been used in various Arctic regions using airborne topographic data (Castellani et al. 2014; Petty et al. 2017). We now aim to extend the applicability of said parameterization onto the high-resolution

pan-Arctic topographic data measured by NASA's IS2 and better characterize the spatio-temporal variability in form drag. With this data product we hope to aid the development of future climate models with integrated form drag parameterization schemes (e.g., Tremblay et al. 1977; Steiner et al. 1999; Tsamados et al. 2014; Yu et al. 2020; Elvidge et al. 2021). Model studies with integrated form drag schemes have been shown to better characterize both ice–atmosphere and ice-ocean interactions as well as inherent properties of sea ice like its thickness (e.g., Tsamados et al. 2016; Martin et al. 2016). However, the degree of uncertainty remains large primarily due to a lack of constraints in these form drag parameterization schemes. While airborne topographic data is perhaps the best record of measured sea ice drag coefficients in the Arctic, it cannot reliably be used to constrain model drag coefficients because of its incomplete temporal and spatial coverage. Satellite drag coefficient evaluations using topography data, on the other hand, have in the past been impractical due to their inability to detect sea ice roughness on sufficiently small scales (e.g., Landy et al. 2015; Castellani et al. 2014). With the launch of NASA's IS2 laser altimeter satellite in 2018, which is able to collect topographic data over sea ice at a resolution that is higher than its predecessors (10s of meters - able to resolve distinct sea ice features), this study aims to make use of the advancements in satellite altimetry to estimate the neutral drag coefficients across the entire Arctic and highlight its regional and seasonal variability for the first time.

4.2 Data and Methods

This section describes the data sets involved in this study as well as the parameterizations used to calculate drag coefficients.

4.2.1 ATLAS on ICESat-2

The Advanced Topographic Laser Altimeter System (ATLAS) is a lidar instrument onboard IS2 that collects high resolution surface elevation data using a sophisticated split-beam photon counting laser system (Neumann et al. 2019). By determining the travel time of reflected laser pulses, ATLAS is able to accurately measure small changes in topography through differences in along-track elevation. The six laser beams are divided into three beam pairs consisting of a strong and a weak beam. The separation between each of the beam pairs is about 3.3 km across-track, whereas the separation between the strong and weak beams making up the pairs is 2.3 km along-track and 90 m across-track (Markus et al. 2017). At an altitude of 500 km, the 10 kHz laser pulses that ATLAS transmits result in roughly 11 m diameter laser footprints (Magruder et al. 2020; Magruder et al. 2021) that are spaced 0.7 m apart. Here what we refer to as a footprint is the spatial extent of the laser energy illumination on the observed surface (Magruder et al. 2020).

In this study we focus on the along-track heights for sea ice and open water leads (IS2 ATL07/L3A level 3a data product). ATL07/L3A takes the global geolocated photon data (ATL03/L2) as input and further processes it to obtain information on sea ice topography (e.g., Kwok et al. 2021b; Kwok

et al. 2019b). For each of the six laser beams, estimates of sea ice surface heights are computed by applying various filters (to remove background photons) and a dual-Gaussian fit to segments of varying length, over which 150 signal photons are accumulated. This is done to reduce the vertical errors from ∼30 cm for each photon height to ∼2 cm (over flat surfaces) for each ATL07 segment height (Kwok et al. 2019a). The segment length varies based on surface type which influences photon counts such that when photon counts are low, segment length is high and vice versa (Kwok et al. 2021b). The spatial resolution is then the sum of the segment length and beam footprint and are on average ∼30 m for the strong beams and ∼70 m for the weak beams (Kwok et al. 2019a). The strong beams (beams 1, 3 and 5) are roughly 4 times stronger in terms of pulse energy than the weak beams (beams 2, 4 and 6), which results in these segment length differences (Kwok et al. 2019b). As a result, we only use the three strong beams for this study to take advantage of the better resolution that they provide. The retrieved heights are referenced to the WGS84 ellipsoid and include various geophysical corrections (e.g. ocean tides, inverted barometer, mean sea surface). ATLAS distinguishes water and ice surfaces by utilizing the surface photon rate, the width of the photon distribution and background rate (Kwok et al. 2021b). ATL07 is also restricted to regions of ice concentration greater than 15% based on passive microwave data.

The IS2 level-2 geolocated photon product ATL03 provides data at higher spatial resolution than the aggregated ATL07 dataset, but at the cost of reduced precision and vastly increased data volume. The use of ATL03 and higher-resolution along-track aggregations has been shown to help better detect and resolve distinct pressure ridge sail heights compared to ATL07 (Ricker et al. 2023). However, for this study, we opted to use the more readily available ATL07 dataset together with our Operation IceBridge downscaling to ensure that our ridge detection and form drag methodology can directly be applied to all existing and upcoming IS2 sea ice elevation data.

4.2.2 ATM Lidar on Operation IceBridge airplanes

The ATM is an instrument suite that contains two high-resolution conically scanning laser altimeters at 1.5° and 2.5° off-nadir, able to measure surface elevation with swath widths 245 m and 40 m, respectively (Studinger 2013; MacGregor et al. 2021; Studinger et al. 2022). Like ATLAS, the lidar uses a 532 nm laser (narrow scanner also uses 1064 nm laser) and a 10 kHz pulse repetition frequency with each laser spot having a footprint of ∼1 m and a vertical precision of ∼10 cm (Martin et al. 2012; Studinger et al. 2022). Here we use the wide scanner (1.5° off-nadir) to take advantage of its high data density at the edges of the swath. NASA carried out several airborne campaigns in the Arctic and Antarctic named "Operation IceBridge" (OIB) during recent years targeting land and sea ice observations (MacGregor et al., 2021). Throughout OIB the ATM lidar instrument has been installed aboard and carried by NASA aircrafts (NASA P3-B and NASA DC8 aircrafts) (Kwok et al. 2019a).

The OIB ATM data set used in this study is from April 2019 when 4 of the flights over sea ice are near-coincident in space and time with IS2. This includes all data from 8, 12, 19 and 22

April 2019 throughout which coincidence was variable but sufficient for comparing observations of similar ice regimes (Kwok et al. 2019a). This data set is used to derive a scaling factor via regression with IS2 ATL07-derived drag coefficients as it is has a better spatial resolution and therefore better resolves sea ice features. By applying this factor to the IS2 ATL07-derived drag coefficients using near-coincident OIB ATM data, we hope to mitigate the spatial sampling biases discussed in section 4.3. In addition, the 6 and 20 April 2019 flights across sea ice that were not coincident with any IS2 tracks, are used to independantly evaluate our IS2 ATL07 monthly pan-Arctic neutral drag coefficient estimates. The OIB flight lines are outlined in Fig. 4.3A of section 4.3.

4.2.3 Extracting sea ice feature data

The Garbrecht et al. (2002) sea ice drag parameterization requires obstacle (sea ice feature e.g., a pressure ridge, rubble field, hummock, snow dune, sastrugi) height and spacing for the calculation of drag coefficients. Regional averages of these quantities are derived from the ATL07 data over segments that are chunked prior to the sea ice feature extraction (please see Fig. B8 in the appendix, where this chunking procedure, as well as the processing steps that follow, are depicted and further described). After experimenting with multiple segment sizes over which to calculate those regional averages, 10 km segments were chosen as in Castellani et al. (2014). 10 kilometres is a typical grid length of a high-resolution regional climate model and is proposed to be a reasonable minimum for the drag parameterizations used (Garbrecht et al. 2002; Lüpkes et al. 2012). Importantly, the data is not equally spaced due to the influence of surface reflectivity on photon counts and thus the along-track distance parameter (in meters) is used to chunk the data into 10 km segments. As a result, the 10 km segments end up having a similar but not equal amount of values. To see the typical spacing between measurements Arctic-wide and the spatial variability thereof, see Fig. B1B in the appendix. Lastly, to increase the number of segments and the stability of drag estimates, the 10 km segments over which average sea ice feature statistics are calculated are shifted by 1 km along-track, i.e., they have large overlap and only every 10th segment is fully uncorrelated. Importantly, 10 km segments with a measurement spacing that exceeds 1 km, a value that is sufficiently higher than what can be attributed to dark non-reflective surfaces, are assumed to have cloud contamination and are therefore omitted.

After segmentation, the surface level is subtracted from all values per 10 km segment. While the surface height estimates are referenced with respect to the mean sea surface (Kwok et al. 2021b), the drag calculations require obstacle heights above level ground and not the sea surface (freeboard). Thus the sea ice heights are first binned (rounded to the nearest centimeter) and then the height of the surface level is calculated by computing the mode for all heights within the 10 km segment. By subtracting this mode, all heights are referenced to the regional ice level surface. For bimodal distributions, the higher mode is used so as to avoid modes associated to leads and young ice.

The produced 10 km segments of elevation from the regional sea ice surface are used to calculate average obstacle height and obstacle spacing per segment. A four-step process is applied to each segment to compute these regional parameters.

1. The first step involves finding local maxima, i.e., obstacle heights along the segment.
2. The second step is to omit obstacle heights that are below a chosen threshold value.
3. The third step is to distinguish individual features by omitting obstacles that do not fulfil the Rayleigh Criterion (explained below).
4. Finally the fourth step is to compute the spacing between the obstacles that fulfil the Rayleigh Criterion.

The Rayleigh Criterion states that two maxima (obstacles) must be separated by a minimum that is less than half the value of the higher maxima for them to be classified as two separate features (e.g., Hibler 1975; Wadhams et al. 1986). After omitting all elevation maxima that do not fulfil the Rayleigh Criterion, the obstacle heights and the spacing between them (both in meters) are averaged over each 10 km segment, before calculating the neutral drag coefficients at this same scale.

While the chosen threshold value of 0.2 m elevation is expected to detect not only pressure ridges but also all topographic features like rubble fields and hummocks, here we define an obstacle as any series of connected elevation values above the cutoff. This is because all obstacles have the ability to impart form drag and it is therefore not necessary to distinguish between them. Nevertheless, some cutoff must be introduced to effectively partition centimeter-scale roughness that is associated to skin drag and form drag associated to obstacles (in this case anything above the 20 cm cutoff), and we chose one which has been used before (e.g., Castellani et al. 2014; Petty et al. 2017) for better a comparison with previous evaluations of Arctic sea ice topography. A more pressure ridge-focused threshold value of 0.8 m (used alongside 0.2 m in Castellani et al. (2014)) was also tested and produced similar results (not shown).

As will be shown in section 4.3, the higher resolution OIB ATM data, that is able to better resolve sea ice features, is used to bias correct and account for sampling differences in IS2 ATL07 data. Prior to extracting sea ice features, the conically scanned along-track topographic two dimensional data from ATM must also be converted into a one dimensional track. To do so, we adopt the methods from Petty et al. (2017) wherein using a given azimuth angle range we can isolate different parts of the conically scanned ATM swath. We use the ranges 355 to 5° and 175 to 185° to extract the outermost narrow parts of the full ATM swath with the highest data density. This narrow track is then ordered as a function of distance from the first data point and interpolated to fix the resolution at 1 m along-track. Once ordered, as with IS2 ATL07 elevation data, the OIB ATM data set undergoes the 10-km chunking and the four-step process outlined above.

The OIB ATM high-resolution airborne data set is then processed and drag coefficients are calculated from the sea ice feature statistics obtained for 10 km segments (see section 4.2.4 for more

about the calculation step). The processed OIB ATM data serves as an independent drag coefficient estimate to which we compare the processed IS2 ATL07 data. The comparison is done on a regional scale by binning both output datasets onto a polar stereographic projection grid with nominal gridded resolution of 12.5 km. The Polar Stereographic projections is true at 70 degrees north with up to 6% distortion at the poles (Knowles 1993); making it an ideal candidate for pan-Arctic maps. The resampling step for the two datasets is done to compare drag coefficients averaged over the same area; this is because the 10-km segments are not perfectly aligned with one another. Once all coincident grid-cells are identified the bivariate distribution of the two gridded data products is generated.

We use the OIB ATM data as reference to account for the spatial sampling differences with the lower resolution IS2 data. A Huber Regressor is calculated from filled grid cells of near-coincident data and model parameters are then used to linearly scale up the IS2 ATL07 drag coefficient estimates. Unlike the traditional linear fit, the Huber Regressor applies a linear loss to samples with an absolute error $|z|$ larger than a given threshold value ϵ (set to 1.35 to achieve 95% statistical efficiency), thereby weighting 'inliers' and 'outliers' differently (Huber et al. 2009). This is done to reduce the sensitivity of the loss function to outliers that are expected in the data due to the high level of uncertainty when comparing quantities averaged over large spatial scales. Importantly, OIB ATM data is taken as the independent true variable upon training the model as IS2 ATL07 is expected to underestimate obstacles due its lower spatial resolution and therefore overestimate obstacle spacing because of the cutoff.

4.2.4 Calculating neutral form drag coefficient

With the extracted sea ice feature statistics, we apply to them the form drag parameterization developed in Garbrecht et al. (2002). The parameterization is based on the formulation of Garbrecht et al. (1999), which itself is built upon findings by Arya (1973) and Arya (1975) and Hanssen-Bauer et al. (1988) on momentum fluxes by single obstacles. While there are other parameterizations of surface drag (e.g., Lüpkes et al. 2012; Lüpkes et al. 2013; Tsamados et al. 2014), here we focus on the one by Garbrecht et al. (2002) as it is optimized for one-dimensional data like IS2 ATL07 and better suited for estimating drag due to obstacles over consolidated ice-cover.

The generalized Garbrecht et al. (2002) formulation for the sea ice–atmosphere form drag coefficient is as follows

$$C_{d,z_r,f} = \frac{1}{2}\frac{c_w}{\Delta x}\left[\frac{1}{\ln(z_r/z_0) - \Psi(z_r/L)}\right]^2 \int_{z_0}^{H_r} \left[\ln(z/z_0) - \Psi(z/L)\right]^2 \, dz \tag{10}$$

where c_w is the coefficient of resistance, z_r is the reference height, z_0 is surface roughness length and $\Psi(z/L)$ is the Monin Obukhov stability correction function. H_r and Δx represent obstacle height and obstacle spacing respectively which, as in Garbrecht et al. (2002), we will generalize to ensemble mean values H_e and x_e. We use a 10 m reference height z_r since it is the widely accepted

value and is often the lowest level available from atmospheric models. Computing drag coefficients without knowing the orientation of obstacles brings with it its own uncertainty and the Garbrecht et al. (2002) parameterization accounts for this problem by reducing the form drag by a factor of $2/\pi$ given the assumption that obstacles are oriented randomly (Mock et al. 1972). An uncertainty of roughly $\pm 20\%$ is introduced on account of this assumption (Castellani et al. 2014). Lastly, to simplify further, we estimate the atmospheric neutral drag coefficient C_d^n only and do not consider the stability correction. The effect of the latter on form drag is explained in Birnbaum et al. (2002) and in more detail by Lüpkes et al. (2015). With all the caveats taken into account and the integral having been evaluated we get the equation as presented in Castellani et al. (2014):

$$C_{d,10,f}^n = \frac{c_w H_e}{\pi x_e} \frac{\left[\ln(H_e/z_0) - 1\right]^2 + 1 - 2(z_0/H_e)}{\left[\ln(10/z_0)\right]^2} \tag{11}$$

This equation goes back to Garbrecht et al. (2002), but since only neutral atmospheric stability conditions are considered, the integrals in the corresponding equation can be solved analytically. Averaged obstacle height H_e and spacing x_e are the two parameters that are extracted from the IS2 sea ice height data as mentioned in the section before. Here we use the Garbrecht et al. (2002) formulation for the coefficient of resistance and compute it as a function of obstacle height $c_w = 0.185 + 0.147 H_e$, where 0.147 is in m^{-1} so that c_w is unitless.

To calculate the total neutral drag coefficient $C_{d,10,s}$ we follow (Arya 1973; Arya 1975) and add the skin drag coefficient using a value that has been derived by Garbrecht et al. (2002) from airborne turbulence measurements over very smooth sea ice. They obtained the value 8.38×10^{-4} by use of

$$C_{d,10,s}^n = \left[\frac{\kappa}{\ln(10/z_0)}\right]^2 \tag{12}$$

with the von Kármán constant $\kappa = 0.4$ and $z_0 = 1 \times 10^{-5}$ m. This value has its own associated uncertainty (see Section 4.4). It is important to note that equation 10, and by extension equation 11, are only valid with the assumption of obstacle spacing being large enough such that the flow can return to its undisturbed state in between obstacles (Garbrecht et al. 2002). In Garbrecht et al. (2002), although the critical value of $H_e/x_e = 0.015$ for which this condition is satisfied was exceeded by the observed aspect ratio, the parameterization that accounts for this effect (Hanssen-Bauer et al. 1988) was neglected since the resulting form drag $C_{d,10,f}$ was changed by less than 3%. Similarly, in Castellani et al. (2014), including the sheltering effect leads to a modification of less than 0.05% of the total drag coefficient. In this study, the sheltering function $(1 - \exp(-0.5 x_e/H_e))^2$ (e.g., Hanssen-Bauer et al. 1988; Lüpkes et al. 2012; Castellani et al. 2014) is multiplied by OIB ATM-derived form drag coefficient estimates (derived via equation 4.3) but not IS2 ATL07 data since due to the smoothing effect overestimating obstacle spacing (discussed further in Section 4.3), the aspect ratio ends up being predominantly less than 0.015 Arctic-wide for IS2. Despite this, we did conduct

our own sensitivity study to see the effect of the sheltering function on IS2 ATL07 topography data and elaborate further on this topic in Section 4.4.

4.2.5 Calculating total neutral drag coefficient

As the last step in our study, we also included the skin drag coefficient of open water $C^n_{d,10,ow}$ and the form drag coefficient of floe edges $C^n_{d,10,e}$. For the drag coefficient over open water $C^n_{d,10,ow}$, we use the constant value $1.5 \cdot 10^{-3}$ which is multiplied by $(1 - A)$ where A is the sea ice concentration. $C^n_{d,10,e}$ is implemented using the parameterization of form drag by floe edges of Lüpkes et al. (2012), given in the most simplified form (hierarchy level 4) as $C^n_{d,10,e} = 3.67(1 - A) \cdot 10^{-3}$ where the latter term $(1 - A)$ when multiplied by A, peaks at 50% sea ice concentration signifying areas with both ice and water. The parameterization does not just represent a simple fit to observations but was rather derived from physical concepts and assumptions based upon the drag partitioning scheme by Arya (1973) and Arya (1975); for further information please see Lüpkes et al. (2012). We use sea ice concentration from the Advanced Microwave Scanning Radiometer 2 (AMSR2) microwave radiometer at 6.25 km grid resolution based on the ASI algorithm (Melsheimer et al. 2019; Spreen et al. 2008). The combined equation for the neutral 10 m sea ice–atmosphere drag, taken from Petty et al. (2017), is then as follows

$$C^n_{d,10,\mathrm{T}} = (1 - A)C^n_{d,10,ow} + A\left(C^n_{d,10,s} + C^n_{d,10,e} + C^n_{d,10,o}\right) \tag{13}$$

where $C^n_{d,10,o}$ is the form drag coefficient caused by obstacles (e.g. pressure ridges, sastrugis) calculated from IS2 elevation data with equation 11. All terms of equation 13 are referenced to a height of 10-m and thus so is $C^n_{d,\mathrm{T}}$. Equation 13 is evaluated on daily IS2 ATL07 tracks and we match daily ASI sea ice concentration maps to the IS2 ATL07 tracks for the given day to ensure consistent sampling approaches from the different data sets.

4.3 Results and discussion

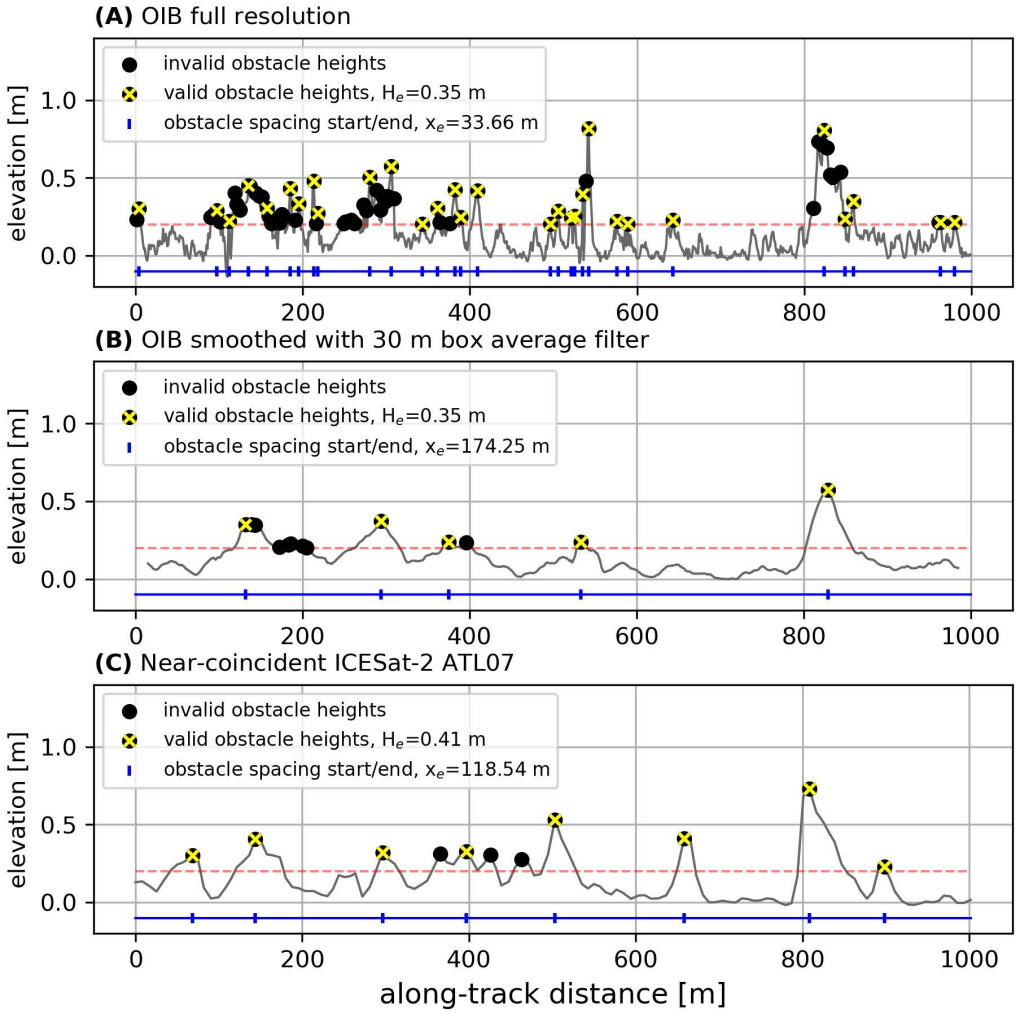

Figure 4.1: (A) Sea ice feature statistics from a sample OIB ATM flight on 19 April 2019 (∼170.7°E, 88.0°N). (B) Same as (A) but smoothed to the IS2 resolution via a moving average filter with box size of 30 m. (C) Sea ice feature statistics from a near-coincident IS2 ATL07 track section. Black dots: all identified maxima; yellow 'x': maxima which satisfy the Rayleigh Criterion; red dashed line: 0.2 m threshold; blue line with dividers: identified obstacle spacing. All data is referenced to level ice (mode).

The four-step process explained in Section 4.2.3 is evaluated on near-coincident OIB ATM data (A,B) and IS2 ATL07 data (C) in Fig. 4.1. Local maxima are found and those below the threshold of 20 cm (marked with a red dashed line in the figure) are omitted (maxima that above the threshold are marked with a filled-in black circle in the figure). Thereafter, the Rayleigh criterion is evaluated (those that fulfil the criterion are marked with a yellow 'x'). That is why we see a lot of unmarked black circles on the side of obstacles, because the Rayleigh criterion assures that only the maximum of the whole feature is considered (most clearly visible in Fig. 4.1A). Figs. 4.1A and 4.1B both depict the same 1 km long ATM segment from an OIB flight carried out on the 19th of April, 2019. The segment chosen is along the 88th parallel north and spans the longitude range 170.60-170.85°E, putting it firmly within the central Arctic. The difference between Figs. 4.1A and 4.1B is that 4.1B has a moving average filter of box size 30 m applied. This is done to simulate the 30 m IS2 ATL07 footprint (see Section 4.2.1) which, as a result of the dual-Gaussian fit needed to reduce vertical uncertainty, also in effect smooths out the topography. For a more detailed description and case study of this smoothing effect, the reader is referred to the publication by Ricker et al. (2023). Once the topography data is smoothed using this 30 m box filter, small clusters of narrow obstacles are viewed as one and the average distance between them for a given length scale is enlarged. In the case presented, average obstacle spacing x_e increases by a factor of ∼5.2. Average obstacle height H_e comes out at 0.35 m for both plots. While the maximum obstacle height is larger in the original data, the smoothed data also has a smaller number of shorter obstacles that bring down the average. In general, we expect the height of tall narrow ridges to be underestimated due to sampling however. We can observe the smoothing effect in Fig. 4.1C wherein near-coincident IS2 ATL07 data, with its low spatial resolution relative to OIB ATM, also exhibits larger average obstacle spacing (factor of ∼3.5) and therefore lower drag coefficient. As Fig. 4.1 covers only a small distance of 1 km to demonstrate the obstacle peak finding method, values presented are likely not representative of all data.

4.3.1 Drag coefficient regression with airborne lidar measurements

Taking the spring 2019 OIB/IS2 underflights (4 days in 2019) that were near-coincident with the measurements of IS2, we can calculate drag coefficients from both data sets and compare the results. The shortest time-lag during the underflight was less than 1 min for 3 of the flights (8, 12 and 19 April 2019) (Kwok et al. 2019a), however, 8 and 12 of April are overlapping racetracks conducted for a time period of ∼8 hours, thus the time-lag is highly variable (all legs were considered to maximize the total amount of data). The shortest time lag on April 22, also used for this comparison, was ∼38 min (Kwok et al. 2019a). We used a subset of all OIB data that fell within the specified azimuthal angle range of the ATM scanner which likely reduced the spatial coincidence as well. As a result, we did not simulate a one to one elevation comparison as has already been done in Kwok et al. (2019a) and Ricker et al. (2023) and thus did not employ any drift correction. Since we look at 10-km averages for the purpose of comparing regional average form drag, it was sufficient to compare

averaged data of similar ice regimes and not to focus on the coincidence itself. Since the averages are not aligned, the data sets are gridded to a 12.5 km grid and the comparison takes place between matching filled-in grid cells (see Fig. 4.2).

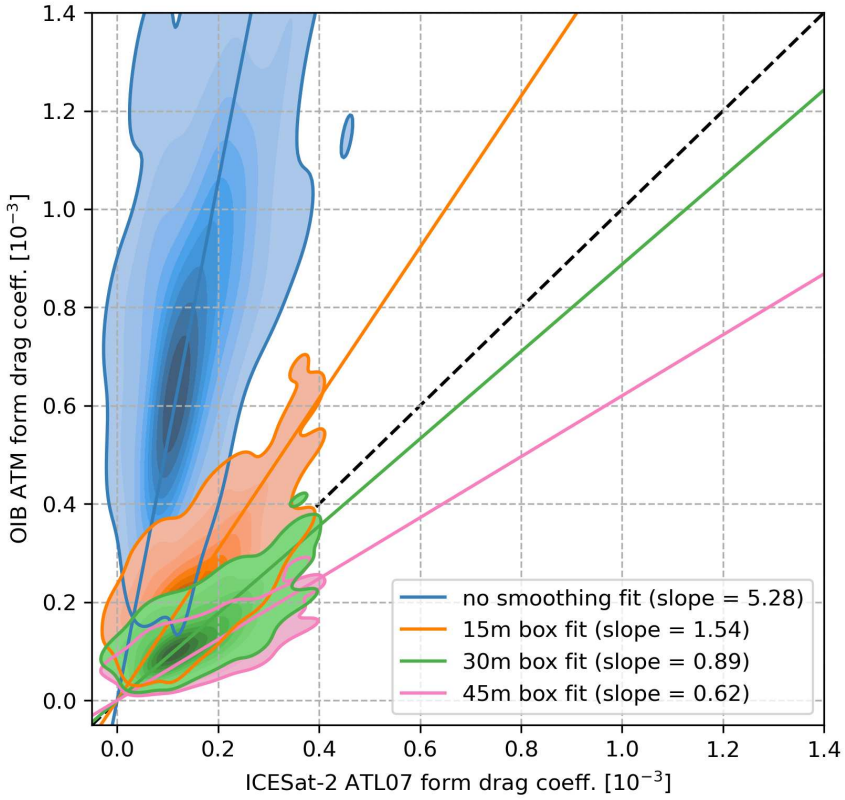

Figure 4.2: Heat maps of 12.5 km grid resampled 10-km average IS2 ATL07 form drag coefficients plotted against those computed from OIB ATM drag coefficients from 4, 8, 19 and 22 April 2019 which are resampled and calculated in the same manner. The blue heat map and line of best fit represent the base drag coefficients from IS2 ATL07 and the full resolution OIB ATM data; this regression is the basis for the scaling applied to IS2 drag coefficients. The other three heat maps feature OIB ATM data smoothed by a moving average filter with a window sizes of 15 m (in orange), 30 m (in green) and 45 m (in pink). The norm for each of the heat maps is different so as to show the full variability of each and avoid oversaturation. The lines represent Huber fits with colour coding matching that of the bivariate heat maps; except for the dashed black line which represents the identity line.

Thus Fig. 4.2 shows a comparison between form drag coefficients calculated from IS2 ATL07 and OIB ATM segments (blue). This slope (in blue) is the scaling that is applied to the IS2 ATL07 drag

coefficients to amplify the retrieved signal, while the orange, green and pink lines are simply tests done to better explain the relation between the satellite and airborne data sets. As expected, the majority of form drag coefficients calculated from OIB ATM occupy a wider range ($\sim 0.3 - 1.3 \cdot 10^{-3}$) than their IS2 ATL07 grid cell counterparts ($\sim 0 - 0.3 \cdot 10^{-3}$). As demonstrated in Fig. 4.1, we can simulate IS2 ATL07 by passing all OIB ATM data through a moving average filter of varying box sizes (15 m, 30 m and 45 m) and observe that we can get the line of best fit to match the one-to-one line depending on the size of the averaging box (Fig. 4.2). Smoothing with a box size of 30 m, which is comparable to the ATL07 strong beam ∼30 m spatial resolution (Kwok et al. 2019b), results in a line of best fit that is the closest match to the one to one line, which is encouraging. Box sizes 15 m and 45 m are shown for comparison's sake and are meant to demonstrate how both too little and too much of this smoothing can fail to produce values comparable to that of IS2.

The beam used for model training is the second strong beam as it is in best spatial agreement with all 4 OIB ATM flight near-coincident data (Kwok et al. 2019a). Using the line of best fit from Fig. 4.2 (in blue) we correct the IS2 ATL07 form drag coefficients towards the OIB ATM form drag coefficient range using the scaling factor 5.28. Here we focused on comparing the average drag coefficients from satellite and airborne instruments rather than the component parameters: obstacle height and obstacle spacing. The reason for this approach is because that is where the best regression was found. Regressing obstacle heights shows decent agreement but evaluating the different box sizes on the OIB values shows very small differences. The differences are small because while the smoothing introduced in ATL07 effectively retrieves the tall narrow ridges as smaller than they really are, this also pushes a lot of small ridges below the cutoff, reducing the sample size. This reduction results in similar averaged values between the smoothed and high-resolution data sets as can be seen in Figs. 4.1A and 4.1B, where the average obstacle height H_e is the same. The only exception are the features that are not detected at all (Ricker et al. 2023), which force the regression to be steeper than expected. With obstacle spacing, the smoothing gets in the way of extracting any meaningful relationship. As can be seen in Figs. 4.1A and 4.1B, the smoothing reduces sample size which is directly proportional obstacle spacing, as less obstacles translates to a higher average spacing between them. It is only through evaluating equation 11 with the input parameters where we see a reasonable relationship. Comparing IS2 ATL07 with OIB ATM form drags with varying box size smoothing applied also shows expected results (Fig. 4.2), further confirming to us that regressing form drags is the best approach.

The correlation found between the drag coefficients computed from the different instruments is 0.61 (blue heat map in Fig. 4.2), and the mean squared error (mse) between the OIB ATM drag coefficients and the IS2 ATL07 coefficients with the scaling factor applied (5.28) is $1.1 \cdot 10^{-4}$. Considering some ridges are not detected (Ricker et al. 2023) due to sampling issues, and the lack of perfect coincidence, we do not expect perfect correlation. Moreover, we're looking at spatial averages here, where the smoothing has a very strong effect on the ridge spacing (as can be seen in Fig. 4.1), that is why a topography comparison where the sampling of IS2 is simulated with the

OIB ATM data, can show better agreement as in Kwok et al. (2019a). However, that is not our aim in this study, here we try to make the Garbrecht et al. (2002) parameterization applicable to IS2 ATL07 data and correct for the sampling issues using OIB ATM. For comparison's sake, we try to simulate IS2 ATL07 with OIB ATM data with the moving average filters in Fig. 4.2, but we chose not to simulate the elliptical footprint of IS2 in detail as in Kwok et al. (2019a) and Ricker et al. (2023) for that is not needed for the monthly pan-Arctic drag coefficient product which is the end result of this study. Unsurprisingly, comparing the correlation and mse with the OIB ATM data (in blue) to the smoothed version (30 m box [in green] which has the best agreement with the identity line), we have found a correlation of 0.72 and a mse of $2.4 \cdot 10^{-6}$ (with the scaling factor 0.89 as in Fig. 4.2) for the latter. This better agreement is observed as here the OIB ATM data is sampled similar to how IS2 ATL07 is, making the methods identical will raise the correlation even higher as in Kwok et al. (2019a). What we require for our study is for the drag coefficients to be calculated as in Castellani et al. (2014) and Petty et al. (2017), making use of high resolution and high sampling of the airborne data sets, and then regressing the OIB ATM values with estimates of the spatially averaged IS2 drag coefficient. In this way, we aim to improve the IS2 product and amplify the signal that is lower than expected due to sampling.

For an inter-comparison of the drag coefficients processed for each of the three strong beams see Fig. B2 in the appendix. Using the first and third strong beams we can produce a similar result despite the model being trained with the second strong beam (the most coincident beam). To incorporate the full available high-resolution data set as well as minimize random sampling errors from here on we use all three strong beams for all IS2 ATL07 parameter maps.

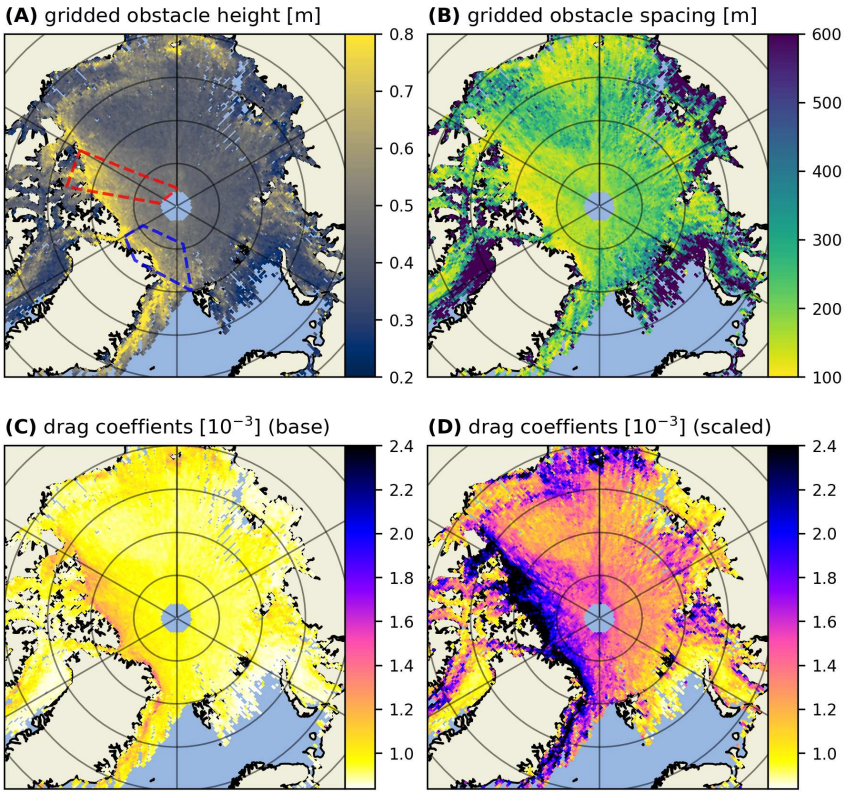

Figure 4.3: Data computed from April 2019 IS2 ATL07 tracks (all three strong beams): (A) average obstacle height, (B) average obstacle spacing, (C) total neutral 10-m atmospheric drag as computed with equation 11 from IS2 average obstacle height and spacing, (D) same as (C) but with the OIB ATM scaling factor (5.28) applied. In (A) zones marked in red and blue represent near-coincident OIB ATM topographic data used to generate the scaling factor via regression (08, 12, 19, 22 April 2019) and data used for evaluation (06, 20 April 2019), respectively.

In Fig. 4.3 we map average obstacle height and spacing used as input in equation 11 as well as the resulting obstacle form drag coefficient ($C^n_{d,10,o}$), with the skin drag coefficient constant ($C^n_{d,10,s}$=8.38 $\times$ 10^{-4}) added, for the month of April, 2019. Here we do not scale with sea ice concentration (A) nor consider floe edge and open water drag components so as to focus on the difference between the scaled and base IS2 ATL07 drag coefficients. The areas outlined in Fig. 4.3A represent the area where near-coincident OIB ATM flights took place (in red) as well as additional topographic data over sea ice from the month of April 2019 (06.04 and 20.04) that is used for the evaluation study in Section 4.3.2 (in blue). Looking just at the drag coefficients, in Figs. 4.3C and 4.3D, we can see that with the OIB ATM scaling factor applied, the data product is in much better agreement with the pan-Arctic maps produced in Petty et al. (2017) as well as the regional drag

assessments conducted in Castellani et al. (2014). The spatial variability across all parameters in Fig. 4.3 also confirms the expectation of multiyear ice that is predominantly north of Greenland and the Canadian Archipelago being more rough ($C_d^n > 1.2 \cdot 10^{-3}$ before scaling up; $C_d^n > 2.2 \cdot 10^{-3}$ after) and as a consequence exhibiting a higher concentration of tall ridges ($H_e > 0.8$ m) and thereby shorter spacing ($x_e < 100$ m) between them.

4.3.2 Evaluation study

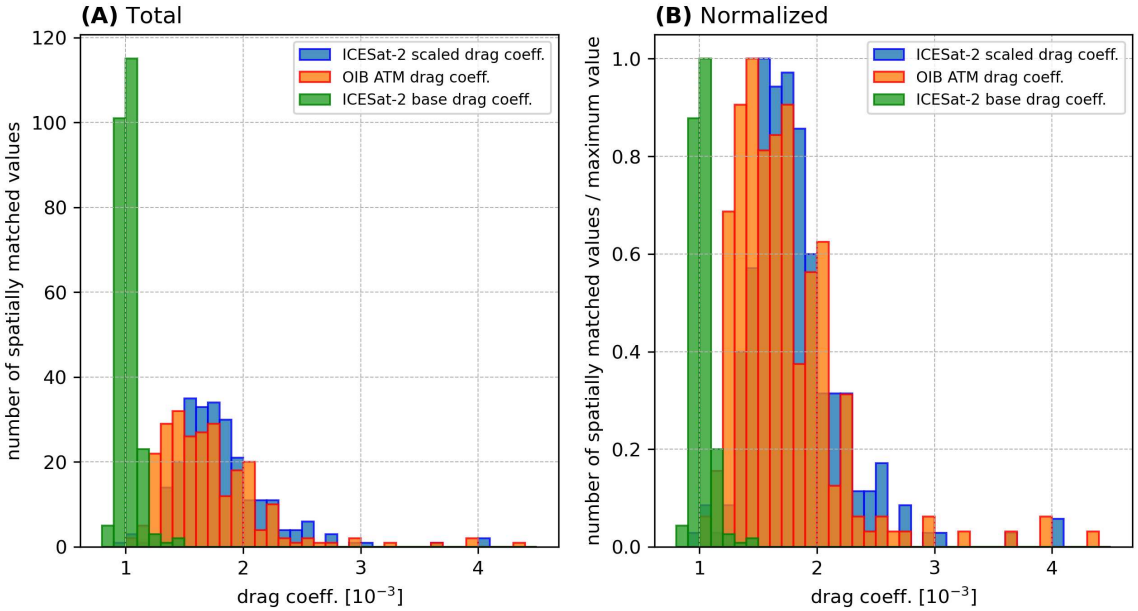

Figure 4.4: Histograms of IS2 ATL07 drag coefficients with (in blue) and without (in green) the scaling factor applied as well as the OIB ATM drag coefficients (in red). Here (A) shows the absolute number of matched grid cells within a given drag coefficient range and (B) is normalized such that every value is divided by the maximum for each data set.

We take advantage of OIB data from north of Greenland (outlined in blue in Fig. 4.3A) and collocate it to IS2 ATL07 drag coefficient data produced for the month of April 2019 to perform an evaluation study of our product. In Fig. 4.4, we compare the drag coefficients computed from the OIB ATM data set using the methods (see Section 4.2.3) that were used on the near-coincident 'training' data set (outlined in red in Fig. 4.3A), to matching grid cells from the 2019 IS2 ATL07 drag coefficient map. Both the original values (Fig. 4.3C) in green and those multiplied by the OIB ATM scaling factor (Fig. 4.3D) in orange are shown along with the ones computed from the OIB ATM data set. Notably, the distribution of the base drag coefficients is overall much narrower than the other two with the main peak centered around $\sim 1.0 \cdot 10^{-3}$ and a secondary peak at $\sim 1.4 \cdot 10^{-3}$. Meanwhile,

the distribution of OIB ATM and scaled IS2 ATL07 drag coefficients both show a similar distribution with the main peaks centered around $\sim 1.6 \cdot 10^{-3}$ and a smaller secondary peaks at $\sim 4.0 \cdot 10^{-3}$. This suggests that our scaled IS2 ATL07 drag coefficients perform reasonably well to represent the drag variability, at least for this part of the Arctic. Given the two data sets are retrieved on different days (within the same month) with ice drifting in between, comparing them grid cell to grid cell is not meaningful since drag coefficients vary in time. If further ATM data becomes available from different regions in the Arctic this evaluation should be extended.

4.3.3 Interannual drag coefficient estimates

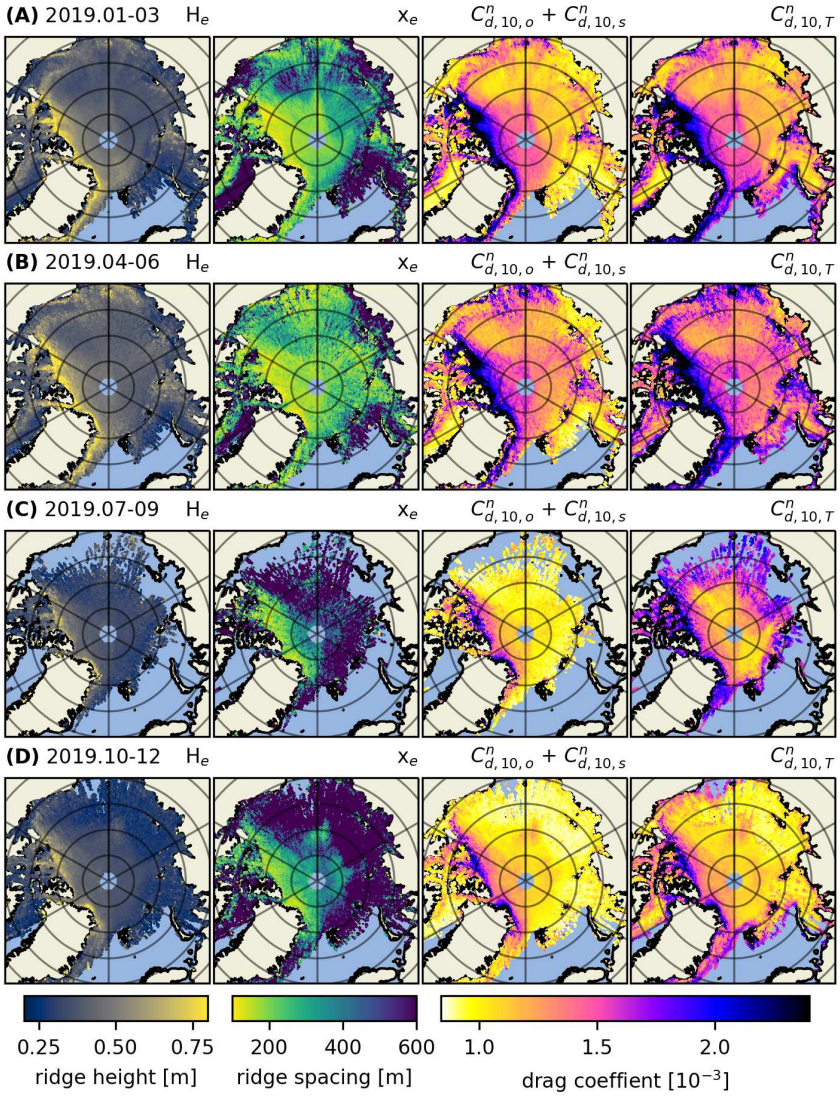

Figure 4.5: 2019 obstacle height (H_e), obstacle spacing (x_e), drag coefficient as a sum of sea ice skin drag and form drag due to obstacles ($C^n_{d,10,o} + C^n_{d,10,s}$), total drag coefficient as a sum of the sea ice skin drag, form drag due to obstacles and floe edges and open water drag ($C^n_{d,10,T}$). Importantly, columns 1 and 2 are the the obstacle heights and spacings as retrieved from ATL07, whereas in columns 3 and 4 the form drag due to obstacles is multiplied by the OIB ATM scaling factor. The periods for which these parameters are calculated are January to March (A), April to June (B), July to September (C) and October to December (D), 2019.

To increase the temporal coverage of Fig. 4.3, we look at spatial variability in 3-month aggregates throughout 2019 in Fig 4.5 (see Figs. B5 and B6 in the appendix for years 2020 and 2021). Here 3 months are chosen to be a reasonable time-frame to maximize the data contained within individual maps on account of IS2's 91-day repeat cycle (e.g., Kwok et al. 2021b; Kwok et al. 2019b). All rows of maps within Fig. 4.5 contain obstacle height, spacing and drag coefficient for consecutive three-month periods.

In the last column (col. IV), we include the floe edge and open water drag coefficient terms according to equation 13; there we can observe drag coefficients $> 1.5 \cdot 10^{-3}$ along the Marginal Ice Zone (Marginal Ice Zone (MIZ)). This combined parameterization is our best estimate for satellite derived sea ice–atmosphere drag. It includes variable form drag due to obstacles and floe edges as well as constants for open water and ice skin drag. However, drag due to floe edges next to over-frozen leads as well as at the edges of melt-ponds in summer is not accounted for (which could be a future enhancement). By looking at the full year separated into 3-month aggregates we can observe the spatio-temporal evolution of drag coefficients Arctic-wide. We observe a seasonal variability of up to $\pm 1.0 \cdot 10^{-3}$ in some multiyear ice regions though there is a thin band of ice close to the Canadian archipelago that is consistently $> 2.0 \cdot 10^{-3}$. Arctic-wide, this effect is comparatively smaller, but nevertheless a change of up to $\pm 0.5 \cdot 10^{-3}$ in total drag coefficient occurs in most areas of the Arctic. This is consistent for the years 2020 and 2021 as well (see Figs. B5 and B6 in the appendix).

For both columns III and IV in Figure 4.5 it is important to mention that the summer months likely exhibit higher levels of uncertainty, e.g., due to data gaps caused by clouds and due to melt ponds that can saturate the IS2 photon detection system (Tilling et al. 2020). This is a consequence of melt ponds being highly specular and typically reflecting a large amount of signal photons. When ATLAS strong beam timing channels receive more photons than they can handle within a dead time interval, they can no longer detect additional incoming photons; which can lead to short gaps in the topography data. See Tilling et al. (2020) for more information on how IS2 views melt ponds.

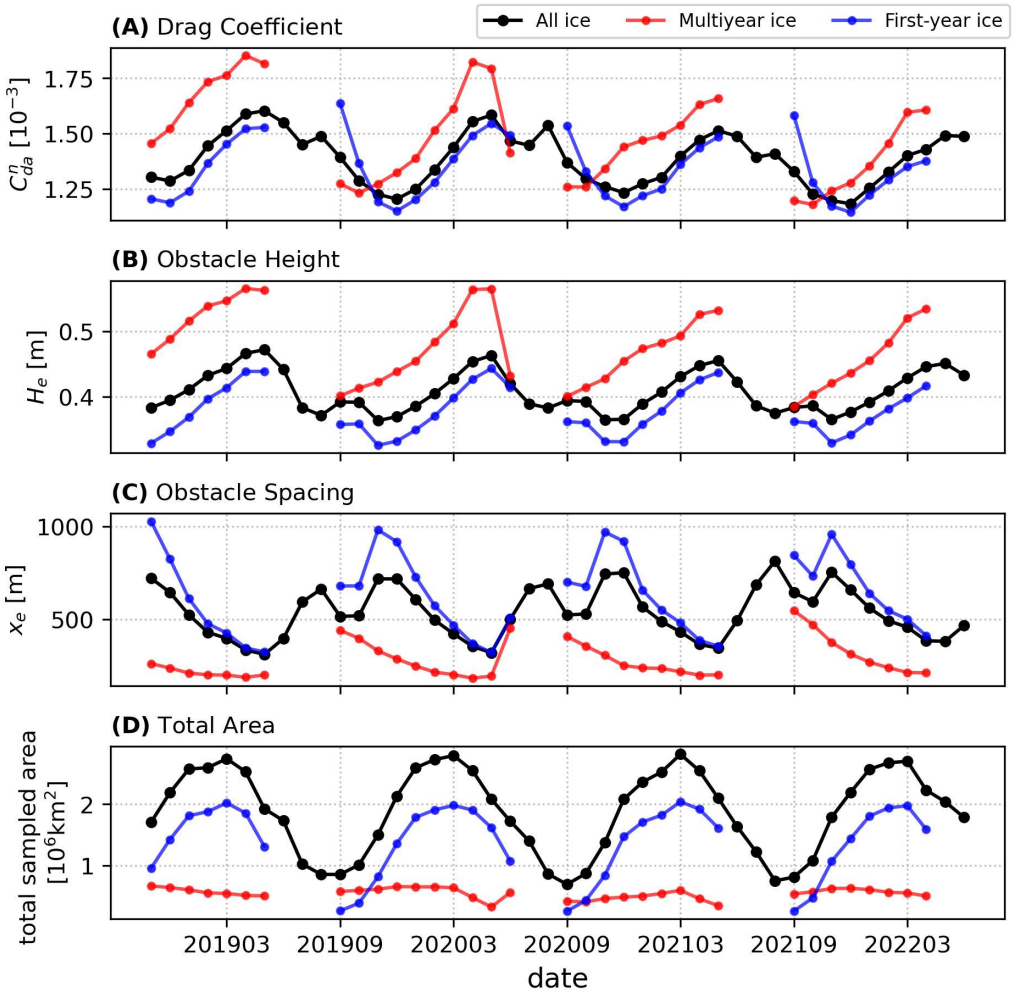

Figure 4.6: Time series from 11.2018 to 06.2022 of total IS2 drag coefficient (as computed in equation 13) with the OIB ATM scaling factor applied (A), obstacle height (B), obstacle spacing (C) and total area covered by IS2 observations (D) for the whole Arctic (in black), multiyear ice (in red) and first-year ice (in blue).

To observe the seasonality as well as the monthly evolution of our best estimate of pan-Arctic total neutral drag coefficients on an interannual scale from November 2018 to June 2022, we plot the average drag coefficient, obstacle height and spacing for each month along with the total area of grid cells covered with IS2 data in Fig. 4.6. Importantly, the total area covered is not the same as sea ice extent and is generally less than the latter due to clouds and returns with ice concentrations $< 15\%$ not being processed (Kwok et al. 2021a). Notably, both obstacle height and spacing is what is used to calculate the base IS2 ATL07 drag coefficients; for these no corrections are applied and thus it

is expected that the heights are underestimated and the spacing overestimated as compared to OIB ATM due to smoothing by the larger IS2 footprint. In addition to pan-Arctic averages, we also produce these statistics for Multiyear Ice (MYI) and First-Year Ice (FYI). Here, we make use of the MYI concentration retrieved using brightness temperatures from the microwave radiometer AMSR2 and radar backscatter from the C-band scatterometer ASCAT (Shokr et al. 2008; Ye et al. 2016a; Ye et al. 2016b; Melsheimer et al. 2023). Sea ice area classified as below 50% MYI according to the retrieval, are considered as FYI and used to compute FYI averages and conversely all values equal to and above 50% are used to compute MYI averages (see Fig. B7 for the distribution of MYI over 3-month time periods when available). By comparing the two ice types we can study the differences in their areal averages. As expected we see higher drag coefficients (MYI: $C_d^n \approx 1.2 - 2.0 \cdot 10^{-3}$, FYI: $C_d^n \approx 1.0 - 1.6 \cdot 10^{-3}$) and obstacle heights (MYI: $H_e \approx 0.4 - 0.6$ m, FYI: $H_e \approx 0.3 - 0.4$ m), and conversely lower obstacle spacings (MYI: $x_e \approx 200 - 500$ m, FYI: $x_e \approx 250 - 1000$ m) in the averages from the MYI ice portion of the Arctic. The MYI concentration data product is only available for winter months and hence the lack of data for the summer months in the time series. As a result this means we are unable to distinguish the FYI contribution of the form drag due to floe edges peak in August and can only estimate that upper bound given the full data set. As for temporal evolution, there is an annual cycle in all three parameters such that the annual maximum (minimum) average drag coefficient and obstacle height (obstacle spacing) in May lags behind maximum sea ice extent which is typically in March.

4.3.4 Spatial and temporal variability

Looking at our 3-monthly spatial analysis (Figs. 4.5, B5 and B6) as well as the monthly time series (Fig. 4.6), we corroborate the results found in Petty et al. (2017) with the MYI sea ice regions north of the Canadian Archipelago and Greenland exhibiting high drag ($C_{d,10}^n > 1.5 \cdot 10^{-3}$) and the smooth FYI sea ice regions of the Beaufort (north of Alaska Western Canada), Chukchi (north of Fram Strait) and Siberian (north of Siberia) Seas exhibiting low drag ($C_{d,10}^n < 1.0 \cdot 10^{-3}$). We corroborate Duncan et al. (2022) in terms of the distribution of spatial variability of 10-km average obstacle spacing, e.g., <200 m near the Canadian Archipelago, for the winters of 2019, 2020 and 2022 that they have produced using the UMD-RDA algorithm. Based on the limited amount of data we analysed, we also corroborate that the drag coefficient variability in space is larger than the variability across seasons as was found by others (Castellani et al. 2014; Tsamados et al. 2014).

We observed interesting features of ice topography, including a tongue of ($C_{d,10}^n > 1.5 \cdot 10^{-3}$) sea ice that forms across the Beaufort Sea and towards a rough ice patch surrounding the Wrangel Island (near Fram Strait along the antimeridiean) only in select months (see Figs. 4.5B and B6B). Similarly, when Arctic sea ice extends across the Arctic Ocean and to Siberia, Severnaya Zemlya is often (but not always) surrounded by rough ice as well ($C_{d,10}^n > 1.5 \cdot 10^{-3}$) (see Figs. 4.5B and B5B). These effects may be attributed to the movement of the Beaufort Gyre as well as to the tendency of ice to ridge near land, respectively. Notably, within the time span we analysed, May is the month

that repeatedly exhibits annual minimum obstacle spacing and annual maximum obstacle height and drag coefficient. This supports the notion that sea ice–atmosphere drag exhibits an annual cycle (e.g., Andreas et al. 2010). By also including drag due to floe edges we also observe a smaller peak in August, when the ice-water boundary is at its longest. We observe a decrease in the yearly maximum average drag coefficient across all ice types during the four years we looked at, but given the short time-frame we cannot attribute this decrease to anything more than natural variability.

4.3.5 Uncertainty due to sampling

While IS2 has a very high resolution when compared with other laser altimeter satellites, it's still larger than the 1 m resolution of the OIB ATM data. The ATL07 segment length of about 30 m, over which 150 signal photons are obtained to lower noise in the height retrieval, smooths out the topography via the dual-Gaussian fit much like the moving average filter we applied to the OIB ATM data. This smoothing effect is discussed in detail in a recent study by Ricker et al. (2023) where coincident IS2 ATL07 and airborne Altimeter Laser Scanner (ALS) data from the Multidisciplinary drifting Observatory for the Study of Arctic Climate (MOSAiC) expedition were compared. Ricker et al. (2023) show that the IS2 ATL07 strong beam could detect only 16% of obstacles above the threshold of 0.6 m that were registered by ALS. A comparatively higher detection rate of 42% was achieved by processing ATL03 by using a higher-resolution topography data set (Duncan et al. 2022). Notably, neither of the two IS2 sea ice height products were able retrieve the full extent of surface topography (Ricker et al. 2023). Assuming the lower threshold value of 0.2 m used in this study, we can expect these detection rates to rise but at some point hit a limit imposed by IS2 ATL03's footprint of 11 m (Magruder et al. 2020; Magruder et al. 2021) that is inferior to the resolution used in most modern airborne surveys looking at topography, e.g., OIB ATM, ALS. Thus for the purposes of our pan-Arctic study, we have chosen to stick with the publicly available and regularly updated ATL07 data set as either of these two data products will require some type of correction if realistic drag coefficient estimates are to be computed from them. While ATL07 has a lower obstacle detection rate locally and the obstacle height (spacing) is typically overestimated (underestimated), the spatial information on Arctic-wide obstacle distribution should be conserved according to our comparisons to airborne data (Section 4.3.1). That is why we use a regression transfer model that is trained by near-coincident OIB ATM to scale up these underestimated IS2 drag values and obtain them closer to the expected form drag range estimated from higher-resolution airborne laser data.

How representative the scaling factor is for the whole of the Arctic is difficult to gauge and with limited spatial and temporal near-coincident coverage we expect there to be some uncertainty. Despite these limitations, the racetrack OIB flights from 8 and 12 April 2019 were flown over two distinct ice types. The 8 April racetrack was ∼100 km north of the Sverdrup Islands (80.5°N) and the 12 April one was centered at 86.5°N in the central Arctic (Kwok et al. 2019a). As a result, the former was over thicker and rougher ice, while the latter was over thinner and smoother ice giving us the opportunity to see how the drag coefficients compare between the two instruments

in the different regimes. The scaling factors derived for the two different days are 4.42 and 5.36 respectively, resulting in an uncertainty that is in the range of ±17.5%. This small discrepancy can also be explained by ATL07 sampling: with a smaller obstacle frequency over smooth ice the likelihood of not detecting the few that are present increases (Ricker et al. 2023) thereby increasing the obstacle spacing used in the calculation of drag coefficients for every 10 km segment. Where the obstacle density is generally high, like in rough deformed areas near the Canadian Archipelago, though the detection rate may be low, there will always be an ample amount per 10 km segment to detect a higher drag coefficient signal. Thus, the sampling issue with regard to computing drag coefficients from topography features is more prevalent over smooth ice than rough ice and a higher correction is needed. As 19 and 22 April OIB flights cover larger areas and the rougher deformed ice near the Archipelago is rather small in extent, the scaling factor derived from all 4 days is closer to that of the April 12 racetrack and more representative for the whole Arctic that is predominantly smoother than the ice surveyed on the 8th of April.

4.4 Discussion and concluding remarks

In this study we used a combination of the Garbrecht et al. (2002) and Lüpkes et al. (2012) parameterizations to calculate obstacle drag coefficients. Although it is important to understand that this method has some uncertainty, it represents the state-of-the-art. Currently, it is the only available parametrization of drag coefficients accounting for the effect of pressure ridges over closed sea ice cover and of floe edges in regions with fractional sea ice cover. In the following, we address the background and the uncertainties of the parameterizations, e.g. on the basis of results obtained with alternative formulations.

The parameterization idea for the effect of ridges (and other sea ice features over closed sea ice) has been first tested by Garbrecht et al. (1999) on the basis of turbulence measurements made at the bow mast of RV Polarstern when the ship was drifting at different positions downstream of a large pressure ridge. Thus, this data set was independent from the airborne turbulence data which were the main data source for Garbrecht et al. (2002). The latter data set was validated once more in a thesis by Ropers (2013), who compared the Garbrecht et al. (2002) drag coefficients with drag coefficients derived from additional airborne turbulence and topography data. Furthermore, Castellani et al. (2014) showed that at least the average neutral 10-m drag coefficient, obtained from the Garbrecht et al. (2002) parametrization with parameters given in Section 4.2.4, agrees well with values for closed sea ice derived from Andreas et al. (2010) using SHEBA data.

It is important to understand that all available sea ice form drag parameterizations including those for the effect of pressure ridges and of floe edges are based on a similar formulation of dynamic pressure acting on these obstacles (Gryanik et al. 2023). While the Lüpkes et al. (2012) approach, first formulated in a modified version by Hanssen-Bauer et al. (1988), is a 2D approach, the Garbrecht et al. (2002) approach is only 1D. Ropers (2013) investigated if more complex assumptions for the

latter scheme concerning the ridge geometry would improve the results, but the main conclusion was that more complex models require input variables, which are usually not available. It is furthermore important that the addition of ridge form drag to the scheme of Lüpkes et al. (2012) considered here does not represent a competing scheme. On the contrary, the formulation of Lüpkes et al. (2012) allowed the specification of the ridge component from the very beginning. Only for simplicity, they assumed an average roughness of ridge-covered sea ice to concentrate their work just on the edge effect. The latter was expected to be dominating in the MIZ and perhaps also in the inner Arctic under melt conditions with many leads and ponds.

The approach for floe edge form drag was also used in mesoscale modelling studies. Vihma et al. (2003) showed that the application of the scheme led to a very good agreement of modelled and observed meteorological mean variables and turbulent fluxes. Inclusion of form drag in the marginal sea ice zones using the Lüpkes et al. (2012) scheme with parameter values based on Elvidge et al. (2016) resulted in an improvement of atmospheric model results (Renfrew et al. 2019). Birnbaum et al. (2002) also investigated the effect of floe-edge generated form drag in the marginal sea ice zone on meteorological parameters by applying a mesoscale nonhydrostatic model. They pointed to the importance of a proper choice of the coefficient of resistance c_w to obtain realistic fluxes when the form drag parameterization was included. Finally, Martin et al. (2016) show that the inclusion of atmospheric form drag leads to improvements in the modelling of sea ice drift. The latter work addresses only floe edge form drag but one can expect that further improvement is possible when ridge-generated form drag is included as well.

Thus, for the analysis of uncertainty we concentrate on the combined approach as described in section 4.2.4. Naturally, the chosen values and formulations for, e.g. the coefficient of resistance, value of the skin drag coefficient and the inclusion of the sheltering function contain their own uncertainties, especially when generalizing in time and space. As mentioned in Section 4.2.4, for the coefficient of resistance c_w, here we use an approach by Garbrecht et al. (2002) where c_w depends linearly on the obstacle height H_e. The given coefficients in this parameterization 0.185 and 0.147 have some uncertainty because they have been derived from pressure measurements over only a few sea ice ridges. For this reason, we performed sensitivity studies with different c_w formulations (e.g., Garbrecht et al. 1999; Ropers 2013). Results are shown in Fig. B4 for April 2019 where the obstacle form drag coefficients have been calculated with the different formulations for the coefficient of resistance, taking into account necessary adjustments (modified aerodynamic roughness length and thus adjusted neutral skin drag coefficient, e.g. in the case of the Ropers (2013) version). The conducted studies showed that the principal results (geographic distribution) were unchanged but small differences between drag coefficients are observed with the different formulations of the coefficient of resistance c_w. The standard deviation (mean) was found to be $2.5 \cdot 10^{-4}$ ($2.9 \cdot 10^{-4}$), $4.6 \cdot 10^{-4}$ ($5.3 \cdot 10^{-4}$) and $5.8 \cdot 10^{-4}$ ($6.1 \cdot 10^{-4}$) for the Garbrecht et al. (2002) formulation with the original coefficients ($c_w = 0.05 + 0.14 H_e$), the version with the natural logarithm ($c_w = 0.22 \ln(H_e/0.2)$) and the Ropers (2013) formulation ($c_w = 0.05 + 0.35 H_e$), respectively. These results are altogether not

too different from the Garbrecht et al. (2002) formulation using $c_w = 0.185 + 0.147 H_e$). The standard deviation (mean) amounts to $4.6 \cdot 10^{-4}$ ($6.0 \cdot 10^{-4}$). Most importantly, the spatial distribution of high and low obstacle form drag regimes is conserved independent of the used c_w parameterization.

Here, we tested a different hierarchy level of the Lüpkes et al. (2012) scheme than that which is used for this study (level 4). It is their level 2 parameterization which allows for specifying the measured grid-cell averaged freeboard. Instead of the constant value 0.41 m that is implicitly used in the Lüpkes et al. (2012) version used in the previous sections, we considered the data from ATLAS/IS2 L3B Daily and Monthly Gridded Sea Ice Freeboard, Version 3 (ATL20) thereby implementing freeboard from satellite remote sensing measurements. Because of the smoothing imposed by sampling the results did not show any significant improvement over using constant freeboard $h_f = 0.41$ m as recommended in Lüpkes et al. (2012) for the simpler level. Ideally, all components of floe edge form drag coefficients should be taken from remote sensing to better monitor the changing Arctic system, but especially with regards to floe edge sizes, IS2 cannot reliably determine this parameter Arctic-wide. Though it is beyond the scope of this study, we encourage future work in this direction with a multi-satellite approach that might remedy the limitations of each individual instrument. However, since in the Lüpkes et al. (2012) parameterization form drag still depends on the sea ice fraction A, the contribution of the form drag is rather small in regions with A near 1. This is the main reason why form drag is still underestimated by the level 2 scheme even when variable freeboard is allowed. This holds especially near Greenland where ridges are tall. With respect to the application discussed here, the Lüpkes et al. (2012) floe edge form drag parameterization has uncertainties imposed by the limitations of satellite remote sensing. Namely, here we use ice concentration derived from passive microwave data (AMSR2 microwave radiometer in this case) as input, overfrozen leads and ponds are not considered. As this freezing can happen already in August, the overall drag from floe edges is likely underestimated then. The proportionality coefficient $3.67 \cdot 10^{-3}$ of the Lüpkes et al. (2012) level 4 hierarchy parameterization, carries with it its own uncertainty. It depends, e.g. on floe sizes and sea ice freeboard (see Lüpkes et al. (2012)). Their uncertainty stems from the fact that the constant is region dependent. For this reason, sensitivity studies were carried out (not shown), in which these values were varied within realistic and recommended ranges given in Lüpkes et al. (2012) (see also Elvidge et al. (2016) and Srivastava et al. (2022)). The result of this sensitivity study was that since the effect of ridge form drag was found to be much larger than the floe edge form drag, the variability of the above-mentioned proportionality constant had only small impact on the total drag coefficient.

The Garbrecht et al. (2002) approach contains in principle also the effect of sheltering by ridges. However, the sheltering function $(1 - \exp(-0.5 x_e / H_e))^2$ (e.g., Hanssen-Bauer et al. 1988; Lüpkes et al. 2012; Castellani et al. 2014), discussed in section 4.2.4, was not applied to the main IS2 ATL07 data after it was tested to see if it produced a non-negligible signal. By comparing the month of Arpil 2019 (shown in Fig. 4.5), with and without the sheltering function implemented, the averaged

absolute difference for all filled 25 km grid cells was $7.39 \cdot 10^{-12}$. Thus, such a negligible difference further confirmed that the use of the sheltering function for IS2 ATL07 data was not significant.

Our value for the skin drag differs from the one used in Lüpkes et al. (2012), since there, the effects of ridges and other obstacles are included in the skin drag coefficient as mentioned. By using the smaller skin drag coefficient and a variable obstacle form drag coefficient (e.g., Castellani et al. 2014; Petty et al. 2017), we may introduce a more realistic obstacle form drag, since, as has been shown in this study, it varies a lot in time and space; whereas skin drag over smooth ice we can assume to be relatively constant in comparison. In the combined total drag (as derived in equation 13), the Garbrecht et al. (2002) obstacle form drag and Lüpkes et al. (2012) floe edge form drag parameterizations are meant to be used together to better assess pan-Arctic drag coefficients.

As mentioned previously in section 4.1, the drag coefficient C_d also depends on the surface roughness dependent stability function f_m, for which numerous versions exist (see e.g. Gryanik and Lüpkes (2018, 2023). For this study we have limited our research to assessing the neutral drag coefficients C_d^n. In case of stable stratification C_d becomes smaller than C_d^n, whereas unstable stratification with more turbulence causes C_d to be greater than C_d^n (Lüpkes et al. 2015). The local-near surface stratification is heavily impacted by open-water that facilitates upward heat fluxes (Andreas et al. 1999; Lüpkes et al. 2015) and as a result varies between the more ice-covered inner Arctic and the MIZ where open water is more common. Thus, it is in summer, where more open water is present across the Arctic ice cap, that our estimates of the neutral drag coefficients C_d^n are likely below C_d. Conversely, over regions with large sea ice cover, the stratification is expected to be more stable in winter during polar nights (Lüpkes et al. 2015), which will act to offset the impact of higher form drag, suggesting our estimates of C_d^n for winter are more representative of C_d.

4.5 Significance and novelty of the analysis

Using our best estimates, we have demonstrated that drag force between Arctic sea ice and the atmosphere varies annually throughout the year (see Fig. 4.6). The implication of this finding is that the turbulent surface flux of momentum, given in equation 9, varies also. In other words, depending on the month of the year, the ice is either more or less susceptible to movement depending on the amount of energy transferred to it via the atmosphere, and by extension, the ocean. We include the ocean here because the sources of atmospheric drag we looked at, primarily form drag due to obstacles, are closely related to the magnitude of oceanic form drag on account of pressure ridges having both a sail (the part above water) and a keel (the part below water) in roughly the same location (Timco et al. 1997; Tsamados et al. 2014). Similarly, form drag due to floe edges is also subject to energy transfer from the ocean for the majority of the ice edge that is below the water level. Thus both oceanic and atmospheric form drag are expected to be both temporally and spatially correlated to one another, wherein the oceanic drag is higher in magnitude (Tsamados et al. 2014).

Form drag from meltpond edges, a parameter we did not look at here, we expect to be a unique component of total atmospheric drag.

We observe that MYI ice exhibits highest drag in May (red line in Fig. 4.6A), due to an increase in the form drag due to obstacles, and FYI ice peaks sometime in July-August (according to the secondary peaks in the black line [all data] in Fig. 4.6A and the associated presumed trajectory of the blue line [FYI data]) from a longer ice-water edge and the associated floe edge drag in summer months. Looking at the gridded data (Figs. 4.5, B5 and B6), we can further comment on developments on regional scales. Notably it is the Lincoln Sea, north of Greenland, which exhibits the highest form drag due to obstacles with high drag coefficients (2-3x higher than smooth FYI areas, e.g. the East Siberian Sea) reaching as far north as 85 deg in the months of spring (rows A and B). However this is not consistent throughout the year as these relatively high drag coefficients tend to retreat towards the Canadian archipelago throughout summer and autumn (rows C and D). Interestingly, it is not consistent across all years either as this behaviour was not observed in 2021 (Fig. B6). Similarly, the neighbouring Beaufort Sea and Fram Strait (mixture of MYI and FYI) also exhibit wide areas of higher form drag coefficients sometime in late spring (row B). All other Arctic Seas (mostly FYI) primarily show an increase in form drag due to floe edges along the MIZ (see column IV), but also in small part higher form drag due to obstacles near land features. Thus, this data proves highly valuable in terms of identifying previously unknown spatial and temporal developments in pan-Arctic and regional drag. This analysis is the first of its kind as previous studies either assumed uniform drag across the Arctic or did not provide sub-yearly temporal information.

In terms of climate modelling, our findings show that assuming a constant drag coefficient in both space and time misrepresents the variability of momentum fluxes near the surface and thus the main forcing of sea ice drift. This misrepresentation might cause in turn many other deficiencies in air ice interaction such as insufficient variability in the sea ice concentration. Accordingly, a suitable further development of drag parameterizations for a more realistic representation of form drag seems necessary. As for understanding Arctic sea ice, we believe this data has the potential to help with better understanding the interaction between sea ice, ocean and atmosphere, better predict the motion of sea ice and identify temporal and spatial variability of pan-Arctic drag coefficients on a monthly basis. Most importantly, this study helps us link yet another crucial sea ice parameter to remote sensing. This link, given IS2 or similar future mission data is available for years to come, has the potential to help us better understand the multiannual changes in Arctic sea ice cover as the local climate warms at an unprecedented pace (e.g., Serreze et al. 2011; Stroeve et al. 2012).

4.6 Summary and outlook

This study makes use of measured sea-ice topography to calculate atmospheric drag coefficients across the Arctic ice cap on monthly and 3-monthly temporal scales. To our knowledge, it is the first analysis of monthly pan-Arctic drag coefficient estimates of its kind. The sea-ice topography is

obtained from the IS2 ATL07 data product at variable resolutions that depend on surface reflectivity but average around 30 m for the strong beams (Kwok et al. 2019b). Using methods developed in Garbrecht et al. (1999) and Garbrecht et al. (2002) according to the drag partitioning scheme proposed by Arya (1973) and Arya (1975), we obtain obstacle, i.e. ridges, height and spacing averages for 10-km segments. We then combine the estimated form drag due to obstacles with sea ice skin drag, drag due to floe edges and a drag due to open water; all of which are incorporated as constants scaled differently with sea ice concentration.

In conclusion, from our analysis of pan-Arctic drag coefficients from the year 2019 and to a lesser extent 2018, 2020, 2021 and 2022, we have observed several noteworthy natural phenomena. Pan-Arctic form drag due to obstacles follows an annual cycle that is similar in both MYI and FYI regions. The yearly maximum average drag coefficient is not connected to the yearly maximum sea ice extent and seems to occur after the sea ice extent maximum. Form drag due to obstacles is primarily spatially variable (high in MYI regions and low in FYI regions) but nevertheless shows some temporal variability (Maximum in May and minimum in December). Our results suggest that form drag due to floe edges is more prevalent during summer months when large areas are broken up and the MIZ expands, whereas form drag due to surface features peaks in late spring when its contribution is magnified from MYI regions north of the Canadian Archipelago and Greenland.

While it is beyond the scope this study, we propose the possibility of extending IS2-based analysis to also estimate form drag due to floe edges from satellite measurements rather than using a constant as mentioned in section 4.4. We encourage the open water drag component to be derived from a parameterization that takes into account wind speed and therefore wave height that might cause additional form drag across water surfaces. We propose the use of lead and meltpond data to account for additional sources of drag not included in our study, e.g. lead and meltpond edges.

5 A model investigation of the effects of drag on sea ice dynamics

This chapter integrates variable form drag in the coupled regional atmosphere-ocean-sea ice model HIRHAM-NAOSIM and is meant to address **RQ**s 5 and 6 detailed in Chapter 1. The following study is not published nor in preparation at the time of writing this dissertation. It relates to Chapter 3, as it too analyzes atmosphere-ocean-sea ice interactions and looks at dynamic and thermodynamic processes that modify sea ice properties. This study is a direct followup to the study contained in Chapter 4, and uses the retrieved form drag coefficient estimates to develop a sea ice thickness-based paramaterization that is then integrated in the coupled model. By comparing the model with and without this new variable form drag implementation, small differences in sea ice properties are revealed. These differences are then analysed and explained through the use of sensitivity studies, in which relevant model parameters were varied.

5.1 Introduction

Once the novel ICESat-2 neutral atmospheric drag coefficient estimate data-set was created (Mchedlishvili et al. 2023), the next step was to incorporate the observed spatiotemporal variability in drag coefficients into an Arctic model. Thereby allowing us to quantify the impact of variable drag on the Arctic climate system, specifically focusing on sea ice parameters such as drift velocities and thickness. To consider all components of the Arctic climate system, e.g., the momentum transfer the sea ice has with both the surrounding atmosphere and ocean, a coupled regional atmosphere-ocean-sea ice model was used. Such models are able to simulate the feedback and interactions between their components at a spatial scale that is too fine to resolve in global models, hence the need for a localized coupled model to look at the impact of form drag on the Arctic climate system. The coupled model used for this task was HIRHAM-NAOSIM (Dorn et al. 2019), consisting of the regional atmospheric climate model HIRHAM5 and the regional ocean-sea ice model NAOSIM. The coupling domain of these two interlinked models is the domain of HIRHAM-NAOSIM which covers all area north of about 60°N, thus all of Arctic Ocean sea ice is fully contained within (see Fig. 2.1).

The version of the model used for this study isHIRHAM-NOASIM version 2.2 (HN2.2), that is further developed than version 2.0 reported on in Dorn et al. (2019). These developments are listed in the supplementary material of Aue et al. (2023). The difference between the two versions that is most relevant to this study is the modification of transfer coefficients. Version 2.2 optionally includes the Lüpkes et al. (2012) and Lüpkes et al. (2015) floe edge form drag parameterization which we made use of in this study. On its own, this parametrization is already evaluated in HIRHAM-NAOSIM in the study by Yu et al. (2020). They report that that the agreement between observed

and modelled ratios of sea ice drift and wind speed is not improved by the inclusion of the floe edge drag parameterization, and that the inclusion of additional sea ice–ocean drag coefficient may further improve these simulated ratios (Yu et al. 2020). In this study, we hope to do just that by modifying the atmospheric and oceanic drag coefficients in parallel (described further in the following sections). Importantly, here the floe edge form drag parameterization option is used in conjunction with the obstacle form drag parameterization developed using Mchedlishvili et al. (2023) data, and the model run that includes form drag uses both components.

Form drag is a parameter that is not typically resolved in models that feature sea ice. Efforts to change the status quo can be traced back to studies such as Tremblay et al. (1997), with more recent developments like the implementations done in the Los Alamos Sea Ice Model (Tsamados et al. 2014) as well as coupled ocean-sea ice model NEMO-LIM3 (Sterlin et al. 2023). Findings from these studies show that including variable form drag improves agreement between model results and measurements, and impacts sea ice parameters in meaningful ways. Tremblay et al. (1997) found their single-layer thermodynamic model with a linear internal-temperature profile for sea ice to better agree with sonar sea ice thickness (SIT) measurements once the variable form drag had been implemented. Tsamados et al. (2014) and Sterlin et al. (2023) both computed obstacle form drag by identifying ridged sea ice volume and area, as well as extrapolating parameters like height and spacing of sails and keels with which both oceanic and atmospheric obstacle form drag can be calculated. These form drag coefficients, in addition to those caused by floe edges and melt ponds, are combined with skin drag to study the model results with variable drag implemented. Their results show that the model runs with the form drag implementation result in less ice volume in the Arctic Ocean due to a thinner sea ice cover, especially in the Western Arctic. Both studies confirm that thermodynamic processes are the main cause behind this significant change. The reasoning behind this is that the momentum transfer coefficient has a direct impact on the heat transfer coefficient, which was modified to explicitly account for variable form drag in these models. Sea ice areas with high drag coefficients thereby also exhibit high heat transfer coefficients that increase the local heat fluxes (Tsamados et al. 2014). One reason why impact of dynamics processes is less clear could stem from how both models heavily overestimate sea ice drift as compared to observations (with and without the form drag implemented) (Tsamados et al. 2014; Sterlin et al. 2023), suggesting the modelled dynamics aren't sufficiently represented. Neither study found a strong impact of variable form drag on sea ice drift velocities for the Arctic. Sterlin et al. (2023) went further to also look at ocean parameters like sea surface temperature, salinity as well as mixed layer depth. Sea surface temperature was found to be warmer in the MIZ, the salinity was found to be higher and the ocean mixed layer was found to be thicker, in the model run with the form drag implemented. Thus, as reported on, the inclusion of variable form drag causes significant changes in the climate system.

One additional model study worth noting here, is the METRAS/MESIM mesoscale (300 km model domain) 2-dimensional model that tested the influence of form drag as well as other parameters on an off-ice floe across the Fram Strait MIZ (Lüpkes et al. 2011). The interplay between wave

radiative stress (momentum flux from waves to the ocean surface) as well as atmospheric and oceanic skin and form drag was analysed over 5 distinct runs with varying conditions. Their findings relevant to this study include the sea ice accelerating effects of atmospheric drag and decelerating effects of oceanic drag. The wave radiation stress was found to have a negligible influence on the ice drift velocity (Lüpkes et al. 2011). In order of highest influence on the sea ice in their model, Lüpkes et al. (2011) found skin drag to be the most important, followed by the oceanic form drag. Atmospheric form drag proved to have a relatively small influence in comparison. Importantly, the geostrophic currents in the model were set to zero, therefore oceanic drag mainly dampened sea ice drift velocities, which in the presence of strong surface currents may have the opposite effect.

Here we aim to test out a SIT-based drag implementation based on our pan-Arctic form drag coefficient estimates (Mchedlishvili et al. 2023) in the coupled atmosphere-ocean-sea ice model HIRHAM-NAOSIM, thereby studying the impact of form drag in every layer of the Arctic climate system. The novelty of this analysis lies in the model being used, which unlike previous models (e.g Lüpkes et al. 2011; Tremblay et al. 1997; Tsamados et al. 2014; Sterlin et al. 2023) with variable form drag implementations that we are aware of, were not coupled atmosphere-ocean-sea ice models and therefore did not fully capture the whole Arctic climate system.

To conduct our analyses, we focus on the changes observed in sea ice properties. The choices in the parameters analysed stem from the principal questions (PQs):

1. Does the separation of drag into individual components change sea ice properties?
2. How sensitive is this analyses to the α parameter used in the obstacle form drag parameterization?
3. How does drag at the sea ice–atmosphere interface interact with its counterpart at the sea ice–ocean interface?
4. Can the changes in sea ice thickness, concentration and volume be explained by dynamic and thermodynamic ice growth changes?

These PQs are the basis for the analyses conducted in this study. As HIRHAM-NAOSIM is a model able to produce multiple output parameters at every level in the Arctic climate system, it was necessary to define clear goals and focus in on them rather than trying to find changes in all parameters across all months of the model runs. As such, with sensitivity studies aimed at carefully varying the main parameters, we try answer the PQs by analysing a select amount of sea ice parameters that are most closely related to drag forces.

5.2 Theory

In this section, HIRHAM-NAOSIM model details that pertain to this study are discussed; for a full breakdown of the model the reader is referred to Dorn et al. (2007), Dorn et al. (2009), and

Dorn et al. (2019). A particularly important detail when it comes to this study that focuses on the changes in sea ice properties, is the unrealistic sea ice concentration (SIC) that is outputted by the coupled model during summer months (Rinke et al. 2003; Dorn et al. 2007), such that most of the Arctic exhibits the SIC that is typically found in the MIZ. As a result, all sea ice parameter analyses in summer months are subject to high uncertainties and need to be considered with them in mind.

To delve into how the two components (HIRHAM and NAOSIM) of the coupled model treat and are impacted by drag, we must first discuss the governing equations where they are featured. The drag force helps quantify the momentum transfer and thereby the momentum flux, it also impacts the heat transfer coefficient and therefore the heat flux. Both of these fluxes are featured in the total flux as modelled in HIRHAM and in the NAOSIM ice-water stress and heat flux equations, respectively. Thus, we start with the fundamentals and isolate the components we mean to modify for the purposes of this study.

5.2.1 HIRHAM

HIRHAM, the atmospheric component of the coupled model, contains a turbulent mixing scheme based on the atmospheric general circulation model ECHAM. This scheme allows for each grid to have fractional land, ocean or sea ice cover and then calculates the associated surface flux for each surface type. The area-weighted grid-cell mean surface flux is then used to determine the turbulent exchange between the surface and lowest model level (roughly at 10 m).

The generalized bulk formula, as it is implemented in ECHAM6, calculates both the dynamic and thermodynamic surface fluxes as

$$\overline{w'\psi'}_0 = -C_\psi |\vec{v}_1 - \vec{v}_s| \left(\vec{\psi}_1 - \vec{\psi}_s\right) \tag{14}$$

where subscripts 1 and s represent the lowest model level and the surface, respectively. The variables on the right hand-side of the equation include the horizontal wind vector $\vec{v}$, the bulk exchange coefficient C_ψ and ψ which represents one of the prognostic variables u (zonal wind), v (meridional wind), h (dry static energy in place of temperature), or q (specific humidity). The left-hand side has the temporal average of the turbulent components of the vertical velocity w and of the prognostic variable ψ. The bulk exchange coefficient C_ψ, what we modify between the two model runs, is given by

$$C_\psi = C_\psi^n f_\psi \tag{15}$$

where C_ψ^n represents the neutral transfer coefficient and f_ψ the stability function. As C_ψ is a scalar quantity here we make the distinction only between prognostic variables associated with the transfer of momentum ($\psi = m$) and those associated with transfer of heat ($\psi = h$), henceforth denoted as such. Consequently we distinguish between the heat transfer coefficient C_h^n and the momentum transfer coefficient C_m^n, also referred to as the drag coefficient. The two are implemented in the

model as

$$C_m^n = \frac{\kappa^2}{(\ln(z_1/z_{0,m}+1))^2} \tag{16}$$

$$C_h^n = \frac{\kappa^2}{\ln(z_1/z_{0,m}+1)\ln(z_1/z_{0,h}+1)} \tag{17}$$

where κ is the von Kármán constant set to 0.4 and z_1 is the height of the lowest model level. $z_{0,m}$ is the roughness length for momentum, also called the aerodynamic roughness length, which depends on the surface type. For land, the roughness lengths are specified on the basis of orography and vegetation, for open ocean the Charnock formula is used, and for sea ice it is assumed to be a constant with the value 1.0×10^{-3} m, when form drag contributions are not considered. Meanwhile $z_{0,h}$ is the roughness length for heat and is assumed to be related to the aerodynamic roughness length as

$$z_{0,h} = z_{0,m} \cdot \exp(2 - 86.276 z_{0,m}^{0.375}) \tag{18}$$

though in the case of no form drag, both $z_{0,h}$ and $z_{0,m}$ are set to 1.0×10^{-3} m as in the original scheme from ECHAM.

In addition to drag, or momentum transfer, there is also heat transfer that takes place. Therefore, the neutral heat transfer coefficient of ice $C_{h,i}^n$ needs to be calculated. To do so, the ratio of the roughness lengths for heat and momentum is required, and in the case of HIRHAM that is derived from the theoretical model of Andreas (1987):

$$\ln(z_{0,h}, z_{0,m}) = b_0 + b_1 \ln R_* + b_2 (\ln R_*)^2 \tag{19}$$

where b_0, b_1 and b_2 are polynomial coefficients (listed in Andreas (1987) and Andreas (2002)) and R_* is the roughness Reynolds number, a dimensionless parameter used in this case to describe the flow of the atmosphere over rough ice. The parameter R_* is defined as follows:

$$R_* = u_* \frac{z_{0,m}}{\nu} \tag{20}$$

where ν =1.338 $\times 10^{-5}\,\mathrm{m^2\,s^{-1}}$ is the kinematic viscosity of air at 0 °C and $u_* = \sqrt{C_{m,i}|\vec{u}_1|}$ is the friction velocity.

Making use of equations 16, 17 and 30, as well as the equality $\ln(z_1/z_{0,h}) = \ln(z_1/z_{0,m}) + \ln(z_{0,m}/z_{0,h})$ given the quotient rule $\ln(a/b) = \ln(a) - \ln(b)$, we can write the neutral heat transfer coefficient C_h^n as

$$C_h^n = \frac{C_m^n}{1 + (\ln(z_{0,h}/z_{0,m})/\kappa)\sqrt{C_m^n}} \tag{21}$$

Substituting $\ln(z_{0,h}, z_{0,m})$ with the left hand side of equation 19 such that $\zeta = b_0 + b_1 \ln R_* + b_2 (\ln R_*)^2$, we get

$$C_h^n = \frac{C_m^n}{1 + (\zeta/\kappa)\sqrt{C_m^n}} \tag{22}$$

Therefore, for the purposes of calculating C_h^n, the exact value of the roughness length for heat $z_{0,h}$ does not have to be known. Given the aerodynamic roughness length and the corresponding drag coefficient are known, it can be derived using equation 19 for diagnostic purposes.

5.2.2 NAOSIM

Fluxes at the ice–ocean interface are parameterized in NAOSIM as

$$\vec{\tau}_{iw} = \rho_w C_{mw} |\vec{u}_i - \vec{u}_w| (\vec{u}_i - \vec{u}_w) \tag{23}$$

$$Q_{oi} = \rho_w c_{pw} C_{hw} |\vec{u}_i - \vec{u}_w| (T_i - T_w) \tag{24}$$

for the ice-water stress $\vec{\tau}_{iw}$ and oceanic heat flux toward the ice–ocean interface Q_{oi}, respectively. In these equations, ρ_w is the density of sea water, c_{pw} is the specific heat capacity of sea water, and C_{mw} and C_{hw} are the ice-water transfer coefficients for heat and momentum, respectively. $\vec{u}_i$ and $\vec{u}_w$ are the ice drift and ocean current velocities, respectively, whereas T_i is the temperature at the ice–ocean interface and T_w is the ocean mixed layer temperature.

C_{hw} is parameterized in NAOSIM as $c_h \cdot \sqrt{C_{mw}}$, where C_{mw} is derived from C_{mi} and $c_h = 0.0006$ is a constant based on McPhee (1992).

5.3 Implementing form drag into the model

The following section details the implementation of form drag into the coupled model. The three sections represent the making of the obstacle form drag parameterization via regression and the implementation of it along with floe edge drag in the atmosphere model HIRHAM and the ocean-sea ice model NAOSIM, respectively.

5.3.1 The obstacle form drag parameterization

Creating a parameterization that links ICESat-2 form drag coefficient estimates with the parameters contained within the model was one of the principal challenges of this study. The most direct proxy for the retrieved data that was available in the coupled model as a parameter was SIT. The link between SIT and form drag coefficients stems from thick MYI ice being typically more ridged than smooth FYI ice. Figure 5.1 shows average (whole Arctic in blue, MYI area in orange and FYI area in green) SIT plotted against averaged ridge heights (A) and form drag coefficients (B), respectively.

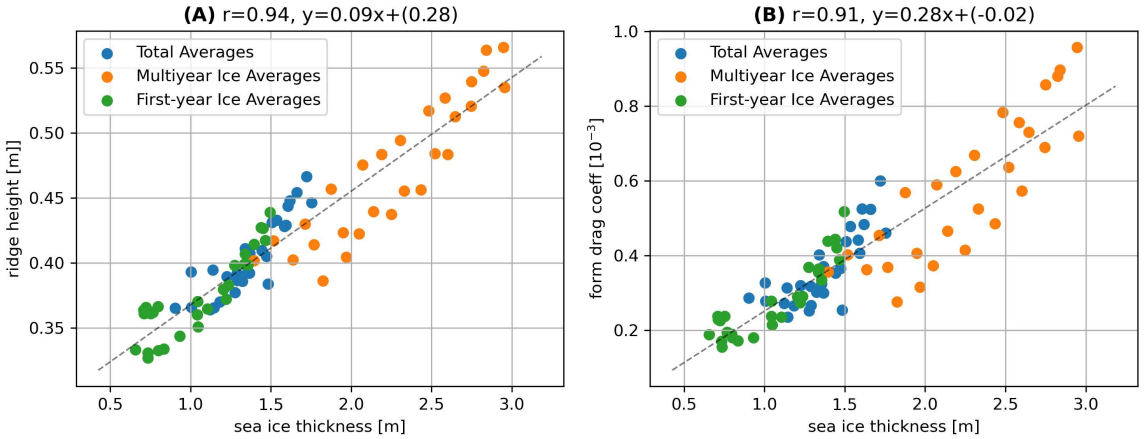

Figure 5.1: Monthly sea ice thickness from ICESat-2 measurements plotted against monthly (A) ridge height and (B) form drag coefficient, for the whole Arctic (in blue), multiyear ice (in orange) and first-year ice (in green). The temporal coverage is identical to the analysis period of Mchedlishvili et al. (2023), 2018.11-2022.06 with summer months omitted since the ICESat-2 SIT data record does not include them due to high uncertainties (Petty et al. 2023).

Using averages subdivided into FYI and MYI portions (masked using the AMSR2/ASCAT MYI concentration dataset (Shokr et al. 2008; Ye et al. 2016a; Ye et al. 2016b; Melsheimer et al. 2023)), it can clearly be seen that on average MYI is typically thicker and more rough than FYI. Meanwhile, parameters like SIC are not able to clearly distinguish between low and high obstacle form drag coefficient areas, in part because the transition zone between FYI to MYI is typically fully ice covered throughout the year. To test the correlation between SIT and obstacle form drag and resolve it better spatially, a full month worth of data of all filled 25 km^2 grid cells was analysed. Unlike in Fig. 5.1 with large spatial averages, the resulting scatter was wide and nonlinear. As a result, multiple regression methods were tested so as to see whether any of them represented the relation better than a simple linear regression would. Among the methods tested were spline, polynomial, linear as well as symbolic regression. The latter method, symbolic regression searches space of mathematical expressions to find the model that best fits the data at hand, both in terms of accuracy and simplicity. In this application, the PySR open-source library for practical symbolic regression was used (Cranmer 2023). PySR's internal multi-population evolutionary search algorithm scores possible mathematical expressions on accuracy and simplicity, however because of the spread of the data it was not able to produce an expression which outscored a simple linear regression. Similarly, by comparing the mean square error of spline and varying degrees of polynomial regressions with that of a simple linear regression, the differences in mean squared error were too small to justify their use. As the final step to finding the parameterization was to evaluate all data and use it to fit the regressions, i.e., all grid cell values from all available months (see Fig. 5.2), only third-

order polynomial and linear regressions were tested at this stage as a result of an even larger data spread as compared to individual months (not shown). Though the general distribution of data was variable across different months, aggregating them over the full time period of study was necessary to derive a time-invariant parameterization able to explore temporal changes caused by the form drag implementation. In the end, the linear regression was once again chosen over the polynomial regression on account of its simplicity and only 6.1×10^{-3} difference in mean squared error.

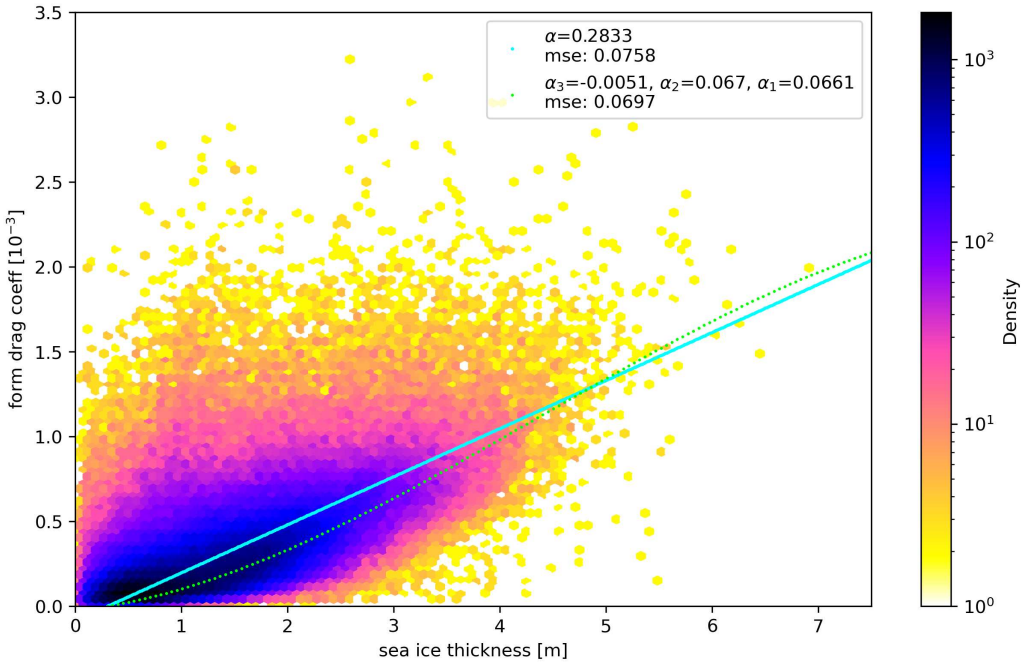

Figure 5.2: Sea ice thickness plotted against form drag coefficients, both of which were retrieved from ICESat-2 laser altimeter measurements. All values are discretized via binning, where the color of each bin represents the data density. The two lines represent the linear regression with slope α (cyan) and the third degree polynomial regression (green) with coefficients α_3, α_2 and α_1 (with subscripts 3-1 corresponding to coefficient order) fit to all available data (2018.11-2022.06 with summer months omitted), while their coefficients and respective mean squared error is reported in the legend. The correlation and p-value are $r = 0.58$ and $p < 0.05$, respectively.

Upon further analyses, it was noted that most linear regression included a negative intercept and indeed, the distribution is such that less than 30 cm SIT produces near-zero obstacle form drag coefficient. From a physical point of view, ice that is sufficiently thin tends to undergo rafting as opposed to ridging, resulting in less pressure ridges and therefore less form drag. In addition, thin ice is smooth and better represented through the notion of skin drag, i.e., centimeter-scale roughness that is treated as a constant in the model. At the same time, the form drag coefficient can't be negative and thus the parameterization later implemented in the model assumed any ice with a thickness below 30 cm generates no obstacle form drag. Thus the finalized parameterization is

$$C_{m,o}^{n} = \begin{cases} \alpha h & \text{if } h \geq h_{\min} \\ 0 & \text{if } h < h_{\min} \end{cases} \tag{25}$$

where $C_{m,o}^{n}$ is the neutral obstacle form drag coefficient, h is sea ice thickness with $h_{\min}$ =0.3 m, and $\alpha = 0.28$ is the coefficient extracted from the linear regression. While α is taken from the regression in Fig. 5.2, it is further supported by the linear regression shown in Fig. 5.1B, which also shares the same slope.

5.3.2 Implementing form drag into HIRHAM

The model details described in Section 5.2.1 detail the setup with constant sea ice drag. In this study we create a modified version of the model with form drag from floe edges and obstacles integrated in it. In this version, the modified equation for the surface drag coefficient over sea ice is

$$C_{m,i} = (C_{m,s}^{n} + C_{m,o}^{n}) f_{m,i} + C_{m,e}^{n}(f_{m,i}A + f_{m,w}(1 - A)) \tag{26}$$

where A is the SIC, $C_{m,o}^{n}$ and $C_{m,e}^{n}$ are the form drag coefficients for obstacles and floe edges, and $f_{m,i}$ and $f_{m,w}$ are the stability functions for ice and open water, respectively. $C_{m,s}^{n}$ is the sea ice skin drag coefficient calculated via equation 16 with the skin drag-related roughness length $z_{0,m,s}$ =1.0×10^{-5} m from measurement over smooth ice by (Garbrecht et al. 2002).

The neutral form drag from floe edges $C_{m,e}^{n}$ is calculated as

$$C_{m,e}^{n} = C_{e10} \left(\frac{\ln(10 \text{ m}/z_{0,m,e} + 1}{\ln(z_1/z_{0,m,e} + 1} \right)^2 (1 - A)^{\beta} \tag{27}$$

with coefficients C_{e10} =2.8×10^{-3} and $\beta = 1.1$. The equation is nearly identical as in (Lüpkes et al. 2015); the prime difference being that here it is not multiplied with A so as to omit a subsequent division of $C_{m,e}^{n}$ by A in equation 26. This change reflects how the equations were simplified to then be incorporated into the model source code.

The basic surface characteristic in HIRHAM is the aerodynamic roughness length $z_{0,m}$, thus it is necessary to calculate it from $C_{m,i}$. First, $C_{m,i}^{n}$ must be calculated as the aerodynamic roughness length itself is not directly dependent on atmospheric stratification. Using equations 26 and 15, the neutral drag coefficient over ice can be derived as follows:

$$C_{m,i}^{n} = C_{m,s}^{n} + C_{m,o}^{n} + C_{m,e}^{n} \left(A + \frac{f_{m,w}}{f_{m,i}}(1 - A) \right) \tag{28}$$

Approximating equation 16, we obtain equation 12 from Chapter 4

$$C_{m,i}^{n} = \frac{\kappa^2}{\left(\ln(z_1/z_{0,m} + 1)\right)^2} \approx \frac{\kappa^2}{\left(\ln(z_1/z_{0,m})\right)^2} \tag{29}$$

we can then derive an expression for $z_{0,m,i}$ as

$$z_{0,m,i} = z_1 \cdot \exp\left(\frac{-\kappa}{\sqrt{C^n_{m,i}}}\right) \tag{30}$$

The heat transfer coefficients of ice $C_{h,i}$, like that of momentum $C_{m,i}$, is impacted by form drag since it modifies the flow above the surface layer. And like $C_{m,i}$ (Eq. 26), $C_{h,i}$ can be calculated by adding up its constituents

$$C_{h,i} = (C^n_{h,s} + C^n_{h,o})f_{h,i} + C^n_{h,e}(f_{h,i}A + f_{h,w}(1 - A)) \tag{31}$$

All the terms are as in equation 26, but for heat instead of momentum. The neutral heat transfer coefficients $C^n_{h,o}$ and $C^n_{h,e}$ associated to the sum of skin drag and obstacle form drag, and floe edge drag, respectively, can be calculated with equation 22. To do so, C^n_m is substituted with the respective drag coefficients $C^n_{m,o}$ and $C^n_{m,e}$ in equation 22 as necessary, and in the case of $C^n_{h,e}$, the $C^n_{m,e}$ in the denominator of equation 22, is multiplied by SIC (A) to take into account the multiplication has been omitted in the definition of $C^n_{m,e}$.

Finally, the heat transfer coefficient for neutral stratification $C_{h,i}$ can be derived using equations 15 and 31

$$C^n_{h,i} = C^n_{h,s} + C^n_{h,o} + C^n_{h,e}\left(A + \frac{f_{h,w}}{f_{h,i}}(1 - A)\right) \tag{32}$$

Thus, in much the same manner as the neutral drag coefficient $C^n_{m,i}$ in equation 28, the neutral heat transfer coefficient $C^n_{h,i}$ is computed as a sum of its components. Together, these two values substitute the base C^n_ψ of the standard model in the bulk exchange coefficient equation 15, and thereby also in equation 14.

5.3.3 Implementing form drag into NAOSIM

The dominant obstacle feature across the sea ice layer is the pressure ridge, which has both a sail and a keel. Therefore, where there is obstacle form drag between sea ice and atmosphere there must also be a complementary exchange of momentum between sea ice and ocean. The same applies in the case of floe edges, as the majority of the exposed edge is submerged. Consequently, form drag was also incorporated into NAOSIM as

$$C_{mw} = C_{mw,s} + C_{mw,r} + C_{mw,e} \tag{33}$$

where $C_{mw,s}$ is the skin drag coefficient, $C_{mw,e}$ and $C_{mw,r}$ are the edge and ridge form drag coefficients. Notably $C_{mw,r}$ has the subscript r indicating ridge instead o for obstacle; this is because rubble fields, hummocks, snow dunes and sastrugis are only relevant at the sea ice–atmosphere boundary. Stability functions, as is generally the case, is not taken into account for calculating the fluxes at the ice–ocean interface.

The implementation of form drag in NAOSIM, given the relative symmetry of sea ice surface features, uses a ratio between the atmospheric C_m and oceanic C_{mw} momentum transfer coefficients, henceforth referred to as C_{da} and C_{dw}, respectively, for simplicity.

Tsamados et al. (2014) report that spatially the range of values goes from $C_{da} < 0.5 \times 10^{-3}$ and $C_{dw} < 3 \times 10^{-3}$ up to $C_{da} \geq 3 \times 10^{-3}$ and $C_{dw} \geq 15 \times 10^{-3}$ in the Canadian Archipelago and north of Greenland ($C_{da}/C_{dw} \sim 0.17$ to $C_{da}/C_{dw} \sim 0.2$). Temporally, the pan-Arctic drag coefficients averages range from $C_{da} \sim 1.0 \times 10^{-3}$ and $C_{dw} \sim 4 \times 10^{-3}$ in December up to $C_{da} \geq 2 \times 10^{-3}$ and $C_{dw} \geq 11 \times 10^{-3}$ in August ($C_{da}/C_{dw} \sim 0.25$ to $C_{da}/C_{dw} \sim 0.2$). Which they attest are consistent with the range of values that have been measured experimentally for both coefficients.

Thus the ratio $C_{da}/C_{dw} = 0.2$, which seems to be a good rounded average, seems reasonable. It is also consistent with Tremblay et al. (1997) which report $C_{da} = 1.2 \times 10^{-3}$ and $C_{dw} = 5.5 \times 10^{-3}$ ($C_{da}/C_{dw} = 0.22$). Lastly, looking at the full range of compiled oceanic drag coefficients presented in Table 1 of Lu et al. (2011) and comparing them with IS2-measured drag coefficients $0.8 \times 10^{-3} < C_{da} < 2.4 \times 10^{-3}$, $C_{da}/C_{dw} = 0.2$ seems to be a better choice than previously used ratios of the type $C_{da}/C_{dw} > 0.4$ presented in Kreyscher et al. (1997).

Therefore a scaling factor of 5 is used to translate the sea ice–atmosphere drag coefficients into ice–ocean drag coefficients which for the constituents in equation 33 translate as follows:

$$C_{dw,s} = 4.19 \times 10^{-3} \tag{34}$$

for ice–ocean skin drag (rewritten as C_{dw} instead of C_{mw}, in line with the previous change in notation),

$$C_{m,o} = \begin{cases} \alpha_w h & \text{if } h \geq h_{\min} \\ 0 & \text{if } h < h_{\min} \end{cases} \tag{35}$$

for ice–ocean ridge form drag, with parameters $\alpha_w = 1.4 \times 10^{-3}\,\mathrm{m}^{-1}$ and $h_{\min} = 0.3\,\mathrm{m}$, and

$$C_{dw,e} = C_{e10}(1 - A)^{\beta} \tag{36}$$

for ice–ocean edge form drag, with parameters $C_{e10} = 14.0 \times 10^{-3}$ and $\beta = 1.1$. C_{hw} can then be calculated as $c_h \cdot \sqrt{C_{dw}}$ with $c_h = 0.0006$ (McPhee 1992).

As a final note, for consistency, we also used the ratio $C_{da}/C_{dw} = 0.2$ for the base version of the model with constant drag. Which given the approximation in equation 29 (equation 12 from Chapter 4), with values $\kappa = 0.4$, $z_1 = 10\,\mathrm{m}$ and $z_{0,m} = 1.0 \times 10^{-3}\,\mathrm{m}$, results in $C_{da} = 1.89 \times 10^{-3}$ and $C_{dw} = 9.43 \times 10^{-3}$ for the base version. For comparison, switching the value $z_{0,m}$ with $z_{0,m,s} = 1.0 \times 10^{-5}\,\mathrm{m}$, gives $C_{da,s} = 8.38 \times 10^{-4}$ (as in Chapter 4) and $C_{dw,s} = 4.19 \times 10^{-3}$. The reason for the reduction in the aerodynamic roughness length is because $z_{0,m}$ is meant to compensate for ridge form drag when it is not integrated, whereas $z_{0,m,s}$ is meant to characterize smooth ice and therefore only the effect of skin drag (Garbrecht et al. 2002).

5.3.4 Model setup and type of analysis

The New Form Drag Run (NFDR), the model run with the new form drag parameterization implemented, is run alongside the Standard Drag Run (SDR), to isolate the impact of form drag. The model is run without spin-up and configured in the same way as the HIRHAM-NAOSIM simulations described in Aue et al. (2023). The period of analysis is 2019-2021, which spans the majority of the ICESat-2 drag coefficient study from which the obstacle form drag parameterization is derived (Mchedlishvili et al. 2023). Thus, in order to help identify recurring patterns in the changes caused by the addition of variable form drag, all the spatiotemporal analysis shown and discussed in this section cover all three years. The differences in the outputted model parameters are assessed using the percent difference (PD) between NFDR and SDR, which is calculated as follows

$$\mathrm{PD} = \left(\frac{\mathrm{NFDR} - \mathrm{SDR}}{|\mathrm{SDR}|} \cdot 100 \right) \tag{37}$$

5.4 Results and discussion

5.4.1 Drag coefficients over sea ice

We first take a look at the drag (momentum transfer) coefficient over sea ice denoted as $C_{d,i}$, in line with nomenclature change in Section 5.3.3. Fig 5.3 shows maps of drag coefficients over sea ice from SDR (A) and NFDR (B) which are averaged over the 2019-2021 model run period to give us seasonal maps from all years. The averaging is such that when all grid cells are filled, the average is computed from all three months over the three years, if a grid value is missing, e.g., in September when total sea ice extent low, then it is not counted in the average. Fig 5.3C shows the PD calculated according equation 37 between the NFDR and SDR averages. In Fig 5.3A we can see the SDR drag coefficient over sea ice $C^n_{d,i}$ computed using equation 29 with $z_{0,m} = 1.0 \times 10^{-3}$ m; the subtle differences Arctic-wide are a result of the stability function $f_{m,i}$. Meanwhile, Fig 5.3B shows the NFDR $C^n_{d,i}$ calculated using equation 26. Here, as mentioned in the closing remarks of Section 5.3.3, $z_{0,m} = 1.0 \times 10^{-5}$ m is used for the calculation of skin drag according to equation 29. The results of this reduction can be seen the Jan-Mar and Oct-Dec columns, where it is quantified in terms of percentage in Fig 5.3C. Importantly, this shows that even with the other constituent terms in equation 26, for the large majority of the Arctic, the drag coefficient $C_{da} = 1.89 \times 10^{-3}$ set in SDR is larger the summation of form and skin drag components in NFDR. On the other hand, along the MIZ, NFDR is significantly larger as result of equation 27 which is maximum at 50% SIC; that is also why the drag coefficient distribution, and the associated positive PD, is so high for the Jul-Sep period when SIC is relatively low Arctic-wide. Because of the erroneous distribution of sea ice in the summer period and the dependency on SIC in the floe edge drag implementation (see Section 5.2), we expect the Jul-Sep period to have high uncertainties and therefore caution the reader in attributing significance to changes in this time frame which likely deviate from observed Arctic

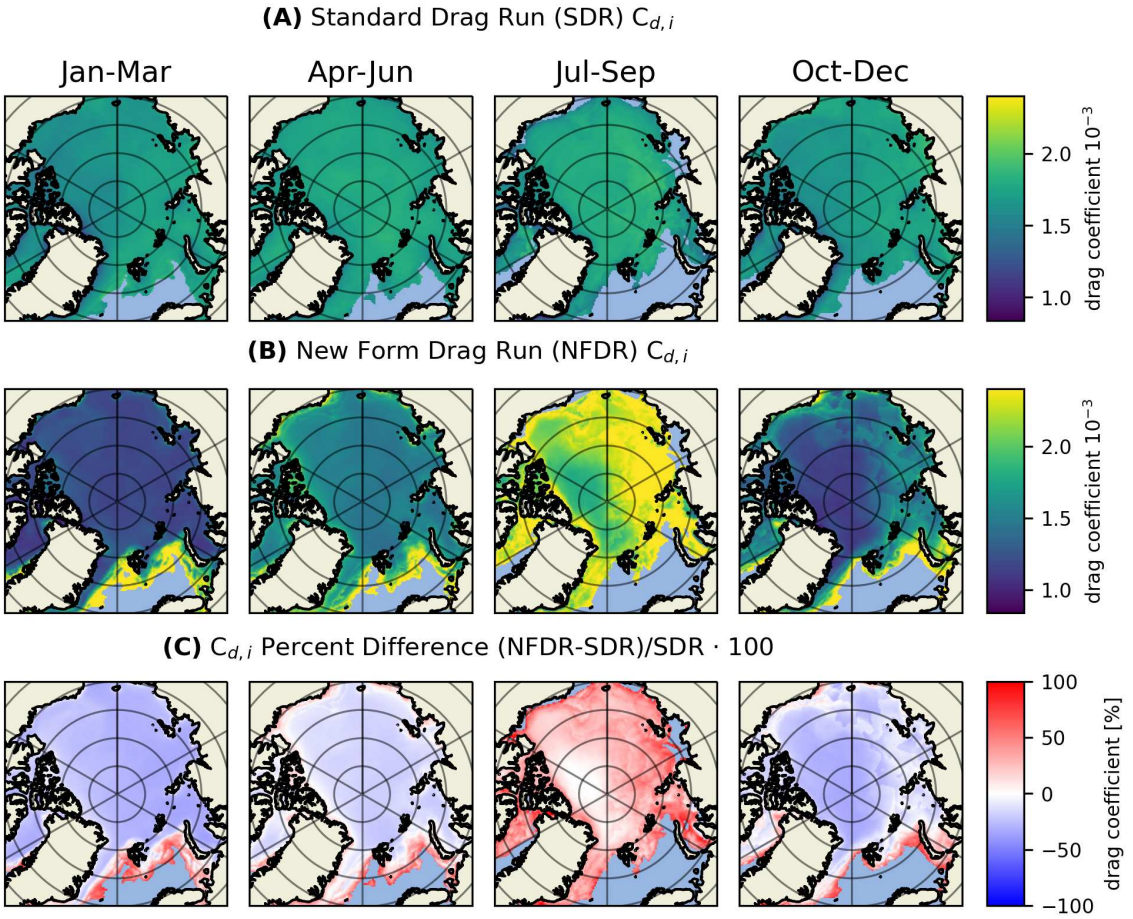

Figure 5.3: 3-month averaged Standard Drag Run (A) and New Form Drag Run (B) drag coefficient over sea ice with the percent difference between the two (C) for the periods January to March, April to June, July to September and October to December (averaged over 2019-2021).

climate conditions. However, this uncertainty is relegated only to Jul-Sep whereas the modelled SIC preforms well in other months (Rinke et al. 2003; Dorn et al. 2007), as such, using the Lüpkes et al. (2015) floe edge drag implementation helps to correct SDR such that the fluxes at the MIZ, which are known to be more pronounced than in the central Arctic (Andreas et al. 2010), are properly modelled.

The influence of obstacle form drag is not as apparent as floe edge drag and can only faintly be seen north of the Canadian Archipelago and Greenland. While the obstacle form drag implementation is directly derived from remote sensing data (Mchedlishvili et al. 2023), the resulting linear regression is likely not capable of fully representing the time-variant sea ice drag coefficient-thickness relationship. Therefore alternative α coefficients in equation 25 were considered (see Section 5.4.3).

Even so, already a small increase near the MYI ice region where the ridge density is highest (Kwok et al. 2019a; Duncan et al. 2022), according to the theory first proposed in Arya (1973), is a step in the right direction.

5.4.2 Sea ice drift

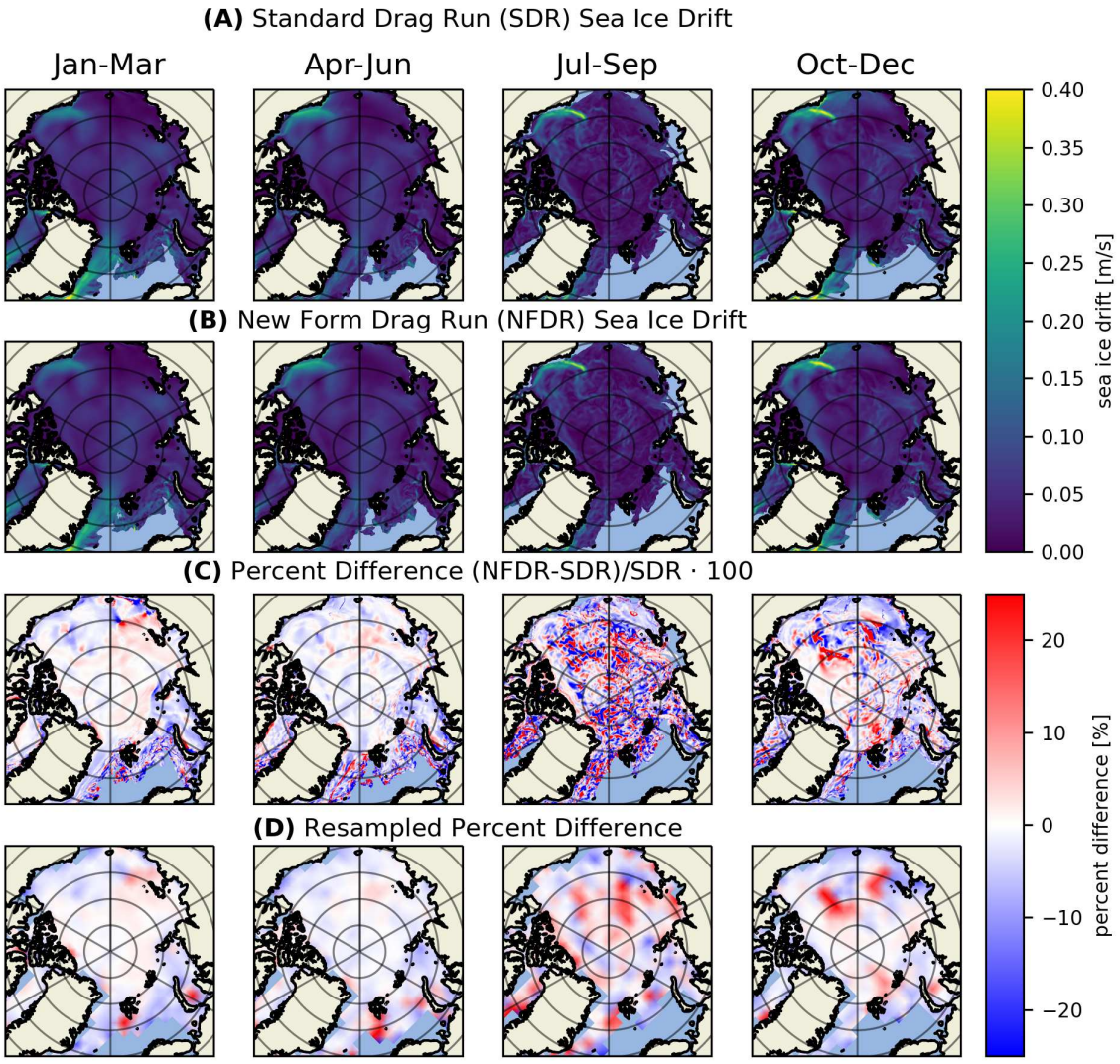

Figure 5.4: 3-month averaged Standard Drag Run (A) and New Form Drag Run (B) sea ice drift velocity with the percent difference between the two (C) for the periods January to March, April to June, July to September and October to December (averaged over 2019-2021). The percent difference maps are then bucket resampled to better depict large spatial differences (D).

We then take a look at sea ice drift as it is the parameter that is most intuitively associated with momentum transfer. Fig. 5.4A and B show NFDR and SDR sea ice drift 3-month averages. It quickly becomes apparent that differences in the model runs are difficult to assess and indeed the PDs in space and time for most parameters are contained within a ±25% range. As a result, from here on out, we will refrain from showing the variables from both SDR and NFDR and primarily focus on the PD maps. Fig. 5.4C shows the PD for the sea ice drift 3-month averages over the 2019-2021 simulation period. Except for the period of Jul-Sep, spatially averaged differences that range from $-1 \times 10^{-4}\,\mathrm{m\,s^{-1}}$ in the central Arctic (>80°N) to $-5 \times 10^{-3}\,\mathrm{m\,s^{-1}}$ in the peripheral seas by the MIZ translate to less than a percent difference in the former and around -3% in the latter. Thus, large spatial averages reveal little when it comes to the differences in drift velocities. Instead there are pockets of more pronounced changes (>10%) that are difficult to attribute to the newly introduced spatiotemporal variability in form drag. Notably in the summer period (Jul-Sep), the patterns become highly sporadic which necessitated the resampling of the percent differences to better see the overall spatial changes across the years (see Fig. 5.4D). Jul-Sep features the highest standard deviation across all sectors of the Arctic and even a mean increase of 1.5-2% in the central Arctic and a 2% increase in the Beaufort, Chukchi and East Siberian seas (all on the order of 1×10^{-4} m/s). This is likely associated to an increase in the MIZ area and the associated spike in floe edge form drag. A pocket of around 20% mean increase in drift velocity can be observed in the East Siberian Sea near the antimeridian in the Jul-Sep average of resampled percent differences, and a more pronounced 25% pocket in the Beaufort Sea in the Oct-Dec average. In reference to PQ1, the effect of our drag coefficient changes on the model drift output are minimal, which is in line with findings by others that included form drag into their models (e.g., Tsamados et al. 2014; Sterlin et al. 2023).

5.4.3 Sea ice thickness

To better answer PQ1 we also take a look at SIT. Fig. 5.5A shows SDR sea ice thickness and its seasonal evolution across the 2019-2021 as outputted by the model, with highest SIT values north of Greenland in Apr-Jun. The SIT PD maps (Fig. 5.5B), with the original form drag implementation ($\alpha = 0.28$), show a small thinning in large parts of the central Arctic. This wide-scale thinning is primarily relegated to the Western Arctic where obstacle form drag implementation is most prevalent. As with drift velocity, the SIT differences are small (on the order of centimeters on average), however unlike drift, we can more clearly observe the Arctic-wide pattern for all seasons in all years to be negative. It is along the MIZ where we see a reversal of this pattern, and in most 3-month averages observe a near-20% increase locally in NFDR. This pronounced difference is consistent with an increase in SIC along the MIZ as well (Fig. C1). Moreover, the observed variation in SIT PD is adequately contained within the ±25% range.

To address PQ2 and check whether larger differences would be observed by increasing the contribution of obstacle form drag, we doubled the α value of 0.28 in equation 25 to obtain $\alpha = 0.56$

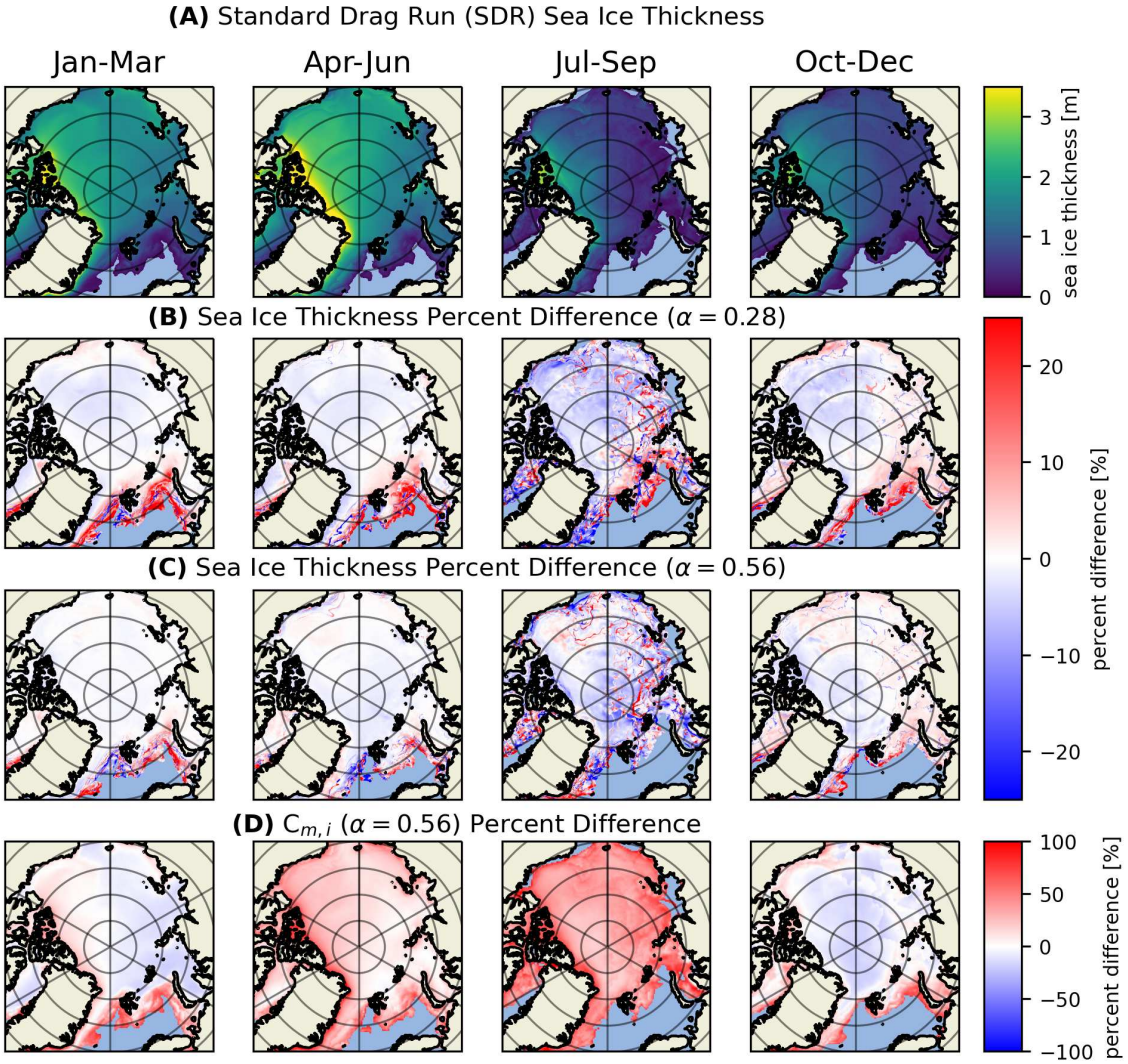

Figure 5.5: 3-month averaged, Standard Drag Run sea ice thickness (A), New Form Drag Run (with distinct α values) sea ice thickness percent differences for $\alpha = 0.28$ (B) and $\alpha = 0.56$ (C) with respect to the Standard Drag Run and drag coefficient NFDR ($\alpha = 0.56$)-SDR percent difference (D), for the periods January to March, April to June, July to September and October to December (averaged over 2019-2021).

(see Fig. 5.5C). This modification, in turn, doubles $\alpha_w = 1.4$ in equation 35 to $\alpha_w = 2.8$. The reasoning behind the doubling was motivated by a hypothesis formed after initial results: that the predominantly low retrieved drag coefficient values of the central Arctic (Mchedlishvili et al. 2023) likely had the effect of pushing down the slope of the linear regression between SIT and the drag coefficient estimates (see Fig. 5.2). Through this sensitivity test, we effectively bring the mean pan-

Arctic drag coefficient of SDR and NFDR closer together, e.g., the mean 2019-2021 PD between NFDR and SDR in the central Arctic (>80°N) is reduced from -26% to -0.81% in Jan-Mar, and from -21% to -8.4% in Oct-Dec with $\alpha = 0.56$. Incidentally that is also when the most pronounced negative PDs across the Arctic Ocean were observed when using $\alpha = 0.28$ (see 5.3). Using this sensitivity study, we can better assess the influence of variable drag as opposed to constant drag Arctic-wide.

Interestingly, this change has the effect of reducing the SIT decrease across the Arctic as well as the increase along the MIZ. For large spatial averages this translates to a reduction of order from centimeters to millimeters change. Locally, the changes are more pronounced, for example in the MIZ for the period Apr-Jun wherein we observe a reversal in SIT change patterns in the Fram Strait (see Fig. 5.5B-C). The drag coefficient PD map between $\alpha = 0.56$ NFDR and SDR (Fig. 5.5D) is noticeably different to Fig. 5.3C. It is no longer the case that drag is primarily reduced when subtracting SDR from NFDR, and in fact Apr-Jun, when SIT values are at their highest, also shows an increase in drag for NFDR. Fig. 5.5D is also more similar to the retrieved drag coefficient estimate distributions of Mchedlishvili et al. (2023), albeit with more floe edge drag influence dominating in the summer months.

5.4.4 Separating atmosphere and ocean drag effects

Next we try to separate the influence of the atmosphere and that of the ocean. With the NFDR model setup, we effectively made two large changes: the integration of form drag at the sea ice–atmosphere interface and at the sea ice–ocean interface. Motivated by PQ3, we separate these modifications, effectively only activating one at a time and keeping the SDR constant drag at the opposing interface. Lüpkes et al. (2011) report that in their mesoscale model often the drag forces at both interfaces had the opposite effects, i.e., atmospheric drag typically accelerated the sea ice floes whereas oceanic drag slowed the floes down. With the sensitivity study we want to check if the same principles hold true Arctic-wide. We also want to see what effects, activating the variable drag scheme at only one interface, has on the sea ice thickness.

The two model runs with these conditions applied are the Atmospheric Form Drag Run (AFDR) and oceanic Oceanic Form Drag Run (OFDR). In the case of SIT (Fig. 5.6), we can see that the thinning in summer and autumn periods, especially in the Beaufort Sea, is largely propagated by the effects of sea ice–atmosphere form drag. Conversely, OFDR as compared to SDR in the Fig. 5.6B PD maps show an MIZ pattern that is more similar to Fig. 5.5B than Fig. 5.6A. This similarity suggests that ocean form drag is largely responsible for the SIT changes at the MIZ observed in NFDR ($\alpha = 0.28$). Whereas Fig. 5.6A shows more similarity to Fig. 5.5B, wherein the above-mentioned reduction of SIT in the Fram Strait for the period Apr-Jun in the $\alpha = 0.56$ run is also visible in AFDR. In general, the differences we do observe are in some part mirrored between Fig. 5.6A and Fig. 5.6B, which suggests that the drag forces below and above sea ice are often acting in such a

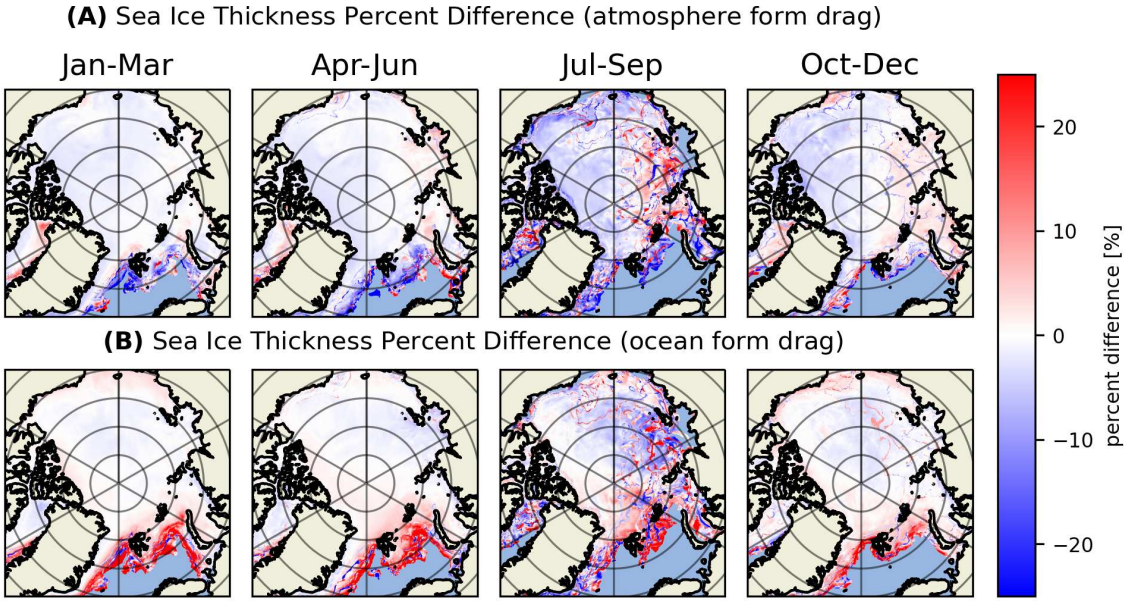

Figure 5.6: 3-month averaged Atmospheric Form Drag Run (A) and Oceanic Form Drag Run (B) sea ice thicknesses are used to calculate percent differences with respect to the Standard Drag Run, for the periods January to March, April to June, July to September and October to December (averaged over 2019-2021).

way as to cancel out the impact of drag on related sea ice parameters. This principle is even more evident in the AFDR-OFDR sea ice drift velocity comparison (Fig. 5.7).

In Fig. 5.7, we see relatively large differences (±20%) that are directly contradicting one another between AFDR (Fig. 5.7A) and OFDR (Fig. 5.7B). This supports findings that the two components of drag have opposite effects on sea ice drift velocities (e.g., Lüpkes et al. 2011). In the case of AFDR with the $\alpha = 0.28$ obstacle form drag parameterization, for most the Arctic sea ice, the mean drag decreases with the $z_{0,m,s}$ =1.0×10^{-3} m to $z_{0,m,s}$ =1.0×10^{-5} m change (see Fig. 5.3). This change has the effect of reducing the friction between the atmosphere and sea ice layers, thereby slowing down the sea ice as compared to SDR. Notably this is not the case along the MIZ and in some periods near the thick ice area north of Greenland and the Canadian Archipelago due to floe edge and obstacle form drag, respectively. Meanwhile, the reduction of the oceanic drag coefficient for most of the Arctic has a similar effect but with the opposite consequences. In the case of sea ice and ocean layers, a reduction in drag and therefore the friction between the layers, results in an increase in sea ice drift velocity since the atmosphere more readily tugs at the sea ice. Interestingly, in Jan-Mar and Apr-Jun, roughly above the Beafort Gyre, the PDs are near-zero, possibly suggesting that reduction in friction is offset by the tugging done by the gyre.

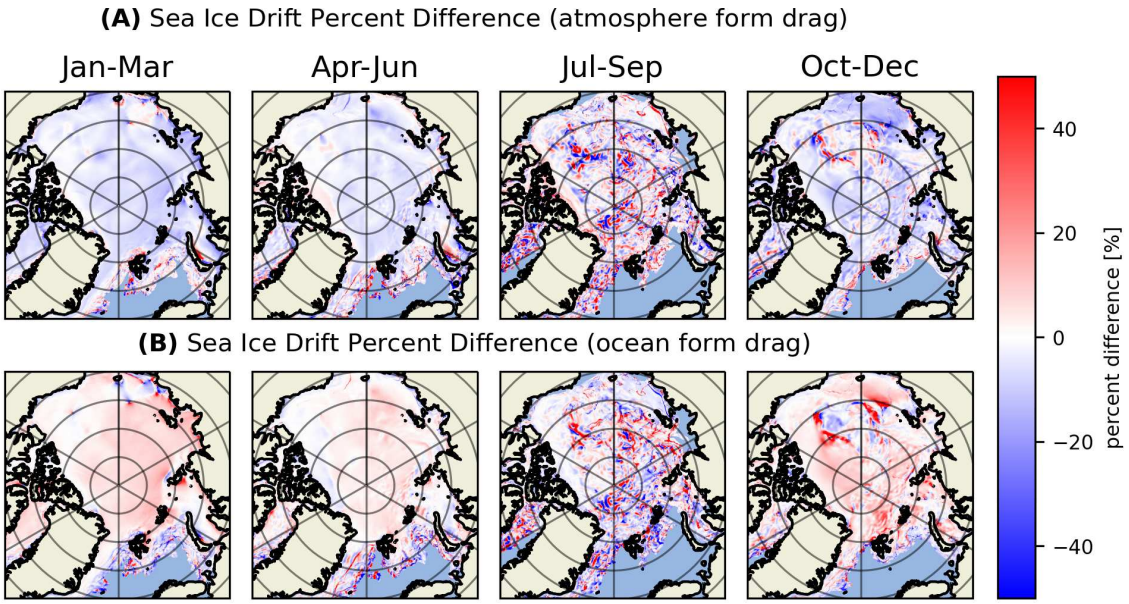

Figure 5.7: 3-month averaged Atmospheric Form Drag Run (A) and Oceanic Form Drag Run (B) sea ice drift velocities are used to calculate percent differences with respect to the Standard Drag Run, for the periods January to March, April to June, July to September and October to December (averaged over 2019-2021).

Between these two runs, the fact that AFDR PD is more similar to Fig 5.4 C-D suggests that changes in the distribution of atmospheric drag have a more direct impact on drift velocities. In other words, though the decelerating effects are reduced in NFDR, it is the reduction in the mean atmospheric drag and the associated accelerating effect that carries over when both these changes are implemented.

5.4.5 Ice growth through dynamic and thermodynamic processes

To study what is causing the changes in sea ice parameters like thickness, concentration and volume (PQ4), we look at sea ice thermodynamic and dynamic growth (Fig. 5.8). Here we show absolute differences as PDs can become very large with small changes from positive to negative growth or vice versa.

Sea ice thermodynamic growth (ITG) (Fig. 5.8A-B) shows minimal differences (less than a $\mathrm{mm\,d^{-1}}$), save for a pronounced melting (negative thermodynamic growth) in the central Arctic close to the antimeridian in Apr-Jun, and additional freezing (positive thermodynamic growth) in the same area for Jan-Mar and Oct-Dec periods. On the other hand, ice dynamic growth (IDG) shows relatively more variability in the difference maps (Fig. 5.8C-D). The absolute differences are still small ($\sim\mathrm{mm\,d^{-1}}$) but noticeably larger than what is observed for thermodynamic growth. The

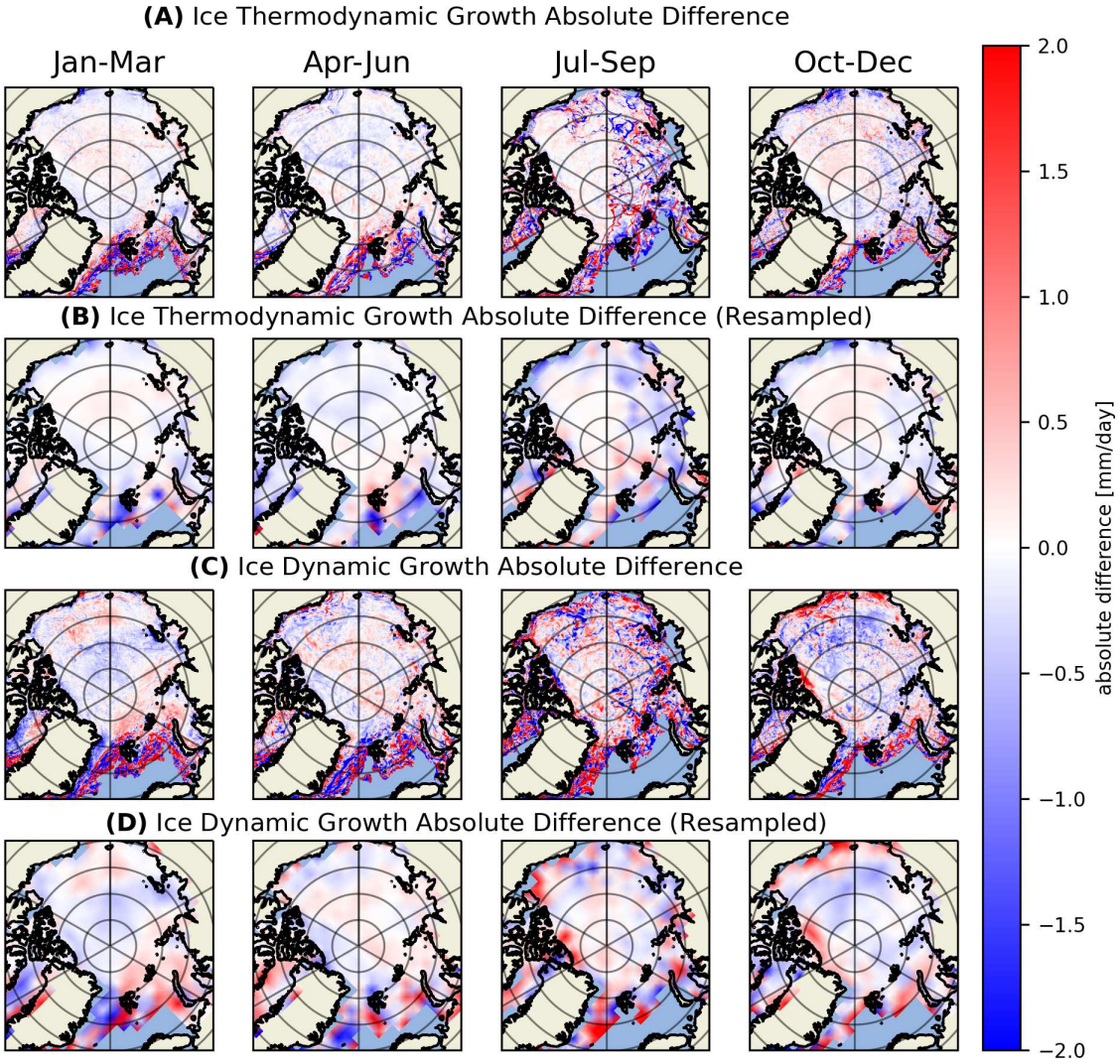

Figure 5.8: 3-month averaged New Form Drag Run ice thermodynamic growth (A) and ice dynamic growth (C) are used to calculate percent differences with respect to the Standard Drag Run, for the periods January to March, April to June, July to September and October to December 2019. The percent difference maps are bucket resampled to better depict large spatial differences for thermodynamic (B) and dynamic growth (D), respectively.

only location where the absolute differences in dynamic and thermodynamic ice growth exceed a $\mathrm{mm\,d^{-1}}$ is along the MIZ, pointing again to the fact that the floe edge drag term is the main driver in sea ice concentration and thickness changes that we observe.

Comparing Fig. 5.5B with Fig. 5.8 maps, it can be assumed that the dynamic contribution to the reduction in SIT is stronger than the thermodynamic in the Western Arctic (Beaufort Sea/Central

Arctic area). This is also the case in the AFDR maps (Fig. 5.6A), suggesting that the atmospheric drag has a stronger part to play in the changes caused by dynamics. In addition, NFDR dynamic growth observed by the coast of Alaska in Oct-Dec is also nicely reflected in NFDR SIT where thermodynamic growth is negative, which suggests melting. Moreover, this case is yet another example of dynamics having a stronger contribution on SIT than thermodynamics. Other areas with notable NFDR dynamic growth don't seem to show up in SIT differences, and as thermodynamic growth differences are predominantly negative, it is likely that they could play a part in offsetting some of the positive dynamic growth differences. Considering both are typically less than a $\mathrm{mm\,d^{-1}}$, it cannot be said that one dominates over the other, nevertheless dynamic growth differences have more similarities with the SIT differences.

5.5 Conclusion and Outlook

In this study, we implemented a form drag parameterization in an otherwise constant drag model. We preformed two model runs, the (new) form drag run (NFDR) with the form drag parameterization implemented as well as a constant (standard) drag run (SDR). We analysed primarily sea ice drift and thickness over the 2019-2021 model run period and studied the results with additional sensitivity studies. The following sensitivity studies were conducted:

1. the doubling of the α parameter in equation 25, which is the scaling factor that is used to calculate the obstacle form drag value from SIT according to equation 25
2. Only modifying the sea ice–atmosphere form drag and keeping sea ice–ocean form drag constant (as in SDR)
3. Only modifying the sea ice–ocean form drag and keeping sea ice–atmosphere form drag constant (as in SDR)

Finally, we also looked in other relevant parameters that help quantify the momentum transfer as well as explain some of the changes we see in sea ice properties. Namely, by analysing dynamic and thermodynamic ice growth, we looked into which processes lead to the changes observed in SIT.

5.5.1 The effects of variable drag on sea ice properties (addressing PQ1)

The first parameter that was analysed was sea ice drift (Fig. 5.4). Sea ice drift was expected to be most directly influenced by drag coefficients, and by extension the friction velocity, which help quantify the momentum transfer between the sea ice and surrounding layers of fluid (atmosphere and ocean). However, the interplay between sea ice drift and drag is complicated and nonlinear, especially when considering drag at both interfaces. The run in which the form drag was implemented only at the sea ice–atmosphere interface (AFDR) was to some extent already evaluated and compared to observations (Yu et al. 2020). Though the Yu et al. (2020) form drag tests are evaluated in

HIRHAM-NAOSIM version 2.0, not HN2.2 as it is done here, and the form drag model run does not include the obstacle form drag parameterization we used, the impact of $\alpha = 0.28$ NFDR proved to be relatively low. Thus AFDR and Yu et al. (2020) findings should, in principle, be comparable. Yu et al. (2020) found that even with floe edge drag implemented, the effects it had on the sea ice drift velocity did not improve agreement with observations. Yu et al. (2020) report that the Kimura et al. (2013) satellite-based daily sea ice drift observations have a higher inter-annual variation than HIRHAM-NAOSIM drift velocities (with and without form drag) and that the latter overestimates the former in winter. They suggest that a higher ice–ocean drag might dampen the sea ice drift in winter such that it then better agrees with observations. In our modified run (NFDR), where both atmosphere and ocean drag increases are occurring together spatially, we see an a reduction in drift speeds in most sectors in Jan-Mar and Apr-Jun periods (see Fig. 5.4C), which would be closer to the retrieved Kimura et al. (2013) drift speeds reported on in Yu et al. (2020). On its own, this does not mean much because the retrieved drift speeds reported on in Yu et al. (2020) are from 2007, the reduction is minimal (in the range of $-1 \times 10^{-4}\,\mathrm{m\,s^{-1}}$ to $-1 \times 10^{-3}\,\mathrm{m\,s^{-1}}$) and there was no comparison to observations done in our study. However, the hypothesis that ocean drag has a role to play and specifically, that where there is more form drag at the sea ice–atmosphere interface there should also be complementary increase at the sea ice–ocean interface was successfully tested in our study. Yu et al. (2020) suggested harmonizing the new parameterization (Lüpkes et al. 2015) with the ice–ocean drag coefficient; such a harmonized setup was the goal of the dual atmosphere-ocean-sea ice variable drag scheme of this study. In addition, the floe edge drag parameterization, first developed in Lüpkes et al. (2012), was meant to be used in tandem with an obstacle form drag scheme; that too was accounted for in our model setup. With all these changes in place, we observe some minor differences, namely the reduction in drift speeds. This reduction is likely associated to the impact of ocean form drag, that is known to have a decelerating effect on sea ice floes (e.g., Birnbaum et al. 2002; Lüpkes et al. 2011)), offsetting the influence of atmosphere form drag locally. This phenomenon is further elaborated on in Section 5.5.3.

Another parameter analysed in this study is SIT, which also gives us an indication on how sea ice volume is affected by the form drag parameterization. SIT differences (from SDR to NFDR) predominantly show a decrease (see Fig. 5.5) on the order of cm, save for the MIZ. In the MIZ there is a strong increase in SIT (Fig. 5.5) and SIC (Fig. C1) that seems to be primarily driven by the form drag implementation at the sea ice–ocean interface (see Fig. 5.6 and the associated discussion in Section 5.5.3). Thus, to answer the question "does the separation of drag into individual components change sea ice properties" (PQ1): yes there is a definitely a change observed and though it is a minor change, in the case of SIT, it is both pan-Arctic and consistent across seasons and the years of the period studied. Whereas for sea ice drift, it is more the case that there are individual pockets of strong influence, especially in Oct-Dec. The changes that are small in magnitude in this study could have a stronger influence over a longer time period, in addition no variation in initial conditions was considered here. Thus, a longer model run and ensemble simulations should reveal if more significant

changes are observed over time and how dependant they are on the initial state of the model. Once that is assessed, and only then, would a comparison to observations be meaningful.

5.5.2 The sensitivity of the analysis to the α parameter (addressing PQ2)

This was an important sensitivity study for two main reasons. Firstly, as mentioned briefly in Section 5.4, the drag coefficient estimates retrieved in (Mchedlishvili et al. 2023) have a wide range as shown in in Fig. 5.2. Outliers above 2×10^{-3} are rare but still represented, however, using the linear regression slope of $\alpha = 0.28$, equation 25 will never compute those values unless SIT is above 7 m! Alternative regression techniques were tested but did not preform better for the full time period analysed, however, this does not mean the linear regression is ideal. Deformation occurs also in thin ice when exposed to storms (Aue et al. 2023) and partly depends on ice age which is also not perfectly linearly dependent on SIT (Tschudi et al. 2016). Therefore testing an α parameter which also embodies the high obstacle form drag values, was necessary. As to what this value should be is unclear and arguments can be made for and against any particular choice, therefore, for the sake of simplicity, we doubled $\alpha = 0.28$ to obtain $\alpha = 0.56$. The second reason has to do with how the new (NFDR) drag coefficient scheme compares with the old one (SDR) with a constant pan-Arctic drag coefficient. Because of the decrease of the aerodynamic roughness length from $z_{0,m}$ =1.0×10^{-3} m to $z_{0,m,s}$ =1.0×10^{-5} m, areas in the central and eastern Arctic that are both thin and far from the MIZ throughout winter, essentially go from $C_{da} = 1.89 \times 10^{-3}$ to $C_{da} = 8.38 \times 10^{-4}$ in terms of sea ice–atmosphere drag and $C_{dw} = 9.43 \times 10^{-3}$ to $C_{dw} = 4.19 \times 10^{-3}$ in terms of sea ice–ocean drag (see Fig. 5.3). This decrease has important ramifications and makes it harder to distinguish whether the changes we are seeing come from the pan-Arctic drag coefficient decreasing or if it is because the constant drag coefficient distribution becomes variable in space and time. With $\alpha = 0.56$, the mean difference decreases and the spatiotemporal variability of drag coefficients over and under sea ice increases (see Fig. 5.5).

With this setup, there are interesting developments observed for SIT in Fig. 5.5. Firstly, and perhaps most surprisingly, the PD maps of Fig. 5.5C actually show smaller PDs Arctic-wide. This could suggest that the variability does not have a strong effect on SIT and that in Fig. 5.5B we mainly see the effects of the reduction of pan-Arctic mean drag coefficient. This is however not the case along the MIZ, where we go from a strong increase in SIT to a decrease in the Fram Strait for Jan-Mar and Apr-Jun periods. As floe edge drag should not have been influenced by the α parameter change, this is likely somehow influenced by the thick ice close to Greenland. Meanwhile for drift (see Fig. C2), this has the effect of increasing drift values. While this is not surprising for Apr-Jun when the drag coefficients are typically larger in NFDR than SDR (see Fig. 5.5D), it is surprising for Jan-Mar when the positivie and negative PDs are more or less balanced. Of course these are all changes on the order of 1×10^{-4} m s^{-1}, but nevertheless it is important to analyse if they are positive or negative. Notably, with $\alpha = 0.56$ you begin to see pockets of increased drift speed velocity close to the Canadian Archipelago and Greenland, which one would expect as the general area features

the thickest sea ice in the Arctic Ocean. However, the main take-away from this sensitivity study as a whole, is that increasing the α parameter in equation 25, and thereby equation 35, does not show a significant increase in the differences we observe. Though this conclusion does not fully answer PQ2 due to the testing of only one other α parameter, based on the single test conducted, it suggests that the analysis is sensitive to the α parameter regarding the direction of observed differences, though not their magnitude. To delve deeper into which variable drag scheme (that of the ocean or atmosphere) is dominating in $\alpha = 0.28$ and $\alpha = 0.56$ variable drag model runs, we needed to isolate their influence.

5.5.3 The opposing effects of atmosphere and ocean drag (addressing PQ3)

NFDR incorporates variable atmosphere and variable ocean drag, such that the spatiotemporal variation is the same for both as it is mirrored across the sea ice layer. Birnbaum et al. (2002) and Lüpkes et al. (2011) report from mesoscale modelling that atmospheric drag has an accelerating effect on sea ice drift, whereas ocean-drag tend to decelerate sea ice floes. This finding is in part what led to PQ3 and the need to study effects of both individually in a pan-Arctic coupled model. For the purposes of isolating the effects of the atmosphere and ocean we ran AFDR, the model run where form drag is implemented only at the sea ice–atmosphere interface, and OFDR, the model run where form drag is implemented only at the sea ice–ocean interface, respectively. The results of these tests are shown in Figs. 5.6 and 5.7. In the case of SIT (Fig. 5.6), we see that the PD maps of AFDR are more similar that of NFDR than OFDR. In other words, an overall thinning is present in both AFDR and NFDR suggesting that the atmospheric drag has a stronger part to play when both are included in NFDR. Meanwhile OFDR is more similar to NFDR with the modified α parameter of 0.56 (see Fig. 5.5C), with some red highlights representing increases especially in the Oct-Dec period. Thus, this could suggest that at a certain α, the ocean obstacle form drag more readily offsets the influence of atmosphere obstacle form drag. Another important effect we're seeing in Fig. 5.6 is the reversal of SIT difference at the MIZ, where AFDR shows a decrease and OFDR shows a pronounced increase. Here, the effect of ocean floe edge drag seems to dominate as when they're both included together in NFDR, we still get an overall increase along the MIZ. Thus, if atmosphere form drag is more important for SIT for most the Arctic but this pattern is reversed along the MIZ, one potential explanation could be that when both atmospheric and oceanic drag are low, the former contributes more, whereas when they're both high, this pattern is reversed. This explanation would also be in line with the finding that OFDR is similar to NFDR with $\alpha = 0.56$.

For drift (Fig. 5.7), the differences are more stark. The explanation behind these differences, as elaborated on in Section 5.4, is the decrease in pan-Arctic atmospheric drag leading to slower drift velocities in AFDR and the decrease in pan-Arctic oceanic drag leading to faster drift in OFDR. Thus here we can conclude that even on a pan-Arctic scale, the atmospheric drag has an accelerating effect and oceanic drag has a decelerating effect, which, given there are currents in the Arctic, is not so trivial. One potential reason why we do no see a direct influence of current systems is that

two the Arctic currents (Transpolar Drift and Beaufort Gyre) are both largely wind-driven (Cottier et al. 2017). In other words, where there is less ocean drag to tug on the sea ice from below in the presence of currents, atmospheric drag would be tugging in the same general direction, minimizing the associated slow-down. Between Fig. 5.7A and B, A seems to be more similar to Fig. 5.4C-D, suggesting that atmospheric drag is a more important contributor to drift than oceanic drag. Notably, as with SIT, this pattern is partially reversed in NFDR with $\alpha = 0.56$. Therefore, here too, it may be the case that atmosphere drag has a stronger influence when both drag coefficients are low and the opposite may be true as they increase. Therefore, though it is beyond the scope of this study, we propose a more thorough investigation into atmospheric and oceanic drag and how their effects evolve when varying coefficients in the obstacle form drag paramaterization. Such a study may be able to help define when and under what conditions either atmospheric or oceanic drag dominates.

5.5.4 Dividing the influence of dynamic and thermodynamic processes on sea ice thickness changes (addressing PQ4)

HIRHAM-NAOSIM has the advantage of outputting multiple parameters that help quantify the causes behind resulting model values. Two such parameters are ITG and IDG (see Fig. 5.8) which can help interpret the changes we observe in sea ice thickness (Fig. 5.5), concentration (Fig. C1), and thereby volume in order to address PQ4. For both parameters, resampling, as done in Fig. 5.4D, was necessary to smooth the sporadic positive-to-negative jumps over relatively small spatial scales (see Fig. 5.8B and C). As with SIT and drift velocity changes, the changes observed are small (on the order of $\mathrm{mm\,d^{-1}}$) Arctic-wide, save for the MIZ where they're above above $\pm 2\,\mathrm{mm\,d^{-1}}$. In general, the ITG pan-Arctic pattern shows melting more so than it does freezing, especially once the smaller oscillations are averaged out using the bucket resampling method (see 5.8B), which is in line with the NFDR SIT changes we observe in Fig. 5.5B. IDG is more sporadic, with large (sometimes $>1 \times 10^5\,\mathrm{km^2}$) patches of positive and negative PD patterns. Looking at the similarities between the IDG PD maps (Fig. 5.8C-D) and Fig. 5.5, certain features like the thicker sea ice at the Southern edges of the Beaufort Sea, by the coasts of the Northern Territories, Yukon and Alaska in Oct-Dec, can clearly be seen in both maps. This feature can also be seen in the SIC maps (Fig. C1), albeit not as clearly. The area in question is a high drift velocity area ($>0.3\,\mathrm{m\,s^{-1}}$) which is most pronounced in Oct-Dec (see Fig. 5.4A-B), therefore it is subject to relatively strong dynamical processes. In NFDR, where drag over sea ice is more pronounced closer to the coasts (see Fig. 5.3), it makes sense that there is more dynamics at play there. As we have discovered in our model results, the dynamics processes lead to an increase in thickness, concentration and therefore volume, locally. Suggesting that the higher than average drag coefficients in the area have an impact on sea ice formation, especially in Oct-Dec. Importantly, the changes observed are dynamic and not thermodynamic, suggesting that the local thickening of sea ice is the result of a dynamic process like ridging.

Elsewhere in the Arctic, patterns are not as clear. Some notable features include the dynamic loss of sea ice the central Arctic (see Figs. 5.5B and 5.8C) close to the antimeredian in Jan-Mar, as well as the sporadic behaviour observed in the MIZ. The MIZ pattern in ITG balances out with resampling as can be seen in Fig. 5.8A-B, however IDG still shows distinct pockets even after averaging (see Fig. 5.8C-D), which are typically more positive than negative closer to the ice edge. This effect can be seen both in SIT (Fig. 5.5) as well as SIC (Fig. C1), suggesting that in NFDR there is a higher volume of sea ice in the MIZ than in SDR. From OFDR and AFDR (see Figs. 5.6A-B and C1C-D), we know that this dynamic process is primarily propagated by the ocean, therefore it is likely that ocean currents play a role here. Especially in the Fram Strait, where currents are known be strong, such a conclusion makes sense. In fact, the influence of the ocean dominates both for SIT and SIC (Figs. 5.6A-B and C1C-D), suggesting the effects of the Atmospheric drag are not the primary contributor to the changes we observe at the MIZ. Notably, as mentioned in section Section 5.4, this pattern is to some extent reversed with $\alpha = 0.56$ plugged into equation 25.

5.5.5 Outlook and final remarks

One of the main findings of this study was that including variable drag at both the sea ice–atmosphere and sea ice–ocean interfaces in parallel often results in the effects of both cancelling each other out. Form drag from features only present at one interface, e.g., meltpond edges at the sea ice–atmosphere interface in summer, were not accounted for in this study. Therefore it would be interesting to see how the interaction between both interfaces develops with distributions that are not paralleled. Similarly, the assumption that obstacle form drag is paralleled comes from the fact that the pressure ridge is a pronounced obstacle at both interfaces, and it is also the most common obstacle distributed throughout the Arctic. However, rubble fields, hummocks, snow dunes and sastrugis are also present and impart their own form drag, therefore models able to recreate snow thickness distributions across the surface should also seek to incorporate such dependencies into their drag coefficient schemes. Lastly, a study that can isolate whether atmospheric or oceanic form drag dominates in terms of changes observed in sea ice properties over the full span of possible drag coefficient values would be highly beneficial to the coupled atmosphere-ocean-sea ice modelling community.

Importantly, the effects of drag on SIT and drift are complicated and likely not fully realized within a time-span as short as three years. Here, we recommend a study that spans a longer time-span, and ideally one that uses ensemble simulations with varying initial conditions to better quantify the impact of variable form drag on sea ice properties. For as has been shown here, within the three year time period, both α form drag paramaterizations show small differences between SDR and NFDR. Nevertheless, we know that drag is not uniform across the Arctic both from theory and observations (e.g., Mchedlishvili et al. 2023; Petty et al. 2017; Castellani et al. 2014; Tsamados et al. 2014) and modelling studies that span longer time periods show that form drag does have a significant impact on sea ice properties (e.g., Tremblay et al. 1997; Tsamados et al. 2014; Sterlin et al. 2023). While no modelling study to our knowledge that tested the variable form drag scheme used

a fully coupled atmosphere-sea-ice model, wherein lies the novelty of this particular study, it is still unlikely that the influence of both atmospheric and oceanic drag in such a model fully cancels out the impact of drag on the sea ice layer. Therefore, as we have found small but reasonable changes, we propose looking at longer periods to analyse the variable drag-induced long-term changes in sea ice properties.

6 Summary, conclusions and outlook

The following section is meant to bring all the studies contained within this dissertation together, summarize them and answer the research questions posed in Chapter 1. In addition, Section 6.3 discusses how the data produced throughout this project could be used in future studies and mentions potential follow-up projects that would address the remaining unresolved questions.

6.1 Tying it all together

In this project, I investigated atmosphere-ocean-sea ice momentum transfer from observations at both Antarctic mesoscale (Chapter 3) and pan-Arctic scale (Chapter 4). The latter of these analyses was then used to create a parameterization which was implemented into a coupled regional atmosphere-ocean-sea ice model, to further study the dynamics of the Arctic climate system (Chapter 5).

In the first study, *Weddell Sea polynya analysis using SMOS–SMAP apparent sea ice thickness retrieval* (Chapter 3), we looked at the main drivers behind the formation of the Weddell Sea Polynya. The study serves not only as a literature review of all previous papers that attribute the polynya to dynamic and thermodynamic processes, but also describes a new method (SMOS–SMAP apparent sea ice thickness (ASIT) retrieval) that was tested for the first time in the study of the anomalous event. In the 11-year Soil Moisture Ocean Salinity (SMOS) record (Fig. 3.2), we were able to identify years in which though the polynya did not form, a thin sea ice thickness (SIT) anomaly of a comparable size was realized (see Fig. 3.7). Based on previous studies, our comparison to ECMWF Reanalysis 5th Generation (ERA5) surface wind speed, as well the ASIT retrieval of multiple thin sea ice anomalies over Maud Rise, we proposed that the Weddell Sea Polynya is in fact caused both by dynamic and thermodynamic processes that must occur simultaneously for it to appear and persist. Open-ocean polynyas are typically described to be caused predominantly by thermodynamic processes (see Section 1.2), whereas in our work we corroborate past studies (e.g., Campbell et al. 2019; Francis et al. 2019; Wilson et al. 2019) and show that dynamic processes are just as important in causing polynyas as well as other sea ice anomalies on top of Maud Rise. In particular, we delved into the impact of near-surface winds using ERA5 data. Strong surface winds interact with the pack ice as they transfer energy and momentum to the sea ice layer, causing breakup and an overall thinning in the area. This momentum transfer is quantified through the sea ice–atmosphere momentum transfer or drag coefficient C_d.

C_d is the main focus of the study *New estimates of pan-Arctic sea ice–atmosphere neutral drag coefficients from ICESat-2 elevation data*, in which we describe the development of a dedicated drag coefficient estimate retrieval that spans the Arctic ice pack. The developed method retrieves neutral form drag coefficient estimates, i.e., the drag associated to large distinct obstacles in a neutrally

stratified atmospheric surface layer. Specifically, we used Ice, Cloud and land Elevation Satellite 2 (IS2) Advanced Topographic Laser Altimeter System (ATLAS) sea ice height data to measure obstacles across the sea ice surface (mainly pressure ridges but also snow features). From this data we then used a paramaterization (equation 11) by Garbrecht et al. (2002) that links sea ice–atmosphere form drag coefficients with surface feature height and spacing. This parameterization has the benefit of being developed for one-dimensional high-resolution data, which is precisely what IS2 provides. However, despite the unprecedented along-track resolution of IS2, it still cannot compete with the resolution of airborne topography measurements, e.g., Operation IceBridge (OIB) Airborne Topographic Mapper (Airborne Topographic Mapper (ATM)) and Multidisciplinary drifting Observatory for the Study of Arctic Climate (MOSAiC) Altimeter Laser Scanner (Altimeter Laser Scanner (ALS)) data. As a result, near-coincident high-resolution OIB ATM data was used to scale up the regional IS2 drag estimates. By combining the retrieved form drag coefficients with drag due to open water, floe edges (derived from sea ice concentration (SIC) according to Lüpkes et al. (2012)) and sea ice skin drag according to equation 13, we produced a time series of monthly averaged pan-Arctic neutral atmospheric drag coefficient estimates from November 2018 to May 2022. The finalized dataset of retrieved neutral sea ice–atmosphere drag coefficient estimates is meant to serve a comparison as well as a means to develop parameterizations for the inclusion of variable drag schemes into models.

In the final study of this project, we conducted a prelimenary analysis of variable form drag in a coupled regional atmosphere-ocean-sea ice model HIRHAM-NAOSIM using our drag coefficient data set. Through a linear regression fit between the IS2 obstacle form drag coefficient estimates and an IS2 SIT data product developed by Petty et al. (2023), we create a parameterization (equation 25) for obstacle form drag within the model. We then combine it with Lüpkes et al. (2015) floe edge paramaterization already implemented in the model and apply both to the sea ice–ocean interface using a ratio based on past studies (Tremblay et al. 1997; Lu et al. 2011; Tsamados et al. 2014). This was done with the assumption that on large spatial scales the form drag due to obstacles (mainly ridges) and floe edges is present both above and below the sea ice layer. Once implemented, the variable drag scheme referred to as the New Form Drag Run (New Form Drag Run (NFDR)) was tested alongside the Standard Drag Run (SDR) which was near-identical to the original state of the model (v2.2) with constant drag throughout the Arctic ice pack. The pan-Arctic percent difference maps calculated according to equation 37 showed changes that were small in magnitude but nevertheless meaningful and able to be explained through theory and additional sensitivity tests.

6.2 Addressing the research questions

6.2.1 Research questions 1 & 2

> **RQ1** Is sea ice–atmosphere momentum transfer as important as oceanic sensible heat flux transfer in forming the Weddell Sea Polynya?

As briefly described in Section 1.2 and shown in Fig. 1.1, an Antarctic open-ocean polynya is described as one that is formed and maintained via the upwelling of Circumpolar Deep Water (Gordon et al. 1988). Then, the warmer surface waters can transfer sensible heat to the ice layer from below, thereby melting it. Also in the case of the Weddell Sea Polynya, thermodynamics has been reported to be the primary driver behind its occurrence since the 1970s large Weddell Sea Polynya occurrences (e.g., Martinson et al. 1981; Martinson et al. 1998; Steur et al. 2007; Wilson et al. 2019; Cheon et al. 2019). For a more detailed discussion on the weak stratification-induced deep convection and heat ventilation into the mixed layer that is thought to be one of the primary causes behind the polynya, see Section 3.1. However, here we mean to answer **RQ1**, and specifically if sea ice–atmosphere momentum transfer from surface winds to the sea ice on top of Maud Rise is as important as thermodynamic processes in forming the polynya.

We have found in our results that both the 2016 (Fig. A1) and 2017 (Fig. 3.5) polynya show clear signs of strong wind activity at the start of each polynya event. These statistics are taken over the frame outlined Fig. 3.1 (northwest corner: 61.78°S, 3.57°W, southeast corner: 67.88°S, 13.11°E), which fully contains both polynya events as well as the sea ice anomalies observed. In the case of the 2017 polynya, we can even see a strong wind feature crossing the area where the polynya forms on 13 Sep 2017, the day it rapidly expands (see Fig. 3.8). Here our findings corroborate the many studies (e.g., McPhee et al. 1996; Goosse et al. 2000; Francis et al. 2019; Campbell et al. 2019; Wilson et al. 2019; Heuzé et al. 2021) linking the formation of the Weddell Sea Polynya to localized atmospheric phenomena. Thus, we can confirm the results of such studies with our analysis and give further credibility to the notion that dynamic processes are just as important. In fact, it can be argued that these are the principal cause behind the formation (Francis et al. 2019; Campbell et al. 2019) whereas thermodynamic processes take over in maintaining the polynya once the ice layer has been sufficiently disturbed and is no longer consolidated.

> **RQ2** What happens when the different drivers behind the formation of the Weddell Sea Polynya do not occur simultaneously?

Chapter 3 briefly summarizes all studies that discuss the mean-state factors that precondition the Weddell Sea Polynya as well as sporadic thermodynamic and dynamic influences that cause and

maintain it. For a detailed discussion of all of these phenomena, the reader is referred to Section 3.1, with a few exceptions that are mentioned later in Section 3.5, such as the work by Francis et al. (2020). This work investigates the effect of intense atmospheric rivers in 1973 and 2017 that brought clouds which helped decouple the sea ice from the atmosphere by increasing snowfall and trapped outgoing longwave radiation in the near vicinity of Maud Rise. 1973 and 2017 mark the years in which the Weddell Sea Polynya occurred, suggesting that atmospheric rivers are yet another driver behind the polynya's formation. It is important to emphasize the word "another" here as it is indeed the case that many studies emphasize different phenomena to be contributing in the formation and survival of the polynya in the select periods it occurred. While some studies emphasize individual phenomena, others point out multiple causes (e.g., Martinson et al. 1981; McPhee et al. 1996; Campbell et al. 2019). Thus, it can be concluded that several different processes need to take place within a given timeframe such that a polynya opens and stays open. A consequence of this assumption is that there are likely also occasions when some but not all of these sporadic processes are taking place, in addition to the mean-state factors that are constantly contributing the anomalous conditions on top of Maud Rise. Thus, the question that remains and needs explanation is **RQ2**: "what happens when the different drivers behind the formation of the Weddell Sea Polynya do not occur simultaneously?"

RQ2 led to an investigation using ASIT retrieved from the satellites, SMOS and Soil Moisture Active Passive (SMAP), to investigate sea ice anomalies on top of Maud Rise in the austral winters the polynya did not occur. Even before the 2016-2017 occurrences of the Weddell Sea Polynya, Lindsay et al. (2004) reported that the 23–year mean SIC for the months of July through November (1979–2001) shows a distinct halo of low ice concentration with a diameter of about 300 km. The last notable Weddell Sea Polynya event before 2016-2017 was the 1973-1976 period in which the Weddell Sea Polynya, though it originated as a small opening on top of Maud Rise initially in 1973, ended up spanning an area of about $250 \times 10^3\,\mathrm{km}^2$ in the eastern potion of the Weddell Sea (1974-1976) (Carsey 1980). Why the 2016-2017 case did not culminate into the same end result is not clear. Studies like Cheon et al. (2019) attribute the lack of polynya in 2018 to the state of the Southern Annular Mode, however it was still unexpected that after the 2017 polynya which formed in September and stayed open until melt, no feature of similar scale followed in 2018. That is where the ASIT analysis shed some light, by revealing that in 2018 a sea ice anomaly that, at its peak (18 Sep: <50cm sea ice region with an area of $300 \times 10^3\,\mathrm{km}^2$), reached an estimated area larger than the United Kingdom (see Fig. 3.6). Suggesting rather than an abrupt end to the anomalous polynya events of 2016-2017, we observe a waning of this phenomenon in the form of the 2018 thin sea ice anomaly. We then used the SMOS ASIT retrieval to investigate the 11-year period from 2010 to 2020 (see Fig. 3.2) and identified multiple instances of thin sea ice anomalies that have developed over this time period (see Fig. 3.7). Thus, through our study we have identified what happens on a larger scale atop Maud Rise in years in which the polynya does not occur. Namely, as a result of the locally present mean-state preconditioning factors as well intermittent thermodynamic and dynamic processes, a thin sea ice anomaly is formed. Such a thin sea ice anomaly is then unable to transition

into a ice-free area when not enough polynya-favourable processes are taking place in tandem so as to push it over the tipping point and trigger lasting processes like wind-driven turbulent mixing (Campbell et al. 2019), deep convection and heat ventilation (Martinson et al. 1981).

RQ3 Can sea ice–atmosphere momentum transfer be better resolved in both space and time through the use of high-resolution altimeter data?

The sea ice height measurements by Advanced Topographic Laser Altimeter System (ATLAS) onboard IS2 have an unprecedented along-track resolution. At an altitude of 500 km, the 10 kHz laser pulses that ATLAS transmits result in roughly 11 m diameter laser footprints (Magruder et al. 2020; Magruder et al. 2021) that are spaced 0.7 m apart. However, these laser footprints have vertical uncertainties of up to ∼30 cm (Kwok et al. 2019a). In order to bring these uncertainties down to as little as ∼2 cm, a dual-Gaussian fit is applied to segments of varying length (based on surface reflectively), over which 150 signal photons are accumulated. The spatial resolution of the sea ice height data (ATL07) is then the sum of segment length and the beam footprint, i.e., 30 m for the strong beams which are used in our drag coefficient retrieval. Despite the reduction in the vertical uncertainty, the transition of 0.7 m to 30 m is sub-ideal for the measurement of ridge heights and thereby the spacing between them, which are then used to calculate neutral form drag coefficients according to equation 11. Hence the basis for **RQ3**, namely are IS2 ATL07 sea ice height measurements good enough to measure surface features, and by extension, estimate drag coefficients?

Though the footprint on average is as large as 30 m, the individual signal photons are likely to come from all surfaces within that segment, i.e., ridges as well as level ice. In the central Arctic, where the ridge density is comparatively low, the dual-Gaussian fit likely removes the influence of lone pressure ridges. However, in the area north of the Canadian Archipelago and Greenland, where the ridge density is high, we can clearly see, taller average obstacle height, shorter average obstacle spacing and therefore higher form drag coefficients (see Fig. 4.3). This distribution of high form drag in the Western Arctic agrees with past studies that estimated drag coefficients from features measured on airborne surveys (e.g., Castellani et al. 2014; Petty et al. 2017). The next issue was the magnitude of drag coefficients estimates calculated, specifically, as a result of the overestimation in obstacle spacing the resulting drag coefficients were significantly lower than those calculated from higher resolution airborne topographic data sets (see Fig. 4.1). Thanks to near-coincident measurement taken by IS2 and OIB ATM in the April of 2019 (Kwok et al. 2019a), we had a direct comparison to work with. Using these data, we used a linear fit to extract a scaling factor able to scale up the ICESat-2 signal, putting it within the expected range of form drag coefficients. Thereby giving us a means to scale up our neutral form drag coefficient estimates in an effort to better quantify pan-Arctic sea ice–atmosphere momentum transfer, as well as better resolve it in

both space and time. In conclusion, though there are uncertainties associated with the retrieval (further elaborated on in Section 4.3.5), it is a novel pan-Arctic monthly data set that agrees with the range and variation of drag coefficients derived from airborne as well in-situ measurements (e.g., Garbrecht et al. 2002; Andreas et al. 2010; Srivastava et al. 2022).

RQ4 Does the satellite-based analysis of drag coefficients reveal the annual evolution of drag and if so, how does it behave?

Fig. 4.6 depicts the the full span of the drag coefficient analyses starting shortly after the launch of IS2 (11.2018) to roughly when the study was complete (06.2022). The figure depicts pan-Arctic average drag coefficient values (in black), as well as averages evaluated over the Multiyear Ice (MYI) (red) and First-Year Ice (FYI) (blue) parts of the Arctic ice pack (divided up using the MYI concentration retrieved using brightness temperatures from the microwave radiometer Advanced Microwave Scanning Radiometer 2 (AMSR2) and radar backscatter from the C-band scatterometer ASCAT (Shokr et al. 2008; Ye et al. 2016a; Ye et al. 2016b; Melsheimer et al. 2023)). As expected, the rougher MYI ice part has higher drag coefficients and obstacle heights as well as lower obstacle spacing in the winter-spring period. The FYI part has the opposite pattern, save for a presumed maximum around the time of the sea ice minimum. "Presumed" because MYI concentration data set is not available in summer months, the masking cannot be done then either, which explains the data gaps in the red and blue time series in Fig. 4.6. However, as can be seen with the total drag coefficient second local maximum occurring in August of each year, it is the influence of floe edge form drag since the the Lüpkes et al. (2012) parameterization peaks at 50% sea ice concentration. With a longer ice-water boundary being formed as sea ice recedes from the Russian coast, the Marginal Ice Zone (MIZ) area increases and so does the number of exposed floe edge, hence the increase in floe edge form drag. The focus of this study however, is the obstacle form drag, which has a direct impact on the total drag coefficient computed via equation 13. This impact can be seen in the maximum of each year consistently occurring in May when the obstacle form drag coefficients are the most pronounced north of Canadian Archipelago and Greenland. Both the floe edge and obstacle form drag maxima can be seen in the 3-month average map figures corresponding to the years 2019 (Fig. 4.5), 2020 (Fig. B5) and 2021 (Fig. B6) in rows corresponding to Apr-Jun (b) and Jul-Sep (c), respectively.

Notably, both the time series and 3-monthly spatial analyses nicely depict the spatiotemporal evolution of drag. There is a clear annual cycle with interseasonal variation, corroborating measurements by Andreas et al. (2010). As mentioned the maximum in Fig. 4.6 is May, which is consistently 2 months after the sea ice extent maximum. One potential explanation for this outcome could be the melt season beginning in late May, effectively melting some of the snow (which is thickest in MYI part of the Arctic (Rostosky et al. 2018)) and exposing pressure ridges making the ice surface rougher. In conclusion, we do see a unique annual evolution that is influenced by several variable components of total drag that each have their own respective maxima.

6.2.2 Research questions 5 & 6

RQ5 Is sea ice thickness a reliable proxy for form drag coefficients and can this relation represent the influence of form drag in a coupled atmosphere-ocean-sea ice model?

The relation between drag coefficients and SIT is based on the the fact that ridging typically results in the build-up of thicker ice (Tremblay et al. 1997; Haas 2017). Specifically, obstacle form drag is directly related to the sea ice surface roughness, which has been demonstrated by Johnson et al. (2022) to be closely correlated with thickness (Spearman's rank correlation coefficient $\rho = 0.66$). In Figs. 5.1 and 5.2, we see the nature of this relation. Namely, in Fig. 5.1, we see a very clear correlation ($r = 0.94$) when looking at averages over the full Arctic as well as the MYI and FYI parts. Upon comparing individual 12.5 km^2 grid cells over the timespan of interest (2018.11-2022.06 with summer months omitted on account of the IS2 SIT product), this correlation drops to $r = 0.58$ due to the nonlinearities in the relationship (see Fig. 5.2). While other regression methods were tested (see Section 5.3.1), no method was able to balance complexity and accuracy sufficiently so as to justify using it instead of a simple linear regression, especially when it came to all data. Thus, a linear regression was fit to the data and the resulting slope $\alpha = 0.28$ was then integrated in the form drag parameterization (equation 25), and through the atmospheric to oceanic drag ratio $C_{da}/C_{dw} = 0.2$, also in equation 35. The choice of α is further supported by by Fig. 5.1, for which the slope is the same.

Notably, the sea ice thickness–form drag coefficient relation implemented as equation 35 is not able to fully represent the range of expected form drag coefficients (see Fig. 5.2). As a result, a sensitivity study with the doubled $\alpha = 0.56$ was conducted to increase the impact of obstacle form drag. As shown in Fig. 4.6 of Chapter 4, form drag due to obtsacles has a significant contribution to the total drag coefficient; whereas based on the modelled distribution of drag coefficients in Fig. 5.3, $\alpha = 0.28$ is unable to generate obstacle form drag coefficients of the same magnitude as the estimates from observations (Figs. 4.5, B5, B6). The reason for the underestimation has to do with most of the form drag coefficient values being retrieved from areas in the central and eastern Arctic that are over thin sea ice, as such the slope of the regression is weighed down. Thus, here we propose an alternative method of assigning $\alpha = 0.56$ that can selectively weigh the high form drag coefficient outliers higher than the lower ones. Given this prerequisite is achieved, a SIT-based integration should be able to model drag coefficient distribution that agree with observation estimates (as partly demonstrated in Fig. 5.5D).

RQ6 Is the impact of form drag significant within a model simulation spanning a period of 3 years? And if not, is more time needed to observe notable changes?

Through our coupled regional atmosphere-ocean-sea ice model analysis over the 2019-2021 period, we have found reasonable changes that were small in magnitude. The changes observed could be explained, and said explanations could then be verified through sensitivity studies. However, modelling studies that span longer time periods show that form drag can have a relatively large impact on sea ice properties (e.g., Tremblay et al. 1997; Tsamados et al. 2014; Sterlin et al. 2023). While a short run period and lack of variation in initial conditions likely both played a role, two main sensitivity studies were conducted to address why the impact of form drag was small in magnitude within the three-year time period. The first was the doubling of the α parameter which determines the impact of obstacle form drag. The working hypothesis when seeing the initial results with $\alpha = 0.28$ and comparing it to the drag coefficient estimate maps of Chapter 4, was that the obstacle form drag contribution was underestimated. Interestingly, though the drag coefficient distribution (Fig. 5.5D) agreed better with the drag coefficient estimates from observations, the impact was still fully contained within a $\pm 25\%$ range for both SIT (Fig. 5.5C) and drift velocity percent differences (Fig. C2). The next sensitivity study was meant to investigate the effects of the atmosphere and ocean separately, by dividing the model run with the new form drag implementation at both the sea ice–atmosphere and sea ice–ocean interfaces into two that each have the implementation at only one of the two interfaces. In these runs, the opposing interface would then be as in the standard run, with constant drag Arctic-wide. The hypothesis behind this study was that since the form drag implementation is paralleled, if the atmospheric and oceanic drag have opposing effects (as is the case for drift in mesoscale modelling studies (e.g., Birnbaum et al. 2002; Lüpkes et al. 2011)), the resulting differences would be smaller. In this sensitivity study (described in detail in Section 5.4.4 with results discussed in Section 5.5.3), we found that even on an Arctic-wide scale in a model that simulates currents, atmospheric drag typically accelerates sea ice motion whereas oceanic drag decelerates it (see Fig. 5.7). The differences in SIT (Fig. 5.6), are smaller but still opposite. As a result, the hypothesis of the second sensitivity study proved to be true. In reality, though over large spatial scales both pressure ridges and floe edges are relevant for both the sea ice–atmosphere and sea ice–ocean momentum exchanges, there are other sources of form drag, e.g., meltpond edges, rubble fields, hummocks and snow dunes that are not present at both interfaces. However, to a certain extent, it holds true that the two sources of form drag offset the impact of each other. For example in the case of the the thick high obstacle form drag MYI north of Canadian Archipelago and Greenland, in addition to internal forces and the proximity to the coast, this opposing effect is likely another reason why it is so slow relative to ice floes close to the ice edge. Nevertheless, the mean absolute differences observed in all our comparison as well as sensitivity tests, save for the MIZ area, are on the order of mm/sec for sea ice drift velocities and cm for SIT. Thus, even

with the opposing effects of atmospheric and ocean form drag taken into account, it is likely that no prominent change was realized within a short time span of 3 years and a longer model run is needed.

6.3 Outlook

With regard to Chapter 3, thin sea ice anomalies were identified over the Maud Rise area in the 11-year SMOS SIT time series (Fig. 3.2). There are many studies that focus on the 1974-1976 and 2016-2017 polynya events (e.g., Carsey 1980; Cheon et al. 2019; Campbell et al. 2019; Francis et al. 2019), but comparatively little attention is given to the thin sea ice anomalies such as those presented in Fig. 3.7. Studies comparing surface winds, snowfall, cloudiness as well as ocean currents, temperature and salinity to the sea ice conditions on top of Maud Rise in the years these anomalies take place can all contribute to our understanding of when and how the polynya occurs. With such studies, we can isolate cases when there are sea ice anomalies, and see what was missing in order for the anomaly to pass the tipping point and transition into a polynya.

A study by Zhou et al. (2022) builds on Mchedlishvili et al. (2022) being able to identify polynya-favourable conditions in 2016 and 2017 roughly a month ahead of each event in the form of low SIT anomalies, to being able to predict them up to 4 months ahead of opening. They do so by accounting for thermodynamics as well as computing surface stresses at both the sea ice–atmosphere and sea ice-ocean interfaces using in-situ and reanalysis data for the ocean and atmosphere. Thus, accounting for both thermodynamic as well dynamic preconditioning, as concluded in Chapter 3, helps to better predict polynya occurrences months ahead of their formation. As we refine our ability to predict the Weddell Sea Polynya, we can better plan in-situ measurement campaigns to match these time periods. This will aid us in improving our understanding of the physical processes occurring in the anomalous region on top of Maud Rise.

For Chapter 4, naturally the best step forward would be better coverage and higher resolution, which, with the advancing field of satellite altimetry, is likely to happen in the near-future. For the present, we need to make do with the satellite measurements that we have. Efforts in making the IS2 retrieval more ridge-focused by relaxing the requirement of a 150 signal photons needed to reduce vertical uncertainties and focusing on the 99th percentile of the photon distributions to isolate ridges have been made (Duncan et al. 2022). In addition, IS2 can be used in tandem with other satellite data products able to infer sea ice roughness like the Multi-angle Imaging SpectroRadiometer onboard Terra (Johnson et al. 2022) and the C-band Advanced Scatterometer on-board MetOp-C (Petty et al. 2017). With such modifications to the drag coefficient retrieval, it is likely that more ridges will be detected and more realistic drag coefficients will be retrieved. However, even with the modified ridge-detection algorithm of Duncan et al. 2022 and the use of additional satellites, there is currently no method able to fully resolve the pan-Arctic distribution of pressure ridges (Ricker et al. 2023). As a result, airborne surveys across the Arctic ice pack, over different ice regimes, is crucial for a better roughness and drag coefficient assessment of the Arctic.

Since the publication of Mchedlishvili et al. (2023) (Chapter 4) and the first monthly pan-Arctic drag coefficient assessment, further development followed. A study by Zhang et al. (2024) created a form drag coefficient time series spanning over 20 years by also incorporating OIB ATM as well as ASCAT carried by ESA's MetOp satellites and the SeaWinds scatterometer onboard NASA's QuikSCAT satellite. For this task they used sea ice surface roughness derived from the Ice, Cloud and land Elevation Satellite (ICESat) and IS2 sea ice heights and linked it with the OIB-based form drag coefficients extrapolated via QSCAT and ASCAT. Thus, building on the methods by Petty et al. (2017) as well as Mchedlishvili et al. (2023), Zhang et al. (2024) created a longer time series that is able to better assess the inter-annual spatiotemporal evolution in drag over longer time scales. In addition, future works in further extending this data set should give us a better understanding of how the variable drag distribution across the Arctic ice pack is evolving in a changing climate.

Lastly in Chapter 5 we took the monthly pan-Arctic neutral atmospheric form drag coefficient estimate data set and implemented it into a coupled regional atmosphere-ocean-sea ice model using sea ice thickness as proxy. As mentioned in 6.2.2, a longer model run would be better suited in revealing significant changes that likely need more than 3 years to materialize. Model studies with variable drag implemented that have found significant changes in sea ice properties have been run for a period more than 20 years (Tsamados et al. 2014; Sterlin et al. 2023) or at least 10 (Tremblay et al. 1997). While the balancing effects of atmospheric and oceanic drag would likely limit the magnitude of these changes in a fully coupled model as our results have shown, given that all changes were small in magnitude including the sensitivity runs (Figs. 5.6 and 5.7), the briefness of the model run is likely still relevant. Additionally, since the correlation of $r = 0.58$ is not ideal for representing all possible obstacle form drag coefficient values as elaborated on in Sections 5.4.3 and 6.2.2, it is likely better to link obstacle form drag coefficients with roughness or ridging if the model includes or calculates any such quantity.

A Appendix to Chapter 3

In Fig. A1 we show the 2016 polynya time series in the same format as the 2017 polynya and 2018 ice thinning anomaly.

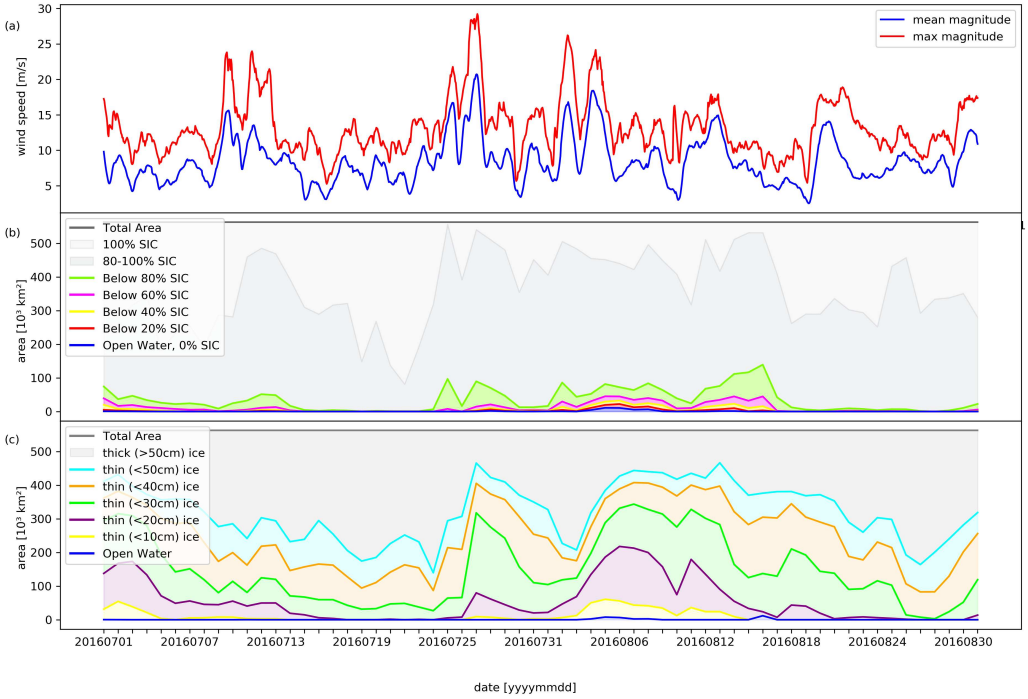

Figure A1: Same format as Fig. 3.5 for July–August 2016. See Fig. 3.5 caption for specifications.

MODIS comparison

In Fig. A2 we show the Weddell Sea polynya of 2017 and the sea ice thinning anomaly of 2018 as seen by the Moderate Resolution Imaging Spectroradiometer (MODIS) instrument onboard the TERRA satellite (processed and made available through NASA Worldview, `https://worldview.earthdata.nasa.gov/`).

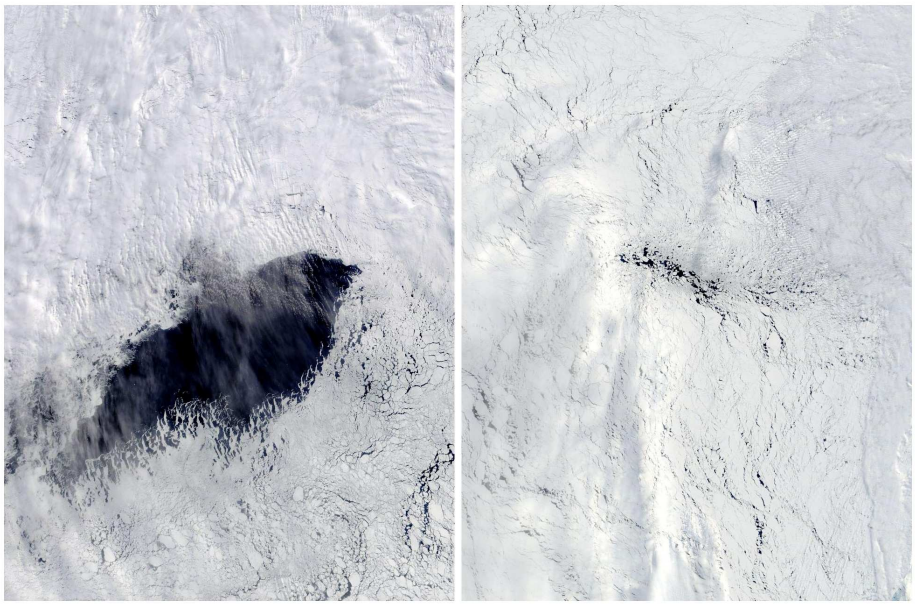

Figure A2: Left: MODIS image of the Weddell Sea polynya (25 September 2017). Right: MODIS image of the sea ice anomaly of 2018 (8 September 2018). Area viewed in both images is the same and chosen by assigning the bottom left corner and top right corner to chosen coordinates upon selection: 67°S, 1°E and 61°S, 8°W, respectively (images from NASA Worldview, `https://worldview.earthdata.nasa.gov/`).

B Appendix to Chapter 4

Using our methods, we obtain a sufficient amount of data to mostly fill a polar-stereographic 25 km grid via bucket resampling for each month to produce a pan-Arctic monthly total neutral atmospheric drag coefficient analysis. On account of IS2 's near-polar orbit the data density is highest around the pole hole and wanes at lower latitudes (see Fig. B1A). As a result, the regional drag coefficient estimates at higher latitudes are more representative of the time periods shown in Figs. 4.3, 4.5, B5 and B6, whereas those at lower latitudes are computed with fewer height measurements (often just a few select days). In other words, rather than a temporal mean of surface topography, it is a data set that is sewn together with the best representation of the temporal mean near the pole hole. However, mind that we do not see any discontinuities due to variable sampling in the final atmosphere-ice drag maps. In Fig. B1B one can observe the typical spacing between ATL07 height estimates, which is typically around around ∼11-13 m but can be higher due to dark surfaces over which up to 200 m might be needed to collect the sufficient signal photons Kwok et al. 2021b. Similarly, clouds can also increase the spacing as no measurements are retrieved beneath them.

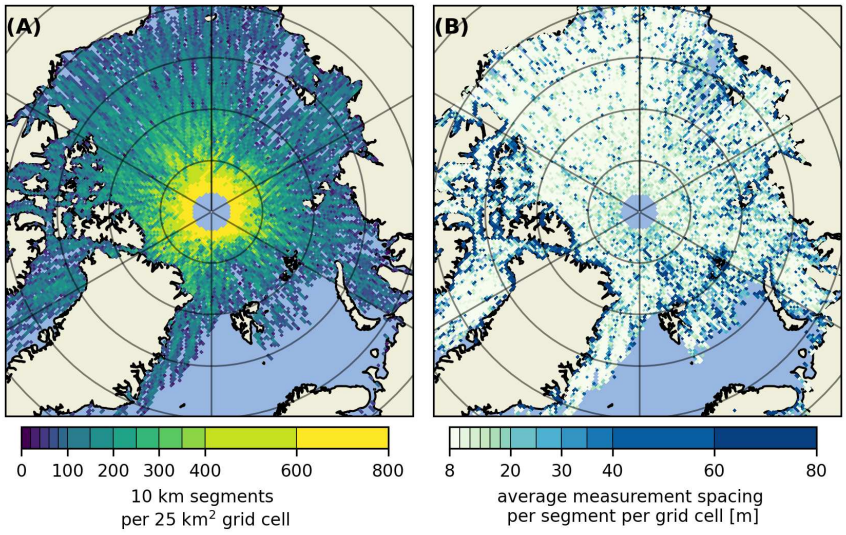

Figure B1: The data distribution for the 04.2019 drag coefficient map given as the number of 10 km segments from all strong beams per 25 km^2 grid cell (A). The average point spacing within each 10 km segment per 25 km^2 grid cell (B).

B APPENDIX TO CHAPTER 4

For a comparison between different beams, all of which we combine in our final data product, we refer the reader to Fig. B2. Inter-beam variability due to different range biases is present and was reported on by the IS2 Project Science Office (PSO) in their preliminary analysis e.g., Bagnardi et al. 2021. In addition, there is the 3.3 km inter-beam spacing which suggests ridges and snow features captured by one beam might not be captured by the rest. At first look Fig. B2D, the inter-beam standard deviation, suggests more variability in the MYI rough ice areas but that is because the OIB ATM scaling factor applied to all data scales up all drag coefficients linearly, and hence the variability is increased in those areas as well.

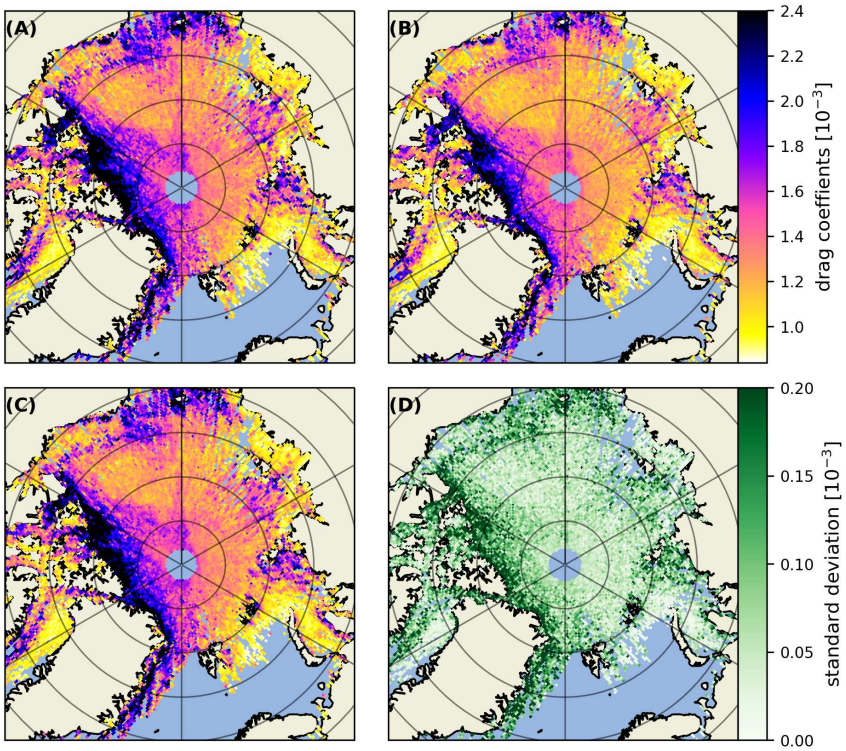

Figure B2: Comparison between drag coefficient estimates (sea ice form drag + skin drag) computed from the 1st (A) 2nd (B) and 3rd (C) strong beams as well as the standard deviation between them (D). All three examples have the OIB ATM scaling factor applied.

B APPENDIX TO CHAPTER 4

Though it is not the subject of this study, we also briefly looked at the relation between the parameters extracted from IS2 ATL07 which were used in equation 11, with respect to each other as well as the form drag due to obstacles derived from them. We corroborate Brenner et al. 2021, who looked at the keels instead of sails of ridges, that indeed obstacle height and spacing exhibit a negative correlation. Though not always associated (Tin et al. 2003), sails and keels are predominantly spatially coincident and are therefore expected to exhibit proportional heights and depths and similar spacing. When looking at the non-linear cutoff at 200 m for ridge spacing that can be seen both in Fig. B3B and Fig. B3C, it is important to once again consider the "smoothing" and low obstacle detection rates (Ricker et al. 2023) of IS2 ATL07, that are likely the cause of average obstacle spacing not being any lower than what is observed.

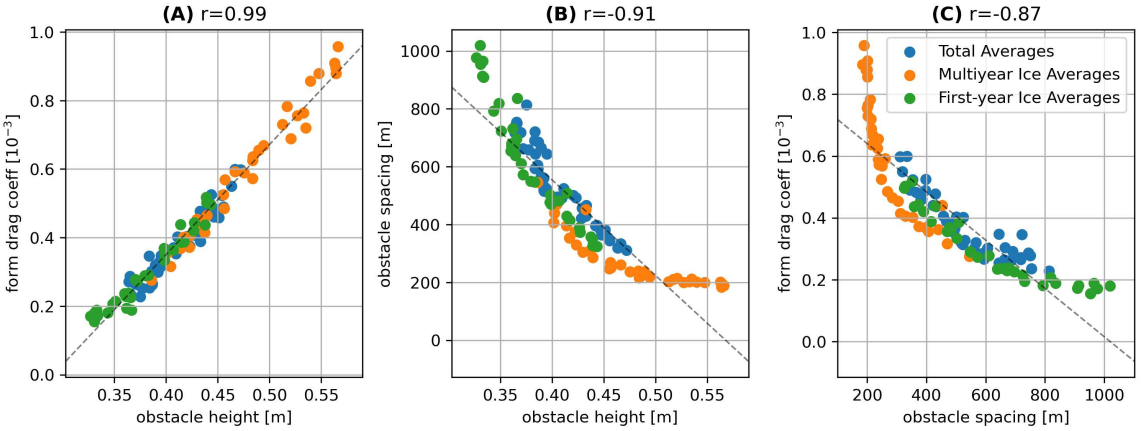

Figure B3: Scatter plots between (A) obstacle height and form drag coefficient, (B) obstacle height and obstacle spacing and (C) obstacle spacing and form drag coefficient. All values are taken from Fig. 4.6, such that blue dots represent the monthly pan-Arctic averages, orange dots represent monthly MYI averages and green dots represent monthly FYI averages.

Here (Fig. B4) we also show the sensitivity studies done with different coefficient of resistance c_w formulations.

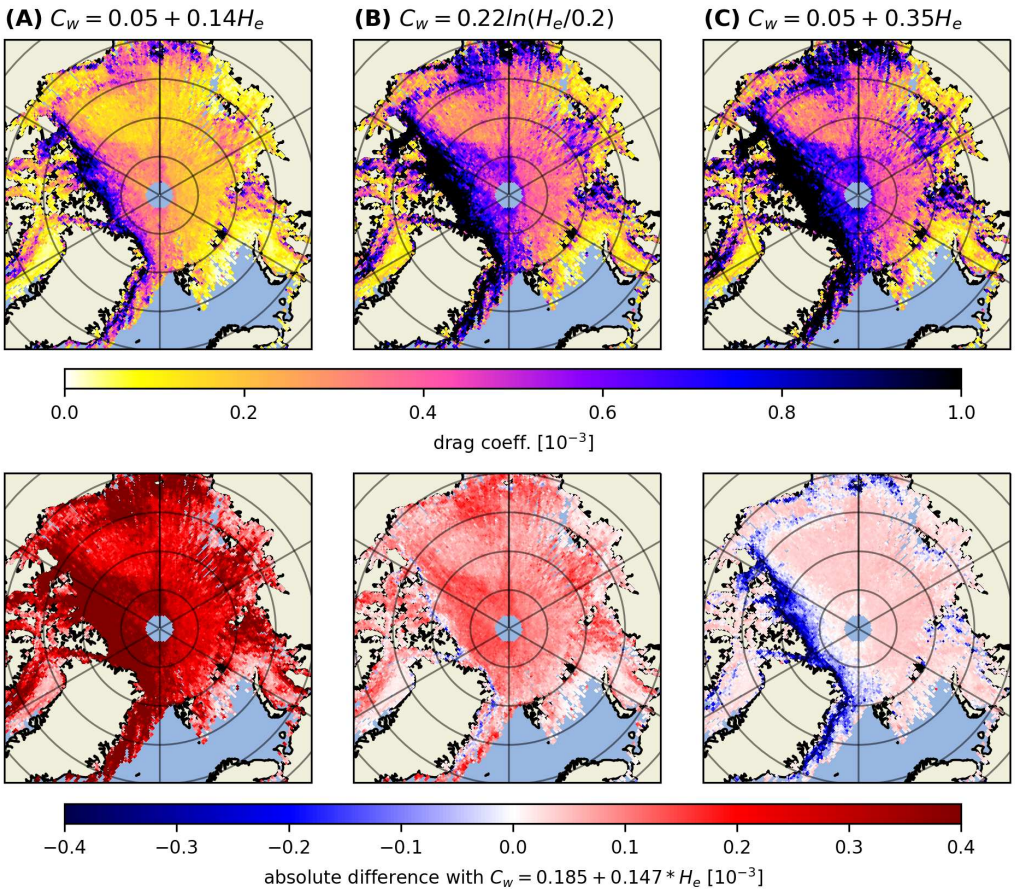

Figure B4: Obstacle form drag coefficient monthly maps for April 2019 subdivided into columns labelled by the coefficient of resistance formulation used. (A) uses $c_w = 0.05 + 0.14H_e$ (Garbrecht et al. 2002), (B) uses $c_w = 0.22\ln(H_e/0.2)$ as suggested by Garbrecht et al. 1999 with all H_e values below 0.5 set to 0.2 to avoid very low and negative values, and (C) uses $c_w = 0.05 + 0.35H_e$ from Ropers 2013 with an adjusted aerodynamic roughness length of $z_0 = 10 \cdot 10^{-7}$ m. The second row shows the absolute difference between drag coefficients for each of these c_w formulations as compared to the one used in this study: $c_w = 0.185 + 0.147H_e$ with the modified coefficients from Garbrecht et al. 2002.)

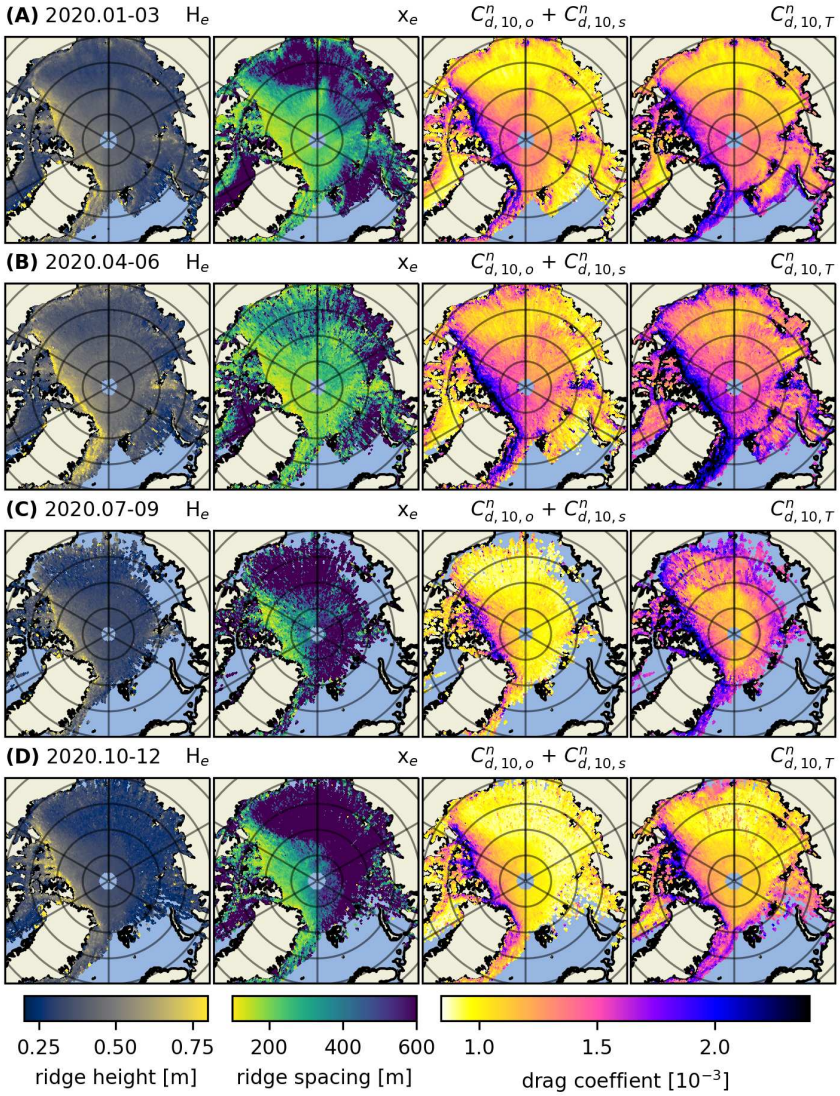

Figure B5: Same as Figure 4.5 but for 2020. Obstacle spacing (x_e), drag coefficient as a sum of sea ice skin drag and form drag due to obstacles ($C^n_{d,10,o} + C^n_{d,10,s}$), total drag coefficient as a sum of the sea ice skin drag, form drag due to obstacles and floe edges and open water drag ($C^n_{d,10,T}$)

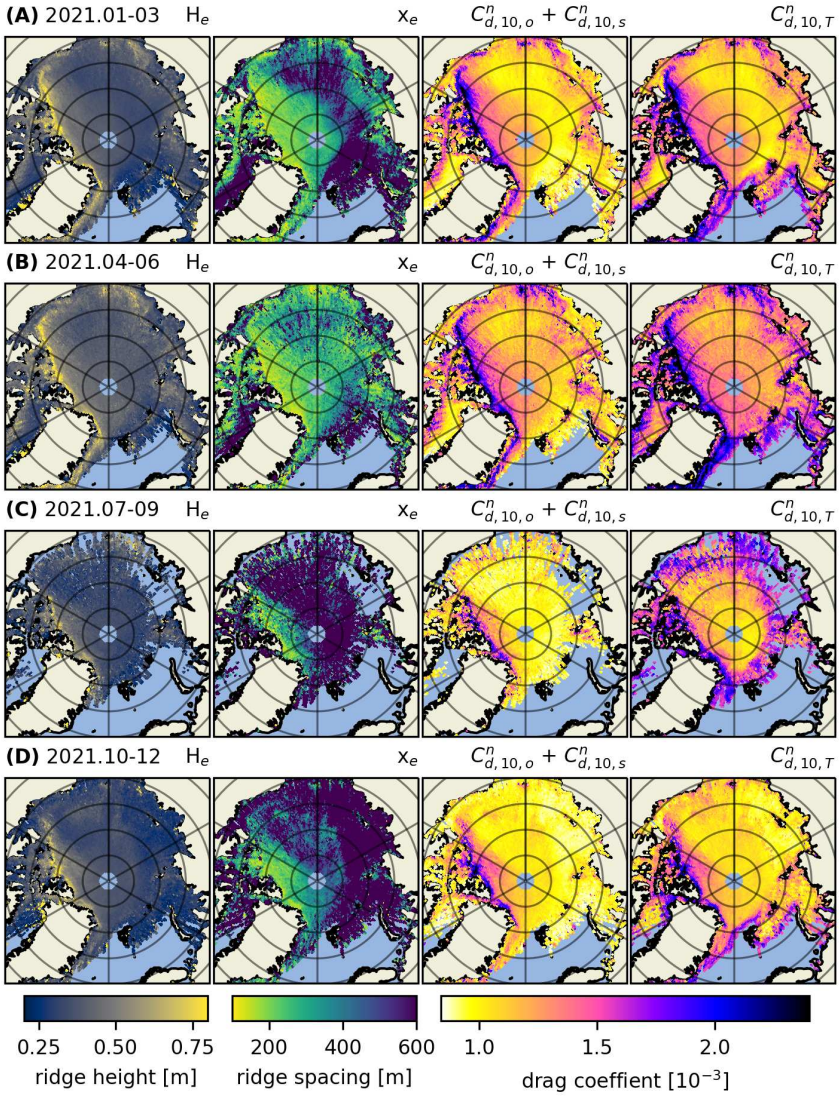

Figure B6: Same as Figure 4.5 but for 2021. Obstacle spacing (x_e), drag coefficient as a sum of sea ice skin drag and form drag due to obstacles ($C^n_{d,10,o} + C^n_{d,10,s}$), total drag coefficient as a sum of the sea ice skin drag, form drag due to obstacles and floe edges and open water drag ($C^n_{d,10,T}$)

B APPENDIX TO CHAPTER 4

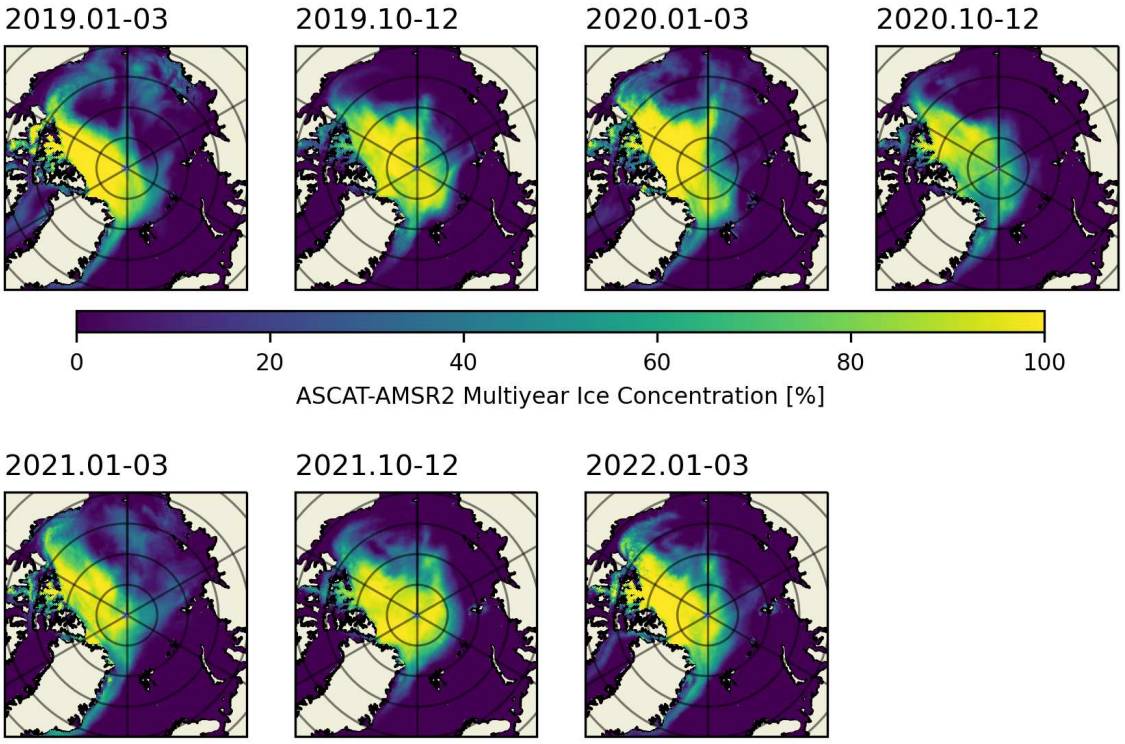

Figure B7: ASCAT-AMRSR2 Multiyear Ice Concentration winter three month averages for the period 2019.01-2022.03.

B APPENDIX TO CHAPTER 4

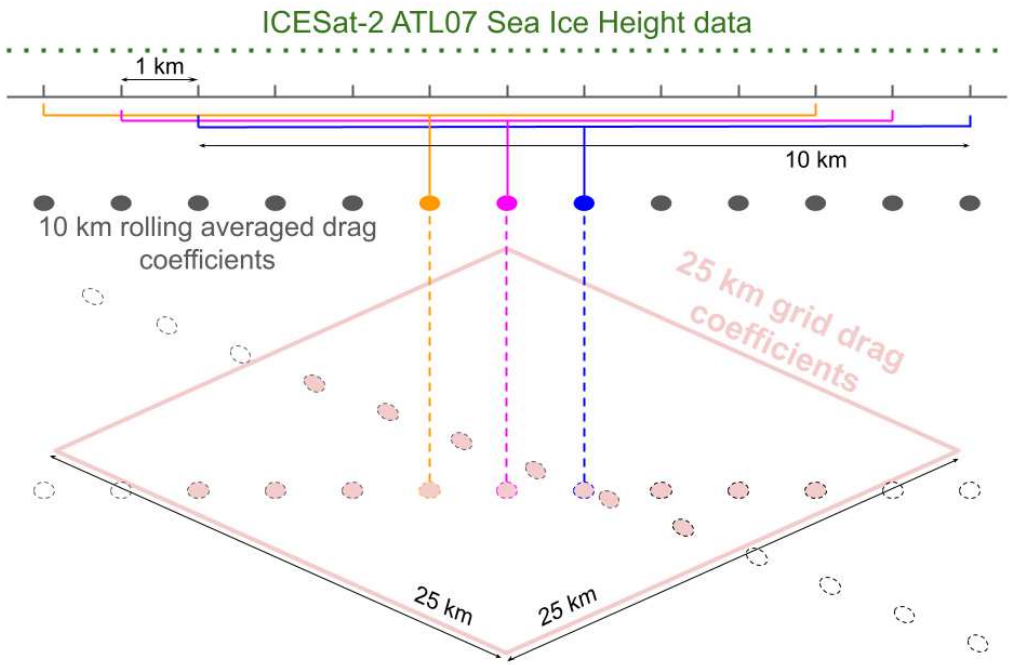

Figure B8: Above is a schematic showing the data processing steps. The green dotted line indicates the ATL07 sea ice height data. The grey line shows 1 km increments and the orange, pink and blue segments show typical 10 km windows over which the obstacle height and spacing are averaged (using which the drag coefficient is then calculated according to equation 11: depicted in the schematic as segments turning into dots). The resulting 10 km average drag coefficients are then gridded (e.g., the orange, pink and blue dots from the given ATL07 track are projected onto a Polar Stereographic grid, along with other values from the same track as well as those from other tracks from the same month). Finally, the values are bucket resampled to give a monthly 25 km gridded drag coefficient map (where an individual grid cell is highlighted in light red in the schametic [not to scale]).

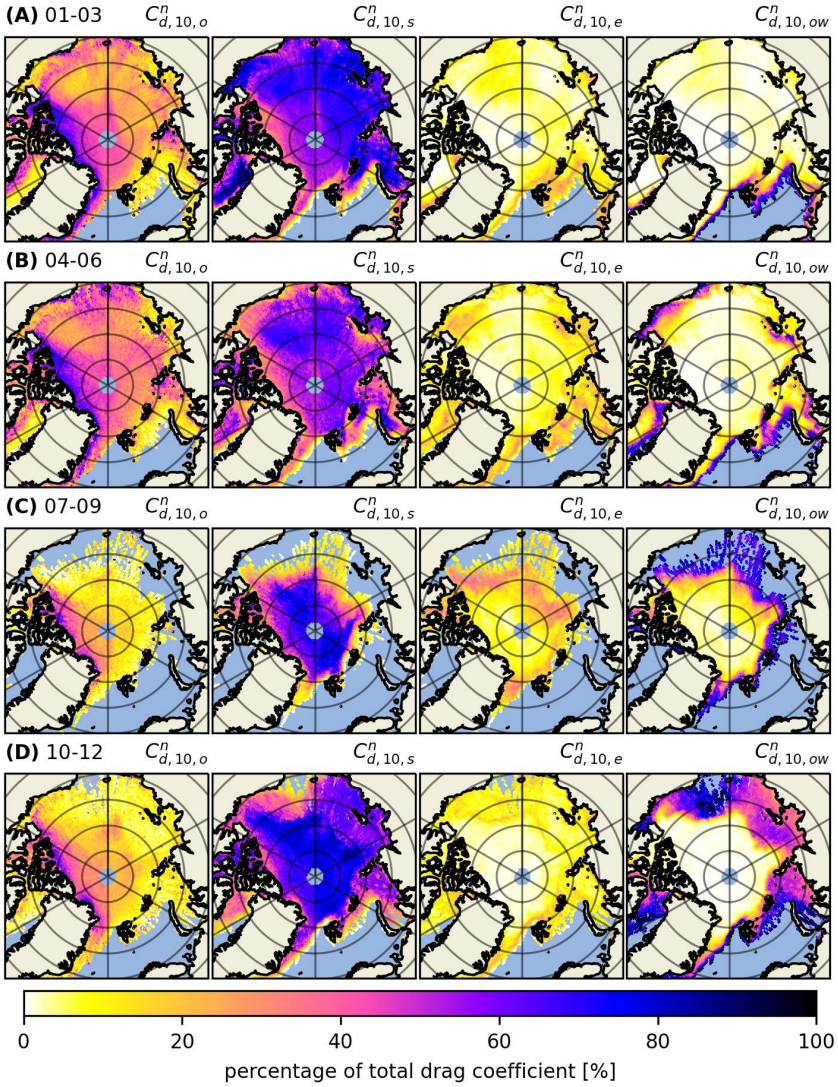

Figure B9: The components of the total drag coefficient given as percentages where the columns are obstacle form drag ($C^n_{d,10,o}$), sea ice skin drag ($C^n_{d,10,s}$), floe edge form drag ($C^n_{d,10,e}$) and open water skin drag ($C^n_{d,10,ow}$), respectively. These 3-monthly averages are from the year 2019 and depict the contribution of the 4 components of the total drag coefficient $C^n_{d,10,T}$ (col. 4 in Fig 4.5).

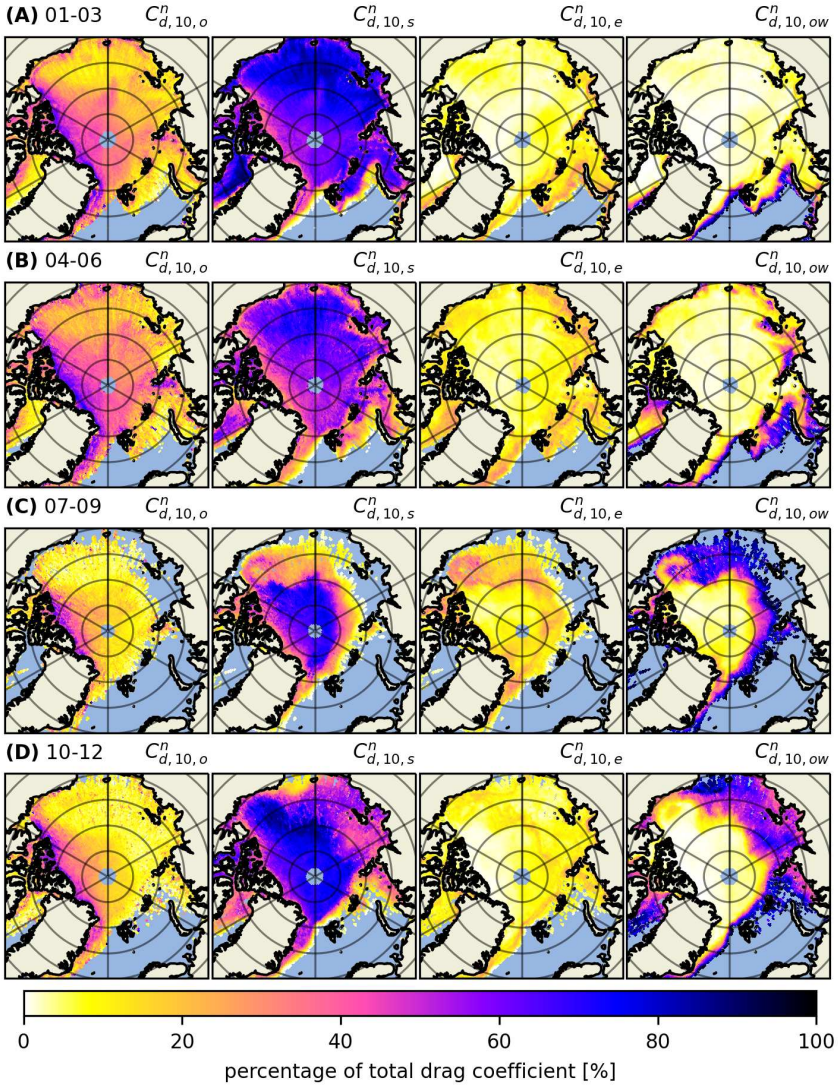

Figure B10: The components of the total drag coefficient given as percentages where the columns are obstacle form drag ($C^n_{d,10,o}$), sea ice skin drag ($C^n_{d,10,s}$), floe edge form drag ($C^n_{d,10,e}$) and open water skin drag ($C^n_{d,10,ow}$), respectively. These 3-monthly averages are from the year 2020 and depict the contribution of the 4 components of the total drag coefficient $C^n_{d,10,T}$ (col. 4 in Fig B5).

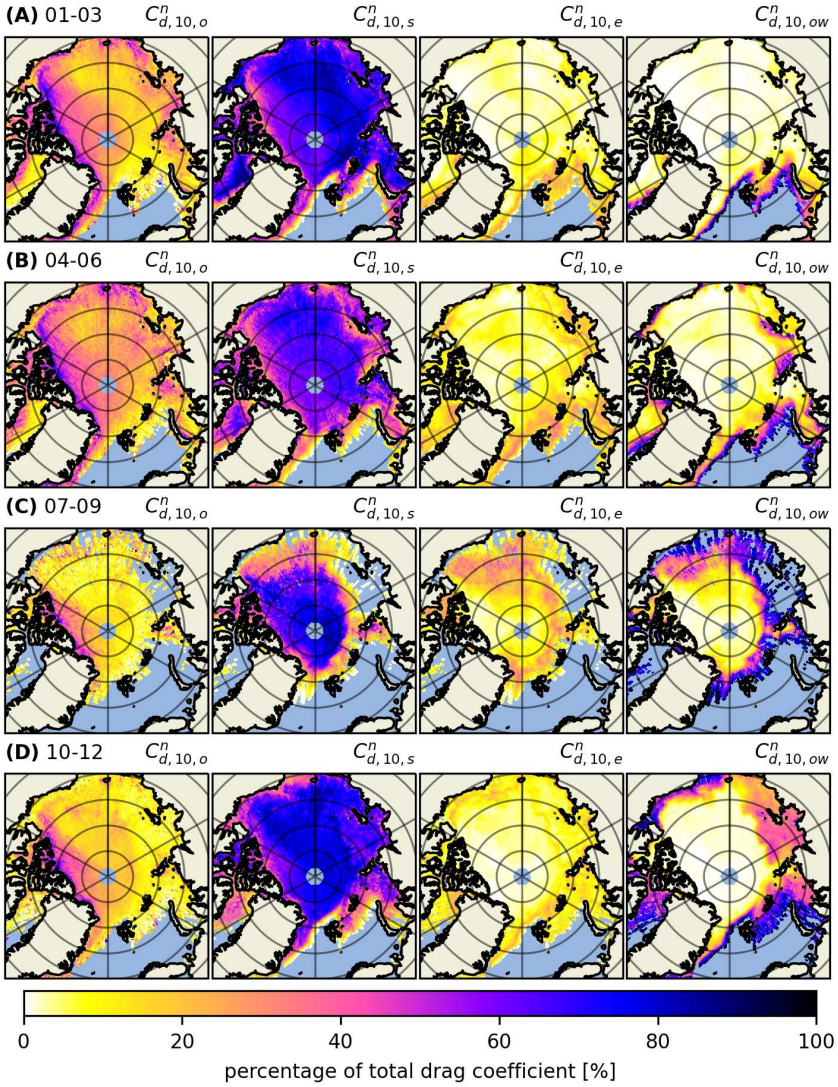

Figure B11: The components of the total drag coefficient given as percentages where the columns are obstacle form drag ($C^n_{d,10,o}$), sea ice skin drag ($C^n_{d,10,s}$), floe edge form drag ($C^n_{d,10,e}$) and open water skin drag ($C^n_{d,10,ow}$), respectively. These 3-monthly averages are from the year 2021 and depict the contribution of the 4 components of the total drag coefficient $C^n_{d,10,T}$ (col. 4 in Fig B6).

C Appendix to Chapter 5

Fig. C1 shows SIC 3-month averages over the 2019-2021 model study period. Unlike other parameters that were masked such that values below 15% SIC were omitted, here all SIC values outputted by the model are included.

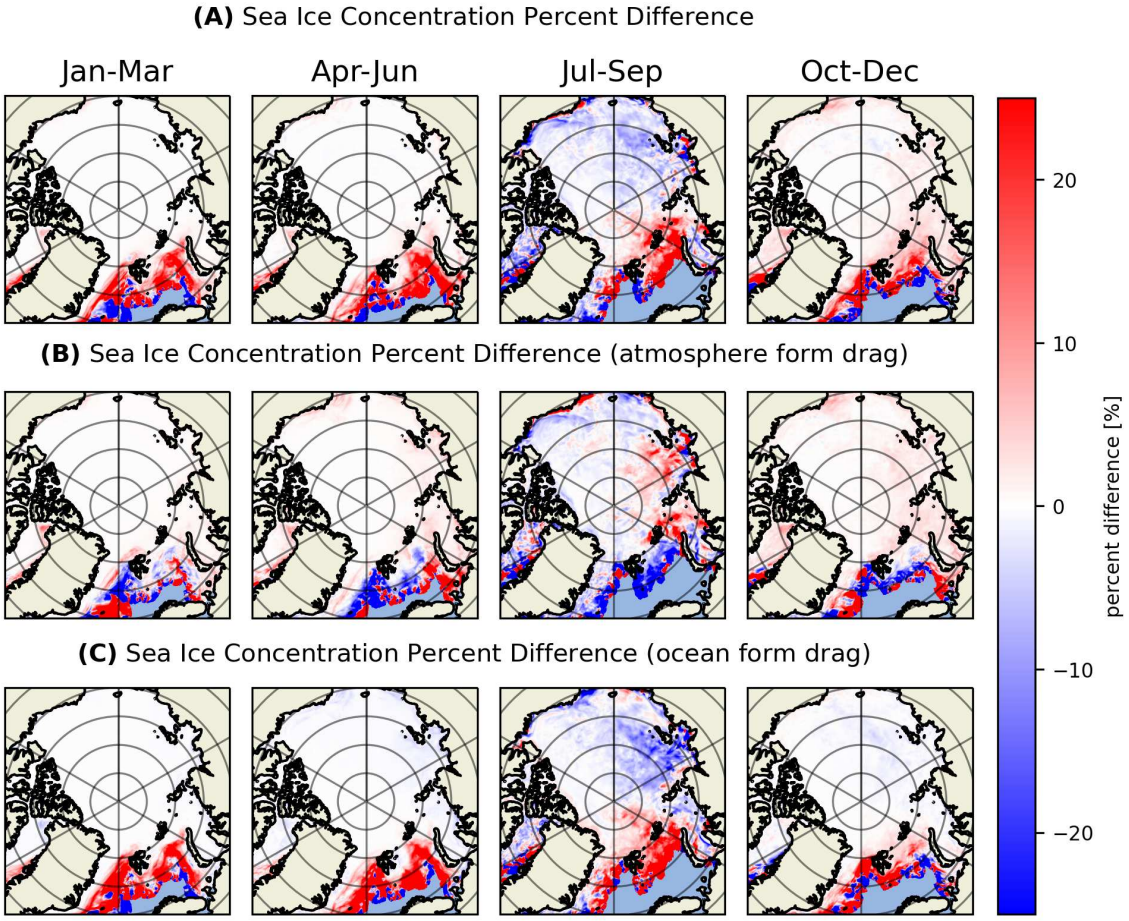

Figure C1: 3-month averaged percent difference maps for New Form Drag Run (A), Atmospheric Form Drag Run (B) and Oceanic Form Drag Run (C) with respect to the Standard Drag Run, for the periods January to March, April to June, July to September and October to December (averaged over 2019-2021)

Fig. C2 is an analogue of Fig. 5.5B-C but for sea ice drift velocity.

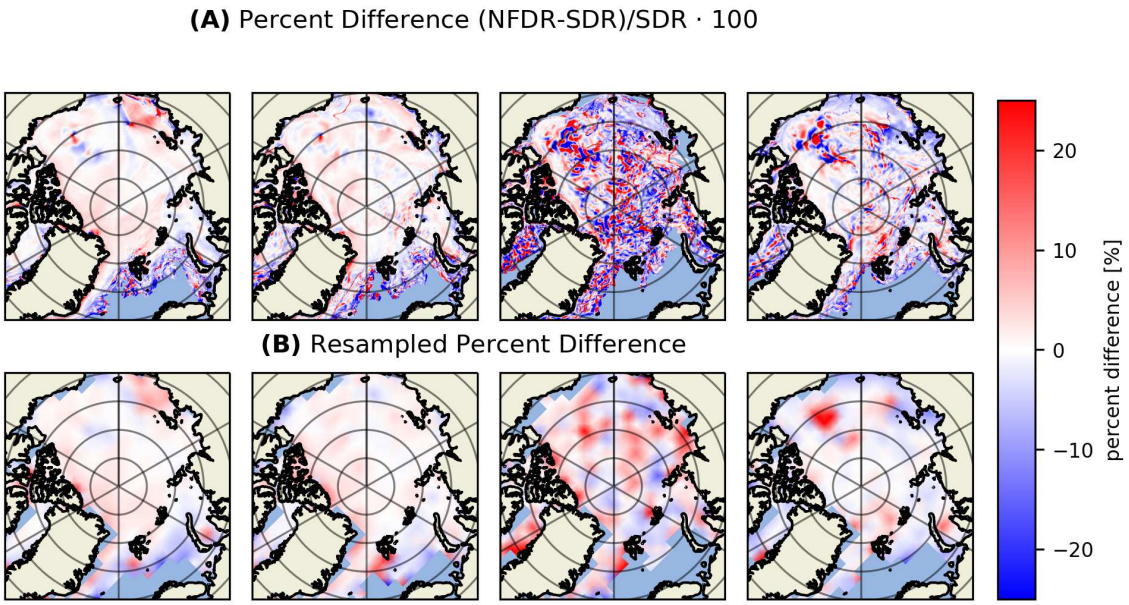

Figure C2: (A): 3-month averaged New Form Drag Run (with distinct α values) sea ice drift percent differences for $\alpha = 0.56$ with respect to the Standard Drag Run for the periods January to March, April to June, July to September and October to December (averaged over 2019-2021). (B): the percent difference maps are then bucket resampled to better depict large spatial differences.

D Science Communication Through Media

While scientists from all fields benefit from educating the public about what they do, in the short-term, science communication by environmental scientists is needed to mitigate potential climate risks. From the perspective of a polar remote sensing scientist who can verify the effects of Arctic Amplification (Arctic Amplification (AA)) from remote sensing data, it is necessary for them to pass this information on to the public. In this way, a more informed public can elect policy-makers that can work with scientists to reduce humanity's carbon footprint, and thereby mitigate climate change. While the issue of mitigating climate change is by no means trivial and requires a lengthy discussion of its own, here I aim to discuss only the first step of this process, in which environmental scientists share their knowledge with people that are not experts in their respective field. Strictly speaking, the transfer of scientific knowledge commonly occurs through published papers, which serve to advance the scientific field and facilitate the exchange of knowledge among scientists within the same or related disciplines. In this way, scientists can work together to advance their collective understanding of natural phenomena. In addition, many scientists work at institutions and universities that are actively engaged in education of students. However, neither of these two processes help spread the scientific knowledge to the public at large, for even if a given paper is openly accessible, it is often too complex for non-experts to understand. In addition, there is no incentive for people to comprehend the complex material. Therein lies the challenge of science communication, because the material being communicated must be attractive or impressive to garner attention, it must be simple for everyone to understand, but it must also hold true to the actual phenomena being explained. Such a balance is hard to achieve but the inability to meet these prerequisites will results in either nobody wanting to engage, nobody being able to engage, or the science being communicated becoming downright inaccurate as a result of oversimplification, respectively.

Figure D1: Early career scientists including myself (center) attending a course held during the International Summer School "Communicating Science" in Berlin from 2 to 6 August 2021 (Source: Wissenschaft im Dialog / Alexander von Humboldt Stiftung).

During my PhD I had the pleasure of attending the International Summer School "Communicating Science" that took place 2 to 6 August 2021 after being selected from a wide array of applicants that applied via a video that was meant to introduce one's self and the research they do. The international summer school was organized by the Alexander von Humboldt Foundation and Wissenschaft im Dialog and was sponsored by the Federal Ministry of Education and Research of Germany. The participants, with the help of the invited speakers and organizers, would then go on to formulate and submit the first draft of their joint recommendations on the future of science communication to Dr Clemens Escher from the German Federal Ministry of Education and Research (Siewert 2021). Throughout the summer school, I learned different platforms for presenting research in a clear and entertaining way, the importance of strategic communication with various stakeholders, as well as the ethics and intercultural aspects of science communication as a whole. Most importantly for my immediate future, it gave me the motivation to start my own science communication project.

Thus, under the pseudonym "The Half Drawn Man" (see `youtube.com/@thehalfdrawnman9270`), I initially embarked on spreading awareness about AA. After all, AA is the overarching topic of the collaborative research initiative *Arctic Amplification: Climate Relevant Atmospheric and Surface Processes and Feedback Mechanisms (AC^3)* which I am a part of, and it is also by extension related

to my PhD project. In a three-part YouTube video series I tried to create material that is engaging, accessible and scientifically correct yet simplified. In addition, I created other videos related to Arctic climate change as well as sea ice remote sensing. In total this project lasted for nearly half a year, and during this time I produced 9 videos, 7 of which were about or related to polar environmental sciences. Here I would like to briefly summarize my successes and failures and what knowledge I have gained as a result of this endeavour, while also briefly covering other more successful science communication projects.

Engagement

For my material, I chose video as a format and YouTube as a platform. As such, I needed to make the videos as engaging as possible since YouTube's underlying algorithm analyzes the content of videos, and based on tags, descriptions as well as viewer engagement, recommends them to more viewers. Moreover, it was critical to raise awareness of my videos which I accomplished primarily through colleagues, friends and family and thereafter by catering to a growing audience of interested viewers. While YouTube is used by a large part of the world population, the algorithm will only outright recommend the content to an audience that occasionally consumes scientific media. Similarly, it will only be recommended to an audience that consumes at least some of their YouTube content in the language the video is in. Despite these two filters, this still allows for a relatively large audience, especially when producing videos in English. In particular, relative to science communication initiatives such as those organized in person, a permanently uploaded video on a platform as commonly used as YouTube can garner a lot more attention for far less organizational costs. I personally achieved a maximum of 2000 views on a single video throughout the period I was active, incidentally this was the case for the final video in the three-part series about AA. Naturally, those who have made this into their careers, i.e. science communicators with a large enough following on YouTube, can easily reach millions of views with a pre-existing subscribed audience. An example of a highly successful science communication-oriented YouTube channel is Kurzgesagt, a German-made animation and design studio founded by Philipp Dettmer (see `kurzgesagt.org`). While the channel has 21.9 million subscribers and often reaches millions of views per video, their animation quality is high enough to require multiple employees working at different stages in the video production chain to produce a single video that takes roughly 1200 hours to complete (see `youtube.com/watch?v=uFk0mgljtns`). The effort put in pays off however, and the company has tackled complex topics like quantum physics, string theory, cell biology and climate change using minimalist animation and clever simplifications of complex scientific phenomena, effectively making science consumable to millions of people that do not have a scientific expertise. Though institutions and universities usually have some kind of science communication initiative, it is unlikely that they can compete with a dedicated company like Kurzgesagt when it comes to disseminating their science among the public.

The YouTube algorithm recommends content based on interests as mentioned before, therefore the more specific the content on a channel is, the less likely it is to get a large following. That is why Kurzgesagt doesn't restrict its science output to a given scientific field and instead has videos that are consumed by an audience that is, in general, to some degree interested in science. Moreover, a principle problem with an initiative by an individual scientist, or even that of whole institutions, is revealed: often the science communication from these sources are too specific for most people. The YouTube channel hosted by Simon Clark (see `simonoxfphys.com`), is a good example of a climate science-oriented channel. With 514 thousand subscribers, it is lower than that of Kurzgesagt and therefore the content reaches far less viewers. This is fairly clear, not only because the former is a team of two and the latter a fully-fledged company with far more employees and higher production value but also, in part, due to the problem that the more general the topics covered are, the higher the number of potential viewers. An exception to this rule is if a given topic is trending, however then a new issue arises: the need for creators to cater to the trends of the moment rather than a logical progression of videos that might be necessary to communicate complex scientific phenomena.

At a 192 subscribers, my channel that was born out of effort put in during evenings when I was not actively working on my PhD project, can not compete with individuals who have made this their job, let alone whole companies. I as an individual had to go through a lengthy video production chain where I played the main part at every stage. Namely,

1. Producing the script after a literature study of relevant scientific publications
2. Deciding how what I will be explaining is illustrated
3. Producing the art for the illustrations
4. Combining all hand-drawn illustrations and narration into a video while also adding components like music from open-access repositories

Presumably, the above-mentioned chain would be shorter if instead of illustrations I simply filmed myself explaining the concepts, but as I have a proficiency in drawing, it made sense to use it in order to potentially increase the number of viewers as a result of producing more unique content. In addition, the role of visual illustrations has been shown to play an important role in knowledge formation of learners (Evagorou et al. 2015). Some of the noteworthy strategies that I found to be successful in engaging with the audience are as follows:

- Spreading news about the videos through social media
- Slowing down the narration and enunciating individual words
- Simplifying complex scientific phenomena using analogies, diagrams and animations
- Using popular culture references in the art along with the science
- Mixing in comedy with scientific explanations to keep the videos light-hearted yet informative

Simplification and Accuracy

The fine balance between simple and accurate is hard to achieve, often science communication must include simplifications, perhaps better defined as inaccurate models, to get the message across. Unlike scientific papers, the communicator cannot depend on the target audience having the prerequisite knowledge to understand what they are explaining. Building the knowledge up from scratch for the this audience can be achieved in a book or maybe a series of courses, but that is what differentiates science communication and science education; how much time and effort is required to understand the material. Thus, science communication needs to convey science in such a way that it takes a reasonable amount of time to understand the science in the moment it is being communicated, and as mentioned before, it needs to be simple enough for a large majority of the public to clearly understand without having any prior knowledge on the subject.

Like climate modelling wherein no model is truly as complex as the actual climate system, so are basic explanations in science communication lacking information on the fine details that drive many different scientific phenomena.

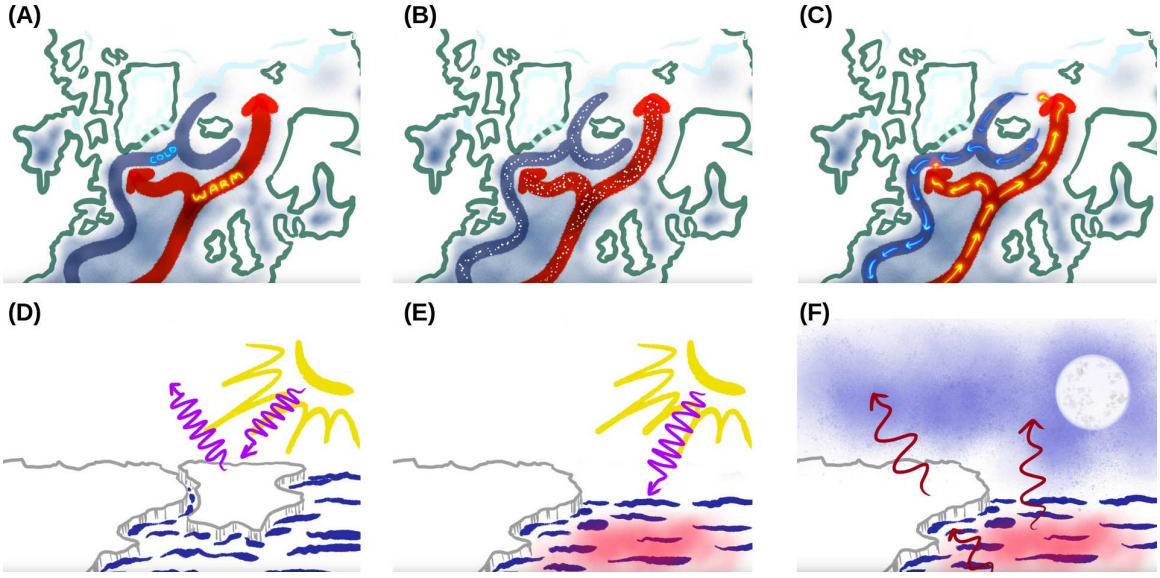

Figure D2: Excerpts from the videos about Arctic Amplification (parts 1 and 2) where A-C is used to describe the Atlantic Meridional Overturning Circulation and the D-F is used to describe the ice-albedo feedback.

Fig. D2 nicely depicts both the simplification and inaccuracies of the diagrams that I sketched and included in my videos to get the message across. Fig. D2A-C shows the Atlantic Meridional Overturning Circulation roughly mapped out across the North Atlantic Ocean. Already here, one can

notice that not all branches of the North Atlantic Current are included, the surrounding continents were not traced but rather drawn with a reference picture, and by all accounts, the reality is far from the simplified diagram that I sketched. Fig. D2A demonstrates the difference in temperature between southward current of North Atlantic Deep Water (blue) and the northward North Atlantic Current (red), and Fig. D2B shows that the overturning process (highlighted in Fig. D2C) is linked to the salinity of the water masses involved. Notably, there is neither actual temperature (in °C) nor actual salinity (in practical salinity units) conveyed in the sketch which of course lends itself to inaccuracies, especially in the case of Fig. D2A where the diagram uses two discrete colours misrepresenting the continuous change in temperature. However, for the sake of explaining the Atlantic Meridional Overturning Circulation to someone who has never heard of it, in a 16 minute video that is not dedicated solely the process itself, these diagrams help me relate the basics of the process in a quick succession of verbal explanations and quick-to-look-at diagrams that need to convey the full extent of the information contained within seconds of being shown. Similarly, Fig. D2D-F shows the basics behind the positive ice-albedo feedback wherein Fig. D2D shows how ice floes reflect short-wave radiation, Fig. D2E shows how, without the ice, the open water readily absorbs the short-wave radiation, and Fig. D2D-E shows how this can lead to Arctic amplification as the warmer ocean returns the heat to the atmosphere in winter (Dai et al. 2019). Here too, there are some basic simplifications, like how ice is fully reflecting the incoming solar radiation while open water is not, even though both are gray bodies. And yet, within a couple of minutes, using these sketches, I can communicate the basics behind the ice-albedo feedback, explain the fundamentals behind it, as well as show some recent findings about the process as presented in Dai et al. (2019). Even if someone has no background in thermodynamics and thermal physics so as to understand that there is no perfect white or black body, assuming that sea ice reflects "light" is true for most frequencies of radiation within the visible spectrum. As long as the simplification does not outright go against or distort the scientific phenomena being explained, it should be deemed acceptable in science communication albeit obviously corrected with time in science education.

Conclusion and Outlook

All in all, my brief dive into the world of science communication taught me the basic skills required, the challenges involved as well as the benefits of sharing scientific knowledge. Naturally, as time went on, and the work required for my PhD became more demanding, I left the hobby behind. In part, due to exhaustion, but also due to certain types of feedback received. A reality scientists who never participate in any science communication initiatives seldom see is the people who are downright against established scientific findings. It is important here to distinguish between scientists who challenge the status quo with rigorous proofs and data, and people that are simply denying science because it clashes with their beliefs or conspiracy theories. It is the case when dealing with controversial topics like anthropogenic climate change, that a given minority will readily try

to undermine the scientific communication efforts by scientists. Here, as I have come to learn, it is important to not engage in a direct confrontation but rather offer an explanation about the arguments they pose and debunk their errors with sufficient proof that does not leave them any opportunity to further poke holes in the science being communicated.

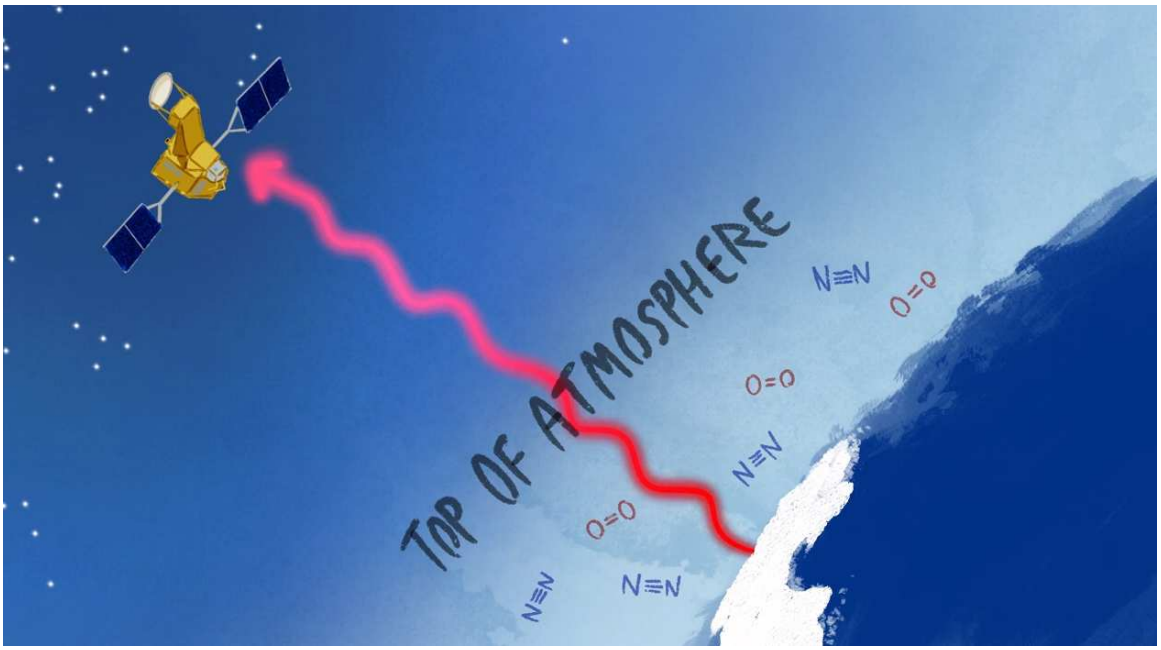

Figure D3: A sketch of AMSR2 onboard GCOM-W1 passively measuring the microwave emissions over the oceans covered in sea ice. This sketch from the video titled "How Do We Know How Much Sea Ice There Is?" is used to explain that the brightness temperature measured is in fact the brightness temperature from the top of the atmosphere.

My final video, in which I used all the feedback I received along this journey and therefore significantly improved the production value, was the closest I came to what I do as a scientist, i.e., satellite remote sensing of sea ice. Fig. D3 shows a sketch from this video where I depicted the GCOM-W1 launched by the Japan Aerospace Exploration Agency (JAXA) as it measures brightness temperatures over sea ice that are retrieved from the top of the atmosphere. In this video, I share more information on how sea ice is measured using satellites, which people with no physics or engineering backgrounds are unlikely to know. At this point I was already exhausted from having to share my videos over social media as the entire project was a hobby and not a job. Instead, I had hoped the increase in production value alone was enough to bring in the viewers. Unfortunately, that was not the case and the video remains with less than 400 views at the time of writing this dissertation. Partly because of the lack of advertising and partly because the topic is neither trending nor something non-experts would commonly look up. At this point I realized the closer I got to my

own specific field of research, the less of a following I would have on a platform like YouTube, and so I stopped for the time being. Despite all that, I am proud of the final video as well as all others that I have produced. I enjoyed and learned a lot from this experience, and am eager to find a science communication outlet in my scientific career that works for me in the future.

Acknowledgments

In this final part of my thesis I would like to thank all the people who have made it possible for me to produce this work. I would like to express my gratitude to the research group Remote Sensing of Polar Regions for having accepted me first as a student assistant, then to write my thesis with them, and finally as a PhD candidate. I would like to thank Gunnar Spreen, my supervisor, for having supported me throughout my project and investing into my future as a scientist. I would then like to thank Christian Melsheimer for all the fascinating scientific and non-scientific knowledge he has shared with me over the years. I would like to thank my fellow PhD candidates that are in my cohort, Janna Rückert and Hannah Niehaus, for having my back and facing the challenges of doing one's PhD with me. I then wish to thank Marcus Huntemann for the many times he helped me solve my programming, cartographic as well as scientific issues along the way. Last but not least, I wish to thank all other group members: Linda Thielke, Malte Gerken, Philip Rostosky, Valentin Ludwig, Karl Kortum, and many more wonderful and brilliant people that all contributed to what made being a part of our work group so awesome.

I want to thank all the members of the collaborative research community that is Arctic Amplification: Climate Relevant Atmospheric and Surface Processes, and Feedback Mechanisms $(AC)^3$, for helping me along the way and providing the crucial funding that made my PhD as well as some conferences, workshops and research stays possible. In particular, I would like to thank fellow PhD candidates Niklas Schnierstein, Nina Maherndl and Finn Heukamp for making all joint $(AC)^3$ events a fun and memorable experience. I would like to thank coordinators Christa Genz and Marlen Brückner for organizing most of these events as well as helping me out with all the needed paperwork along the way. Of the many principal investigators involved with $(AC)^3$ who have given me valuable and informative feedback, I would like to extend a special thank you to Christof Lüpkes who has time and time again supported me with his theoretical expertise.

Special thanks goes to Alek Petty, for giving me all the necessary information to work with the Ice, Cloud and land Elevation Satellite 2, as well as helping me organize my research stay at University College London (UCL). I want to express my gratitude towards the Centre for Polar Observation and Modelling (CPOM) who took me in at UCL and made me welcome during my research stay in the summer of 2022. I would like to thank Michel Tsamados for being a great host and providing his expertise on my work. In addition, a special shout-out goes out to Tom Johnson, Carmen Nab, Connor Nelson and Diarmuid Corr for making my stay at UCL such a fun experience. I want to thank Annette Rinke for helping me organize a stay at the Alfred Wegener Institute (AWI) Potsdam as well as Wolfgang Dorn for his help in facilitating the model study in my final months of the project. I want to thank Takenobu Toyota for his informative insights and for facilitating a brief research stay at the Institute of Low Temperature Science, Hokkaido University. My gratitude goes to the Atmosphere-Ocean Interaction Group there who took extra care to make my stay there pleasant.

ACKNOWLEDGMENTS

Lastly, I would like to thank the people who helped me get through the three years of my PhD project by keeping me company along the way. I would like to thank my close friends Anish, Joni, Nils, Justin and Olta for the fun times times we have had and helping me maintain a healthy work-life balance. I want to express my appreciation for my animal companions Pebble, Morph and Tangerine who each have, on multiple occasions, helped me unwind by just being their silly little selves. A heartfelt thanks goes to my family who have supported me throughout my life and made it possible for me to one day pursue a PhD. In particular, I want to thank my mother who initially sparked my fascination towards the field of physics those many years ago. And finally, I want to thank my partner and significant other, Isa, whose love and support were what kept me going and what allowed me to reach the finish line.

Acronym List

AA Arctic Amplification

ACC Antarctic Circumpolar Current

AFDR Atmospheric Form Drag Run

AIDJEX Arctic Ice Dynamics Joint Experiment

ALS Altimeter Laser Scanner

AMSR2 Advanced Microwave Scanning Radiometer 2

ATLAS Advanced Topographic Laser Altimeter System

ATM Airborne Topographic Mapper

ASI ARTIST sea ice

ASIT apparent sea ice thickness

AWI Alfred Wegener Institute

CFDD Cumulative Freezing Degree Days

CPOM Centre for Polar Observation and Modelling

ERA5 ECMWF Reanalysis 5th Generation

ESMR Electrically Scanning Microwave Radiometer

FYI First-Year Ice

HN2.2 HIRHAM-NOASIM version 2.2

ICESat Ice, Cloud and land Elevation Satellite

IDG ice dynamic growth

IFS Integrated Forecasting System

ITG ice thermodynamic growth

IS2 Ice, Cloud and land Elevation Satellite 2

LBCs lateral boundary conditions

MIZ Marginal Ice Zone

ACRONYM LIST

MODIS Moderate Resolution Imaging Spectroradiometer

MOSAiC Multidisciplinary drifting Observatory for the Study of Arctic Climate

mse mean squared error

MSLP mean sea level pressure

MYI Multiyear Ice

NFDR New Form Drag Run

OIB Operation IceBridge

OFDR Oceanic Form Drag Run

ORAS5 Ocean Reanalysis System 5

PD percent difference

PIOMAS Pan-Arctic Ice Ocean Modeling and Assimilation System

RQ Research Question

SAM Southern Annular Mode

SDR Standard Drag Run

SIC sea ice concentration

SIT sea ice thickness

SMAP Soil Moisture Active Passive

SMOS Soil Moisture Ocean Salinity

UCL University College London

YAC Yet Another Coupler

References

Andreas, E. L. and B. A. Cash (1999). "Convective heat transfer over wintertime leads and polynyas". In: *Journal of Geophysical Research: Oceans* 104.C11, pp. 25721–25734. DOI: https://doi.org/10.1029/1999JC900241.

Andreas, E. L. et al. (2010). "Parametrizing turbulent exchange over summer sea ice and the marginal ice zone". In: *Quarterly Journal of the Royal Meteorological Society* 136.649, pp. 927–943. DOI: 10.1002/qj.618.

Andreas, Edgar L. (Jan. 1987). "A theory for the scalar roughness and the scalar transfer coefficients over snow and sea ice". en. In: *Boundary-Layer Meteorology* 38.1, pp. 159–184. ISSN: 1573-1472. DOI: 10.1007/BF00121562.

— (Aug. 2002). "Parameterizing Scalar Transfer over Snow and Ice: A Review". EN. In: *Journal of Hydrometeorology* 3.4, pp. 417–432. ISSN: 1525-7541, 1525-755X. DOI: 10.1175/1525-7541(2002)003<0417:PSTOSA>2.0.CO;2.

Arya, S. P. S. (1973). "Contribution of form drag on pressure ridges to the air stress on Arctic ice". In: *Oceans and Atmospheres* 78(30), pp. 7092–7099. DOI: 10.1029/JC078i030p07092.

— (1975). "A drag partition theory for determining the large-scale roughness parameter and wind stress on the Arctic pack ice". In: *Journal of Geophysical Research (1896-1977)* 80.24, pp. 3447–3454. DOI: 10.1029/JC080i024p03447.

Aue, Lars et al. (2023). "Impact of three intense winter cyclones on the sea ice cover in the Barents Sea: A case study with a coupled regional climate model". In: *Frontiers in Earth Science* 11. ISSN: 2296-6463. URL: https://www.frontiersin.org/articles/10.3389/feart.2023.1112467.

Bagnardi, M. et al. (2021). "Sea Surface Height Anomalies of the Arctic Ocean From ICESat-2: A First Examination and Comparisons With CryoSat-2". In: *Geophysical Research Letters* 48.14, e2021GL093155. DOI: 10.1029/2021GL093155.

Bersch, Manfred et al. (1992). "Topographic effects of the Maud Rise on the stratification and circulation of the Weddell Gyre". In: *Deep Sea Research* 39, pp. 303–331. DOI: https://doi.org/10.1016/0198-0149(92)90111-6.

Birnbaum, G. and C. Lüpkes (2002). "A new parameterization of surface drag in the marginal sea ice zone". In: *Tellus A: Dynamic Meteorology and Oceanography* 54:1, pp. 107–123. DOI: 10.3402/tellusa.v54i1.12121.

Bourke, R. H. and R. P. Garrett (1987). "Sea ice thickness distribution in the Arctic Ocean". In: *Cold Regions Science and Technology* 13.3, pp. 259–280. ISSN: 0165-232X. DOI: 10.1016/0165-232X(87)90007-3.

Brenner, S. et al. (2021). "Comparing Observations and Parameterizations of Ice-Ocean Drag Through an Annual Cycle Across the Beaufort Sea". In: *Journal of Geophysical Research: Oceans* 126.4, e2020JC016977. DOI: https://doi.org/10.1029/2020JC016977.

Campbell, Ethan C. et al. (2019). "Antarctic offshore polynyas linked to Southern Hemisphere climate anomalies". In: *Nature* 570, pp. 319–325. DOI: https://doi.org/10.1038/s41586-019-1294-0.

Carsey, F. D. (1980). "Microwave Observation of the Weddell Polynya". In: *Monthly Weather Review* 108. DOI: https://doi.org/10.1175/1520-0493(1980)108<2032:MOOTWP>2.0.CO;2.

Cassano, John J. et al. (Aug. 2017). "Development of the Regional Arctic System Model (RASM): Near-Surface Atmospheric Climate Sensitivity". EN. In: *Journal of Climate* 30.15, pp. 5729–5753. ISSN: 0894-8755, 1520-0442. DOI: 10.1175/JCLI-D-15-0775.1.

Castellani, G. et al. (2014). "Variability of Arctic sea-ice topography and its impact on the atmospheric surface drag". In: *J. Geophys. Res. Oceans* 119, pp. 6743–6762. DOI: 10.1002/2013JC009712.

Cavalieri, D. J., P. Gloersen, and W. J. Campbell (1984). "Determination of sea ice parameters with the NIMBUS 7 SMMR". en. In: *Journal of Geophysical Research: Atmospheres* 89.D4, pp. 5355–5369. ISSN: 2156-2202. DOI: 10.1029/JD089iD04p05355.

Cheon, Woo Geun and Arnold L. Gordon (2019). "Open-ocean polynyas and deep convection in the Southern Ocean". In: *Scientific Reports* 9. DOI: https://doi.org/10.1038/s41598-019-43466-2.

Cheon, Woo Geun et al. (2014). "The Relationship of Weddell Polynya and Open-Ocean Deep Convection to the Southern Hemisphere Westerlies". In: *Journal of Physical Oceanography* 44, pp. 694–713. DOI: https://doi.org/10.1175/JPO-D-13-0112.1.

Cheon, Woo Geun et al. (2015). "Replicating the 1970s' Weddell Polynya using a coupled ocean-sea ice model with reanalysis surface flux fields". In: *Geophysical Research Letters* 42, pp. 5411–5418. DOI: https://doi.org/10.1002/2015GL064364.

Cheon, Woo Geun et al. (2018). "The Role of Oscillating Southern Hemisphere Westerly Winds: Southern Ocean Coastal and Open-Ocean Polynyas". In: *Journal of Climate* 31, pp. 1053–1073. DOI: https://doi.org/10.1175/JCLI-D-17-0237.1.

Cohen, J. et al. (Jan. 2020). "Divergent consensuses on Arctic amplification influence on midlatitude severe winter weather". en. In: *Nature Climate Change* 10.11, pp. 20–29. ISSN: 1758-6798. DOI: 10.1038/s41558-019-0662-y.

Comiso, J. C. and A. L. Gordon (1998). "Interannual Variability in Summer Sea Ice Minimum, Coastal Polynyas, and Bottom Water Formation in the Weddell Sea". In: *Antarctic Sea Ice: Physical Processes, Interactions and Variability* 74, pp. 293–315. DOI: https://doi.org/10.1029/AR074p0293.

Comiso, Josefino C. et al. (1997). "Passive microwave algorithms for sea ice concentration: A comparison of two techniques". In: *Remote Sensing of Environment* 60.3, pp. 357–384. DOI: https://doi.org/10.1016/S0034-4257(96)00220-9.

Cottier, Finlo, Michael Steele, and Frank Nilsen (2017). "Sea ice and Arctic Ocean oceanography". In: *Sea Ice*. John Wiley & Sons, Ltd. Chap. 7, pp. 197–215. ISBN: 9781118778371. DOI: https:

//doi.org/10.1002/9781118778371.ch7. eprint: https://onlinelibrary.wiley.com/doi/pdf/10.1002/9781118778371.ch7. URL: https://onlinelibrary.wiley.com/doi/abs/10.1002/9781118778371.ch7.

Cranmer, M. (May 2023). *Interpretable Machine Learning for Science with PySR and SymbolicRegression.jl*. en. DOI: 10.48550/arXiv.2305.01582. URL: https://arxiv.org/abs/2305.01582.

Dai, Aiguo et al. (Jan. 2019). "Arctic amplification is caused by sea-ice loss under increasing CO2". en. In: *Nature Communications* 10.11, p. 121. ISSN: 2041-1723. DOI: 10.1038/s41467-018-07954-9.

Dammann, D. O. et al. (2018). "Traversing Sea Ice—Linking Surface Roughness and Ice Trafficability Through SAR Polarimetry and Interferometry". In: *IEEE Journal of Selected Topics in Applied Earth Observations and Remote Sensing* 11.2, pp. 416–433. DOI: 10.1109/JSTARS.2017.2764961.

Degnan, John J. (Oct. 2002). "Photon-counting multikilohertz microlaser altimeters for airborne and spaceborne topographic measurements". In: *Journal of Geodynamics* 34.3, pp. 503–549. ISSN: 0264-3707. DOI: 10.1016/S0264-3707(02)00045-5.

Dorn, W., K. Dethloff, and A. Rinke (Jan. 2009). "Improved simulation of feedbacks between atmosphere and sea ice over the Arctic Ocean in a coupled regional climate model". In: *Ocean Modelling* 29.2, pp. 103–114. ISSN: 1463-5003. DOI: 10.1016/j.ocemod.2009.03.010.

— (Sept. 2012). "Limitations of a coupled regional climate model in the reproduction of the observed Arctic sea-ice retreat". English. In: *The Cryosphere* 6.5, pp. 985–998. ISSN: 1994-0416. DOI: 10.5194/tc-6-985-2012.

Dorn, W. et al. (2007). "Sensitivities and uncertainties in a coupled regional atmosphere-ocean-ice model with respect to the simulation of Arctic sea ice". en. In: *Journal of Geophysical Research: Atmospheres* 112.D10. ISSN: 2156-2202. DOI: 10.1029/2006JD007814. URL: https://onlinelibrary.wiley.com/doi/abs/10.1029/2006JD007814.

Dorn, Wolfgang et al. (Aug. 2019). "Evaluation of the Sea-Ice Simulation in the Upgraded Version of the Coupled Regional Atmosphere-Ocean- Sea Ice Model HIRHAM–NAOSIM 2.0". en. In: *Atmosphere* 10.88, p. 431. ISSN: 2073-4433. DOI: 10.3390/atmos10080431.

Duncan, K. and S. L. Farrell (2022). "Determining Variability in Arctic Sea Ice Pressure Ridge Topography with ICESat-2". In: *Geophysical Research Letters* n/a.n/a, e2022GL100272. DOI: 10.1029/2022GL100272.

Elvidge, A. D. et al. (2016). "Observations of surface momentum exchange over the marginal ice zone and recommendations for its parametrisation". In: *Atmospheric Chemistry and Physics* 16.3, pp. 1545–1563. DOI: 10.5194/acp-16-1545-2016.

Elvidge, A. D. et al. (2021). "Surface Heat and Moisture Exchange in the Marginal Ice Zone: Observations and a New Parameterization Scheme for Weather and Climate Models". In: *Journal of Geophysical Research: Atmospheres* 126.17, e2021JD034827. DOI: 10.1029/2021JD034827.

Evagorou, Maria, Sibel Erduran, and Terhi Mäntylä (July 2015). "The role of visual representations in scientific practices: from conceptual understanding and knowledge generation to 'seeing' how science works". In: *International Journal of STEM Education* 2.1, p. 11. ISSN: 2196-7822. DOI: 10.1186/s40594-015-0024-x.

Feltham, Daniel L. (2008). "Sea Ice Rheology". In: *Annual Review of Fluid Mechanics* 40.1, pp. 91–112. DOI: 10.1146/annurev.fluid.40.111406.102151.

Francis, D. et al. (2019). "Polar Cyclones at the Origin of the Reoccurrence of the Maud Rise Polynya in Austral Winter 2017". In: *Journal of Geophysical Research: Oceans* 124. DOI: https://doi.org/10.1029/2019JD030618.

Francis, Diana et al. (2020). "On the crucial role of atmospheric rivers in the two major Weddell Polynya events in 1973 and 2017 in Antarctica". In: *Sci Adv* 6. DOI: https://10.1126/sciadv.abc2695.

Garbrecht, T. et al. (1999). "Influence of a sea ice ridge on low-level airflow". In: *Journal of Geophysical Research: Atmospheres* 104.D20, pp. 24499–24507. DOI: 10.1029/1999JD900488.

Garbrecht, T. et al. (2002). "Atmospheric drag coefficients over sea ice–validation of a parameterisation concept". In: *Tellus A: Dynamic Meteorology and Oceanography* 54, pp. 205–219. DOI: 10.3402/tellusa.v54i2.12129.

Garratt, J. R. (1992). "The atmospheric boundary layer". In: *Robust Statistics, 2nd Edition*. Cambridge University Press, p. 316. ISBN: 0-521-38052-9. DOI: 10.1002/qj.49712051919. URL: https://rmets.onlinelibrary.wiley.com/doi/10.1002/qj.49712051919.

Goosse, H. and T. Fichefet (2000). "Importance of ice-ocean interactions for the global ocean circulation: A model study". In: *Journal of Geophysical Research Oceans* 104, pp. 23337–23355. DOI: https://doi.org/10.1029/1999JC900215.

Gordon, Arnold and Josefino Comiso (July 1988). "Polynyas in the Southern Ocean". In: *Scientific American* 258. DOI: 10.1038/scientificamerican0688-90.

Gordon, Arnold L. and Bruce A. Huber (1990). "Southern ocean winter mixed layer". In: *Journal of Geophysical Research Oceans* 95. DOI: https://doi.org/10.1029/JC095iC07p11655.

Gryanik, V. M. and C. Lüpkes (2018). "An Efficient Non-iterative Bulk Parametrization of Surface Fluxes for Stable Atmospheric Conditions Over Polar Sea-Ice". In: *Boundary-Layer Meteorology* 166, pp. 301–325. DOI: 10.1007/s10546-017-0302-x.

— (2023). "A Package of Momentum and Heat Transfer Coefficients for the Stable Surface Layer Extended by New Coefficients over Sea Ice". In: *Boundary-Layer Meteorology* 187, pp. 41–72. DOI: 10.1007/s10546-022-00730-9.

Haas, Christian (2017). "Sea ice thickness distribution". In: *Sea Ice*. John Wiley & Sons, Ltd. Chap. 2, pp. 42–64. ISBN: 9781118778371. DOI: https://doi.org/10.1002/9781118778371.ch2. eprint: https://onlinelibrary.wiley.com/doi/pdf/10.1002/9781118778371.ch2. URL: https://onlinelibrary.wiley.com/doi/abs/10.1002/9781118778371.ch2.

Hanssen-Bauer, I. and Y. T. Gjessing (1988). "Observations and model calculations of aerodynamic drag on sea ice in the Fram Strait". In: *Tellus A* 40A.2, pp. 151–161. DOI: 10.1111/j.1600-0870.1988.tb00413.x.

Hersbach, Hans et al. (2020). "The ERA5 global reanalysis". In: *Quarterly Journal of the Royal Meteorological Society* 146.730, pp. 1999–2049. DOI: https://doi.org/10.1002/qj.3803.

Heuzé, Céline et al. (2021). "Spaceborne infrared imagery for early detection of Weddell Polynya opening". In: *The Cryosphere*. DOI: https://doi.org/10.5194/tc-15-3401-2021.

Heygster, G. et al. (2014). "Response of passive microwave sea ice concentration algorithms to thin ice". In: *2014 IEEE Geoscience and Remote Sensing Symposium*, pp. 3618–3621. DOI: https://doi.org/10.1109/IGARSS.2014.6947266.

Hibler, W. D. (1975). "Characterization of Cold-Regions Terrain Using Airborne Laser Profilometry". In: *Journal of Glaciology* 15.73, pp. 329–347. DOI: 10.3189/S0022143000034468.

Holland, D. M. (2001). "Explaining the Weddell Polynya–a Large Ocean Eddy Shed at Maud Rise". In: *Science* 292, pp. 1697–1700. DOI: https://doi.org/10.1126/science.1059322.

Hopkins, M. A. (1998). "Four stages of pressure ridging". In: *Journal of Geophysical Research: Oceans* 103.C10, pp. 21883–21891. DOI: 10.1029/98JC01257.

Huber, P. J. and E. M. Ronchetti (2009). "Regression". In: *Robust Statistics, 2nd Edition*. John Wiley & Sons, Ltd, p. 172. ISBN: 978-0-470-12990-6. DOI: 10.1002/9780470434697.ch7. URL: https://onlinelibrary.wiley.com/doi/abs/10.1002/9780470434697.ch7.

Huntemann, M. et al. (2014). "Empirical sea ice thickness retrieval during the freeze-up period from SMOS high incident angle observations". In: *The Cryosphere* 8, pp. 439–451. DOI: https://doi.org/10.5194/tc-8-439-2014.

Hutter, Nils et al. (Oct. 2023). "Digital elevation models of the sea-ice surface from airborne laser scanning during MOSAiC". en. In: *Scientific Data* 10.1, p. 729. ISSN: 2052-4463. DOI: 10.1038/s41597-023-02565-6.

Jena, B., M. Ravichandran, and J. Turner (2019). "Recent Reoccurrence of Large Open-Ocean Polynya on the Maud Rise Seamount". In: *Geophysical Research Letters* 46. DOI: https://doi.org/10.1029/2018GL081482.

Johnson, Thomas et al. (Jan. 2022). "Mapping Arctic Sea-Ice Surface Roughness with Multi-Angle Imaging SpectroRadiometer". en. In: *Remote Sensing* 14.2424, p. 6249. ISSN: 2072-4292. DOI: 10.3390/rs14246249.

Jutila, Arttu et al. (Jan. 2022). "Retrieval and parameterisation of sea-ice bulk density from airborne multi-sensor measurements". English. In: *The Cryosphere* 16.1, pp. 259–275. ISSN: 1994-0416. DOI: 10.5194/tc-16-259-2022.

Kaleschke, L. et al. (Oct. 2001). "SSM/I Sea Ice Remote Sensing for Mesoscale Ocean-Atmosphere Interaction Analysis". In: *Canadian Journal of Remote Sensing* 27.5, pp. 526–537. ISSN: 0703-8992. DOI: 10.1080/07038992.2001.10854892.

Kaleschke, L. et al. (2010). "A sea-ice thickness retrieval model for 1.4 GHz radiometry and application to airborne measurements over low salinity sea-ice". In: *The Cryosphere* 4, pp. 583–592. DOI: https://doi.org/10.5194/tc-4-583-2010.

Kaleschke, L. et al. (2013). *ESA Support To Science Element (STSE) SMOS Sea Ice Retrieval Study (SMOSIce) Final Report ESA ESTE Contract No .: 4000101476 / 10 / NL / CT*.

Kimura, Noriaki et al. (Nov. 2013). "Influence of winter sea-ice motion on summer ice cover in the Arctic". en. In: *Polar Research*. ISSN: 1751-8369. DOI: 10.3402/polar.v32i0.20193. URL: https://polarresearch.net/index.php/polar/article/view/3087.

Knowles, K. W. (1993). *A Mapping and Gridding Primer: Points, Pixels, Grids, and Cells*. URL: https://nsidc.org/data/user-resources/help-center/mapping-and-gridding-primer-points-pixels-grids-and-cells.

Kongoli, Cezar et al. (Jan. 2011). "A New Sea-Ice Concentration Algorithm Based on Microwave Surface Emissivities—Application to AMSU Measurements". In: *IEEE Transactions on Geoscience and Remote Sensing* 49.1, pp. 175–189. ISSN: 1558-0644. DOI: 10.1109/TGRS.2010.2052812.

Kreyscher, Martin, Markus Harder, and Peter Lemke (Jan. 1997). "First results of the Sea-Ice Model Intercomparison Project (SIMIP)". en. In: *Annals of Glaciology* 25, pp. 8–11. ISSN: 0260-3055, 1727-5644. DOI: 10.3189/S0260305500013719.

Kwok, R. et al. (2019a). "ICESat-2 Surface Height and Sea Ice Freeboard Assessed With ATM Lidar Acquisitions From Operation IceBridge". In: *Geophysical Research Letters* 46, pp. 11, 228–11, 236. DOI: 10.1029/2019GL084976.

Kwok, R. et al. (2019b). "Surface Height and Sea Ice Freeboard of the Arctic Ocean From ICESat-2: Characteristics and Early Results". In: *Journal of Geophysical Research: Oceans* 124.10, pp. 6942–6959. DOI: 10.1029/2019JC015486.

Kwok, R. et al. (2021a). *ATLAS/ICESat-2 L3A Sea Ice Height, Version 5*. DOI: 10.5067/ATLAS/ATL07.005. URL: https://nsidc.org/data/ATL07/versions/5.

Kwok, R. et al. (Nov. 2021b). *ICESat-2 Algorithm Theoretical Basis Document for Sea Ice Products (ATL07/ATL10), Release 005*. Goddard Space Flight Center, Greenbelt, Maryland 20771. URL: https://nsidc.org/sites/nsidc.org/files/technical-references/ICESat2_ATL07_ATL10_ATL20_ATL21_ATBD_r005.pdf.

Landy, Jack C., Jens K. Ehn, and David G. Barber (2015). "Albedo feedback enhanced by smoother Arctic sea ice". In: *Geophysical Research Letters* 42.24, pp. 10, 714–10, 720. DOI: 10.1002/2015GL066712.

Leppäranta, Matti (2005). *The drift of sea ice*. Springer. ISBN: 3-540-40881-9.

Lindsay, R. W., D. M. Holland, and R. A. Woodgate (2004). "Halo of low ice concentration observed over the Maud Rise seamount". In: *Geophysical Research Letters* 31. DOI: https://doi.org/10.1029/2004GL019831.

Lu, Peng et al. (2011). "A parameterization of the ice-ocean drag coefficient". en. In: *Journal of Geophysical Research: Oceans* 116.C7. ISSN: 2156-2202. DOI: 10.1029/2010JC006878. URL: https://onlinelibrary.wiley.com/doi/abs/10.1029/2010JC006878.

Lüpkes, C. and V. M. Gryanik (2015). "A stability-dependent parametrization of transfer coefficients for momentum and heat over polar sea ice to be used in climate models". In: *Journal of Geophysical Research: Atmospheres* 120.2, pp. 552–581. DOI: 10.1002/2014JD022418.

Lüpkes, C. et al. (2013). "Effect of sea ice morphology during Arctic summer on atmospheric drag coefficients used in climate models". In: *Geophysical Research Letters* 40.2, pp. 446–451. DOI: 10.1002/grl.50081.

Lüpkes, Christof et al. (2011). *Mesoscale modelling of the Arctic atmospheric boundary layer and its interaction with sea ice*. DOI: 10.1007/978-94-007-2027-5.

Lüpkes, Christof et al. (2012). "A parametrization, based on sea ice morphology, of the neutral atmospheric drag coefficients for weather prediction and climate models". en. In: *Journal of Geophysical Research: Atmospheres* 117.D13. ISSN: 2156-2202. DOI: 10.1029/2012JD017630. URL: https://onlinelibrary.wiley.com/doi/abs/10.1029/2012JD017630.

MacGregor, Joseph A. et al. (2021). "The Scientific Legacy of NASA's Operation IceBridge". In: *Reviews of Geophysics* 59.2, e2020RG000712. DOI: 10.1029/2020RG000712.

Magruder, L. A., K. M. Brunt, and M. Alonzo (2020). "Early ICESat-2 on-orbit Geolocation Validation Using Ground-Based Corner Cube Retro-Reflectors". In: *Remote Sensing* 12.21. DOI: 10.3390/rs12213653.

Magruder, L. A. et al. (2021). "Passive Ground-Based Optical Techniques for Monitoring the On-Orbit ICESat-2 Altimeter Geolocation and Footprint Diameter". In: *Earth and Space Science* 8.10, e2020EA001414. DOI: 10.1029/2020EA001414.

Maqueda, M. A. Morales, A. J. Willmott, and N. R. T. Biggs (2004). "Polynya Dynamics: a Review of Observations and Modeling". In: *Reviews of Geophysics* 42. DOI: https://doi.org/10.1029/2002RG000116.

Markus, T. et al. (2017). "The Ice, Cloud, and land Elevation Satellite-2 (ICESat-2)". In: *Remote Sensing of Environment* 190, pp. 260–273. ISSN: 0034-4257. DOI: 10.1016/j.rse.2016.12.029.

Martin, C. F. et al. (2012). *Airborne Topographic Mapper Calibration Procedures and Accuracy Assessment*. Technical Memorandum, 215891. Greenbelt, Maryland 20771. Goddard Space Flight Center. URL: https://ntrs.nasa.gov/api/citations/20120008479/downloads/20120008479.pdf.

Martin, T. et al. (2016). "The impact of variable sea ice roughness on changes in Arctic Ocean surface stress: A model study". In: *J. Geophys. Res. Oceans* 121(3), pp. 1931–1952. DOI: 10.1002/2015JC011186.

Martinson, Douglas G. and Richard A. Ianuzzi (1998). "Antarctic Ocean-ice Interaction: Implications from Ocean Bulk Property Distributions in the Weddell Gyre". In: *Antarctic Research Series* 74, pp. 243–271. DOI: https://doi.org/10.1029/AR074p0243.

Martinson, Douglas G., Peter D. Killworth, and Arnold L. Gordon (1981). "A Convective Model for the Weddell Polynya". In: *Journal of Physical Oceanography* 11. DOI: https://doi.org/10.1175/1520-0485(1981)011<0466:ACMFTW>2.0.CO;2.

Mazloff, M. R., P. Heimbach, and C. Wunsch (2009). "An Eddy-Permitting Southern Ocean State Estimate". In: *Journal of Physical Oceanography* 40, pp. 880–899. DOI: https://doi.org/0.1175/2009JPO4236.1.

Mchedlishvili, Alexander et al. (Feb. 2022). "Weddell Sea polynya analysis using SMOS–SMAP apparent sea ice thickness retrieval". English. In: *The Cryosphere* 16.2, pp. 471–487. ISSN: 1994-0416. DOI: 10.5194/tc-16-471-2022.

Mchedlishvili, Alexander et al. (Sept. 2023). "New estimates of pan-Arctic sea ice–atmosphere neutral drag coefficients from ICESat-2 elevation data". English. In: *The Cryosphere* 17.9, pp. 4103–4131. ISSN: 1994-0416. DOI: 10.5194/tc-17-4103-2023.

McLaren, Alfred S. (Apr. 1989). "The under-ice thickness distribution of the Arctic Basin as recorded in 1958 and 1970". In: *Journal of Geophysical Research* 94. ADS Bibcode: 1989JGR....94.4971M, pp. 4971–4983. ISSN: 0148-0227. DOI: 10.1029/JC094iC04p04971.

McPhee, M. G. et al. (1996). "The Antarctic Zone Flux Experiment". In: *Bulletin of the American Meteorological Society* 77, pp. 1221–1232. DOI: https://doi.org/10.1175/1520-0477(1996)077<1221:TAZFE>2.0.CO;2.

McPhee, Miles G. (1992). "Turbulent heat flux in the upper ocean under sea ice". en. In: *Journal of Geophysical Research: Oceans* 97.C4, pp. 5365–5379. ISSN: 2156-2202. DOI: 10.1029/92JC00239.

Meier, Walter N. (2017). "Losing Arctic sea ice: observations of the recent decline and the long-term context". In: *Sea Ice*. John Wiley & Sons, Ltd. Chap. 11, pp. 290–303. ISBN: 9781118778371. DOI: https://doi.org/10.1002/9781118778371.ch11. eprint: https://onlinelibrary.wiley.com/doi/pdf/10.1002/9781118778371.ch11. URL: https://onlinelibrary.wiley.com/doi/abs/10.1002/9781118778371.ch11.

Melsheimer, C. and G. Spreen (2019). *AMSR2 ASI sea ice concentration data, Arctic, version 5.4 (NetCDF) (July 2012 - December 2019)*. DOI: 10.1594/PANGAEA.898399. URL: 10.1594/PANGAEA.898399.

Melsheimer, C. et al. (2023). "First results of Antarctic sea ice type retrieval from active and passive microwave remote sensing data". In: *The Cryosphere* 17.1, pp. 105–126. DOI: 10.5194/tc-17-105-2023.

Meredith, Michael P. and Mark A. Brandon (2017). "Oceanography and sea ice in the Southern Ocean". In: *Sea Ice*. John Wiley & Sons, Ltd. Chap. 8, pp. 216–238. ISBN: 9781118778371. DOI: https://doi.org/10.1002/9781118778371.ch8. eprint: https://onlinelibrary.wiley.com/doi/pdf/10.1002/9781118778371.ch8. URL: https://onlinelibrary.wiley.com/doi/abs/10.1002/9781118778371.ch8.

Mock, S. J., A. D. Hartwell, and W. D. Hibler (1972). "Spatial aspects of pressure ridge statistics". In: *Journal of Geophysical Research (1896-1977)* 77.30, pp. 5945–5953. DOI: 10.1029/JC077i030p05945.

Motoi, Tatsuo, Nubuo Ono, and Masaaki Wakatsuchi (1987). "A Mechanism for the Formation of the Weddell Polynya in 1974". In: *Journal of Physical Oceanography* 17. DOI: https://doi.org/10.1175/1520-0485(1987)017<2241:AMFTFO>2.0.CO;2.

Muench, R. D. et al. (2001). "Maud Rise revisited". In: *Journal of Geophysical Research: Oceans* 106, pp. 2423–2440. DOI: https://doi.org/10.1029/2000JC000531.

Neumann, T. A. et al. (2019). "The Ice, Cloud, and Land Elevation Satellite – 2 mission: A global geolocated photon product derived from the Advanced Topographic Laser Altimeter System". In: *Remote Sensing of Environment* 233, p. 111325. ISSN: 0034-4257. DOI: 10.1016/j.rse.2019.111325.

Parkinson, C. L., J. C. Comiso, and H. J. Zwally. (2004). *Nimbus-5 ESMR Polar Gridded Sea Ice Concentrations, Version 1*. Ed. by W. N. Meier and J. Stroeve. DOI: 10.5067/W2PKTWMTY0TP. URL: https://nsidc.org/data/NSIDC-0009/versions/1.

Paţilea, Cătălin et al. (2019). "Combined SMAP–SMOS thin sea ice thickness retrieval". In: *The Cryosphere* 13, pp. 675–691. DOI: https://doi.org/10.5194/tc-13-675-2019.

Petrich, Chris and Hajo Eicken (2017). "Overview of sea ice growth and properties". In: *Sea Ice*. John Wiley & Sons, Ltd. Chap. 1, pp. 1–41. ISBN: 9781118778371. DOI: https://doi.org/10.1002/9781118778371.ch1. eprint: https://onlinelibrary.wiley.com/doi/pdf/10.1002/9781118778371.ch1. URL: https://onlinelibrary.wiley.com/doi/abs/10.1002/9781118778371.ch1.

Petty, A. A., M. C. Tsamados, and N. T. Kurtz (2017). "Atmospheric form drag coefficients over Arctic sea ice using remotely sensed ice topography data, spring 2009–2015". In: *J. Geophys. Res. Surf.* 122, pp. 1472–1490. DOI: 10.1002/2017JF004209.

Petty, A. A. et al. (2016). "Characterizing Arctic sea ice topography using high-resolution IceBridge data". In: *The Cryosphere* 10.3, pp. 1161–1179. DOI: 10.5194/tc-10-1161-2016.

Petty, Alek A. et al. (Jan. 2023). "Winter Arctic sea ice thickness from ICESat-2: upgrades to freeboard and snow loading estimates and an assessment of the first three winters of data collection". English. In: *The Cryosphere* 17.1, pp. 127–156. ISSN: 1994-0416. DOI: 10.5194/tc-17-127-2023.

Polyak, Leonid et al. (July 2010). "History of sea ice in the Arctic". In: *Quaternary Science Reviews*. Special Theme: Arctic Palaeoclimate Synthesis (PP. 1674-1790) 29.15, pp. 1757–1778. ISSN: 0277-3791. DOI: 10.1016/j.quascirev.2010.02.010.

Rantanen, Mika et al. (Aug. 2022). "The Arctic has warmed nearly four times faster than the globe since 1979". en. In: *Communications Earth & Environment* 3.11, pp. 1–10. ISSN: 2662-4435. DOI: 10.1038/s43247-022-00498-3.

Renfrew, I. A., A. D. Elvidge, and J. M. Edwards (2019). "Atmospheric sensitivity to marginal-ice-zone drag: Local and global responses". In: *Quarterly Journal of the Royal Meteorological Society* 145.720, pp. 1165–1179. DOI: 10.1002/qj.3486.

Ricker, R. et al. (2023). "Linking scales of sea ice surface topography: evaluation of ICESat-2 measurements with coincident helicopter laser scanning during MOSAiC". In: *The Cryosphere* 17, pp. 1411–1429. DOI: 10.5194/tc-17-1411-2023.

Rinke, A. et al. (2003). "A case study of the anomalous Arctic sea ice conditions during 1990: Insights from coupled and uncoupled regional climate model simulations". en. In: *Journal of Geophysical Research: Atmospheres* 108.D9. ISSN: 2156-2202. DOI: 10.1029/2002JD003146. URL: https://onlinelibrary.wiley.com/doi/abs/10.1029/2002JD003146.

Ropers, M. (2013). "Die Auswirkung variabler Meereisrauigkeit auf die atmosphaerische Grenzschicht". PhD thesis. University of Bremen.

Rostosky, Philip et al. (2018). "Snow Depth Retrieval on Arctic Sea Ice From Passive Microwave Radiometers—Improvements and Extensions to Multiyear Ice Using Lower Frequencies". en. In: *Journal of Geophysical Research: Oceans* 123.10, pp. 7120–7138. ISSN: 2169-9291. DOI: 10.1029/2018JC014028.

Schneider, T. et al. (2022). "Sensitivity to changes in the surface-layer turbulence parameterization for stable conditions in winter: A case study with a regional climate model over the Arctic". In: *Atmospheric Science Letters* 23.1, e1066. DOI: https://doi.org/10.1002/asl.1066.

Serreze, M. C. and R. G. Barry (2011). "Processes and impacts of Arctic amplification: A research synthesis". In: *Global and Planetary Change* 77.1, pp. 85–96. ISSN: 0921-8181. DOI: 10.1016/j.gloplacha.2011.03.004.

Shokr, M., A. Lambe, and T. Agnew (2008). "A New Algorithm (ECICE) to Estimate Ice Concentration From Remote Sensing Observations: An Application to 85-GHz Passive Microwave Data". In: *IEEE Transactions on Geoscience and Remote Sensing* 46.12, pp. 4104–4121. DOI: 110.1109/TGRS.2008.2000624.

Shokr, Mohammed and Nirmal K. Sinha (2015). *Sea Ice*. Wiley. ISBN: 978-1-119-02789-8. DOI: 10.1002/9781119028000.

Siewert, Stephanie (2021). *International Summer School "Communicating Science"*. URL: https://www.humboldt-foundation.de/en/explore/organisation/international-summer-school-communicating-science.

Spreen, G., L. Kaleschke, and G. Heygster (2008). "Sea ice remote sensing using AMSR-E 89-GHz channels". In: *Journal of Geophysical Research: Oceans* 113. DOI: https://doi.org/10.1029/2005JC003384.

Spreen, Gunnar, Ron Kwok, and Dimitris Menemenlis (2011). "Trends in Arctic sea ice drift and role of wind forcing: 1992–2009". en. In: *Geophysical Research Letters* 38.19. ISSN: 1944-8007. DOI: 10.1029/2011GL048970. URL: https://onlinelibrary.wiley.com/doi/abs/10.1029/2011GL048970.

Srivastava, P. et al. (2022). "Ship-based estimates of momentum transfer coefficient over sea ice and recommendations for its parameterization". In: *Atmospheric Chemistry and Physics* 22.7, pp. 4763–4778. DOI: 10.5194/acp-22-4763-2022.

Stammerjohn, Sharon and Ted Maksym (2017). "Gaining (and losing) Antarctic sea ice: variability, trends and mechanisms". In: *Sea Ice*. John Wiley & Sons, Ltd. Chap. 10, pp. 261–289. ISBN: 9781118778371. DOI: https://doi.org/10.1002/9781118778371.ch10. eprint: https://onlinelibrary.wiley.com/doi/pdf/10.1002/9781118778371.ch10. URL: https://onlinelibrary.wiley.com/doi/abs/10.1002/9781118778371.ch10.

Steele, M. et al. (1997). "The force balance of sea ice in a numerical model of the Arctic Ocean". In: *J. Geophys. Res. Oceans* 102(C9), pp. 21061–21079. DOI: 10.1029/97JC01454.

Steiner, N., M. Harder, and P. Lemke (1999). "Sea-ice roughness and drag coefficients in a dynamic–thermodynamic sea-ice model for the Arctic". In: *Tellus A: Dynamic Meteorology and Oceanography* 51:5, pp. 964–978. DOI: 10.3402/tellusa.v51i5.14505.

Sterlin, Jean et al. (Aug. 2023). "Effects of sea ice form drag on the polar oceans in the NEMO-LIM3 global ocean–sea ice model". In: *Ocean Modelling* 184, p. 102227. ISSN: 1463-5003. DOI: 10.1016/j.ocemod.2023.102227.

Steur, Laura de et al. (2007). "The warm-water "Halo" around Maud Rise: Properties, dynamics and Impact". In: *Deep Sea Research Part I Oceanographic Research Papers* 54, pp. 871–896. DOI: https://doi.org/10.1016/j.dsr.2007.03.009.

Strabo (1917). *Geography, Volume I: Books 1-2*. Trans. by Horace Leonard Jones. Loeb Classical Library 49. Cambridge, MA: Harvard University Press.

Stroeve, J. et al. (2012). "Atmospheric drag coefficients over sea ice–validation of a parameterisation concept". In: *Climatic Change* 110, pp. 1005–1027. DOI: 10.1007/s10584-011-0101-1.

Studinger, M. (2013). *IceBridge ATM L1B Elevation and Return Strength, Version 2*. DOI: 10.5067/19SIM5TXKPGT. URL: https://nsidc.org/data/ILATM1B/versions/2.

Studinger, M. et al. (2022). "High-resolution imaging of supraglacial hydrological features on the Greenland Ice Sheet with NASA's Airborne Topographic Mapper (ATM) instrument suite". In: *The Cryosphere* 16.9, pp. 3649–3668. DOI: 10.5194/tc-16-3649-2022.

Swart, Sebastiaan et al. (2018). "Return of the Maud Rise Polynya: climate litmus or sea ice anomaly? [in "State of the Climate in 2017"]". In: *Bulletin of the American Meteorological Society* 99. DOI: https://doi.org/10.1175/2018BAMSStateoftheClimate.1.

Thorndike, A. S. and R. Colony (1982). "Sea ice motion in response to geostrophic winds". In: *J. Geophys. Res. Oceans* 87(C8), pp. 5845–5852. DOI: 10.1029/JC087iC08p05845.

Thorndike, A. S. et al. (1975). "The thickness distribution of sea ice". In: *Journal of Geophysical Research (1896-1977)* 80.33, pp. 4501–4513. DOI: 10.1029/JC080i033p04501.

Tian-Kunze, X. et al. (2014). "SMOS-derived thin sea ice thickness: Algorithm baseline, product specifications and initial verification". In: *The Cryosphere* 8, pp. 997–1018. DOI: https://doi.org/10.5194/tc-8-997-2014.

Tilling, R. et al. (2020). "Detection of Melt Ponds on Arctic Summer Sea Ice From ICESat-2". In: *Geophysical Research Letters* 47.23, e2020GL090644. DOI: 10.1029/2020GL090644.

Timco, G. W. and R. P. Burden (1997). "An analysis of the shapes of sea ice ridges". In: *Cold Regions Science and Technology* 25.1, pp. 65–77. DOI: 10.1016/S0165-232X(96)00017-1.

Tin, T. et al. (2003). "Estimating the thickness of ridged sea ice from ship observations in the Ross Sea". In: *Antarctic Science* 15.1, pp. 47–54. DOI: 10.1017/S0954102003001056.

Tremblay, L.-B. and L. A. Mysak (1977). "Modeling Sea Ice as a Granular Material, Including the Dilatancy Effect". In: *J. Phys. Oceanogr* 27(11), pp. 2342–2360. DOI: 10.1175/1520-0485(1997)027<2342:MSIAAG>2.0.CO;2.

— (Jan. 1997). "The possible effects of including ridge-related roughness in air–ice drag parameterization: a sensitivity study". en. In: *Annals of Glaciology* 25, pp. 22–25. ISSN: 0260-3055, 1727-5644. DOI: 10.3189/S0260305500013744.

Tsamados, M. et al. (2014). "Impact of Variable Atmospheric and Oceanic Form Drag on Simulations of Arctic Sea Ice". In: *Journal of Physical Oceanography* 44(5), pp. 1329–1353. DOI: 10.1175/JPO-D-13-0215.1.

Tsamados, M. et al. (2016). "Processes controlling surface, bottom and lateral melt of Arctic sea ice in a state of the art sea ice model". In: *Phil. Trans. R. Soc. A* 373. DOI: 10.1098/rsta.2014.0167.

Tschudi, Mark A., Julienne C. Stroeve, and J. Scott Stewart (June 2016). "Relating the Age of Arctic Sea Ice to its Thickness, as Measured during NASA's ICESat and IceBridge Campaigns". en. In: *Remote Sensing* 8.66, p. 457. ISSN: 2072-4292. DOI: 10.3390/rs8060457.

Vihma, T., J. Hartmann, and C. Lüpkes (2003). "A Case Study Of An On-Ice Air Flow Over The Arctic Marginal Sea-Ice Zone". In: *Boundary-Layer Meteorology* 107, pp. 189–217. DOI: 10.1023/A:1021599601948.

Wadhams, P. and T. Davy (1986). "On the spacing and draft distributions for pressure ridge keels". In: *Journal of Geophysical Research: Oceans* 91.C9, pp. 10697–10708. DOI: 10.1029/JC091iC09p10697.

Wilson, Earle A. et al. (2019). "Winter Upper-Ocean Stability and Ice–Ocean Feedbacks in the Sea Ice–Covered Southern Ocean". In: *Cover Journal of Physical Oceanography Journal of Physical Oceanography* 49. DOI: https://doi.org/10.1175/JPO-D-18-0184.1.

Yang, Guangning et al. (2019). "IceSat-2 ATLAS photon-counting receiver: initial on-orbit performance". en. In: *Advanced Photon Counting Techniques XIII*. Ed. by Mark A. Itzler, K. Alex McIntosh, and Joshua C. Bienfang. Baltimore, United States: SPIE, p. 10. ISBN: 978-1-5106-2621-8. DOI: 10.1117/12.2520626. URL: https://www.spiedigitallibrary.org/conference-proceedings-of-spie/10978/2520626/IceSat-2-ATLAS-photon-counting-receiver--initial-on-orbit/10.1117/12.2520626.full.

Ye, Y., G. Heygster, and M. Shokr (2016a). "Improving Multiyear Ice Concentration Estimates With Reanalysis Air Temperatures". In: *IEEE Transactions on Geoscience and Remote Sensing* 54.5, pp. 2602–2614. DOI: 10.1109/TGRS.2015.2503884.

Ye, Y. et al. (2016b). "Improving Multiyear Sea Ice Concentration Estimates with Sea Ice Drift". In: *Remote Sensing* 8.5. DOI: 10.3390/rs8050397.

Yi, Donghui et al. (Jan. 2022). "Arctic Sea-Ice Surface Elevation Distribution from NASA's Operation IceBridge ATM Data". en. In: *Remote Sensing* 14.1313, p. 3011. ISSN: 2072-4292. DOI: 10.3390/rs14133011.

Yu, X. et al. (2020). "Evaluation of Arctic sea ice drift and its dependency on near-surface wind and sea ice conditions in the coupled regional climate model HIRHAM–NAOSIM". In: *The Cryosphere* 14.5, pp. 1727–1746. DOI: 10.5194/tc-14-1727-2020.

Zhang, Zhilun et al. (2024). "Winter Arctic Sea Ice Surface Form Drag During 1999–2021: Satellite Retrieval and Spatiotemporal Variability". In: *IEEE Transactions on Geoscience and Remote Sensing* 62, pp. 1–20. ISSN: 1558-0644. DOI: 10.1109/TGRS.2023.3347694.

Zhou, Lu, Céline Heuzé, and Martin Mohrmann (2022). "Early Winter Triggering of the Maud Rise Polynya". en. In: *Geophysical Research Letters* 49.2, e2021GL096246. ISSN: 1944-8007. DOI: 10.1029/2021GL096246.

Zine, S. et al. (2008). "Overview of the SMOS Sea Surface Salinity Prototype Processor". In: *IEEE Transactions on Geoscience and Remote Sensing* 46, pp. 621–645. DOI: https://doi.org/10.1109/TGRS.2008.915543.

Zuo, Hao et al. (2019). *The ECMWF operational ensemble reanalysis–analysis system for ocean and sea ice: a description of the system and assessment.* DOI: 10.5194/os-15-779-2019.